FROM A SINGLE GRAIN TO MICROSTRUCTURE: HOW EXPLOSIVE GRAINS INTERACT UNDER SHOCK COMPRESSION

BY

LAWRENCE SALVATI III

DISSERTATION

Submitted in partial fulfillment of the requirements
for the degree of Doctor of Philosophy in Chemistry
in the Graduate College of the
University of Illinois Urbana-Champaign, 2023

Urbana, Illinois

Doctoral Committee:

Professor Dana Dlott, Chair
Professor Prashant Jain
Professor Nancy Makri
Associate Professor Nicholas Jackson

ABSTRACT

This dissertation seeks to develop shock compression experiments that are sensitive to microstructural features in plastic explosives. Plastic explosives, or PBXs, are mixtures of high-explosive grains packed together and suspended in polymer binders. These experiments target phenomena occurring on the micron-scale and nanosecond to microsecond time regime, known as the mesoscale. At this scale, shock waves interact with microstructural defects in plastic explosives, producing pockets of heat which can initiate deflagration but remain hard to simulate. The experiments in this work will use shock compression as a tool to pump plastic explosive mixtures with high-temperature hot spots and optically probe the deflagration progress. The future goal is for these experiments to be used by simulations of shock to detonation or shock to deflagration transitions. Compact laser-driven flyer plates will be used on to produce shock to deflagration experiments on many of different PBX compositions. Laser-driven flyer plate production is small scale (sub-mm) and high throughput compared to other shock compression methods. Because of these traits, many different solid explosives with different internal structures can be tested to better understand how the microstructure of a PBX changes the fate of a shock wave interacting with it. This will enrich discussions about the resistance against accidental detonations and inform engineering efforts such as machine learning workflows to predict the performance of specific solid explosive mixtures.

First, the introductory principles of shock-to-detonation chemistry will be introduced, including shock waves, basic detonation theory and current understanding of how structured materials create hot spots. Then, this work will explore methods of measuring and quantifying shock-to-deflagration at different time steps within in a lab setting, and the third and fourth

chapter will discuss methods to prepare high explosives and measure their internal structure. The chapters proceeding this put these concepts together to tell different stories of how a pocket of energy inside a bomb spread through different structures. The final discussion will be directly measuring shock waves as an initial shock transitions into a full detonation within plastic explosives. Put together, micron-sized defects inside of a plastic bomb interact with shock waves to form pockets of energy which spread inside a bomb to make an explosion; this dissertation will describe that journey.

The research described in this study is based on work at the University of Illinois, currently supported by the US Air Force Office of Scientific Research under awards FA9550-19-1-0027 and FA9550-19-1-0318, and the US Army Research Office under award W911NF-19-2-0037. Characterization of materials was carried out in part in the Materials Research Laboratory Central Research Facilities, University of Illinois.

ACKNOWLEDGMENTS

I lived and worked around individuals who I say, with no exaggeration, are extraordinary. The research could get rocky, and I could become quite mercurial. I believe it takes a strong stomach to be my friend, and I'm deeply thankful for everyone who has chosen to look past this and make my last 6 years great. This creates a unique challenge: expressing my appreciation in a couple paragraphs is proving more difficult than writing 258 pages of original research. Where do you even start?

My mother proved the sturdy rock of my life. Not unlike a well-made filing cabinet: my life was put in order and free from entropy's grip thanks to her. I owe a great deal of my life successes to her. My sister Anna, another battle-hardened chemist, was a source of guidance for me. Further, I'd like to also thank Wen and Ethan, who I consider surrogate family. This dissertation would not have been possible without you.

To those I have met in Champaign: without you, Illinois would have just been a barren corn field. In particular, the friends I met in my graduate program, many of whom I now consider dear friends. I'd like to give particular thanks to Siva Valluri, who not only shaped me as a scientist but has proven a brilliant friend. Dave Bianchi, Sean Carney and Duncan Nall, for always being there to talk to, hang out with, or run with in good times and bad. I'd like to thank the running club for providing a sense of community. Finally, those whose lives I had the privilege of intersecting with during my time here, it was an honor to have met you. I think there are some things you could learn by reading this dissertation, but if you only learn one it should be this: you are all incredible people. Thank you.

TABLE OF CONTENTS

CHAPTER 1: INTRODUCTION TO SHOCK WAVES AND HOW SHOCKS INITIATE PLASTIC EXPLOSIVES

1.1 Overview

This chapter will cover the basic concepts behind shock-wave induced chemistry. Including what shock waves are, what detonations are, and why this process is more complicated in plastic explosives than homogeneous materials. Shock waves produce chemistry because it instantaneously sends materials to a higher pressure and temperature state. This fact is already complicated because it is fast and irreversible since shock waves strongly perturb the very structure of the material. In materials with micron-scale defects, however, the process is even more complicated. Every small feature, from a dislocation inside of each crystal to the morphology of the crystals to the topological arrangement of crystals have a tangible influence on shockwave attenuation or propagation as it travels through a PBX. These considerations dramatically affect the success or failure of a detonation, as well as the kinetics of the initiation process.

1.2 Shock Wave Theory

1.2.1 Introduction

A shock wave is simply defined as a supersonic wave producing discontinuous jump in pressure: behind this wave the pressure is significantly higher than the ambient condition ahead of it. This is similar in principle to an acoustic wave, where a pressure wave is produced by molecules being pushed together along a wave. What makes a shock wave different is that the velocity of the pressure wave, referred to as the shock velocity, is faster than the translational speed of the molecules being pushed together, referred to as the particle velocity. That is, the

pressure disturbance is supersonic, creating extreme pressure-volume conditions while travelling through the material. For perspective, this work will explore shock waves travelling anywhere between 3 km/s up to 9 km/s, for some points of comparison, orbital debris is typically travelling at relative velocities of around 8-9 km/s. The pressure ranges being explored in this work range from around 10-40 gigapascals (GPa) and temperature jumps between 200-5000K. Understanding how the process unfolds is important in telling the story of shock initiation of explosives.

1.2.2 Theory: Conservation Equations and the Shock Hugoniot

The discussion of shock waves should be started by the simplifying case that it is purely one-dimensional to understand *how exactly* it is perturbing the systems being studied. Figure 1.1(a) shows a basic diagram of this simplified system: a 1-D supersonic pressure wave travelling at U_s with corresponding particle velocity u_p. The unperturbed region ahead of the wave is at thermodynamic equilibrium, at state (P_0, v_0, E_0) describing pressure, volume, and internal energy, respectively. The laws of conservation are enforced during a shock wave, imputing the following relationships between the shocked and unshocked states:

Mass: $$\frac{v}{v_0} = \frac{(U_s - u_p)}{U_s} \tag{1.1}$$

Momentum: $$P - P_0 = \rho_0 U_s u_p \tag{1.2}$$

Energy: $$E - E_0 = \frac{P(v_0 - v)}{2} \tag{1.3}$$

These equations already allow for estimates of some state variables. However, in experiments there are usually only a limited number of observables that experimentalists have access to. In this work, the particle velocity u_p is the primary observable: it can be directly measured in experiments by velocimetry. The remainder of these observables, such as pressure

and volume, are determined by the above equations and the material's Hugoniot relationship. The Hugoniot is not an equation of state, but an empirically derived relationship between the particle velocity and the shock velocity.[1,2] This relationship is typically linear for most materials in the range for which experiments in this dissertation will be performed, taking the following general formula:

$$U_s = A + bu_p \tag{1.4}$$

Parameters A and b are empirical parameters fit to experimental data of materials being shock compressed at different particle velocities and the velocity of the shock wave are simultaneously measured. There are hundreds, if not thousands of mixtures of explosives, powder sizes, and binders that make up the library of PBX materials, each with unique Hugoniot parameters. The parameters for many materials are available in literature databases[2], but for opaque materials is impossible to measure by optical probes such as interferometry (a method leaned on heavily in this dissertation). Where possible, these parameters will be used alongside estimations using shock impedance matching to predict shock pressures induced by flyer plates. Unfortunately, for certain mixtures being studied in this dissertation, it was impossible to limit the scope of study to materials in the data bases, meaning sometimes these parameters are unavailable. Where applicable, material Hugoniots will be predicted based on known material properties such as density and composition.

1.3 Shock-Induced Chemistry in Explosives

The chemical reactions which occur during shock compression often differ quite substantially from STP. When temperatures and pressures are high enough, the use of purely Arrhenius kinetics and thermal decomposition data tends to be unable to accurately model emerging detonation waves in solid explosives. If it does, then the specific decomposition

kinetics have very little internal consistency between experiments, as shown by Udaykumar *et al.*[3]

The problems faced by the shock physics community are twofold: difficulty of molecular-scale simulations to be scaled up, and a lack of experimental data at the so-called mesoscale. The mesoscale refers to the length scale of microns and nanosecond timescale. At this scale there are two major factors that complicate attempts at multiscale models: hot spot formation from physical defects and the reaction-kinetics limited emergence of detonation waves.

1.3.1 Hot Spot Theory

Hot spot theory in polymer-bound explosives (PBX) is a central concept to this dissertation, the main idea is simple: heterogeneities sensitize explosives to shock initiation. The sensitization is caused by the shock-generated, high-temperature pockets of localized heat, referred to as 'hot spots'. In Arrhenius-like models of decomposition, the locally high temperature dramatically shifts reaction rates in these localized regions, creating higher than average reaction rates. Figure 1.2 is a depiction of this process, where localized hot spots form during the shock compression of voids, cracks, crystalline defects, or impedance boundaries at crystal vertices. The locally high reaction rates result in heat propagating outward to where materials are only heated by the bulk change in temperature caused by the high pressure and volume state from the shock compression. These hot spots can potentially coalesce and grow to form a reaction front which is when it becomes a detonation.

PBXs are mainly a packed bed of explosive grains bound by a polymeric binder material. The result is an environment rife with structural characteristics. Figure 1.3 consists of electron micrographs of what the insides of these look like. They contain voids inside of crystals, voids in

the binder material, points where polymer binders delaminate from the explosive grains, and crystallite boundaries. When these sites are subject to the high pressures and strain rates involved in a shock wave, high temperatures are created by adiabatic compression[4, ,5], strain of crystals, especially at defects,[6,7] and 'reshocks' caused by shocks reflecting off the impedance boundaries between low-density binders and high density explosive crystals.[8]

The effect of this is clear, when taking homogeneous explosives, such as liquid nitromethane, and introducing heterogeneities and sources of hot spots, the material is rendered more sensitive to shock initiation.[8,9] The specifics, on the other hand remain difficult to pin down. It should be clear why: any experiment or theory to predict this behavior must be sensitive to hundreds, if not thousands, of different plausible reaction sites. This need for microstructurally aware data and theory has been the primary challenge in this field of research so far. The issues exist in the so-called mesoscale, on the order of nanoseconds timescales and micron length scales.

Various predictive models have been employed to moderate success. The most prevalent is the 'Ignition and Growth' model introduced by Tarver and Lee.[10] This reactive flow model is described by the following equation:

$$\frac{df}{dt} = I(1-f)^b \left(\frac{\rho}{\rho_0} - 1 - a\right)^x + G_1(1-f)^c P^y + G_2(1-f)^e f^g P^z \qquad (1.5)$$

Where f is the reaction progress (represented as mass fraction), ρ_0 is initial density, ρ is density, and $I, G_1, G_2, a, b, c, d, e, g, x, y$ and z are constants.[1,10] Each of the additive terms in the equation represent different stages observed, illustrated also in Fig 1.2: ignition of hot spots, hot spots propagating through material, and transition to detonation when hot spots coalesce, respectively. This is a phenomenological model, where the parameters are fit to shock initiated explosives at large scales, also found in large databases.[11] This system is not ideal for predictive

studies on explosives, especially if the type of shock or the PBX mixture being used is not thoroughly studied.

Further refinements were introduced later to help better inform the theory. Tarver and Nichols introduced the concept of hot spot criticality, which acknowledges the complicated interplay between decomposition kinetics and heat transfer of the unreacted material.[12] The theory is important because it acknowledges that not all hot spots are created equal, they must reach a specific size relative to its temperature in order to be able to breach thresholds for thermal run away and form a detonation front. This concept will be revisited quite often in this dissertation as effort is taken to isolate specific sources of heat and how they propagate.

The state of hot spot theory remains a purely phenomenological one, but more recent efforts are becoming much more sensitive to microstructures. One limitation was the lack of temperature probes sensitive to hot spot temperatures. Bassett *et. al* used emission pyrometry, a technique more sensitive to the highest temperature compared to bulk[13] by evaluating black body spectra, to determine how the presence of micron-sized voids increased the size and duration of hot spots by ~1000K.[4] This technique was later refined by Johnson *et. al* to track hot spots formed by crystalline defects and delaminations.[14,15] The complexity of this problem runs deep, the exact geometries of voids are being accounted for in models[5,16] , as well as molecular dynamics simulations to unify molecular scale reaction kinetics with micron-scale localization of energy.[17]

However, the complexity of structures needed for accurate predictions makes scaling molecular-level reactions up to hydrocode scales very computationally expensive, and it is still unclear how to simplify these structures.[18] There remains a gap in experimental data available to refine these studies in the case of molecular crystals embedded in shocked material. Commonly

available hydrocodes in theory and large gas-driven flyer plates have been useful for large length scales (millimeters or more) and bulk material properties. Meanwhile picosecond laser ablation experiments are useful to observe picosecond-resolution ignition of explosives, an aid for molecular-level models of phonon up-pumping needed for shock energy to couple to mechanical shock energy.[19,20] More data is needed on the mesoscale to aid in methods to unify these methods, such as Udaykumar's 'meso-informed' ignition and growth models.[21,18]

1.3.2 Detonation Theory

There are multiple paths for a shock to form a detonation front. The first one, previously mentioned is when localized pockets of high heat propagate the reaction. The alternative is homogenous detonation mechanisms, widely understood to be dominant once conditions reach certain pressure thresholds. The most prevalent model is the Zel'dovich von Neuman Doring model (ZND).[22] The process is illustrated in Fig 1.4, an initial pressure spike, higher in magnitude than the detonation wave leads the shock wave. The effect of this is to send the unreacted explosive to an extreme pressure-volume state, through a combination of local heating and phonon up-pumping[20] reaches a chemically excited state in which rapid decomposition can initiate. What proceeds is the chemically excited molecules in the leading edge of the shock wave decompose to generate heat, and pressure in the form of large volume of hot gas, that translates to, mechanical work which propels the shock wave. Most of these explosives consist of nitrate esters where decomposition is auto oxidized, making this process very fast. The region referred to as the reaction zone, is a region after the shock wave in which mass flow from decomposition exceeds bulk sound speed of the material (though subsonic in the frame of the leading shock). As a result, the chemistry that happens in this region is what sustains the shock wave, giving it the characteristic of being a detonation. This region can range from <100 μm,

such as in the sensitive Pentaerythritol tetranitrate (PETN) used often in demolition cords, and 100s of microns in the much less sensitive Triamino trinitrobenzene (TATB) commonly used for explosive lensing in nuclear bombs.[1,22] During this time, a majority of available chemical energy is released over the time span of nanoseconds, producing heat and work characteristic of explosives. The back end of this wave is mostly gaseous products, if decomposition is still occurring it is happening too slowly to contribute to the detonation wave sub-sonic. The plane where the reaction zone ends and subsonic chemistry begins is called the Chapman-Jouget plane (CJ plane) and the pressure and location of this plane is indicative of the decomposition kinetics of the particular explosive being studied.[1] The anatomy of a detonation wave speaks a lot to the kinetics happening during the process, but looking inside a detonation wave after it has already formed does not directly elucidate details on mechanisms and also misses what happens as the wave is initially forming.

Exact understanding of the non-equilibrium chemistry occurring in this type of decomposition is a point of interest for theorists. The process was previously assumed to be instantaneous[22] but now is understood to include complexities such as induction times involved in the excitation process and breakdown of Arrhenius kinetics at extreme temperatures typical of detonations (>1000K).[23,24] It stands to reason that rate limiting chemistry should be observed on the mesoscale, where the time and length scales of the reaction zones lay. In fact, the Dlott group did observe detonation waves forming slower than continuum scale predictions anticipated in the homogenous explosive nitromethane.[25] The open question is whether laser-driven flyer plate methodology can be used to track the evolution of detonation waves. This would answer important questions such as what shock pressure regimes are necessary for microstructure to matter, and whether evolution of the shock wave into a detonation, known as the shock to

detonation transition (SDT) can be measured on the micron scale and used for chemical kinetics calculations. Since laser-driven flyer plates produce shocks only lasting from 5-20 ns, and cylindrical samples of length between 30 μm to several hundred microns can be produced, it is possible this length scale can show interesting mesoscale effects on reaction kinetics.

1.4 Research Objectives

The current work with laser-driven flyer plates on plastic explosives lacks detailed information on the structures formed by grains bound in polymers, and how this behavior changes the shock sensitivity and reaction kinetics. These are very difficult problems requiring the marriage of flyer plate shock experiments with theoretical models of shock to deflagration and shock to detonation. The goal of this work is developing the methods by which this work can be done on the experimental end. In saying, answering the questions left open when emission pyrometry of explosives was developed: how this can be developed into a quantitative measure of how structure changes chemistry. There are many components to this issue that will be broken down as such:

1. How to create micron-sized plastic explosive samples with repeatable microstructures
2. How can microstructure of these samples be directly observed in these samples?
3. In what ways can the microstructure be reduced to lower dimension measurements?
4. Can emission pyrometry, including radiance and temperature measurements, be used as a quantitative tool to compare shock ignition success rates at different steps of the process?
5. Can emission pyrometry and microstructure observations be unified to determine limiting behavior of explosives?
6. Can emerging detonation waves be measured with these new methods?

1.5 Organization of this Dissertation

This dissertation is organized to chronologically answer the preceding questions. First, the methods of producing small-scale shock waves on a tabletop microscope are described, including how to track light production and pressure waves with nanosecond time resolution. Then a study of how to image the inside of these disordered mixtures of organic binders and molecular crystals, a problem made difficult by the need for sub-micron resolution on materials not amenable to most probing techniques. Following this, a study of a densely packed, insensitive explosive igniting will outline how emission pyrometry data is analyzed to quantitatively gauge different steps of the shock initiation process. These concepts will be put together in the next part where the concentration of an explosive in a soft polymer binder is changed, exploring a very low to very high concentration ranges. By doing this, the explosive changes from a simplified, idealized mixture of isolated grains in binder, to adding progressively higher orders of structural complexity. A new method of quantifying microstructure will be evaluated by isolating one individual factor in particular: grain clustering. Proposed methods of photographing the process of shock initiation of these grain clusters to track reaction progress across grains proceeds this. Finally, the discussion will shift to an extensive discussion on how emerging shock waves caused by shock initiation are tracked and analyzed.

1.6 Figures

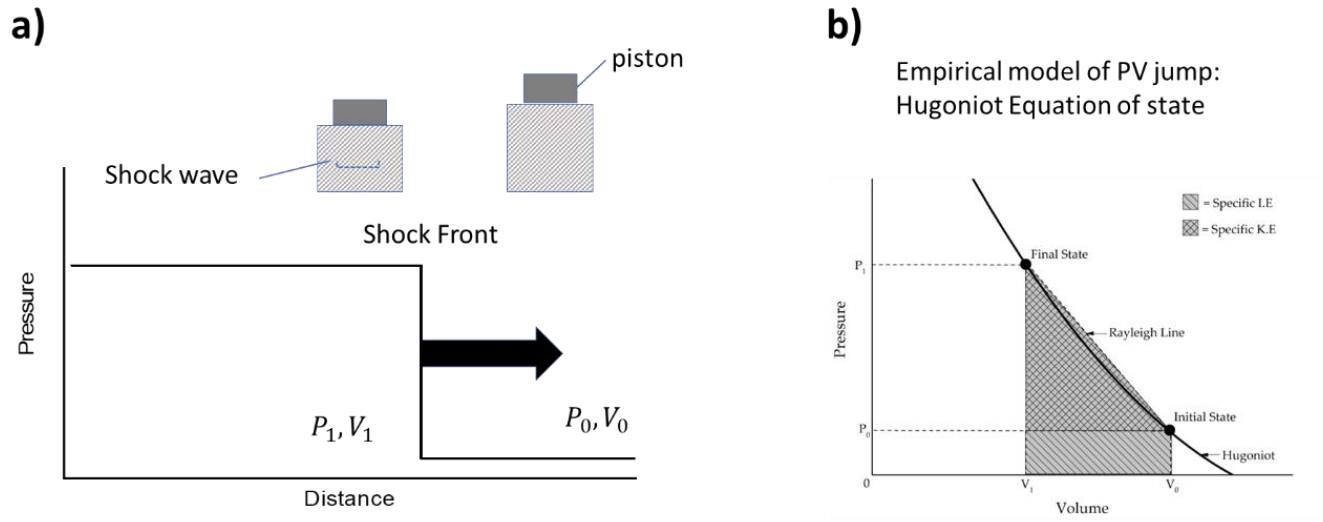

Figure 1.1 A simplified 1-dimensional view of a shock wave in non-reactive material (a)[1]. The empirical equation of state relating the pressure-volume state of the uncompressed material to its compressed state, called the hugoniot, is a nonlinear curve whose PV states are connected by the intersection of a Rayleigh line (b).

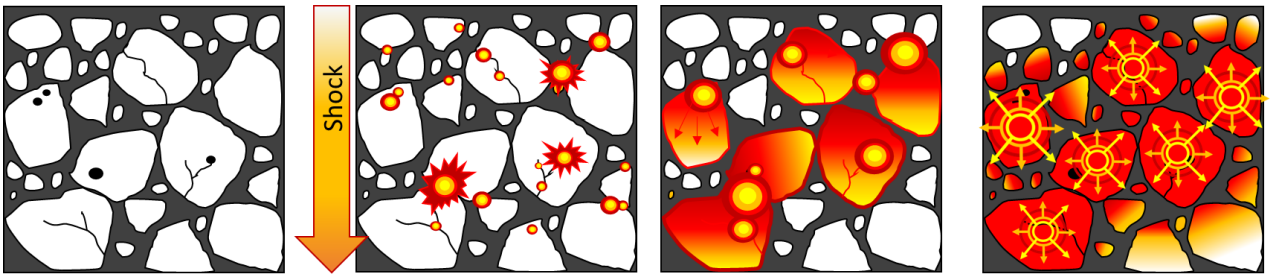

Figure 1.2 An illustration of the hot spot ignition and growth model of explosive initiation. A structure containing many defects are exposed to a shock wave, producing pockets of energy that initiate decomposition of the surrounding material. The burn centers begin to overlap and form a reaction front that eventually becomes a detonation wave.

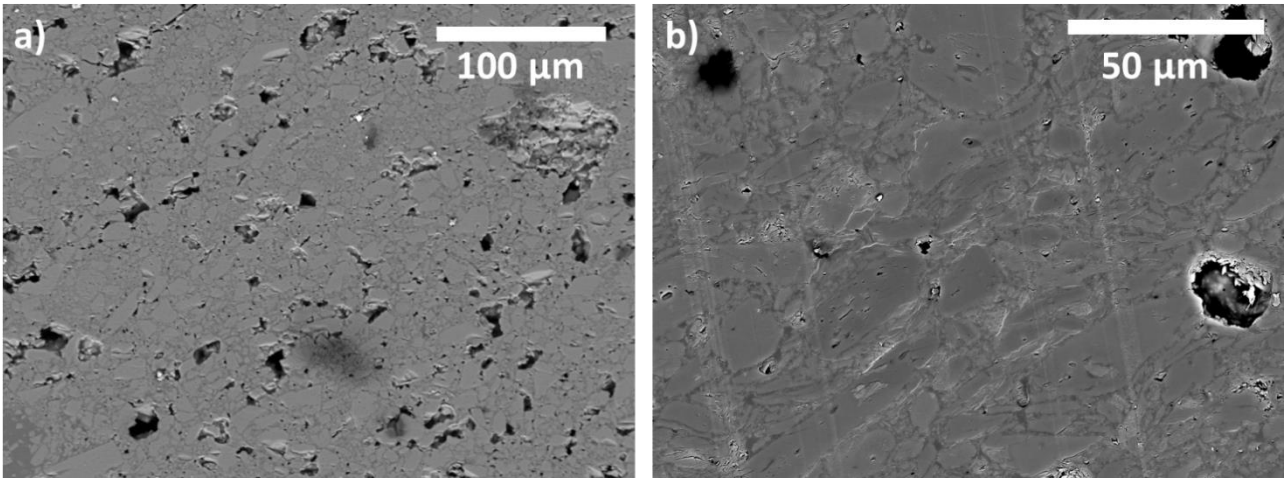

Figure 1.3 SEM micrographs showcasing the highly structured nature of plastic explosives (PBXs) on the micron scale. These are microtomed samples of explosive crystals in epoxy binder, the light phase is the explosive crystals and the dark phase is the soft binder. Two different materials were shown, 85 wt.% fine crystals of PETN (a) displaying many voids due to the packing dynamics, and 85 wt.% of graphitic-like TATB crystals in binder (b). These concentrations are typical of commonly used explosives, albeit slightly less dense.

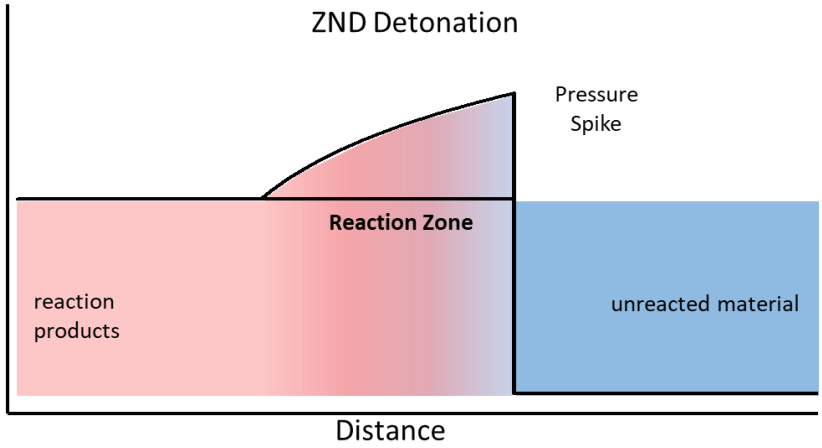

Figure 1.4 An illustration of a detonation wave in a high explosive modeled under the Zel'dovich von Neuman Doring model.

1.7 References

1. Forbes, J. W. *Shock Wave Compression of Condensed Matter: A Primer*; Springer Berlin Heidelberg: Berlin, Heidelberg, 2012.
2. Marsh, S. P. *LASL Shock Hugoniot Data*; University of California Press, Berkeley, 1980.
3. Rai, N. K.; Koundinyan, S. P.; Sen, O.; Schweigert, I. V.; Henson, B. F.; Udaykumar, H. S. Evaluation of Reaction Kinetics Models for Meso-Scale Simulations of Hotspot Initiation and Growth in HMX. *Combust. Flame* **2020**, *219*, 225–241.
4. Bassett, W. P.; Johnson, B. P.; Neelakantan, N. K.; Suslick, K. S.; Dlott, D. D. Shock Initiation of Explosives: High Temperature Hot Spots Explained. *Appl. Phys. Lett.* **2017**, *111* (6), 061902.
5. Rai, N. K.; Udaykumar, H. S. Void Collapse Generated Meso-Scale Energy Localization in Shocked Energetic Materials: Non-Dimensional Parameters, Regimes, and Criticality of Hotspots. *Phys. Fluids* **2019**, *31* (1), 016103.
6. Sewell, T. D.; Menikoff, R.; Bedrov, D.; Smith, G. D. A Molecular Dynamics Simulation Study of Elastic Properties of HMX. *J. Chem. Phys.* **2003**, *119* (14), 7417–7426.
7. Roy, S.; Johnson, B. P.; Zhou, X.; Nguyen, Y. T.; Dlott, D. D.; Udaykumar, H. S. Hot Spot Ignition and Growth from Tandem Micro-Scale Simulations and Experiments on Plastic-Bonded Explosives. *J. Appl. Phys.* **2022**, *131* (20), 205901.

8. Menikoff, R. Hot Spot Formation from Shock Reflections. *Shock Waves* **2011**, *21* (2), 141–148.

9. Turley, W. D.; La Lone, B. M.; Mance, J. G.; Staska, M. D.; Stevens, G. D.; Veeser, L. R.; Dattelbaum, D. M. Experimental Observations of Shock-Wave-Induced Bubble Collapse and Hot-Spot Formation in Nitromethane Liquid Explosive. *J. Appl. Phys.* **2021**, *129* (14), 145102.

10. Lee, E. L.; Tarver, C. M. Phenomenological Model of Shock Initiation in Heterogeneous Explosives. *Phys. Fluids* **1980**, *23* (12), 2362. https://doi.org/10.1063/1.862940.

11. Dobratz, B. M. *Properties of Chemical Explosives and Explosive Simulants*; UCRL--51319, UCRL--51319(REV.1), 4285272; 1972; p UCRL--51319, UCRL--51319(REV.1), 4285272.

12. Tarver, C. M.; Chidester, S. K.; Nichols, A. L. Critical Conditions for Impact- and Shock-Induced Hot Spots in Solid Explosives. *J. Phys. Chem.* **1996**, *100* (14), 5794–5799.

13. Bassett, W. P.; Dlott, D. D. Multichannel Emission Spectrometer for High Dynamic Range Optical Pyrometry of Shock-Driven Materials. *Rev. Sci. Instrum.* **2016**, *87* (10), 103107.

14. Johnson, B. P.; Zhou, X.; Ihara, H.; Dlott, D. D. Observing Hot Spot Formation in Individual Explosive Crystals Under Shock Compression. *J. Phys. Chem. A* **2020**, *124* (23), 4646–4653. https://doi.org/10.1021/acs.jpca.0c02788.

15. Johnson, B. P.; Zhou, X.; Dlott, D. D. Shock Pressure Dependence of Hot Spots in a Model Plastic-Bonded Explosive. *J. Phys. Chem. A* **2022**, *126* (1), 145–154.

16. Li, C.; Strachan, A. Shock-Induced Collapse of Porosity, Mapping Pore Size and Geometry, Collapse Mechanism, and Hotspot Temperature. *J. Appl. Phys.* **2022**, *132* (6), 065901.

17. Lee, B. H.; Sakano, M. N.; Larentzos, J. P.; Brennan, J. K.; Strachan, A. A Coarse-Grain Reactive Model of RDX: Molecular Resolution at the μ m Scale. *J. Chem. Phys.* **2023**, *158* (2), 024702.

18. Nguyen, Y. T.; Seshadri, P. K.; Sen, O.; Hardin, D. B.; Molek, C. D.; Udaykumar, H. S. Multi-Scale Modeling of Shock Initiation of a Pressed Energetic Material. II. Effect of Void–Void Interactions on Energy Localization. *J. Appl. Phys.* **2022**, *131* (21), 215903.

19. Dlott, D. D.; Fayer, M. D. Shocked Molecular Solids: Vibrational up Pumping, Defect Hot Spot Formation, and the Onset of Chemistry. *J. Chem. Phys.* **1990**, *92* (6), 3798–3812.

20. Jaramillo, E.; Sewell, T. D.; Strachan, A. Atomic-Level View of Inelastic Deformation in a Shock Loaded Molecular Crystal. *Phys. Rev. B* **2007**, *76* (6), 064112.

21. Nguyen, Y.; Seshadri, P.; Sen, O.; Hardin, D. B.; Molek, C. D.; Udaykumar, H. S. Multi-Scale Modeling of Shock Initiation of a Pressed Energetic Material I: The Effect of Void Shapes on Energy Localization. *J. Appl. Phys.* **2022**, *131* (5), 055906.

22. Bdzil, J. B.; Stewart, D. S. The Dynamics of Detonation in Explosive Systems. *Annu. Rev. Fluid Mech.* **2007**, *39* (1), 263–292.

23. Tarver, C. M.; Forbes, J. W.; Urtiew, P. A. Nonequilibrium Zeldovich-von Neumann-Doring Theory and Reactive Flow Modeling of Detonation. *Russ. J. Phys. Chem. B* **2007**, *1* (1), 39–45.

24. Tarver, C. M. Chemical Energy Release in Self-Sustaining Detonation Waves in Condensed Explosives. *Combust. Flame* **1982**, *46*, 157–176.

25. Bhowmick, M.; Nissen, E. J.; Dlott, D. D. Detonation on a Tabletop: Nitromethane with High Time and Space Resolution. *J. Appl. Phys.* **2018**, *124* (7), 075901.

CHAPTER 2: MEASURING SHOCK INITIATION ON THE TABLETOP

2.1 Introduction[1]

Shock compression experiments exist in many forms with varying geometries and sources of impact. Shock physicists have been tasked with comparing data from pound-scale compressed gas guns whose shocks last several milliseconds all the way down to laser-ablation experiments which last picoseconds. It is of great importance to describe shock compression setups of any kind in detail with two goals in mind: first, to convey its similarities and differences to the wider shock field, and second, to explain the fidelity with which the data can be understood. This chapter will be dedicated to accomplishing both goals.

The experimental setup used in the research consists of a laser-driven flyer plate setup sitting inside an inverted microscope (Olympus IX73) and an output flange that directs emitted lights and photographic images to a wide array of detectors. The schematic of these distinct parts is referred to collectively as the 'Shock Microscope', shown in Figure 2.1. Several publications from within Dana Dlott's group have explained the anatomy of this design of experiment and can be explored

[1] The introduction to photon doppler velocimetry (PDV) and its uses is partially adapted from work published in the original research article- Bhowmick, M.; Basset, W. P.; Matveev, S.; Salvati, L.; Dlott, D. D. Optical Windows as Materials for High-Speed Shock Wave Detectors. *AIP Advances* **2018**, *8* (12), 125123, with the permission of AIP Publishing. The PDV data collection of glass over several conditions was collected and analyzed by Lawrence Salvati. The analysis methods for PDV were developed by Lawrence Salvati adapted from previous works[1,2].

for further reading[3,4,5,6]. This chapter will emphasize the aspects most relevant to understanding the proceeding results. Starting with explaining the individual parts then converging to how they work in tandem.

2.2 Laser-Driven Flyer Plates

Flyer plates, as briefly discussed in Chapter 1, refer to flat, usually cylindrical plates launched at a surface to induce a briefly supported shock wave. Traditionally this method employs a pressurized gas and several meters of tubing to take plates to their terminal velocities. Laser-driven methodologies are far less orthodox, instead using plasma generated by a laser to propel cylindrical foil cutouts to their terminal velocity. Figure 2.2 draws out the exact anatomy of this procedure. A high energy infrared laser is focused onto a foil backing to achieve a small projectile.

Using pulsed lasers to generate foil projectiles is not by any means new or novel, with its first examples coming from the 1990s and being adopted by the Dlott lab as a means of generating small scale shock waves[3,4]. The pulsed source in question is a Neodinium-doped YAG (Yttrium Aluminum Garnate, henceforth referred to as Nd:YAG) laser (SpectraPhysics Quanta Ray Pro) capable of producing a 10 nanosecond duration ($1/e^2$) of up to 2.5 Joules of total energy (elongated to 20 ns by pulse stretching[3]. Nd:YAG lasers are common in pulsed systems, capable of generating high energy and the fundamental wavelength (1064 nm, just past near infrared) has good transmission through glass while readily heating up organic materials such as epoxies.

The shape of this laser must be modified to produce the desired effect when cutting out a piece of foil: it must be roughly cylindrical and planar across a known diameter. Figure 2.3 is a picture of the beam profile after it is modified to launch flyer plates. A diffractive optic (Silios) is

used to create a first order diffraction pattern whose image is a spatially flat profile across approximately 500 microns.

The experiments in this work often deals with materials which are opaque in nature, thus impossible to directly measure the pressure or duration of the shock produced by these foils. Nor is it possible for us to gather the exact size and shape of the *entire* projectile via direct means, and most often analysis of the projectile relies on postmortem analysis, though some studies of the flyer in situ using flash photography verify the approximate size estimates[7]. For this work, a laser-driven flyer plate will be defined as such: a cylindrical projectile with a 500-micron diameter, planar surface made from a metal foil launched by a focused, high-energy laser.

In the case of aluminum foils, the duration of shock support and maximum pressure sit at far lower values than in traditional flyer plates. Depending on the thickness of the aluminum foil, flyer plat shocks have durations between 4 ns and 20 ns. In this case of 25 μm thick aluminum foil, the velocity history of a flyer plate in launch and impact is shown in Figure 2.4. However, laser driven flyer plates carry an important upside: very high throughput. Because the plate is generated and launched *in situ* by a laser focused on foil, a single 3-inch square sheet of aluminum foil can generate up to 187 flyer plates which can be shot and measured on the time scale of an hour. The data in this work will often leverage this feature by testing a large array of sample compositions and shock conditions all at once.

2.2.1 Preparation of Flyer Plates

The laser-driven flyer plates are produced from a glass (Pyrex) sheet with a metal foil glued to the surface of the flyer plate. Two 2” square or 3” square, 6mm-thick Pyrex glass sheet are cleaned using Alkanox surface cleaner, then rinsed with ethyl alcohol. The glass plates are

dried with wiped clean using a razor edge, then dried with a nitrogen gas line. The metal foil is rinsed using ethyl alcohol then placed on the clean face of one of the glass sheets. A stainless-steel rod is rolled onto the foil to flatten the surface and remove any wrinkles from the foil. The surface is then dried with a nitrogen gas line. This surface will have the epoxy applied to it.

The glue is a 2-part epoxy (Loctite Abelstik 24, Henkel), part A is weighed in a scintillating vial, and 28 wt.% of part B is added. After thorough manual mixing until the solution becomes clear, the mixture is placed under mild vacuum for 5-10 minutes to relieve bubbles from the mixture. Using a 3 mL pipette, 3-4 drops of epoxy mixture are placed on the aluminum surface. The second sheet of glass is then placed on the glue/foil surface clean-side down. A third sheet of glass is placed on top of the stack for even pressure, and 2 spring clamps are used to hold the setup together. The epoxy can be cured at room temperature for 24 hours or in a 100° C oven for 1-2 hours. The epoxy generally ranges from 3-5μm thickness.

The most common foils used are Aluminum 1100, in thicknesses of 25,50,75 or 100μm due to having the highest range of flyer velocities available to the shock microscope. This is due to the lower density of aluminum compared to more ideal alternatives such as Tantalum foil, Iron, or Stainless steel. The high density of these materials makes it difficult to drive by a laser, even with 2.5J. Higher energy lasers can be used to drive these materials to speeds amenable to experiments. As Fig 2.2 shows, the flyer is placed inside an assembly of a vacuum manifold (custom built) with a stainless-steel spacer to allow free flight (cutom built, from 375μm-1mm thick) and a victim sample. The vacuum prevents air-compression from occurring, which producing large quantities of light and heat that spoils experimental results. While this can be used as a rudimentary trick for time-of-flight calculations, it is otherwise detrimental and

requires vacuum below 1 Torr to avoid. Most experiments range from 100-250 mTorr vacuum environments.

2.3 Photon Doppler Velocimetry (PDV)

2.3.1 Overview

Velocimetry, the ability to measure speed and velocity of surfaces, is a necessity in shock compression experiments to be able to describe the impactor speeds and pressures of events. The shock compression microscope uses Photon Doppler Velocimetry (PDV), a measurement technique that relies on the doppler-shift of light reflecting off a normal surface to determine speed. A diagram of the PDV is shown in Fig 2.6. This setup is constructed from an infrared fiber optic laser coupled to standard fiber optic hardware based on the work of Strand *et. al.*[8] By measuring the doppler-shift of the laser reflected off of a reflective moving object, it is able to measure a beat frequency by mixing with a reference.

A 1550 nanometer continuous wave fiber laser is first amplified by a Erbium-Doped Fiber Amplifier (EDFA) from ~+7.0 Dbm (~5 mW) to +17 mW (50 mW). The higher power is needed to offset poor infrared transmission through the objective lenses used but is capped at 50 mW to prevent damage at fiber interfaces. Fibers used are generally single-mode FC/APC terminated, with a mode-field diameter of 10.5μm (Thorlabs SMF-28 Ultra Fibers, see appendix A.4 for components list). This beam is split by a 90:10 beam coupler: the 90% signal beam will be reflected off a moving surface, and the 10% reference beam will be used as a frequency reference. For optimum PDV signal, the signal and reference channels should be equal in intensity[9]. Accounting for the loss of the optics in the shock microscope and the somewhat poor reflectivity of unpolished aluminum, this splitter gave the most optimal signal. The signal and

reference beams were combined in a 3×3 mixer (OEQuest). Three 20 GHz AC-coupled photodiodes, Narda Miteq SCMR-100K20G, detected the mixer output, and their signals were fed into an 8 GHz digital oscilloscope, Tektronix DPO70804. The oscilloscope sampled the outputs of the three detectors with a 25 GHz sampling rate (40 ps per point) on three channels. For a few measurements, we were able to borrow a 23 GHz digitizer, Tektronix DPO73304SX, with a 100 GHz sampling rate on two channels. With the 3×3 mixer, the three photodiode signals are nominally 120◦ out of phase. The signals are averaged from the three detectors. The signal from any of the three detectors is described by the following equation[10,9]:

$$I(t) = 2\sqrt{AI_rI_c}\cos\big(\Phi(t)\big) \qquad (2.1)$$

A is an amplitude normalization factor to account for slightly different coupling efficiencies and detector sensitivities. This is an empirical factor determined by taking a long, slow PDV signal of near constant intensity for all three channels. The maximum amplitude of each channel is normalized with factor A_i for $i = 1,2,3$ specific to each detector such that $I_1 = I_2 = I_3 \approx 1/3$. I_r and I_c are the reference and signal beam intensities, and $\Phi(t)$ is the modulated part of the signal reflected from the moving surface. The result is a sinusoidal plot of the beat frequencies, referred to as the interferogram, with a time dependent frequency f_{shift}.

When the signal beam is reflected off the surface of the flyer plate in motion, its frequency changes by the quantity f_{shift} described by the following equation:

$$f_{shift} = f_{laser}\left(\frac{c}{c+v_s}\right) \qquad (2.2)$$

Where c is the speed of light and v_s is the surface velocity. When modified, flyer velocity can be calculated by the following equation:

$$v_s = f_{shift}\left(\frac{\lambda_{laser}}{2}\right) \quad (2.3)$$

Where $\lambda_{laser} = 1550$ nm is the laser wavelength. The doppler shift (f_{shift}) measured by mixing the reference (source) frequency with the signal (doppler-shifted) frequency using a 3x3 optical coupler, resulting in a beat frequency equal to the doppler shift. This is measured by an AC-coupled photodetector and digitized on an 8 GHz oscilloscope. The AC coupling isolates the signal modulation due to beat frequencies from the reference light source and some inherent phase offsets from the different optical paths of each leg. The resulting beat wave (the interferogram) can be converted to a beat frequency in post processing. Figure 2.5 is an example of the raw interferogram and how it looks when transformed to a frequency history.

2.3.2 Short-Time Fourier Transform Analysis

To get a velocity from PDV, the interferogram must be converted from an intensity-time plot to a time-dependent frequency plot. This study relies on two methods of measuring frequency, which will depend on the specific needs of the study: Short time Fourier transform (STFT) and algorithmic fringe counting. STFT is the most common method of analysis due to its speed and versatility, with the latter procedure requiring a very high signal to noise ratio to work properly. This method is outlined in Dolan's reports[9,11], in his publication on accuracy and uncertainty[12], and shown the thesis work of William Shaw[1] for additional reading. The following description only serves to enumerate essential points needed to describe the fidelity and limitations of velocimetry data done in this work. STFT methods rely on polling wave frequencies inside limited time windows across a data set, compared to a typical Fourier transform which collects a single frequency spectrum across an entire waveform. The window chosen for each time point is often is truncated along the edges, and in this case is a Hamming

window. The following weighted waveform is then Fourier transformed, giving a spectrum whose peak is representative of the frequency of the wave. The fitted center point can then be plotted over several time points to evaluate doppler shift over the time of the event being measured.

This method carries the intrinsic property of all Fourier transformations: the uncertainty principle. The width of the Hamming window used is inversely proportional to the frequency uncertainty of the final frequency plot:

$$\Delta f\tau \geq \frac{1}{4\pi} \tag{2.4}$$

This equation identifies the hard limits on using Fourier transformations for data analysis. A common Hamming-window width in time-dependent data analysis is 5 ns. In this case the flyer velocity cannot expect to be known beyond $\Delta f \geq 12.5$ m/s. It is important to mention this as a limit but will be contextualized later in the chapter. There are generally significantly greater sources of uncertainty in these measurements from operator error alone, and most importantly signal aliasing from lower frequency signals, and many experiments deal with phenomena whose surface velocities exceed 1 km/s. In the case of simply estimating terminal flyer velocities, this is counteracted by taking a long time Fourier transform of a flyer that has reached terminal velocity. The spectrum collapses into a spike whose width can be quantified as the error. The exact implementation of this analysis can be found in Appendix A.2.3.

2.3.3 Velocity Determination by Peak-Finding

Shock pressure data often highlights the limitations of STFT due to frequency changing on the nanosecond time scale and covering a high range of pressures in short time. The biggest shortcoming of STFT is the need for a Hamming window, and the resultant lack of precision that

comes along with it. While it's generally sufficient for >100 ns phenomena, it will inevitably produce a smoothing effect while also producing high amounts of aliasing at velocities under 1 km/s unless the Hamming window width is increased beyond 10 ns. However, if the signal to noise is good then it is possible to algorithmically find the peaks and troughs of the interferogram. The time resolution of an interferogram is still limited to the minimum distance between fringes. It is inversely proportional to the velocity measured. Figure 2.7 shows the velocity history of a flyer impacting glass using STFT and peak-finding analysis. The improvement to time resolution is generally subtle but does prevent both aliasing effects and smoothing effects. It is very slightly more accurate for dynamic events like <2 ns rise times if the signal to noise is very good. However, STFT is still quite accurate when this is not possible.

Because PDV is the result of multiplexing a signal and a reference frequency through a 3x3 optical coupler, there are 3 signal sources in the PDV. This is commonly leveraged for quadrature analysis to determine velocity rather than speed since the signals arrive at a $2\pi/3$ phase offset. The effect is an increase in the density of fringes, dramatically increasing the time resolutions of PDV data. The extra detectors also adds the ability to determine the direction of the velocity vector[13]. However, quadrature analysis and complex Fourier transforms go beyond the scope of this dissertation as they are not used since the direction of motion is always known *a priori*. For more reading on this see Ref. 1. See Appendix A for details on how this analysis is executed in practice.

2.4 Using PDV to Measure Pressure of Impacts

Having a robust methodology to study intensive properties of shocked materials, namely pressure and temperature, is necessary to understand shock-initiated systems. Measuring pressure is often done directly by inserting several transducers, materials whose resistance changes with

pressure, inside the sample while being shocked[14]. These methods are more precise but difficult to implement on the high-throughput, small scale shock compression microscope. An alternative route to pressure measurements is measuring the velocity of a reflective surface by PDV. Knowing this velocity would provide the particle velocity of the shock wave, which can be converted to pressure from the Hugoniot relations. The reflective surface needs to be between the studied sample and a transparent medium, be it free space or a window. In either case, what PDV will be measuring at an impedance boundary. As mentioned in Chapter 1, when a shock meets an impedance boundary, the shock pressure will be equal at the interface, and some shock energy will inevitably be reflected into the shocked material. The result is that the interface between sample and window is where particle velocity, and therefore shock pressure can be measured in any materials. This is not a perfect measure, but the most amenable to the shock compression microscope. To continue using this, its properties and limitations must be discussed.

2.4.1 Using Optical Windows for Shock Experiments

We performed experiments using PDV to study the nanosecond time scale response of various window materials to planar shocks produced by 1-4 km/s flyer plate impacts or by planar detonation shocks generated in high explosives. When used as a shock wave detector material, the window is placed adjacent to the sample of interest, and the velocity imparted to the window material when the shock breaks out of the sample medium into the window is measured using PDV But a shock wave detector differs from ordinary detectors, because while measuring the shock wave profile, the detector material itself is destroyed. The physical properties of the detector material change dramatically during the shock measurement process. In addition, shocked windows exhibit strong hysteresis. Window response to compression is generally quite different from its response to tension, and since shock waves ordinarily have a steep compressive

shock front and an expansive tail[14], the detector material responds differently to the imparted tension and compression. These factors greatly complicate the problem of deducing the desired but unknown input waveform from the detector output.

Here we will focus on the problem of understanding what is the best window material for reconstructing the waveform of a detonation shock produced by a high explosive[15]. For common model explosives such as nitromethane and secondary explosives they experience <2 ns rise times[16,17] peak pressures of tens of GPa and durations of tens of nanoseconds. We studied polycrystalline windows (sapphire, CaF2 and LiF), inorganic glasses (Pyrex, BK7, fused silica and Gorilla Glass) and glassy organic polymers (Plexiglas and Lexan). Figure 2.8 depicts our technique for measuring a detonation shock using an optical window. A flyer plate launches a shock in the explosive that evolves into a detonation. When the detonation breaks out, it drives a shock into the window that first passes through an ultrathin mirror (which we view as nonperturbative since its shock ring-up time2 <0.1 ns). PDV measures the velocity profile of the mirror, which is equivalent to the velocity of the contacted explosive-window interface. Knowing this material velocity profile, denoted $U_p(t)$, the time-dependent pressure and density in the window can be computed given the window materials Hugoniot equation[14,18]. Having measured the detector output to yield the window velocity profile, we then wish to infer the sample velocity profile, which, knowing the sample Hugoniot, can be used to compute the time-dependent pressure and density in the sample.

When the shock arrives at the window, the nature of the transmitted waveform depends on the shock impedance[14] $Z = \rho U_s$, where Z is the impedance, ρ the density and U_s the shock velocity. Harder materials such as diamond and sapphire have higher shock impedances while softer

materials such as organic polymers have lower shock impedances[18]. For a steady shock of pressure P_a moving from medium a to medium b, the pressure in medium b is given by[14],

$$P_b = \frac{2P_a}{1+\frac{Z_a}{Z_b}} \tag{2.5}$$

Although Eq. 2.5 refers to steady shock propagation, and our shocks are short-duration and transient, in our simplified approach we use Eq. 2.5 by treating the shock impedance of medium b as pressure and time dependent. The pressure and time dependence of the shock impedance arise because material properties that ultimately give rise to the impedance, such as density and temperature, are time dependent. If the window impedance increases during the shock, it can be viewed as the shocked material becoming harder or stiffening up. If the window impedance decreases during the shock, it can be viewed as the shocked material losing strength (becoming softer). The time-dependent impedance of the window material will affect the velocity profile of the moving mirror in Fig. 2.9. The time dependence and magnitude of the impedance change during the measurement process will distort the detected shock waveform. We need to understand how the impedance depends on velocity and time in both compression and expansion. Obviously, this method is an approximation that extends Eq. 2.5 from steady shocks to into the transient shock and transient shock impedance regimes. We deal with this problem by conducting experiments where we study window response to reference shocks whose amplitudes and durations are in the same range as the detonation shocks we wish to measure. Even though many of the window materials we study here have been investigated before, most published data uses shock durations in the 0.1 to 10 μs range, and we need data on the nanosecond time scale to resolve detonation shock structure.

We studied polycrystalline windows, inorganic glass windows and glassy organic polymer windows. The polycrystalline windows were A-plane cut sapphire from Rubicon Technology, Inc., LiF from Alkor® and CaF2 from University Wafer, Inc. The inorganic glass windows were Pyrex from Chemglass®, and BK7, Gorilla Glass and fused silica from Edmund Optics. The glassy polymer windows were Plexiglas from McMaster Carr, and Lexan from Illini Plastics. Plexiglas is a proprietary form of PMMA and Lexan a proprietary form of polycarbonate. For PDV measurements, the windows were coated with ~100 nm thick electron-beam deposited Au mirrors. The mirrors are generated using a Temescal Ebeam Evaporator, the recipe applies a 5 nm Chromium layer to aid gold adhesion (particularly in the case of glass), followed by ~100 nm of Au coating. This is highly reflective to IR light, while simultaneously being thin enough to have little impact on the shock impedance. If optical transparency is needed, then Au layers need to be < 15 nm thick.

When evaluating PDV through a shock compressed window, it is important to consider the transit time of the probe laser through the material. As a material is compressed by shock, the index of refraction increases relative to specific volume (i.e density) by the following relation:

$$n = a(\lambda) + b(\lambda)\rho \qquad (2.6)$$

The two coefficients $a(\lambda), b(\lambda)$ are material and wavelength dependent and empirically derived. The change in refractive index causes a slowing of the light, thus a frequency shift, as it passes through the shock compressed section moving at shock and particle velocity (U_s, u_p) resulting in a systematic offset of the apparent or measured velocity and the actual particle velocity, u_p of the interface.

$$u_{p,apparent}(t) = n_0 U_s\text{-}n(\lambda, \rho)\big(U_s\text{-}u_p(t)\big) \qquad (2.7)$$

Therefore,

$$u_{p,apparent} = a(\lambda)u_p(t) \quad (2.8)$$

So $a(\lambda)$, referred to here as the window correction factor is an effective scaling factor used to correct the affect of refractive index changes with increasing density from shock[10]. These values are material specific (for single crystals it's also specific to the crystalline face[19,20]) and usually determined from static compression experiments. The shock impedances and window corrections (denoted n_c) are listed in Table 2.1. These are important as all particle velocity measurements used in this dissertation require this correction factor to be accurate.

Table 2.1. Shock impedances and PDV corrections

Material	10^{-3} × density, kg/m^3	10^{-3} × sound speed, m/s	Impedance $10^{-6} \times Z_0$, kg/(m^{2}s)	Window correction n_c, unitless
Sapphire	4.0	~10	~40	1.7284[10]
CaF_2	4.62	6.50	30.2	1.25[19]
Al	2.7	5.1	13.8	N/A
Fused silica	2.20	5.97	13.1	1.0765[10]
Pyrex	2.23	5.64	12.6	1.0627[2]
BK7 Glass	2.20	5.26	11.6	1.08[a]
LiF	2.64	2.49	6.57	1.2669[10]
Plexiglass	1.19	2.40	2.86	1.48[21]
Lexan	1.19	2.40	2.86	1.48[a]
Gorilla glass	--	--	--	1.08[a]

[a]Assumed to be similar to fused silica.

[b]Assumed to be similar to Plexiglass

In Fig. 2.9, at left we see the final stage of the flyer free flight at U_f = 4 km/s. The instant of impact is denoted t = 0. The impact drops the flyer velocity from U_f to U_p, where U_p is the flow velocity of the flyer-window interface. The magnitude of the velocity drop is determined by the relative shock impedances of the flyer plate and window. The higher the window shock impedance, the larger the velocity drop, and sapphire has a shock impedance more than three times greater than Pyrex. After the impact there is an ~4 ns duration steady shock drive where the window material moves at velocity u_p. This drive is not perfectly steady because the Al flyer plate undergoes some mechanical deformations because of the large and slightly nonuniform stresses during launch and during the impact. The steady drive is followed by an unloading process consisting of a faster velocity drop and a longer tail in the velocity profile. The faster velocity drop in sapphire is ~1 ns and 2-3 ns in Pyrex. The tail in Pyrex has a much larger amplitude and longer decay time. This is likely due to the Hugoniot elastic limit observed in glass materials when shocked[22]. The result is that the material becomes plastic after a certain pressure, making it a worse shock dissipator[23]. Overall, sapphire has a much faster response to the 4 ns shock than Pyrex.

The flyer-window impact would theoretically occur in less than 1 ps if the flyer and window were perfectly flat and parallel. The inset in Fig. 2.9, which shows the velocity profile, used the 23 GHz detection system and fringe-counting analysis to obtain the maximum available time resolution. (The impact in the inset was a Pyrex shot obtained at a different velocity than in the main panel.) The faster detection scheme showed that the impact occurs in <0.5 ns.

Figures 2.10-2.11 show velocity-dependent 25 μm thick Al flyer plate impacts with various window materials. Fig. 2.10 shows inorganic glass windows and Fig. 2.11 shows organic

polymer glass windows. The polycrystalline windows have the fastest overall response to the impact, followed by the inorganic glasses and the polymers.

A problem with optical windows as shock wave detector materials is that the detector material is transformed into a radically different mechanical state during the compressive and expansive stages of the measurement. This strong detector-signal interaction makes it quite complicated to deduce the input waveform from the output waveform. In this study we put forth a simple way of dealing with this problem, namely that the shock impedance, a measure of the mechanical hardness which controls how the shock wave is transferred from the shock source into the detector window, is both shock pressure (i.e. impact velocity) and shock duration dependent. The pressure dependence distorts the measured shock amplitude profile, and the time-dependence distorts the measured shock temporal profile. Using this model, we interpreted the output waveforms from various detector windows when each was subjected to the same input shock, a nitromethane detonation shock. We did not offer a comprehensive solution where we characterized the pressure and duration dependence of the window response at all pressures and durations. Instead, we interpreted the window behavior in terms of reference experiments where the window response to different impact velocities (1-4 km/s) and durations (4-12 ns) was measured in velocity and time ranges comparable to the detonation waveform being studied. This regime of higher shock pressures and shorter shock durations is the most critical one, because the time dependence of the window material transformation cannot be ignored, as it might be with slower shock measurements. All the window materials responded instantaneously to the compression produced by the steeply rising shock front, where instantaneous means within our 0.5 ns PDV response time. Our instruments cannot tell if the compressive response is the same for all materials or whether it varies within the 0.5 ns time resolution. We note that if the window

material had sufficient porosity, shock fronts in the window would have slower, clearly resolvable rise times.

The polycrystalline windows gave the fastest response to shocks. This suggests that the polycrystalline windows give the most faithful representation of the input shock. However, these windows produce the most ringing, particularly in sapphire. Kanel et al. observed similar ringing in shocked sapphire windows and attributed it to heterogeneity of deformation[20].

Finally, impedance matching should be accounted for, as it is desirable to find the closest impedance match between the sample and the window. Neglecting this will result in a strong 're-shock' of the sample as the shock reflects off the window into the sample. Off-hugoniot states like this perturbs the measurements of the explosive in experiment. Ideally, a window material of matching density and impedance to most explosives ($\rho \approx 1.8\text{-}2$). Kel-F is often considered a theoretically perfect material for this purpose[24], which is part of the reason it's such a common binder material in polymer-bound explosives (PBXs)[25]. However, due to the comparatively low cost, relatively low density and *decent* impedance match to some softer explosives, Pyrex is the most common material used in this dissertation. This carries some significant limitations with it, as listed here, but for reaction zone dynamics and overall shock energy measurements Pyrex has been proven adequate[16,26].

2.4.2 Measuring Pressure, Flux, and Fluence in Energetic Materials

In several instances it is useful to measure the energy of the shock wave being transited through a material. Either for measuring energy absorption[27,28], or energy addition of reactive materials, namely PBXs[26,29]. Pressure can be inferred from particle velocity of a sample/window interface if the Hugoniot of the window material is known:

$$P(t) = \rho_{window} U_s(t) u_{p,window}(t) \quad (2.9)$$

Where u_p is derived from window interface velocity, as shown in the previous section:

$$P(t) = \rho\left(Au_p + Abu_p^2\right) \quad (2.10)$$

From the pressure mass flux, J can be derived from the conversion to kinetic energy[2]:

$$J(t) = \frac{1}{2}\rho_0(U_s u_p)u_p = \frac{1}{2}\rho_0\left(Au_p^2 + Abu_p^3\right) \quad (2.11)$$

The time integral yields fluence

$$\phi(t) = \int_0^t J(x)dx \quad (2.12)$$

The Hugoniot-based parameters A, b are known for Pyrex, the most common material used in these experiments. However, the U_s-u_p curve for Pyrex behaves nonlinearly due to its Hugoniot Elastic limit[18]. The parameters A, b in this case can be written as a step function for 3 linear regimes: 0-0.57 km/s, 0.57-1.5, and 1.5-3 km/s. Alternatively, the Hugoniot from literature can be fitted to a quadratic function to fit quite well:

$$U_s = c_1 + c_2 u_p + c_3 u_p^2 \quad (2.13)$$

This method is more amenable to computer scripts and is the preferred method in this dissertation. See Table 2.1 for relevant parameters.

If particle velocity cannot be directly measured, impact pressures must be predicted using the flyer velocity and the Hugoniot equations for the flyer material and the sample material. An impedance-matching calculation can be performed using equations 2.10 and the conservation equations in Chapter 1 to predict flyer impact pressures. The details on these calculations can be found in Appendix E.

2.5 High Speed Camera Measurements of Dynamic Events

Quantitative analysis of shock compression events, while useful, are enriched greatly by the addition of photography, which serves quantitative and qualitative purposes alike. Throughout this dissertation, the Shock Compression Microscope has had a few different cameras equipped to it. For Chapter 7, a single frame intensified CMOS camera is used, in which case separate shock events are stitched into one timeline by changing the time of camera exposure. On the other hand, Chapters 6 uses an 8-frame high-speed camera (Specialized Imaging SIMX8) which uses an array of beamsplitters coupled to 8 different iCMOS cameras to collect 8 images in one shock experiment. All these iCMOS detectors have exposure times down to 5 ns to maximize time resolution. Unless otherwise stated, all of these cameras image only the auto emission of reactive samples such as explosives. These samples produce enough light to create good exposure for all the CMOS chips, albeit at near maximum gain.

Figure 2.12 is a schematic of the optical path of the camera used throughout the dissertation, regardless of the camera used. The visible light is collected by a 10X or 20X objective (Olympus LMPFLN10X NA = 0.25, Olympus LUCPLFLN20X NA = 0.45). It is sent through the microscope assembly out of the output flange. The IX73 is a modified biological microscope containing a condenser lens, and the light must be collimated by a tube lens outside the microscope. A 200-mm focal length (Thorlabs TTL200MP) tube lens is used to roughly match the NA of the 10X objective. The beam is directed up by a 10:90 T:R beam splitter to another tube lens to project an appropriately size image onto the detector iCMOS. For the 8-frame camera, this is done by placing the focus of the beam 54 mm away from the input flange of the camera, according to device specifications.

The beam splitter is used to send light emission to an emission pyrometer to quantify light intensity, determine the spectrum, and calculate temperature and emissivity of the light produced. Mentioned in the proceeding section. More detail on how the camera is used will be covered in proceeding chapters.

2.6 Emission Pyrometry During Shock Experiments

Aside from temperature, the other measurable intensive property, temperature, can be inferred by the temperature of shock emission, known as pyrometry. This section will focus strictly on the instrumentation, which was built by William Bassett and extensively described and characterized in his dissertation[30] and his published instrument review[31]. These can be referred to for more information. Appendix B outlines how this is implemented in Matlab code.

When explosives are shock initiated, the heat generated, resulting in temperatures that can go past 5000K, generate blackbody emissions. The spectral radiance, $L(T,\lambda)$ is described by the following equation:

$$L(T,\lambda)d\lambda = \varepsilon \times \frac{2hc^2 d\lambda}{\lambda^5\left[e^{\frac{hc}{kT\lambda}}-1\right]} \qquad (2.14)$$

h refers to Planck's constant, c is the speed of light, k is the Boltzmann constant. ε is the spectral emissivity – the ratio of emitted light to an ideal black body. Generally, this is considered wavelength and temperature dependent. For all experiments in this dissertation, the gray body assumption is applied, wherein ε is temperature and wavelength independent. Therefore, if the spectrum of light can be determined, then the temperature can be inferred. Figure 2.13 is a schematic of the pyrometry design of experiment. The light is reflected off a dichroic mirror which filters out the 1550 nm laser used for PDV. The light is directed through a prism which

refracts the light to separate the wavelengths. The image is projected onto an array of fibers, that feed to 32 photomultiplier tubes (PMTs). The fiber array is a set of 100μm-core optical fibers bundled such that each PMT has a roughly 10 nm spectral width[30]. The PMTs are digitized by a set of digitizers, which collect data every 0.5 ns with a time range up to milliseconds. PMTs are preferred to diode arrays due to the very high dynamic range. The result is a very high dynamic range both in time and light intensity, allowing for time measurements of nanosecond response, microsecond dynamics, and hundred microseconds to millisecond burn behavior. It is worth noting that while data is collected every 500 ps, the rise of the response function of the PMTs gives an effective time resolution of ~2 ns.

To reduce the computational requirements of processing such a huge time range, logarithmic binning of the data is performed. Every time decade (after 10 ns) is binned to 30 points. The PMT voltage measurements of the binned data can be converted to a spectral radiance by spectral calibration. A radiometric source of known spectral radiance is directed into the PMT array, these values are divided by the measured radiance of the source to give a calibration factor. Using spectral radiance also makes all data sets directly comparable, and emissivity can be strictly known. Spectral radiance, $L(\lambda, T)$ is converted to radiance simply by integrating over the measured wavelengths. This reduces the dimension of the emission intensity for better comparison.

The spectral radiance is fitted to a gray body using a Matlab program (See Appendix B) to determine temperature, $T(t)$ and emissivity $\varepsilon(t)$ over all binned time points. An example shock experiment of an ignited explosive showing the temperature, radiance and emissivity measurements is shown in Fig 2.14. Knowing temperature and emissivity simultaneously as the

reaction evolves is a powerful tool that will be used throughout this dissertation. However, it is not a monolith; emission pyrometry has some strengths and limitations that must be mentioned.

Emission pyrometry is powerful because it is indirect, making it easy to couple if given access to the emission. However, it tends to be most robust when the temperature is homogeneous because it is most biased towards the hottest temperature of a given field. From equation 2.14, the emission intensity is proportional to T^4, but inside of the visible light range (400-800 nm), the proportionality reaches T^6. Thus, if the temperature field is inhomogeneous, the emission temperature will invariably be the highest in the field.

This weakness is also a strength for studying hot spots formed in explosives. Direct probes such as embedded thermocouples read a homogenized temperature of the entire high explosive, which means local temperature spikes are largely smoothed over. By comparison, in the range of 2000-5000 K events studied in this dissertation, if even 1 vol% of the field is at 5000 K the temperature will measure very near 5000K. This will *only* be the case in the nanosecond (10^{-7} - 10^{-9} seconds) time range of PBX initiation, where reaction dynamics are altered by localized heat pockets called hotspots[32]. This can be accommodated by treating graybody emissivity as an intensive property of the unreacted explosive and incorporating an extensive factor, emission volume. This was devised by Bassett *et. al.* where the experimentally measured emissivity is modified to factor Φ:

$$\Phi(t) = \varepsilon_0 V^* \qquad (2.15)$$

Where ε_0 is the known emissivity (under graybody assumption) of the material studied, usually derived from literature, and V^* is the volume fraction of the emitter. In the case of an inhomogeneous temperature field, the emissivity can qualitatively (or quantitatively if data is

available) determine how much of the field is at the emission temperature. In effect, this will allow for treatment of nanosecond emissivity measurements to be a stand-in for the volume of hot spots in experiments. The ideal would be for emissivity to measure reaction progress, but without data to calibrate *exact* emissivity or volume of homogenous emission fronts, this cannot yet be done.

2.7 Figures

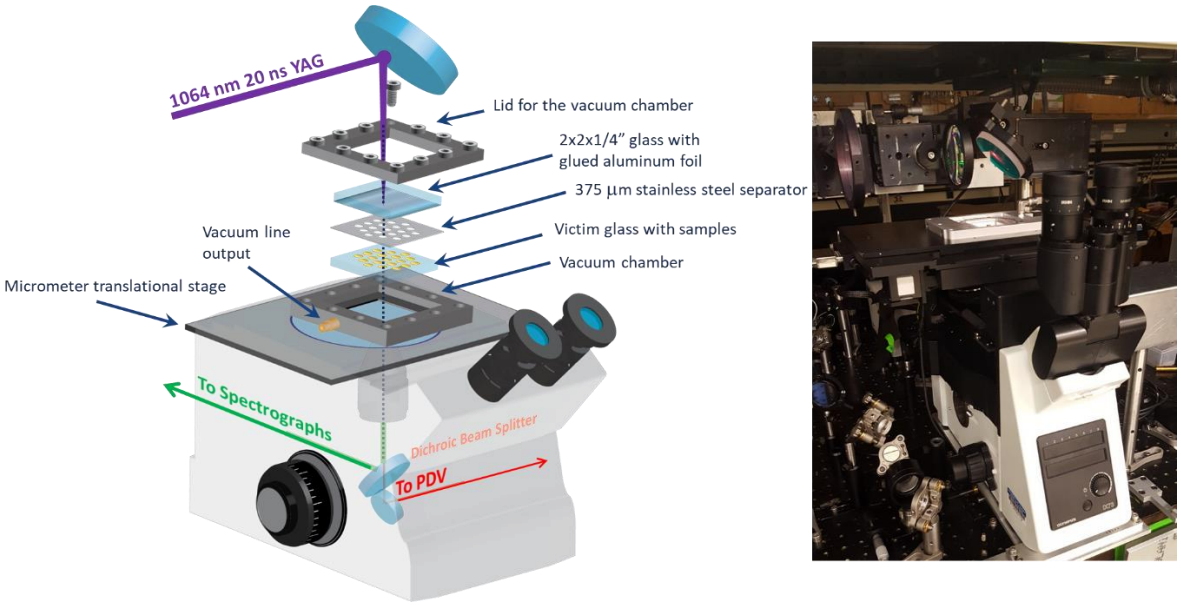

Figure 2.1 Diagram of the Shock Compression Microscope (left), an inverted microscope modified to conduct shock experiments and use optical probes to track shock-compression chemistry. The microscope is coupled with external laser lines to conduct these experiments (right).

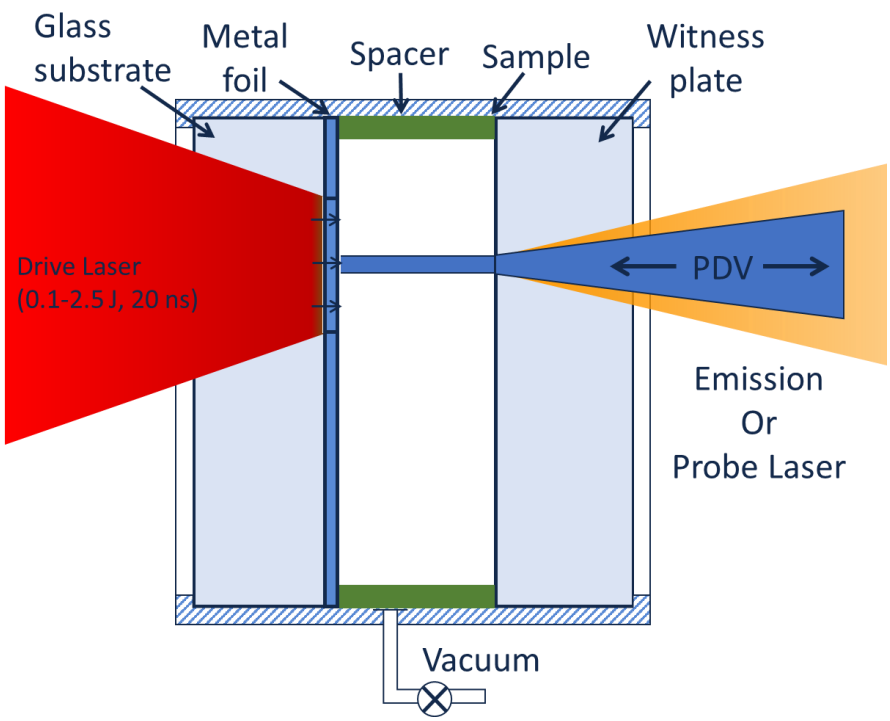

Figure 2.2 Diagram of how laser driven flyer plates work. Metal foil glued to a glass substrate is irradiated with a 1064 nm pulsed laser that has been shaped to have a spatially flat top. When the foil is irradiated by the pulsed laser, a 500 μm disk is punched out of the foil, creating the projectile, called the flyer plate. This foil flies across a vacuum to reach the victim sample, a material sitting on top of a transparent glass or crystal substrate. Upon impact, a 4-20 ns shock wave is created and the proceeding chemistry can be evaluated using optical probes, such as photon doppler velocimetry (PDV), probe lasers, or spectrographs to quantify emissions.

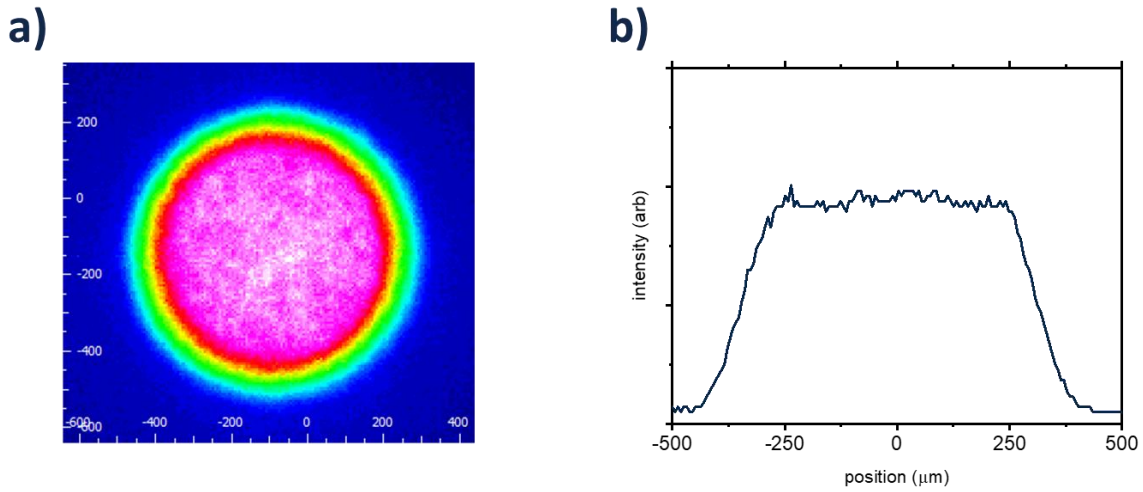

Figure 2.3 (a)Optical beam profile of the launching laser needed to produce 500 μm diameter flyer plates. After treatment *via* a diffractive optic, a round, spatially flat beam is produced across a 500 μm diameter, when irradiating a foil, a projectile, called a flyer plate, is launched to produce the shocks. (b) A 1-dimensional intensity profile across the x-axis of the beam to show the flat top, spanning ~500 μm.

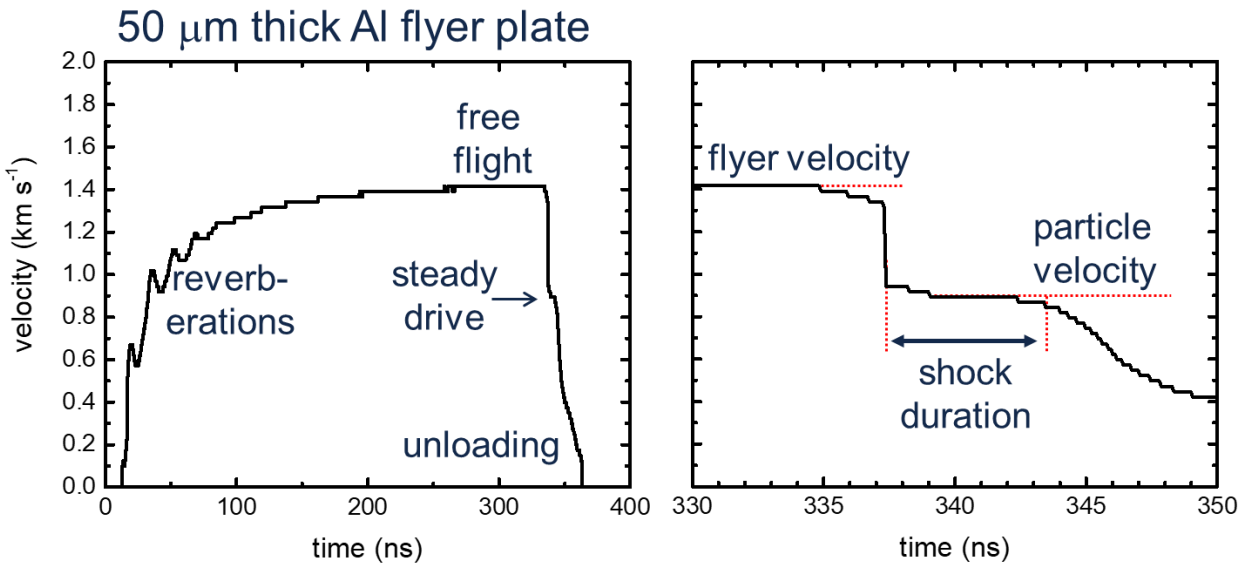

Figure 2.4 Example of velocity history of a aluminum foil flyer plate launching through vacuum and impacting glass, similar to Fig 2.2. After some time to accelerate to terminal velocity, the flyer plate impacts the material. Particle velocity, where mass flow of aluminum foil matches the target surface, is sustained for several nanoseconds before the pressure wave is relieved.

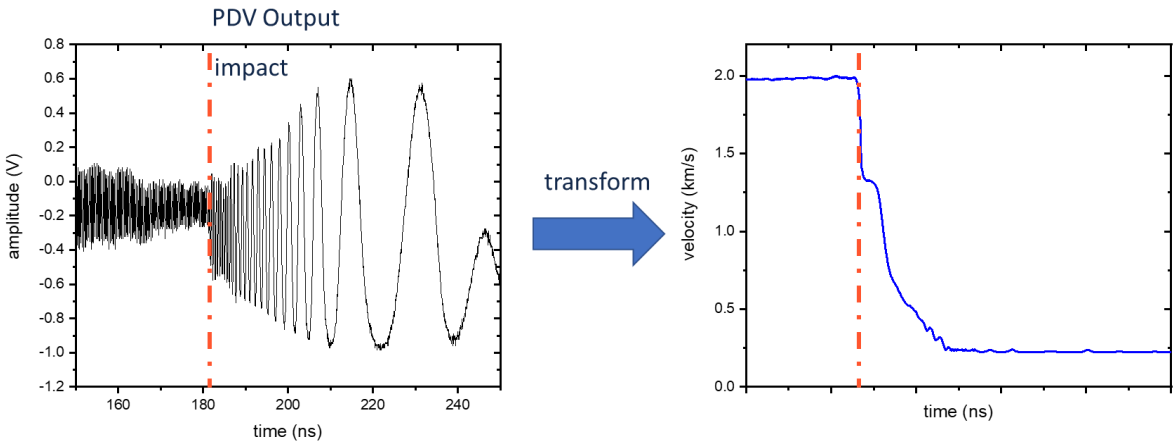

Figure 2.5 (Left) raw output of the Photon Doppler Velocimeter, a waveform created from the beat frequency caused by mixing a laser frequency with doppler-shifted light when reflected off of a moving object. (Right) When transformed from intensity space to frequency space and converted to a velocity using a fourier transform, a smooth velocity history of projectiles or surfaces can be obtained.

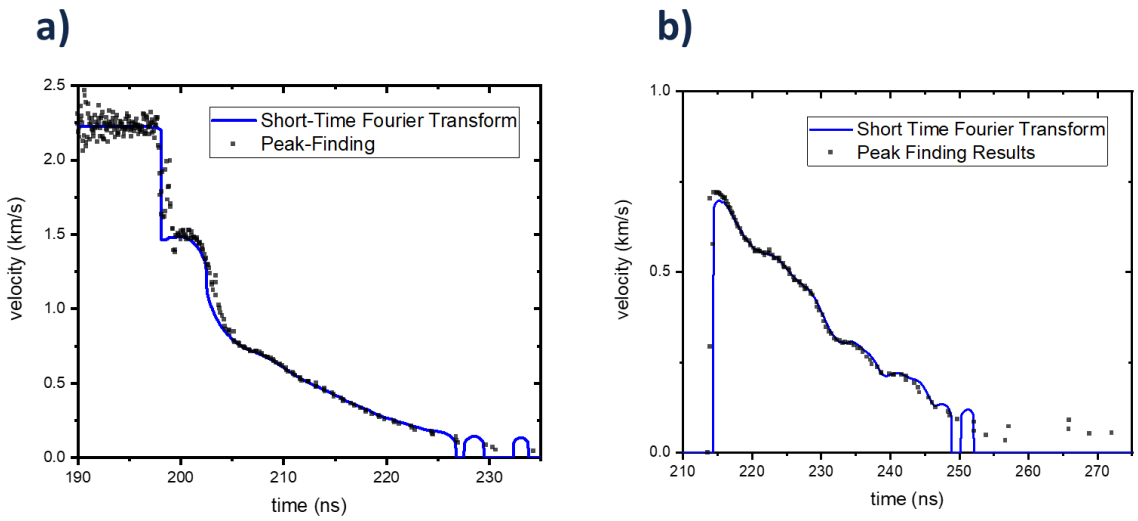

Figure 2.6 Evaluation of the differences between short time fourier transform to process velocimetry versus algorithmically finding fringes of the oscilloscope waveform. (a) An example of aluminum foil (25 μm) impacting glass. (b) An example of the particle velocity of a plastic explosive exerting pressure on a glass window. In both cases, the difference between methods to measure beat frequency are very subtle, despite peak-finding theoretically being more accurate.

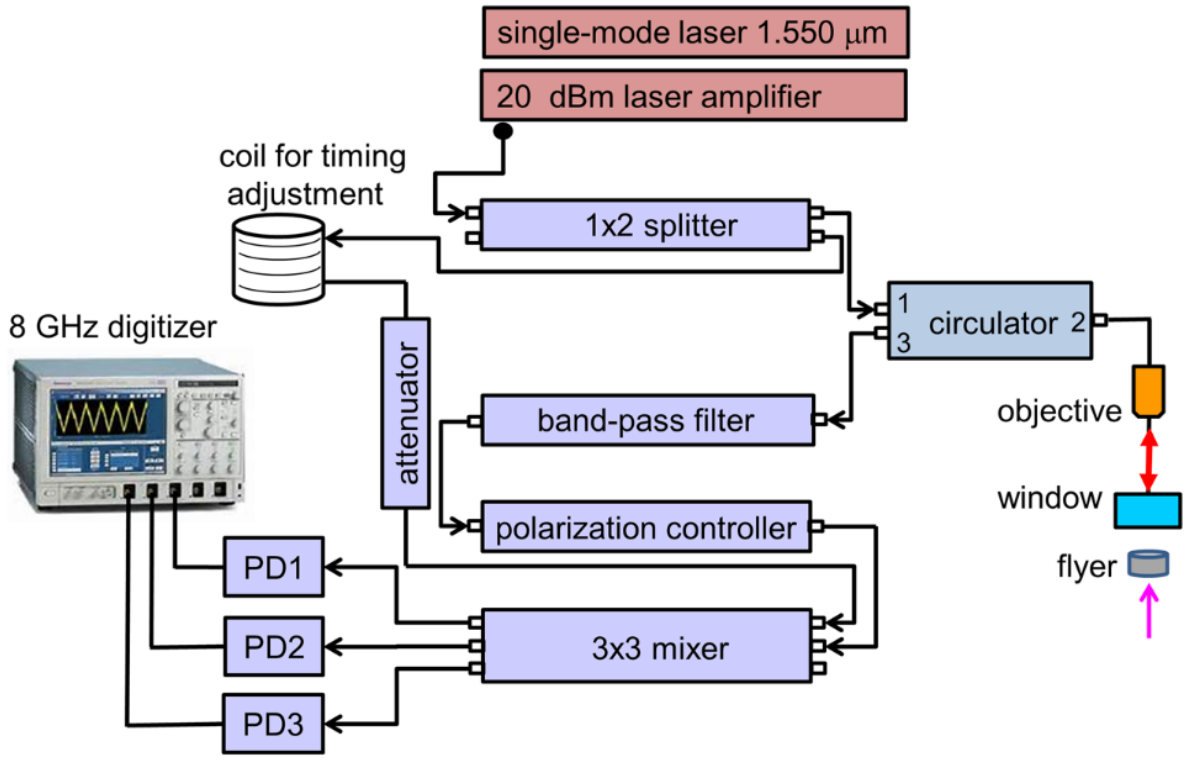

Figure 2.7 Diagram of the photon-doppler-velocimeter setup (PDV), constructed from fiber-optic components. A 1.55-micron fiber laser is amplified by an Erbium-Doped Fiber Amplifier, then split by a 90:10 coupler. The 90% portion is inserted into a circulator which goes through the shock microscope, the return signal, now doppler shifted is filtered for stray light. After the band pass filter, a polarization controller is used to correct shifts in polarization due to the components and reflections through the microscope, which is needed to match the polarization of the reference beam. The reference beam is placed in a coil to match the time of transit of the signal beam through the shock microscope (about 14 meters). The signals are mixed with a 3x3 optical coupler and each output, 120° phase offset, are read by a photodetector, and measured by an 8GHz oscilloscope.

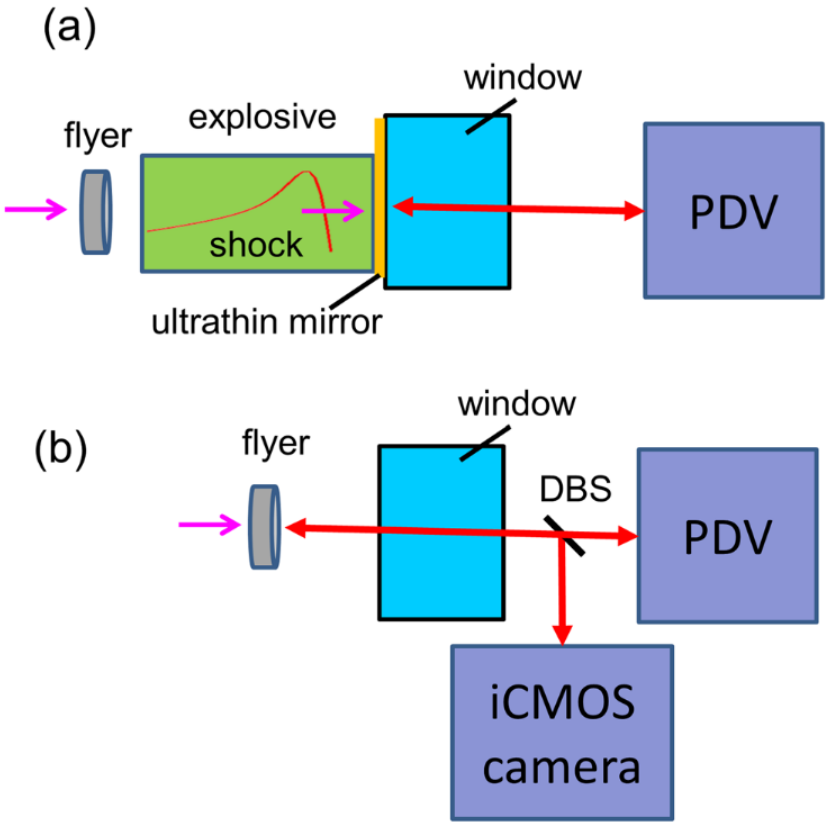

Figure 2.8 (a) Schematic to measure shock wave pressure using a high reflector at the interface of the sample material (usually an explosive material) and an optically clear window. PDV = photon Doppler velocimeter. (b) Using a dichroic beam splitter, PDV signal (at 1550 nm) can be simultaneously measured with high-speed camera images. In this case used to measure flight and impacts of Aluminum flyer plates against optical windows.

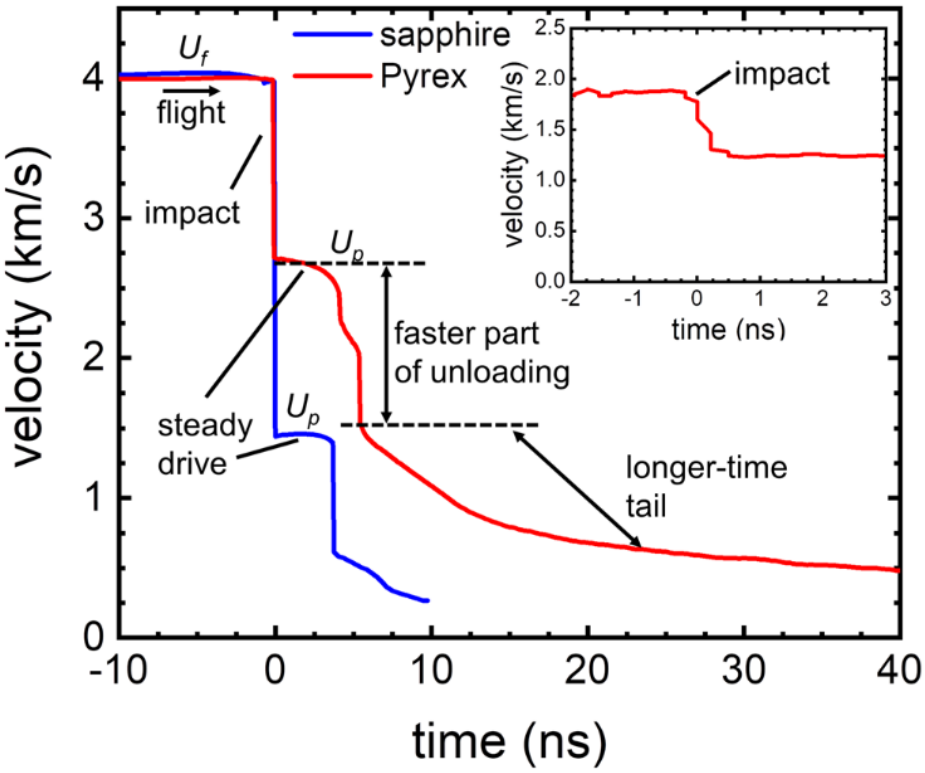

Figure 2.9 PDV data for 25 μm thick Aluminum flyer plate impacting two different window materials: Pyrex glass and sapphire crystal. A faster digitizer was used on a different impact experiment to better resolve the moment between flight and impact, lasting about 0.5 ns. Pyrex, due to its plasticity at lower PV states, has a much longer rarefaction wave than crystal windows, such as sapphire. In the case of perfectly flat impactors, these differences would be minor, but because of curvature at the edge of the flyer, rarefaction waves take longer to fan out from the edge into the center, where PDV is probed.

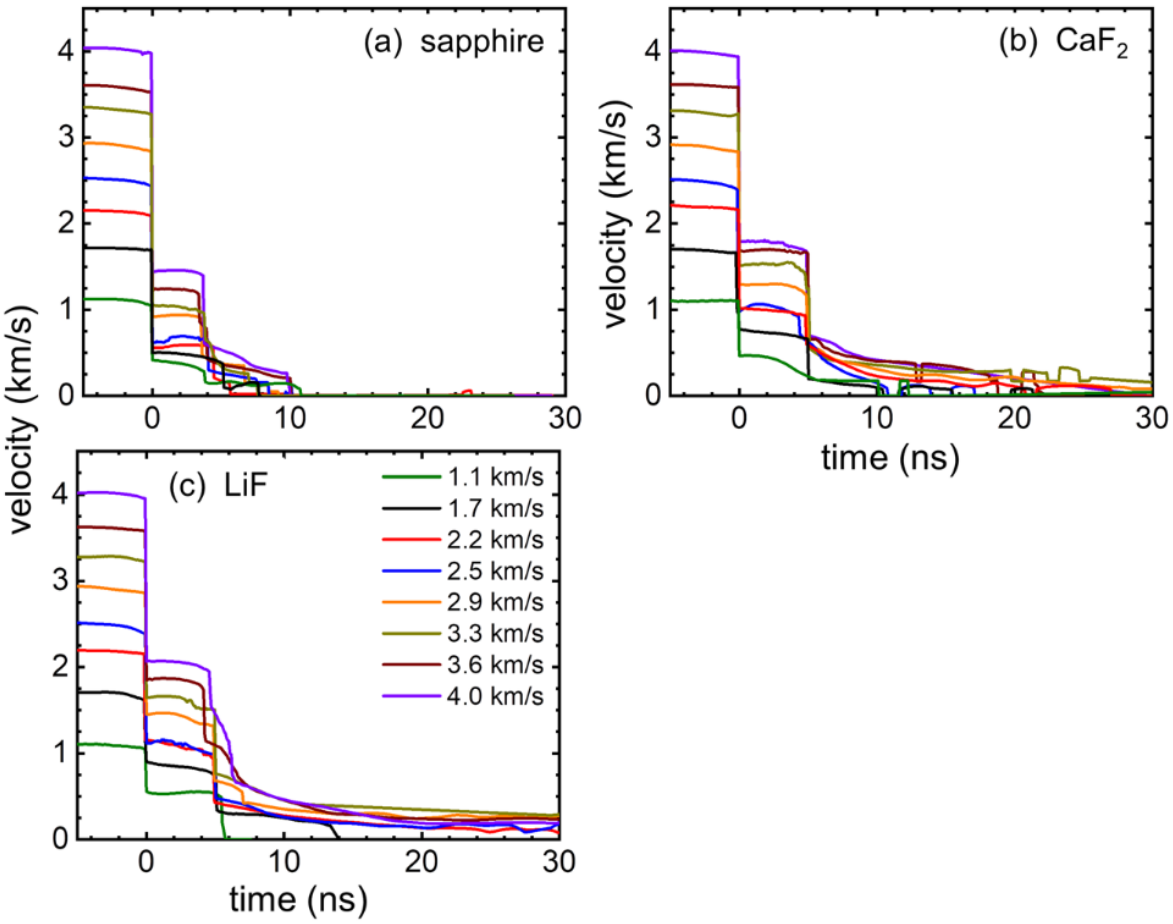

Figure 2.10 Velocity profiles of 25 μm thick Al flyer plates across several velocities when impacting (a) sapphire (C-cut) (b)CaF_2 and (c) LiF. Because of the high elasticity of these crystals, the relief waves – the decay after the 0-4 ns steady portion- is much faster than glassy materials which exhibit high elasticity.

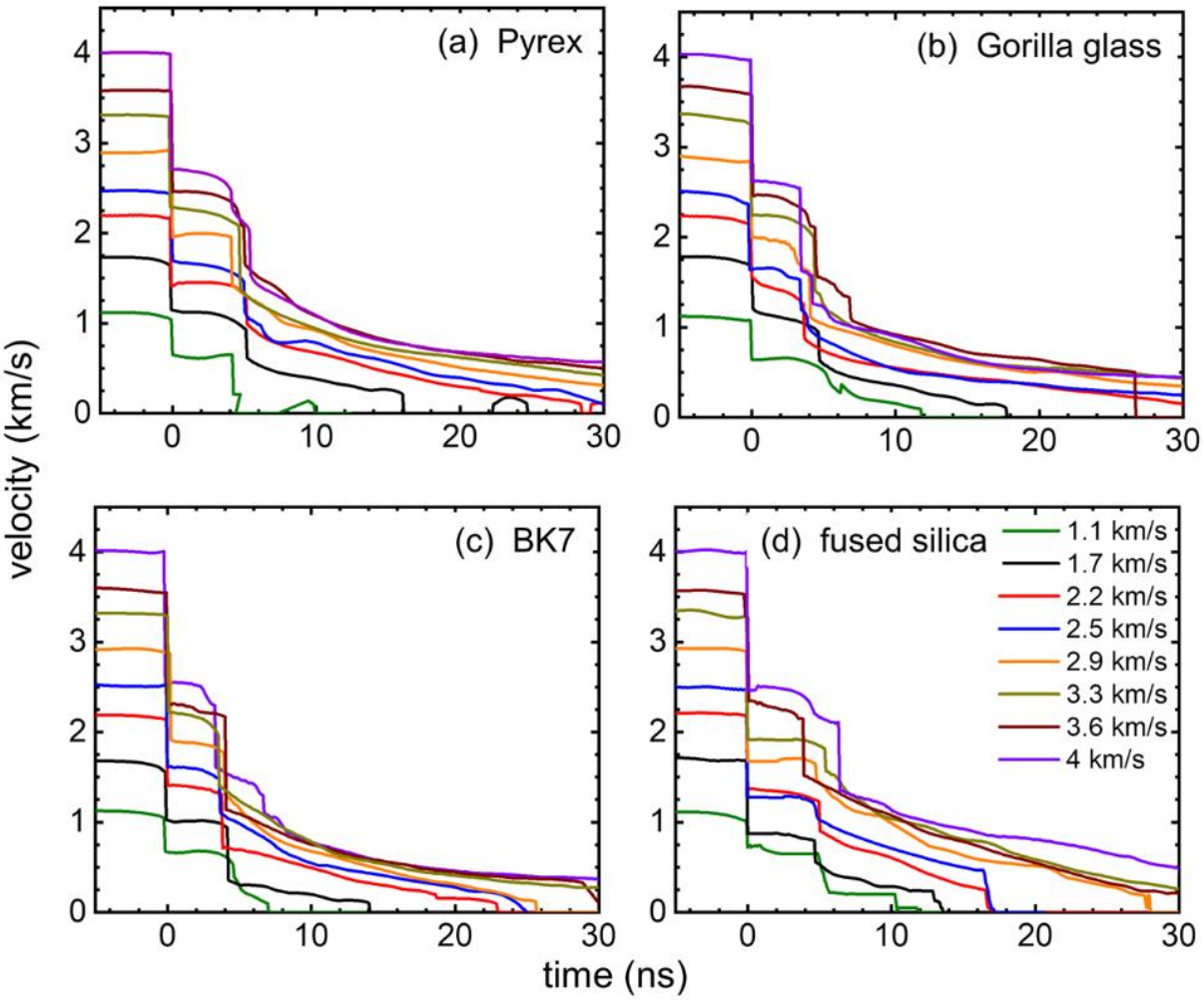

Figure 2.11 Velocity profiles for 25 μm thick Al flyer plates when directly impacting (a) Pyrex glass, (b) Gorilla glass, (c) BK7 glass and (d) fused silica. Most of these materials are shocked to high enough pressures to exceed their Hugoniot elastic limits. The resultant failure results in a highly plastic-like relief wave, higher amplitude, and longer duration than crystals.

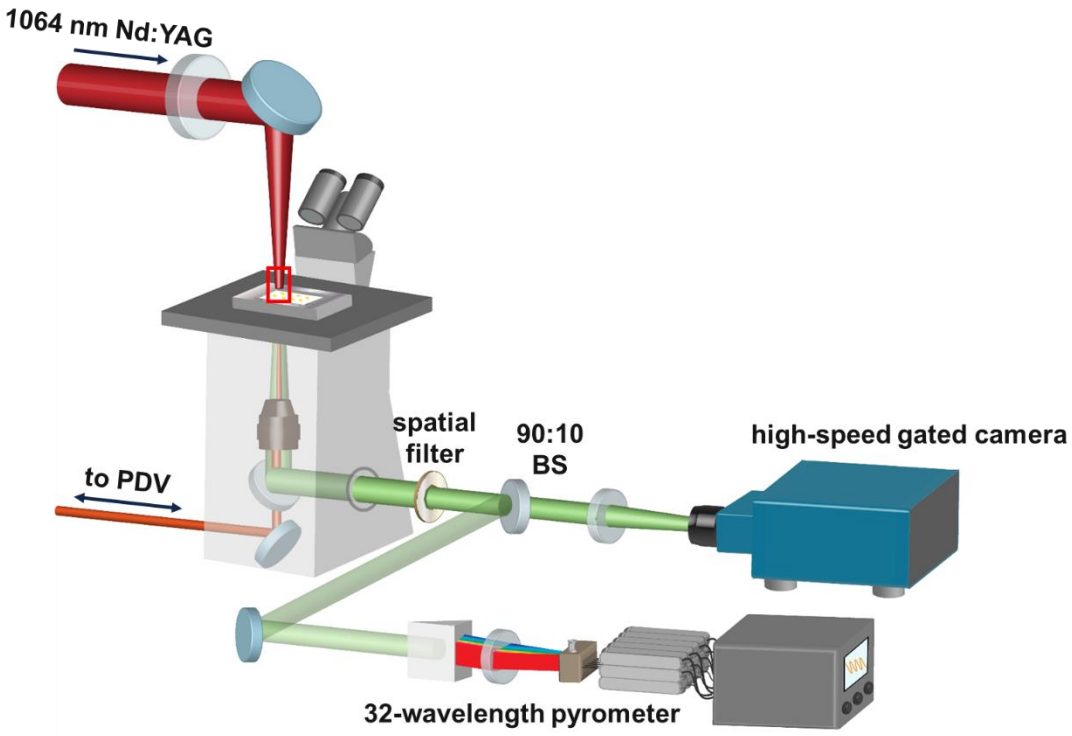

Figure 2.12 Schematic of high speed gated photography design of experiment. The shocked window produces light which is directed through a beam splitter to simultaneously view emission statistics *via* a photomultiplier tube array and to a high-speed camera. The spatial filter is used to isolate the 500-μm region in which the flyer plate is impacting the sample.

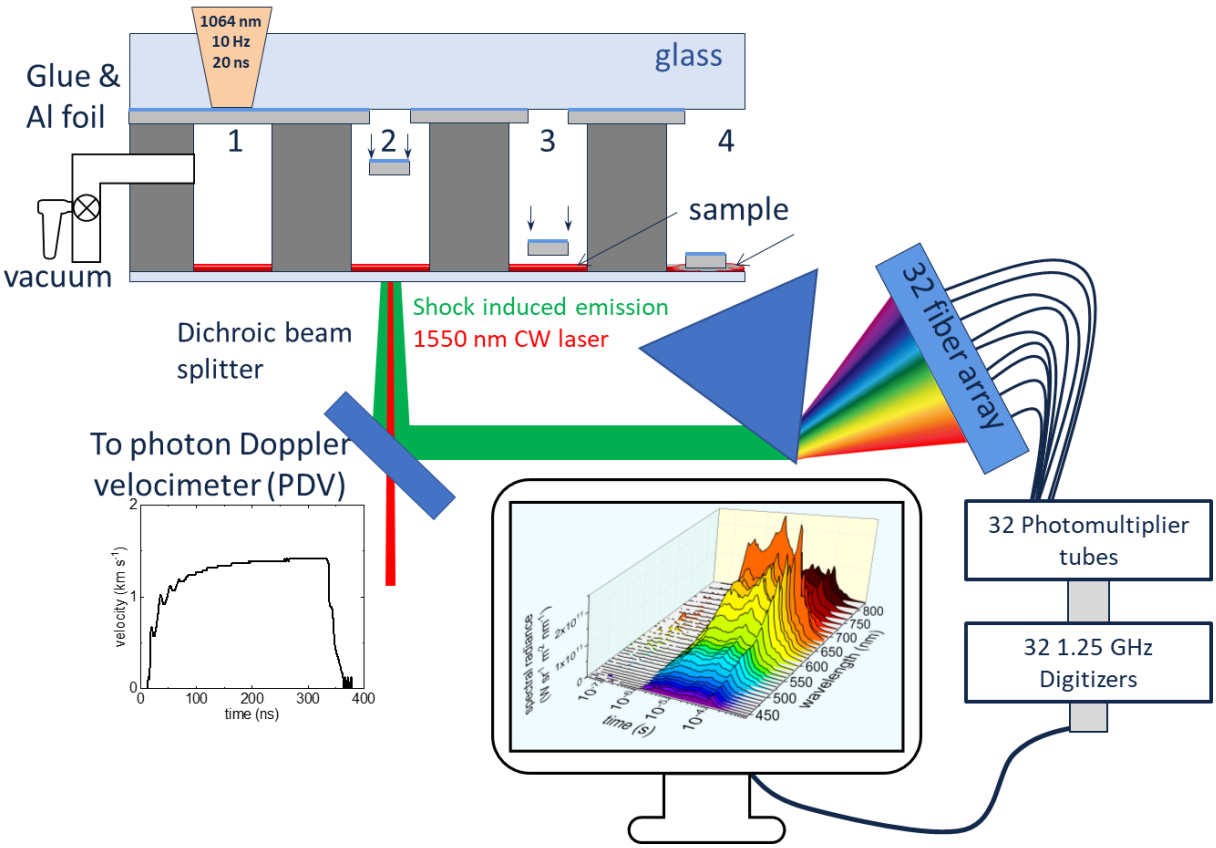

Figure 2.13 Schematic of emission pyrometry design of experiment. A dichroic filter separates visible light emission from the infrared PDV probe. The visible light is spectrally separated by a prism projected into a set of 32 fibers of sizes chosen to produce an even spacing between channels. Each channel is fed into a photomultiplier tube which is digitized by an oscilloscope array.

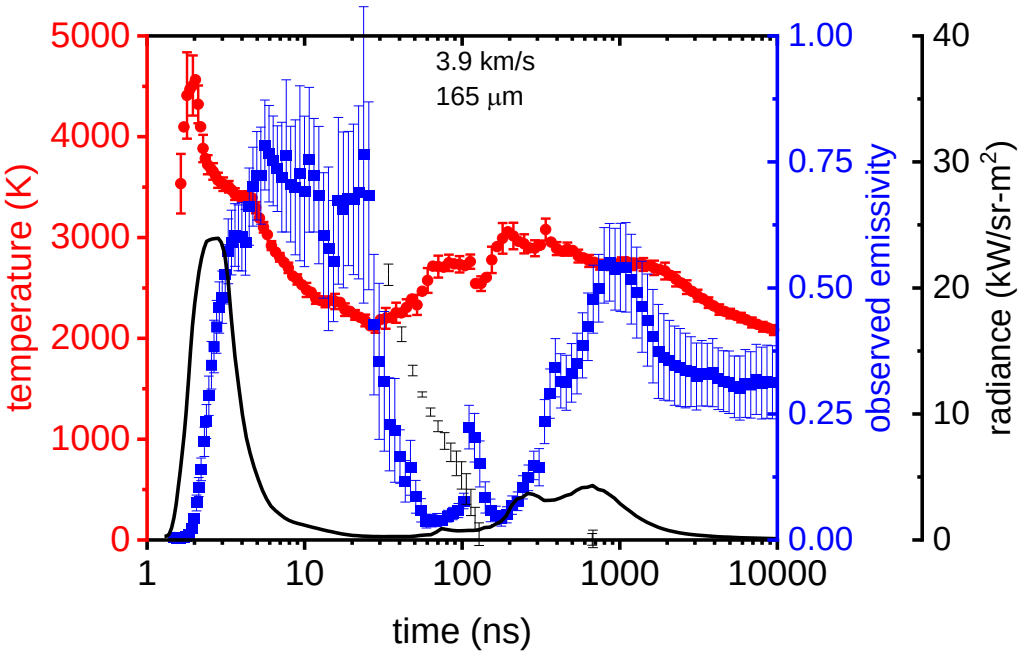

Figure 2.14 A plot of emission pyrometry data from an explosive igniting from a shock ignition. Plotted in log-time to span a multitude of timescales. Emission pyrometry collects light emitted by reactive samples to provide integrated spectral radiance (black), emission temperature (red) and observed emissivity, Φ (blue) simultaneously for every shock experiment.

2.8 References

1. Shaw, W. L. REACTIVE SOLIDS UNDER SHOCK COMPRESSION. 230.
2. Shaw, W. L.; Ren, Y.; Moore, J. S.; Dlott, D. D. Mechanochemistry for Shock Wave Energy Dissipation; Tampa Bay, Florida, USA, 2017; p 030026.
3. Brown, K. E.; Shaw, W. L.; Zheng, X.; Dlott, D. D. Simplified Laser-Driven Flyer Plates for Shock Compression Science. *Rev. Sci. Instrum.* 2012, *83* (10), 103901.
4. Curtis, A. D.; Banishev, A. A.; Shaw, W. L.; Dlott, D. D. Laser-Driven Flyer Plates for Shock Compression Science: Launch and Target Impact Probed by Photon Doppler Velocimetry. *Rev. Sci. Instrum.* 2014, *85* (4), 043908.
5. Bassett, W. P.; Johnson, B. P.; Salvati, L.; Nissen, E. J.; Bhowmick, M.; Dlott, D. D. Shock Initiation Microscopy with High Time and Space Resolution. *Propellants Explos. Pyrotech.* 2020, *45* (2), 223–235.

6. Dlott, D. D. Laser Pulses into Bullets: Tabletop Shock Experiments. *Phys. Chem. Chem. Phys.* 2022, *24* (18), 10653–10666.

7. Banishev, A. A.; Shaw, W. L.; Bassett, W. P.; Dlott, D. D. High-Speed Laser-Launched Flyer Impacts Studied with Ultrafast Photography and Velocimetry. *J. Dyn. Behav. Mater.* 2016, *2* (2), 194–206.

8. Strand, O. T.; Goosman, D. R.; Martinez, C.; Whitworth, T. L.; Kuhlow, W. W. Compact System for High-Speed Velocimetry Using Heterodyne Techniques. *Rev. Sci. Instrum.* 2006, *77* (8), 083108.

9. Dolan, III, D.; Ao, T. *SIRHEN : A Data Reduction Program for Photonic Doppler Velocimetry Measurements.*; SAND2010-3628, 989357; 2010; pp SAND2010-3628, 989357.

10. Jensen, B. J.; Holtkamp, D. B.; Rigg, P. A.; Dolan, D. H. Accuracy Limits and Window Corrections for Photon Doppler Velocimetry. *J. Appl. Phys.* 2007, *101* (1), 013523.

11. Jones, S.; Dolan, D. *THRIVE : A Data Reduction Program for Three-Phase PDV/PDI and VISAR Measurements.*; SAND2008-3871, 942210; 2008; pp SAND2008-3871, 942210.

12. Dolan, D. H. Accuracy and Precision in Photonic Doppler Velocimetry. *Rev. Sci. Instrum.* 2010, *81* (5), 053905.

13. Dolan, D. H.; Jones, S. C. Push-Pull Analysis of Photonic Doppler Velocimetry Measurements. *Rev. Sci. Instrum.* 2007, *78* (7), 076102.

14. Forbes, J. W. *Shock Wave Compression of Condensed Matter: A Primer*; Springer Berlin Heidelberg: Berlin, Heidelberg, 2012.

15. Detonation: Theory and Experiment. By W. F ICKETT & W. C. D AVIS . Dover, 2000. 386 Pp. ISBN 0 486414566. *J. Fluid Mech.* 2001, *444*, 408–411.

16. Bhowmick, M.; Nissen, E. J.; Dlott, D. D. Detonation on a Tabletop: Nitromethane with High Time and Space Resolution. *J. Appl. Phys.* 2018, *124* (7), 075901.

17. Sheffield, S. A.; Bloomquist, D. D.; Tarver, C. M. Subnanosecond Measurements of Detonation Fronts in Solid High Explosives. *J. Chem. Phys.* 1984, *80* (8), 3831–3844.

18. Marsh, S. P. *LASL Shock Hugoniot Data*; University of California Press, Berkeley, 1980.

19. Li, Y.; Zhou, X. M.; Liu, C. L.; Luo, S. N. Refractive Indices of CaF_2 Single Crystals under Elastic Shock Loading. *J. Appl. Phys.* 2017, *122* (4), 045901.

20. Kanel, G. I.; Nellis, W. J.; Savinykh, A. S.; Razorenov, S. V.; Rajendran, A. M. Response of Seven Crystallographic Orientations of Sapphire Crystals to Shock Stresses of 16–86 GPa. *J. Appl. Phys.* 2009, *106* (4), 043524.

21. Glam, B.; Porat, E.; Horovitz, Y.; Yosef-Hai, A. The Rarefaction Wave Propagation in Transparent Windows; Tampa Bay, Florida, USA, 2017; p 050019.

22. Brar, N. S.; Bless, S. J.; Rosenberg, Z. Impact-induced Failure Waves in Glass Bars and Plates. *Appl. Phys. Lett.* 1991, *59* (26), 3396–3398.

23. Stekovic, S.; Springer, H. K.; Bhowmick, M.; Dlott, D. D.; Stewart, D. S. Laser-Driven Flyer Plate Impact: Computational Studies Guided by Experiments. *J. Appl. Phys.* 2021, *129* (19), 195901.

24. Gibson, L. L.; Dattelbaum, D. M.; Bartram, B. D.; Lang, J. M.; Jones, J. D. Extension of the Window Correction for Kel-F 800: A near Impedance-Matched Window for High Explosives; Portland, OR, USA, 2020; p 040004.

25. Stevens, L. L.; Dattelbaum, D. M.; Ahart, M.; Hemley, R. J. High-Pressure Elastic Properties of a Fluorinated Copolymer: Poly(Chlorotrifluoroethylene-Co-Vinylidene Fluoride) (Kel-F 800). *J. Appl. Phys.* 2012, *112* (2), 023523.

26. Salvati, L.; Johnson, B. P.; Bassett, W. P.; Dlott, D. D. Probing Shock-Initiation of Plastic-Bonded Explosives with a Tabletop Microscope; Portland, OR, USA, 2020; p 030027.

27. Zhou, X.; Miao, Y.-R.; Banlusan, K.; Shaw, W. L.; Strachan, A. H.; Suslick, K. S.; Dlott, D. D. Shock Wave Dissipation by Metal Organic Framework; St. Louis, MO, USA, 2018; p 150043.

28. Zhou, X.; Miao, Y.; Suslick, K. S.; Dlott, D. D. Mechanochemistry of Metal–Organic Frameworks under Pressure and Shock. *Acc. Chem. Res.* 2020, *53* (12), 2806–2815.

29. Bassett, W. P.; Johnson, B. P.; Salvati, L.; Dlott, D. D. Hot-Spot Generation and Growth in Shocked Plastic-Bonded Explosives Studied by Optical Pyrometry. *J. Appl. Phys.* 2019, *125* (21), 215904.

30. Bassett, W. P. SHOCK INITIATION OF EXPLOSIVES UNDER THE MICROSCOPE. 178.

31. Bassett, W. P.; Dlott, D. D. Multichannel Emission Spectrometer for High Dynamic Range Optical Pyrometry of Shock-Driven Materials. *Rev. Sci. Instrum.* 2016, *87* (10), 103107.

32. Bassett, W. P.; Johnson, B. P.; Neelakantan, N. K.; Suslick, K. S.; Dlott, D. D. Shock Initiation of Explosives: High Temperature Hot Spots Explained. *Appl. Phys. Lett.* 2017, *111* (6), 061902.

CHAPTER 3: MEASURING MICROSTRUCTURE OF PLASTIC EXPLOSIVES

3.1 Overview

The goal of this chapter is to describe the methods developed in this dissertation by which the test plastic explosives (PBX) can be consistently synthesized and their internal microstructure subsequently imaged with micron-scale resolution. The focus will be first on manufacturing PBX in a repeatable fashion, then on cross-sectioning methods and thin-film preparations needed to image the internal structure of these plastic explosives with micron resolution. This is crucial because continuum-scale studies of plastic explosives (PBX) work on heavily simplified models of single grains in polymer[1,2] but the micron-scale structures present in these mixtures is crucial for predicting an explosive's sensitivity to shock.

This study leans heavily on the use of Polydimethyl Siloxane (PDMS)-based PBX mixtures with concentrations much lower than the 90-98 wt.% explosive composites that are typically studied. These are materials whose microstructure we have very little explicit knowledge about. So far, work previously done in our group has shown that hot spots can form at crystalline defects, polycrystalline defects[1,2], as well as from the adiabatic compression of void spaces inside the material.[3,4] Further, we also know that press extrusion fundamentally changes void collapse behavior.[3] Beyond this point, unfortunately, the ability to infer greater detail is limited. To expand the discussion on how to quantify and compare microstructure between several explosives, further detail on what the explosives look like is needed. Unfortunately, compared to many commercially implemented binders, PDMS is much softer. This is beneficial for the shock microscope because the mixtures are highly extrudable making sample preparation very fast. The downside is that microscopy methods such as cross-sectioning and X-Ray probing

are quite difficult. This chapter will investigate how to determine the structure of PDMS-based plastic explosives, and how, or if, epoxy can be used as an analogue material for softer plastic matrices. The results of this investigation will be applied heavily to subsequent chapters.

Starting with how PBX samples can be prepared, then discussing methods by which cross-sections can be created which are amenable to SEM measurements. Then a brief discussion of other methods of determining microstructural features like clustering tendency and percolation limits of explosive crystals. Finally, this chapter will provide some commentary on how preparation method affects microstructure. Discussions on how 'microstructure' can be quantified and how this changes shock initiation behavior will be in the following chapters.

3.2 Materials and Method of PBX Preparation

The following section is general for any mixture of explosive powder and soft polymer binders, however the primary example will use 1,3,5,7-Tetranitro-1,3,5,7-tetrazocane (HMX), a common high explosive. Using this example is beneficial for two reasons: first, it is a common explosive throughout this dissertation and availability of comparable legacy work on single crystal from shock ignition experiments.[1] Second, the recrystallization procedure creates fine, monodisperse grains (< 10 μm) with complicated geometries, making it more challenging to measure.

3.2.1 Preparing PDMS-based PBX

PDMS used was Sylgard® 182 from Ellesworth Adhesives, HMX crystals were made via crash precipitation of bulk HMX stock in an Acetone water mixture. The particle size distribution was consistent and when evaluated by image analysis of secondary electron micrographs (SEM) (JEOL 7000F) and a light scattering mastersizer (Horiba) had a mean particle size of 4.5 μm equivalent diameter and 2.8 μm median equivalent diameter. The particles produced were a fine-

grained powder consisting of a combination of tetragonal shapes and platelet structures [Fig 3.1(a)]. If approximated as spherical particles, the particle size distribution derived from light scattering methods is a unimodal polydispersion [Fig 3.1(b)].

HMX used in this work was extracted from a stock of N-5 material by dilution in acetone followed by a filtration through no. 55 filter paper in a Buchner funnel. To achieve a consistent particle size distribution, HMX is then recrystallized again using the following procedure: 300 mg of HMX is measured then dissolved in acetone to saturation. Following this, a 3 mL pipette is used to crash precipitate the HMX using several successive 3 mL aliquots DI water. The crystals are filtered through no. 55 filter paper using a Buchner funnel then air dried for 30 minutes.

The particle size distribution is determined by taking the HMX crystals and suspending it in Ethylene glycol (Fisher). Due to the small crystal size of HMX particles, ethylene glycol was ideal to prevent clustering which superficially increases particle size distributions. A Horiba mastersizer is used to determine the volumetric particle size distribution. This data was verified by measuring the loose powder on a scanning electron microscope (SEM) (JEOL 7000F). 7 nm of a gold palladium coating was applied to the powder after being affixed to double-sided copper tape and an accelerating voltage of 10 KeV was used.

The HMX grains created by this process are polycrystalline, and irregular shapes, often flat triangles. Tendency towards a very fine, unimodal size distribution proved amenable to evaluating clustering tendencies. Compared to bimodal distributions, which pack better, it would be harder to decouple grain-sized based phenomena from cluster size dependent behavior. While the effect of larger grains in comparison to clusters will be evaluated in a later chapter, unimodal size distribution allows these to be decoupled. However, the high aspect ratio of these crystals requires phenomenological evaluation of their packing tendencies. Some literature theorizes maximum

packing fractions of polydisperse mixtures of irregular shape[5,6], allowing for an estimate of the approximate maximum packing fraction of the HMX crystals.

If these HMX crystals are assumed to be spherical and polydisperse with size distributions from Fig 3.1(b), the maximum packing fraction would be about 74 vol.% or about 85 wt.%.[6] However, the platelet-like structures seen in this particular crystal better resemble a mixture of spheres and hard disks. This will cause lower maximum packing fractions than predicted with spheres and the prominence of jamming of crystals packed in binder at higher concentrations.[7,8] Shock initiating PBX at different packing fractions allows us to observe differences caused by packing inefficiency.[9] This will be covered in more detail in Chapter 5.

Finally, HMX has several different crystalline phases, which can dramatically affect how they respond to shock compression, namely due to the anisotropy between crystalline planes[10]. The β crystalline phase is the most stable under STP conditions[11], however as a matter of due diligence XRD was collected to verify the identity of all the HMX used in this experiment. Similar experiments were done on the TATB that will be studied in Chapter 4 to ensure the change of behavior is only caused by particle size distribution changes. See Appendix D for XRD and characterization data.

PDMS is the binder of choice for most experiments outlined in this dissertation due to it creating highly extrudable compounds. This is beneficial because it allows for fast and consistent casting of micron-thin wells of material to be studied. PDMS is a relatively uncommon binder for PBXs, with harder binders such as estane, Viton or Kel-F[12], which are also harder, more durable materials. However, Extex, or XTX-8003 (otherwise known as LX-13) is a mixture of 80wt% of the high explosive 2,2-Bis[(nitrooxy)methyl]propane-1,3-diyl dinitrate, otherwise known as Pentaerythritol Tetranitrate (PETN), with Sylgard 182 PDMS binder and extruded through a mill.[13]

This material is engineered to be highly extrudable, and most PBX mixtures studied here are based off this procedure. Our effort used PDMS obtained as Sylgard® 182 from Ellesworth Adhesives.

The procedure to prepare PBX is loosely adapted from the technique developed in a study by Basset *et. al.* to produced PETN-based XTX-8003.[3] PBX was prepared by adding 150 mg quantities of EM crystals with PDMS to the appropriate mass fraction, using hexanes as a process solvent diluting the PDMS stock to 70-80 mg PDMS/1 mL of Hexanes. The standard error of the measurements propagates to 2% relative error for the final mass loading number. On this basis, we choose to not employ more than 5 wt% granularity when ranging the mass fraction from 5-85 wt%. The process solvent is left to vaporize while mixing EM grains and PDMS, then manual kneading is performed to better homogenize the mixture.

For cross sectioning studies, the mixture is then inserted into a silicone embedded mold that has been treated with Teflon spray. The sample is covered with Teflon tape, clamped between two 4-inch square cuts of glass, and inverted to be Teflon-tape side down. The assembly is placed into a 70-80°C oven for 12-16 hours.

When used for shock compression experiments, the final mixture is extrusion cast into 30-250 micron deep Kapton wells affixed to a Pyrex glass substrate. The molds are cured at 60-70°C for 12-16 hours to match XTX standard operating procedures derived from literature[13]. The exact length of the final charges was verified by optical profilometry (Keyence VK-X1000) for height error and surface roughness. (See Appendix D for profilometry data).

3.3 Developing Cross Sectioning methods for PDMS-based PBX

PDMS-based PBX mixtures pose a unique challenge for cross sectioning because most mechanical methods rely on the material to be hard or brittle. PDMS (in this case Sylgard 182) is

a very soft material, and its mechanical properties greatly contrast from molecular crystals such as HMX, PETN or TATB. Experiments in this lab were unable to find robust, repeatable methods for creating cross sectional data on any PDMS-based PBX mixtures; only very limited successes were found. The tested techniques ranged from simple abrasive methods such a mechanical polishing on a silicon-carbide/diamond ultra fine grit polishing paper on Allied MultiPrep^{TM} system to high precision techniques such as facing on microtome operated at cryogenic conditions, and ion-milling using ionized Argon. In all cases, defects persisted in the form of dislodged crystals, selective deterioration of HMX and polymer-crystal delamination. A few promising directions have been elaborated in detail in the subsequent subsections.

3.3.1 Molded Flat Surfaces for Electron Microscopy

To avoid the issues intrinstic to mechanical cross sectioning of soft samples, a flat surface necessary for imaging was manufactured by mixing PDMS-based PBX and curing it onto a flat mold. Using a silicone mold for SEM (Pelco Embedding Mold #110), uncured PBX was poured and overfilled into a mold and clamped to a sheet of glass with a thin Teflon film in between. The Teflon film imprints a surface that is <100 nm roughness and makes the crystal layer immediately beneath the surface visible by SEM. An added step of plasma treatment was added as an attempt to further improve the contrast. An RF Plasma Asher (March Plasmod). The surface was treated for 3 minutes at 200V. The result was a glassy surface on the PDMS that had many fracture lines. This did not appear to notably change the contrast on SEM measurements.

The results were initially promising but difficult to repeat and very fragile. Figure 3.2 shows two examples of images obtained from pressed smooth surfaces showing HMX in PDMS matrix, where the explosive crystal phase (dark) can be readily contrasted from the binder phase (light) in both a low and intermediate concentration of sample. The problem was twofold:

electron beam damage and occlusion of some particles due to the layer of PDMS covering the entire sample. With more refinement, this has the potential to be a method suitable for estimating volumetric distribution of explosive grains in the PBX, but proved too inconsistent and fragile to produce the quantities of data needed for meaningful analysis.

3.3.2 Drop-casting PBX mixtures for optical microscopy

However, clustering tendencies of explosive grains in a binder matrix depend on the grain composition, it's size distribution, the properties of the binding matrix and grain-binder interactions. This dissertation chose to create a thin film of PBX on a microscope slide. By press extruding the film to 20 μm, the particle size distribution yielded from Fig 3.1(a) would imply that this would approximate a monolayer of crystal grains in polymer binder. This allows for an optically accessible layer of PBX which can be imaged and characterized. Such extruded samples made from PDMS and a surrogate binder can be compared to establish validity of the surrogate as PDMS replacement to obtain representative cross sections for imaging as described in subsequent section 3.4. This technique of looking at extruded PDMS-based PBX is also pursued as an alternative to cross-sectioning as well.

The process of preparing these thin films is illustrated in Fig 3.3. To prepare PDMS thin films, a 1-gram quantity of Sylgard® 182 base is mixed with 10 wt.% curing agents followed by 1-10 wt.% EM. After manual mixing, a ~100 μL droplet of the mixture is cast onto a glass microscope slide, then pressed down with a #1.5 cover slip and second glass slide to apply even pressure. Once the film is extruded to a thin layer, it is placed in an oven at 70°C for 8-12 hours.

The final slides are measured on a metallurgical microscope using a cross-polarized light assembly. This allows for high enough contrast to easily measure cluster size by image

thresholding (Fig 3.4). Using Fiji[14], the image is segmented by thresholding, binarized, then undergoes particle size analysis. Because this study is interested in particles, a size filter of 20μm^2, or ~2.5 μm equivalent diameter, is imposed to avoid individual particles being included. The measured concentration is determined from the area fraction of crystals relative to the frame, and the analysis utilizes an image area of 550x425μm for all images. Figure 3.4 shows two examples of thin films imaged by cross-polarized light. The contrast and resolution of the images are generally quite good.

The final concentration of these slides inferred from the area fraction of total HMX grain cross sectional area, will be significantly higher than the stock solution due to sediment beds being formed from press extrusion, as well as the films still being 3-dimensions unlike SEM cross section micrographs. In effect, 3 dimensions are being projected into two dimensions, resulting in interleaving of already existing clusters, meaning cluster size will monotonically increase with the frequency of clusters in the solution. Table 3.1 shows the result of this in terms of mass fractions created from different base solutions being drop cast. The complexity of this process limits this to a purely comparative measure of binder zeta potentials rather than an absolute measure of cluster propensity. This is not a true cross section, since the processes involved in press extrusion don't truly match how bulk PBX samples are produced in experiments. However, the lack of alternatives available at the time of writing makes this the best analogue for viewing clustering behavior.

Table 3.1 Drop cast vs actual PBX concentration when press-extruded on a microscope slide. The measured concentration is used to compare binder material via image analysis of light microscope images.

Stock Concentration (wt%)	Measured Concentration (area%)	Measured Concentration (wt%)	Standard Deviation (vol%)
3	2.4	4.1	1.3
4	8.9	14.6	1.5
5.5	11.9	18.9	3.9
10	26.1	32.9	8.8
15	38.8	52.4	0.7

3.3.3 Summary of Cross-Sectioning PDMS

As hypothesized, most means of mechanically cross-sectioning PDMS-based mixtures were difficult and unreliable. In this case, press-extruding the material against Teflon tape proved the most reliable, creating a sub-100 nm surface roughness adequate for cross sectional imaging, and the relative cross-sectional sectional areas of HMX compared to PDMS matched the predicted concentration of the PBX mixtures. Currently, the best available method is drop casting thin layers of PDMS-based PBX on microscope glass to produce thin layers for imaging. Unfortunately, this limits the ability to procure details on the scale of single grains, but only clusters of several grains.

A proposed alternative would be using a focused ion beam to mill a flat surface. In testing, this method worked very effectively but covers very little surface area so it simply is not practical for these studies. X-Ray computed tomography (CT) can also be used to probe the inside of soft binder-based explosives. However, success using this method would require a relatively high energy X-Ray source such as Tungsten[15] and micro CT instruments are typically capped at 2.2

μm voxel resolution making it harder to pursue small micron sized particles in PBX. For grain-scale resolution of these mixtures using cross-sectioning, the harder epoxy binder was necessary.

3.4 Epoxy as an Analogue for PDMS

Using epoxy as a binder to create analogues for the PDMS-based explosives has the benefit of allowing mechanical cross sectioning methods to be done. These methods create surfaces that have much better contrast on SEM and are easier to make.

3.4.1 Preparing Epoxy-based PBX

For cross sectioning with a microtome, a PBX analogue using an epoxy-based binder material was used. Loctite Abelstik 24, a two-part epoxy, was mixed then HMX crystals are added. Epoxy is denser than PDMS meaning the HMX relative volume in these epoxy-analogues is matched to PDMS-based PBX samples. For clarity, this data will be presented in terms of equivalent mass fraction in PDMS.

It is reasonable to question whether some phenomena such as clustering will be comparable across different binder materials which are also prepared in slightly different manners, at least at lower than max packing fraction concentrations.

3.4.2 Microtome to Produce True Cross-Sections of Epoxy-based PBX

The epoxy-based PBX was cast in an embedded mold [Fig 3.5(left)] (Pelco Embedded mold #110). A Leica ultramicrotome was used for all microtome experiments. Starting at a 1 μm cut depth with a glass blade to prepare the surface. After a few cuts it is reduced to 200 nm depth with a feed rate of 120 cuts per minute. A 6 mm length diamond blade (Diatome Histo) was used for the final cuts. 30 cuts at 100 nm depth were performed. This method left a rough finish due to

the blade catching on crystals inside of the soft PDMS binder, but works ideally in the case of PBX cast with epoxy

3.4.3 Cross Section Surface Preparation for SEM

Due to the low thermal and electrical conductivity of polymer binders, and especially high explosives, some surface treatment must be performed on PBX layers in order to avoid burning from the electron beam. A gold palladium coater was used as an alternative to carbon-rod coating and it was determined that the surface was equally amenable to electron back scattering imaging. Further, using a 14 nm gold palladium coating allows higher throughput and reduces the chance of carbon dust blemishing the surface of the PBX. The samples are cleaned with hexanes and dried with nitrogen, then put into the gold sputtering machine (Emitech K-575) and run at 20mA for 55 seconds at an approximate deposition rate of 2.5 Angstroms/second.

3.4.4 Cross Sectioning Results

For cross-sectioned PBX samples, the electron back-scattering (BSE) detector can readily make out particle-level details of the cross section at 15 keV and high probe current, with the sample being adequately conductive after the above pre-treatment. For epoxy-based cross sections, 15 keV with medium probe current is adequate to resolve crystals from binder. Often secondary electron (SE) measurements are performed on the same frame to ensure that there is little to no surface texture and be able to differentiate a particle from a surface-level defect which would be otherwise invisible to BSE measurements. Samples of some of these cross sections can be seen in Fig 3.6.

Once the images of the cross sections are obtained, we post process the image to create a binary image that determines the EM phase from the binder phase. This usually only requires

basic thresholding techniques if particle feature-scale resolution is not needed. Thresholding is performed using Fiji, if there is lower contrast, hand-painting regions or a machine-learning classifier is performed using the LabKit plugin. For more complex thresholding, a Python script was used (see Appendix C.3) is used to take particle centroids, particle sizes, and clustering behavior such as cluster size and distances. Figure 3.7 displays an example of determining clusters of particles, defined as two or more grains with touching borders, and drawing bounding rectangles. It is an example of how grain clusters can be evaluated in epoxy-based cross sections.

3.5 Conclusions

Robust methods of measuring and quantifying structures in PBX materials are crucial to continuing microstructure analysis. While PDMS-based materials are useful for designing small-scale shock experiments, they are quite difficult to measure from the inside. Most methods of cross sectioning materials greatly favor the use of harder materials, such as epoxy, as a binder. It is concluded that using a microtome to cross section epoxy-based PBX is the most reliable solution available at the time of this dissertation. Any measure relying on solvent properties, such as delamination and clustering will require additional steps to directly compare the properties of PDMS and Epoxy.

With a high energy X-Ray source, softer binders can sufficiently be contrasted against the high-density grains even with a Tungsten anode and appropriate scanning durations[15]. If such equipment were available, this would become the ideal alternative to cross-sectioning and allow for 3-D mapping of a whole EM pellet rather than limited cross sections. However, if evaluating pure packing dynamics at high concentrations, binder composition is less relevant to analyzing microstructures. Going forward, epoxy-based PBX cross sections will be used for all structure analysis on densely packed mixtures of explosive grains in binders. For more sparse

concentrations where surface potentials, affecting factors such as grain clustering, are relevant, drop-cast layers will be employed instead.

3.6 Figures

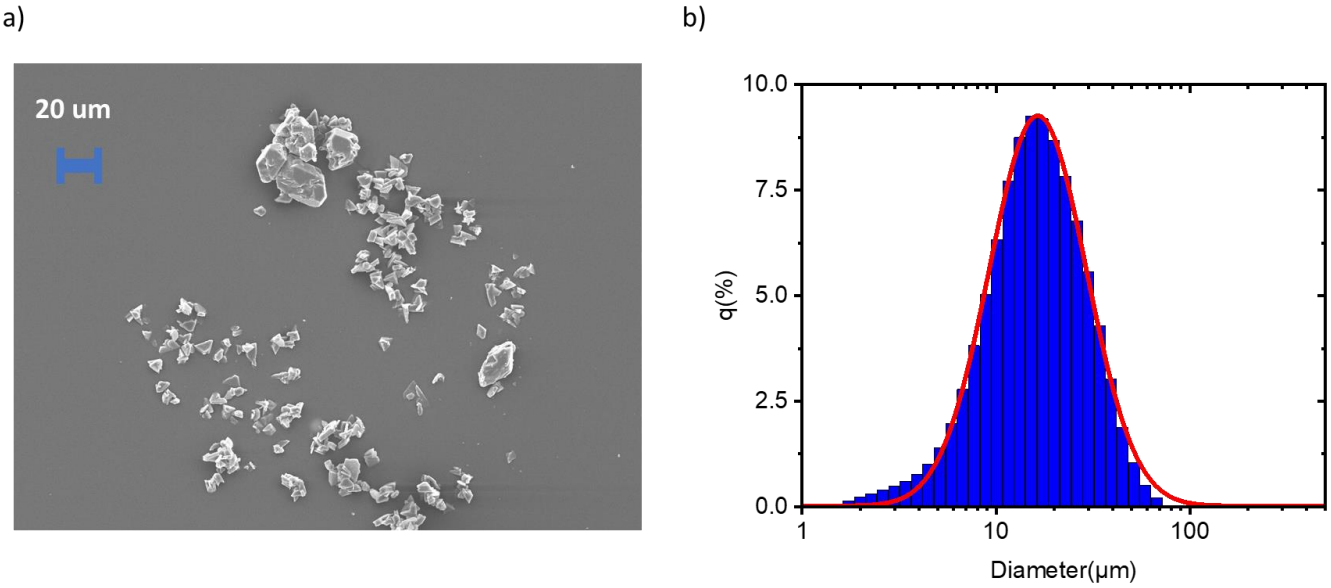

Figure 3.1 Electron micrograph of loose HMX powder used for PBX formation (left). The powder is rather fine polycrystalline wedges formed from crash-precipitation from saturated acetone solution. Volume based particle size distribution determined by a laser-light scattering particle sizer (right).

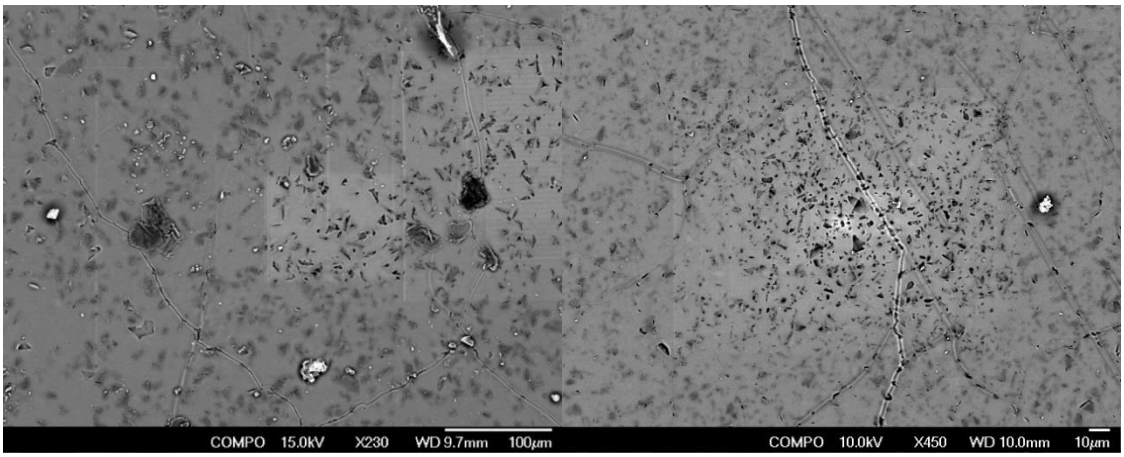

Figure 3.2 Back-Scattered Electron Micrographs of 20 wt% HMX in PDMS (left) and 40 wt% HMX in PDMS (right). Notice the areas of beam damage where a closer focus was used. The fault lines are a known consequence of oxygen plasma treatment and not inherent to the microstructure of these samples. There is also some occlusion from the layer of PDMS covering the entire surface, obscuring some particle level detail. This method is promising as it effectively contrasted the HMX from the PDMS. Unfortunately, the results proved highly inconsistent and difficult to repeat over many samples. The micrographs show clear damage from the electron beam which is a result of PDMS also being a poor conductor of electrons, even with an added carbon or gold layer.

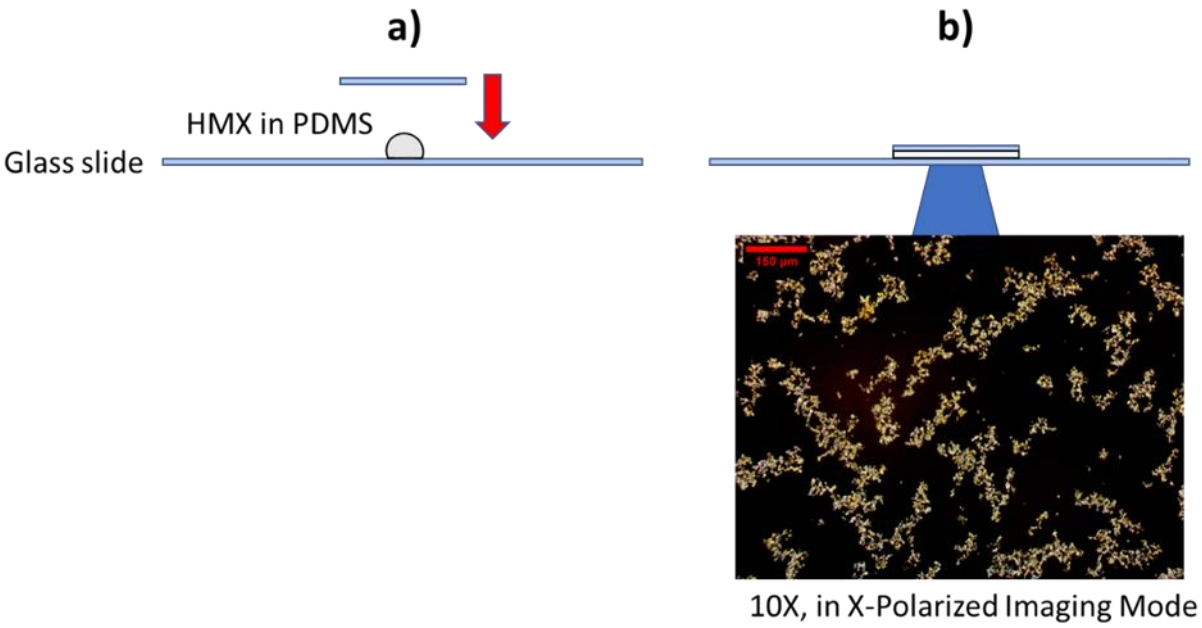

Figure 3.3 Example of drop cast microscope slides of HMX in PDMS preparation technique to produce ~20 µm thick layers of plastic explosive. A small drop of HMX suspended in uncured PDMS is placed on a microscope slide(a). When pressed by a cover slip, the layer is extruded to ~20 µm thick, verified by optical profilometry. Based on the particle size distribution, this approximates a monolayer of crystals and grains.

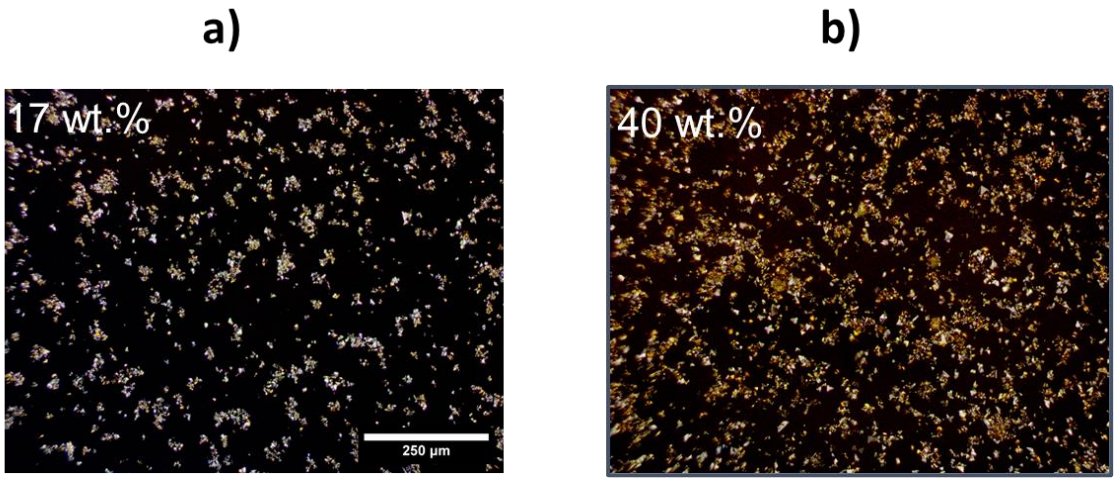

Figure 3.4 Example of drop cast microscope slides of HMX in Sylgard 182 PDMS. Though this has many differences to true cross sections of PBX, it is the best available analogue at the time of this dissertation. Examples show a disperse solution of HMX in PDMS (a) where cluster propensity is high. And 40 wt.% HMX in PDMS where percolation of grains begins to occur (b).

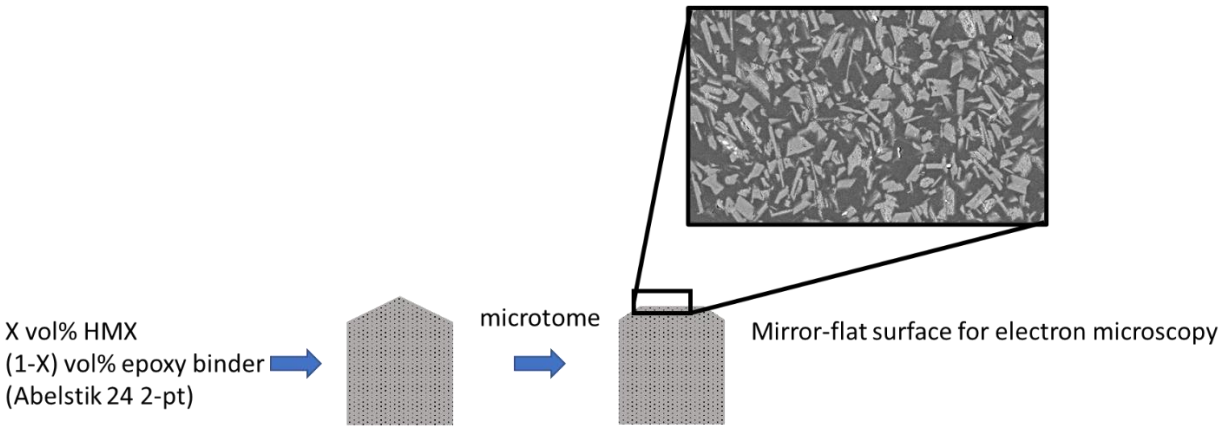

Figure 3.5 Schematic showing the samples used to produce true cross-sections for electron microscopy. A mixture of explosive grains and epoxy binder is cast into a silicone mold. The pointed end of the mold is ideal for cross sectioning *via* a microtome. The result is a mirror-flat surface suitable for electron microscopy.

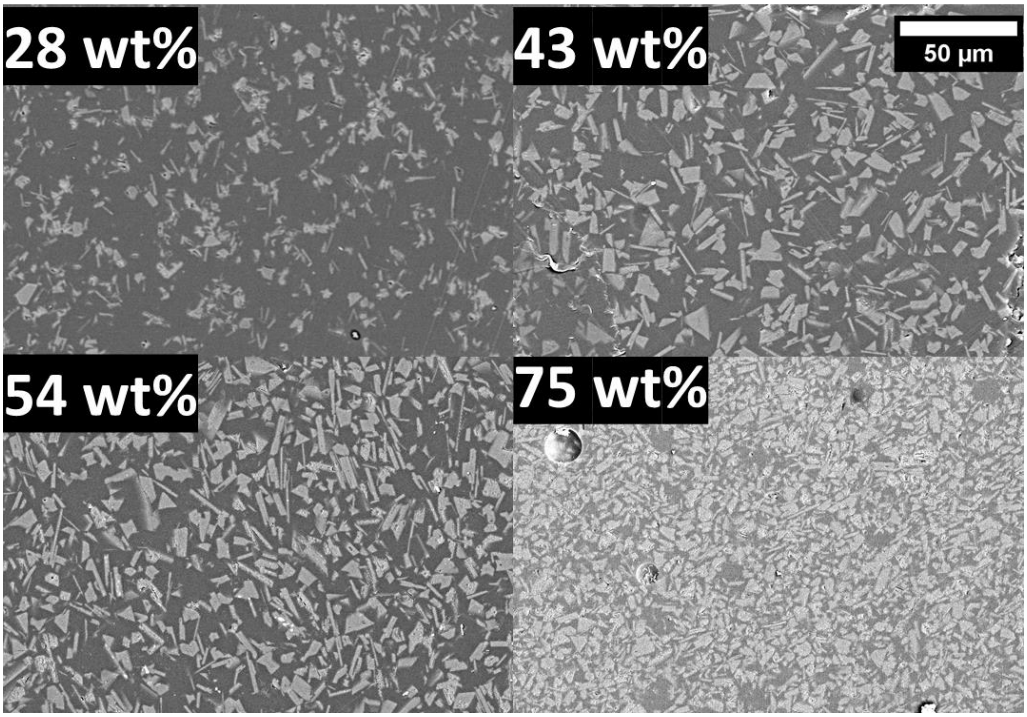

Figure 3.6 Electron Micrographs displaying true cross sections of explosive grains suspended in epoxy binder. These were prepared by microtome, and the high resolution available to electron microscopy allows PBXs to be viewed on the particle scale. For low mass fractions of explosive in binder, however, it cannot be verified that surface potential of crystals in epoxy is equal to PDMS. This technique gives exquisite detail but is only used for fully packed systems, 70 wt.% and higher.

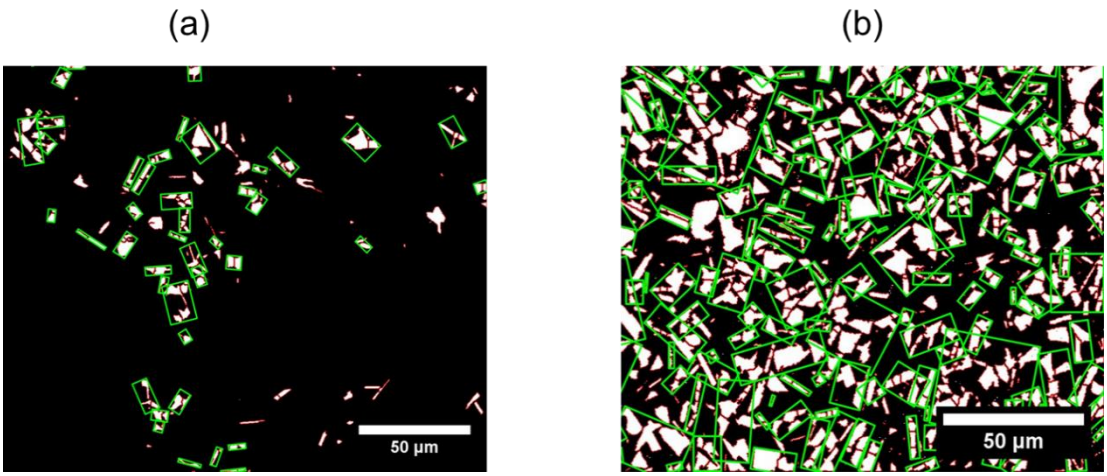

Figure 3.7 Example of how clusters can be evaluated on the individual-particle basis. Green squares are drawn around groups of two or more particles that are all touching in a 'friends of friends' framework for clustering behavior. (a) A very sparsely concentrated system where clustering dominates and different groups are well separated. (b) a higher concentration of explosive-binder mixture showing how clustering algorithms perform in much busier systems beginning to show signs of percolation.

3.7 References

1. Johnson, B. P.; Zhou, X.; Ihara, H.; Dlott, D. D. Observing Hot Spot Formation in Individual Explosive Crystals Under Shock Compression. *J. Phys. Chem. A* **2020**, *124* (23), 4646–4653.

2. Johnson, B. P.; Zhou, X.; Dlott, D. D. Shock Pressure Dependence of Hot Spots in a Model Plastic-Bonded Explosive. *J. Phys. Chem. A* **2022**, *126* (1), 145–154.

3. Bassett, W. P.; Johnson, B. P.; Neelakantan, N. K.; Suslick, K. S.; Dlott, D. D. Shock Initiation of Explosives: High Temperature Hot Spots Explained. *Appl. Phys. Lett.* **2017**, *111* (6), 061902.

4. Rai, N. K.; Udaykumar, H. S. Void Collapse Generated Meso-Scale Energy Localization in Shocked Energetic Materials: Non-Dimensional Parameters, Regimes, and Criticality of Hotspots. *Phys. Fluids* **2019**, *31* (1), 016103.

5. Mutabaruka, P.; Taiebat, M.; Pellenq, R. J.-M.; Radjai, F. Effects of Size Polydispersity on Random Close-Packed Configurations of Spherical Particles. *Phys. Rev. E* **2019**, *100* (4), 042906.

6. Desmond, K. W.; Weeks, E. R. Influence of Particle Size Distribution on Random Close Packing of Spheres. *Phys. Rev. E* **2014**, *90* (2), 022204.

7. Lu, B.; Torquato, S. Nearest-Surface Distribution Functions for Polydispersed Particle Systems. *Phys. Rev. A* **1992**, *45* (8), 5530–5544.

8. Donev, A.; Torquato, S.; Stillinger, F. H.; Connelly, R. Jamming in Hard Sphere and Disk Packings. *J. Appl. Phys.* **2004**, *95* (3), 989–999.

9. Nguyen, Y.; Seshadri, P.; Sen, O.; Hardin, D. B.; Molek, C. D.; Udaykumar, H. S. Multi-Scale Modeling of Shock Initiation of a Pressed Energetic Material I: The Effect of Void Shapes on Energy Localization. *J. Appl. Phys.* **2022**, *131* (5), 055906.

10. Perriot, R.; Cawkwell, M. J. Thermal Conductivity Tensor of β -1,3,5,7-Tetranitro-1,3,5,7-Tetrazoctane (β -HMX) as a Function of Pressure and Temperature. *J. Appl. Phys.* **2021**, *130* (14), 145106.

11. Bowlan, P.; Henson, B. F.; Smilowitz, L.; Levitas, V. I.; Suvorova, N.; Oschwald, D. Kinetics of the γ–δ Phase Transition in Energetic Nitramine-Octahydro-1,3,5,7-Tetranitro-1,3,5,7-Tetrazocine. *J. Chem. Phys.* **2019**, *150* (6), 064705.

12. Marsh, S. P. *LASL Shock Hugoniot Data*; University of California Press, Berkeley, 1980.

13. Dobratz, B. M. *Properties of Chemical Explosives and Explosive Simulants*; UCRL--51319, UCRL--51319(REV.1), 4285272; 1972; p UCRL--51319, UCRL--51319(REV.1), 4285272.

14. Schindelin, J.; Arganda-Carreras, I.; Frise, E.; Kaynig, V.; Longair, M.; Pietzsch, T.; Preibisch, S.; Rueden, C.; Saalfeld, S.; Schmid, B.; Tinevez, J.-Y.; White, D. J.; Hartenstein, V.; Eliceiri, K.; Tomancak, P.; Cardona, A. Fiji: An Open-Source Platform for Biological-Image Analysis. *Nat. Methods* **2012**, *9* (7), 676–682.

15. Manner, V. W.; Yeager, J. D.; Patterson, B. M.; Walters, D. J.; Stull, J. A.; Cordes, N. L.; Luscher, D. J.; Henderson, K. C.; Schmalzer, A. M.; Tappan, B. C. In Situ Imaging during Compression of Plastic Bonded Explosives for Damage Modeling. *Materials* **2017**, *10* (6), 638.

CHAPTER 4: QUANTIFING SHOCK INITIATION USING EMISSION PYROMETRY, A STUDY ON INSENSITIVE EXPLOSIVES

4.1 Introduction[2]

TATB (1, 3, 5-trinitro-2, 4, 6-triaminobenzene) is an energetic material with several unique properties. It is of special interest because it combines insensitivity to external perturbations with high energy release.[1,2] Understanding TATB sensitivity is important because, in the form of microstructured plastic-bonded explosive (PBX), it is used in nuclear weapon triggers where predictable and safe behavior is paramount. One issue for assuring TATB consistency is the difficulty of controlling TATB microstructure, which can affect both shock sensitivity and detonation.[3] It is possible to recrystallize most energetic materials under controlled conditions to reduce microstructure variability, but that is difficult with TATB, which is insoluble in virtually all solvents. Instead, TATB microstructure develops spontaneously during the final step in the synthesis, amination, as the newly generated TATB crash-precipitates out of solution. Small changes in the temperature or the amount of water introduced during this final step can have a large effect on the microstructure.[3] In this study, we fabricated TATB into a PBX with 20% binder (Sylgard 182) and minimized void volume with a hydraulic press.[4,5] Collecting several different TATB powder samples, which exhibit different particle size and

[2] This chapter was partly adapted to highlight work published in the original research article- Akhtar, M.; Salvati, L.; Valluri, S. K.; Dlott, D. D. Shock Ignition and Deflagration Growth in Plastic-Bonded TATB (1, 3, 5-Trinitro-2, 4, 6-Triaminobenzene) Microstructures, Appl. Phys. Lett. 2022, 121(6), 064101, with the permission of AIP Publishing. This chapter is adapted to focus mostly on how the radiance analysis and materials characterization were used in this paper.

shape factors, the goal is to develop robust methods of determining how these powders affect the performance of a PBX. Emission pyrometry will be performed and cross-referenced with various characterization methods of the powders to better understand how to correlate microstructure with performance.

4.2 Experimental

4.2.1 Emission Pyrometry

We measured the nanosecond time-resolved spectral radiance of the visible (450–825 nm) thermal emission following powerful short-duration 4 ns shocks. The spectral radiance, with units of $\frac{W}{m^2\text{-}sr}$, is the emission spectrum vs a calibrated intensity standard (see Chapter 2). Absolute intensity measurements allow quantitative comparisons between different samples under different shock loads.[5] The spectral radiance from thermal emitters can be used to determine temperatures via the graybody approximation.[6] A shocked PBX will initially have a spatially inhomogeneous temperature distribution, i.e., there will be hot spots. Because the intensity of a graybody emitter is the fourth power of the temperature, graybody temperatures at shorter times primarily represent hot spots. Graybody temperatures are reliable only if the emission being analyzed is purely thermal. There may be atomic line or molecular band emission superimposed on the thermal emission,[7,8] and there may be absorbing species in the reaction plume between the sample and the detector that distort specific regions of the spectrum,[5] potentially leading to large errors in temperature determinations. We have previously developed a procedure for displaying time-dependent spectral radiances in a linearized form, so deviations from a graybody spectrum are easily identified when fitting the spectral radiance to a graybody.[4] Atomic and molecular emissions were largely absent in our TATB experiments, but TATB, which is yellow, absorbs light <550 nm. As the shocked TATB reacts, it decomposes into

colorless products, but at shorter times, there will be some unreacted TATB in the line of sight between the sample and the detector.[4] Our procedure allows us to discard spectral regions where the thermal emission is distorted by this absorption.

4.2.2 Laser-Driven Flyer Plate Experiments

Our experimental method, which is described in more detail elsewhere,[4,7,9] as well as in Chapter 2, uses short-duration (4 ns) shocks produced by laser-launched 1.8–4.7 km/s Al-1100 flyer plates that were 0.5 mm in diameter and 25 μm thickness.[10,11] Using an 8 GHz photon Doppler velocimeter (PDV), we previously showed that the shot-to-shot variation of the flyer velocity was ±2%.[10] The shock rise time is <2 ns, even after the shock passes through a 90 μm thick TATB PBX.[12] An array of 186 cylindrical PBX charges, all fabricated from the same source material, was prepared by mixing TATB powder with 20 wt.% Sylgard 182. Pressing the sample reduced the void volume to <5%, previously determined by sampling some of the PBX with x-ray computed tomography.[4,5]

Each TATB PBX charge is a cylinder with a 1 mm in diameter and 90 lm in length, weighing about 100 lg, and having a unique microstructure. The most common TATB particle [Fig. 1(c)] is about 20 μm, and it weighs about 15 ng, so there are many thousands of particles in each charge. However, the region being observed is 60-90 μm^2 at the center of the shocked volume. The depth of this probed region is roughly the photon scattering length in the PBX, which we do not know accurately. Still, if for illustration, we estimate this depth as 25 μm, the probed volume would weigh about 150 ng, and we would be probing microenvironments with tens of TATB particles.

4.2.3 Explosive Powder Characterization

TATB powders were provided externally and measured as received. We measured the TATB particle size distribution in the source powder and in the pressed PBX. The powder was suspended in ethylene glycol, which, we observed, hinders TATB aggregation, and laser light scattering was used to determine the size distribution of equivalent spherical particles. The results of 10 different sample lots of TATB is shown in Fig 4.1(a). However, powder size distributions are expected to be altered from the source material due to press extrusion process. By microtoming epoxy based TATB PBX samples after press extrusion, the effect of press extrusion on particle size distribution can be evaluated. Cross-sectional images were analyzed using the ImageJ/Python software to obtain sizes by fitting ellipses to each particle and computing an equivalent diameter as the average of major and minor axes. Figure 4.1(b) compares the particle size volume fraction in powder and in PBX. These distributions appear identical for smaller 20 μm particles, but the pressed PBX contains far fewer of the larger particles, which were pulverized in the hydraulic press. Unfortunately, this experiment could not be conducted on very many of the ten available particle size distributions, simply due to a limited availability of powder compared to the large quantities needed to generate cross-sectional samples.

Figure 4.2 shows typical electron micrograph of the PBX surface, using back-scattered imaging. While the exact structures won't be evaluated too critically in this chapter, it is important to note the distribution of polymer spaces (the lighter phase), and the distribution of micro to nanoscale pores inside of explosives. It will be shown in the next chapter that the local distributions of polymer islands are quite important to properly modeling the system and is an important field of study in the future.

In order to isolate the differences between samples as purely microstructural versus chemical differences, some characterization of the crystalline structure and decomposition kinetics of the powders were performed. Powder XRD was performed on each powder to probe for major differences between crystallite size, and crystalline strain. These experiments were conducted using a Bruker D8 advanced. No substantial differences were found in crystallite strain, but differences were found in crystallite size, which is to be expected for powders prepared differently. TGA experiments were also conducted to rule out major differences in decomposition kinetics. A 1 mg sample of each powder was loaded into a crucible and run in the TGA (TA instruments Q50) at 20 Kpm in inert (N_2) atmosphere. The plots can be found in Appendix D, but showed no substantial differences in reaction rates. Therefore, all differences can be isolated to purely microstructural differences due to the crystallization methods.

4.2.4 Emission Radiance Measurements and Integration

A typical TATB record is shown in Fig. 4.3, where the impact velocity was 1.8 km/s. The results are the average of 18 shots, and the temperature error bars represent 95% confidence limits.[7] The time-resolved radiance is the wavelength integral of the spectral radiance. The radiance from shocked TATB is a few $\frac{\text{kW}}{\text{sr-m}^2}$. The radiant intensity depends on both temperature and quantity of emissive material in the detected volume. Our time resolution, using a nanosecond shock and a nanosecond spectrograph (pyrometer), results in time-resolved radiance profiles with two distinct peaks: one around 20 ns and the other around 5 μs. The vacuum and the optical geometry resulted in minimal detected light from adiabatic gas compression, so the observed radiance emanates from TATB. The temperature and radiance profiles are interpreted in terms of the cartoon description shown in Figs. 4.3, which builds on prior work by Howe and co-workers. The interaction of the shock with the TATB microstructure [Fig. 2(b)] produces an

inhomogeneous temperature distribution,[13] with the highest temperatures typically at crystal defects, voids within TATB crystalsor crystal-binder interfaces. Since we see minimal radiant emission until after the 4 ns shock has dissipated, we infer that the hot spot temperatures initially produced by the shock are below our noise floor of 1500 K. Some hot spots are large enough and hot enough to ignite a small volume of TATB, so the 20 ns peak is attributed to thermal emission from an ensemble of TATB hot spots of varying sizes and temperatures. The process that creates these hot spots will be termed, "shock ignition." Note this differs from shock initiation, a term often used in studies of bulk PBX to describe the onset of chemical reactivity sufficient to produce a detonation. As described by Tarver and co-workers,[14] the heat flow out of the TATB hot spots may quench the reaction, or the reaction may spread into the surroundings. The smaller, colder hot spots that die out are termed "subcritical," while the larger hotter hot spots that grow are termed "critical." The hot spot growth process is a deflagration. As opposed to combustion, which is rate-limited by mass diffusion of fuel and oxidizer, a deflagration is a reaction in a "premixed" medium rate-limited by thermal transfer. Since TATB molecules contain both fuel (e.g., carbon) and oxidizer (e.g., nitro groups), hot spot growth in TATB is a deflagration. In our interpretation, the 5 μs radiance peak represents deflagration, and the rising edge of this peak characterizes deflagration growth. We subdivide the radiance profile into regions associated with these processes, as indicated in Fig. 4.3. In order to quantitatively compare results at different impact velocities, we compute "response functions" for these processes as the time-integral of the radiance in each region. These response functions have units of J/sr/m2. The time integral up to the first radiance peak is denoted the shock response. It describes how effectively the shock produces prompt high temperature thermal emission from TATB. Special attention is paid to the saddle point between the two radiance peaks around 500 ns, where the temperature is about 2200

K, since the radiance there must be due primarily to the surviving hot spots, i.e., the critical hot spots, that ignite widespread deflagration. The critical hot spots might be quite small, since according to Tarver and coworkers,[14] TATB hot spots >2000 K are critical if they are larger than 0.1 lm, but more likely the critical hot spots are fully ignited TATB particles, because based on previous work on HMX (cyclotetramethylene-tetranitramine) crystals,[15,16] 500 ns is more than enough time for a hot spot to ignite an entire crystal. The time integral from the first peak maximum to the saddle point the particle response, describes how effectively the shock produces critical hot spots. The time integral from the saddle point onward, the bulk response, describes how effectively the heat from the shock-generated hot spots overcomes the thermal barrier of insulating polymer binder to ignite adjacent TATB particles. The bulk response arises from widespread deflagration, which eventually terminates through cooling and flow of reaction products out of the observed volume. Our experiments cannot produce detonations because the sample diameter is less than the TATB critical diameter, and the sample length is less than the reaction zone. The shock-to-detonation transition in PBX typically proceeds by producing hot spots, deflagration and a deflagration-to-detonation transition, so the ability to produce a widespread deflagration, described by the bulk response, can be viewed as a necessary condition to produce a detonation. Our method is microstructurally sensitive because we observe only a small number of TATB particles in the observation volume viewed by a high-power objective.

4.3 Results

4.3.1 Velocity dependence of a single powder composition (Lot 2)

To begin this analysis, a single powder is chosen to exemplify how these response functions give insight into initiation and growth as shock pressure increases. In this case, TATB lot 2 was chosen simply because it was the most abundant.

In Fig. 4.4, we show radiances from four representative impact velocities selected from the 12 velocities we studied between 1.8 and 4.7 km/s. Each panel shows the radiance for each of the 15 or more shots at each impact velocity as well as the linear average. Each shot produces the characteristic two-peak structure, but there is considerable variance from shot-to-shot. This variance is too large to arise from the 2% flyer plate velocity variation, so it is attributed to variations in the TATB microstructure in the region of the PBX charge being observed. Figure 4.5 summarizes the impact velocity dependence of the shock response, the particle-scale response, and the bulk response, along with temperatures at the maxima of the two radiance peaks and the saddle point. This shows that the shock response and particle response [Figs. 4.5(a) and 4.5(b)] have similar impact velocity dependences. Unlike the bulk response, the shock response and the particle response do not increase monotonically with impact velocity, while the saddle point and bulk temperatures are largely independent of impact velocity [Figs. 4.5(c) and 4.5(d)]. The shock and particle response might be expected to decrease at higher impact velocities as the ignited TATB produces low-emissivity gas that hardly emits light and whose expansion cools the hot spots. The heat of explosion is about 8 kJ/cm^3,[2] so the maximum possible energy release of the shocked TATB can be estimated at about 140 mJ.

The kinetic energy of the 0.5 mm diameter, 25 μm thick Al flyer equals 140 mJ at 4.7 km/s, so around 4 km/s, the flyer plate energy begins to add significantly to the chemical energy release. The saddle point and the bulk response temperatures are largely independent of impact velocity because these temperatures are measured long after the shock has dissipated, and they are determined by the competition between heat generation from reacting TATB and thermal dissipation from the heated volume. The saddle point temperature associated with hot spots is lower than the bulk temperature because the hot spots at the saddle point lose heat because they

are small and surrounded by colder material. We have been able to time resolve hot spot ignition, the competition for survival among critical and subcritical hot spots, and deflagration growth because we used a short-duration shock and a high-speed spectrograph. The variation of the shock ignition and deflagration growth in different microstructures was expected, but the magnitude of the variation was not. There are some hot microenvironments that release energy much faster than the average, and these may play a role in determining shock sensitivity. The existence of hot microenvironments has implications for microstructure experiments and, especially, simulations done on small computer-generated structures that might not be representative of an inhomogeneous bulk. Our model and the ability to generate much information in a short time, and our previously demonstrated ability to use these techniques on PBX formulations other than TATB suggest a number of possible future investigations. It should be worthwhile to characterize the small volume being observed using optical or x-ray microscopy prior to shocking each sample, to understand the relationship between microenvironment and hot spot generation. Hot spot growth rates on individual particles, information useful for the development of improved kinetic models of chemical energy release,[17] can be studied by systematically varying the particle size distribution in the PBX. Deflagration growth starting from individual ignited particles can be studied by varying the binder fraction, since the ability of the ignition reaction to spread is most likely limited by thermal conduction across insulating binder layers between adjacent particles.

4.3.2 Comparison between different powder size distributions

This analysis method can be used to compare the different powder compositions, whose differences are mainly the particle size distributions of pure powders (Fig 4.1(a)). While these particle size distributions vary compared to the pressed samples which were shocked (Fig

4.2(b)), microstructures can still be compared with the caveat that particle sizes larger than ~20 μm effective particle diamters will likely be broken into smaller particles (between 10-20 μm). The main questions to be answered are: do the different particle size distributions change ignition behavior, and if so, why? Figure 4.6 gives an immediate answer to this question: plots of TATB powders at 3 different velocities show clear and repeatable differences in auto emission.

A starting point would be to analyze the particle size distributions in terms of maximum packing fraction, or TMD. If a polydisperse powder mixture is forced to pack at a volume ratio higher than physically possible, pores, polymer isles or defects (such as cracks) will form which can tangibly change the kinetics of the ignition process. With the particle size distributions of the 'as-received' powders, you can derive a theoretical maximum packing fraction of the powders using estimates derived from literature.[18,19] This will be discussed in more detail in the next chapter where that measure is relevant. In this case, the maximum packing fraction estimates show very little correlation with the initiation, bulk response, or particle-scale response integrals. In no small part this is because those numbers are rendered irrelevant by the effect of hydraulic pressing to homogenize the sample. This was originally performed to eliminate larger pores to lower the initial hot spot formation, a process described by Bassett *et. al* in detail.[20]

No single measurement seemed to provide a compelling trend to explain the differences in behavior between the various powder samples. Figure 4.7 provides two interesting graphs: the trend of bulk response integral – the measure of the deflagration progress, and the ratio between shock initiation and bulk response integral. For all samples, monotonic trends can be noticed which are similar to the observations made in the previous section. Where they differ is in the magnitude of change, lot 9 appearing to give the largest bulk response, and lot 3 consistently giving the worst bulk responses. The shock initiation integrals, a measure of the quantity of hot

spots formed or the conversion of mechanical energy to heat, doesn't appear to trend upward with flyer velocity, and in some cases trends downward. Meanwhile, bulk response integrals, a measure of the deflagration success, consistently trend upward as a function of flyer velocity. A distinct possibility is that a plurality of hot spots being formed in TATB are much lower temperature due to the excellent thermal conductivity of the graphitic-like structure.

What is likely happening is that more complex structural trends are contributing to the performance of these explosives than simply particle size. This could be anything ranging from more nuanced morphological factors of TATB, such as complex internal pore structures[21], the hydraulic pressing process, or even the distribution of polymer isles caused by packing phenomena such as jamming. All of these factors could explain the differences. All that can be concluded is that TATB powders with different size distributions crystallized in different ways have a significant impact on the performance measured by emission pyrometry. There is an immediate need to better understand of the structure of these explosives, and why they change performance. The use of radiance integrals is an important first step in establishing a body of high quality data to assist theoretical models of PBXs. The next chapter will explain how this method is extended to isolating the impact of clustered grains inside of polymer.

4.4 Figures

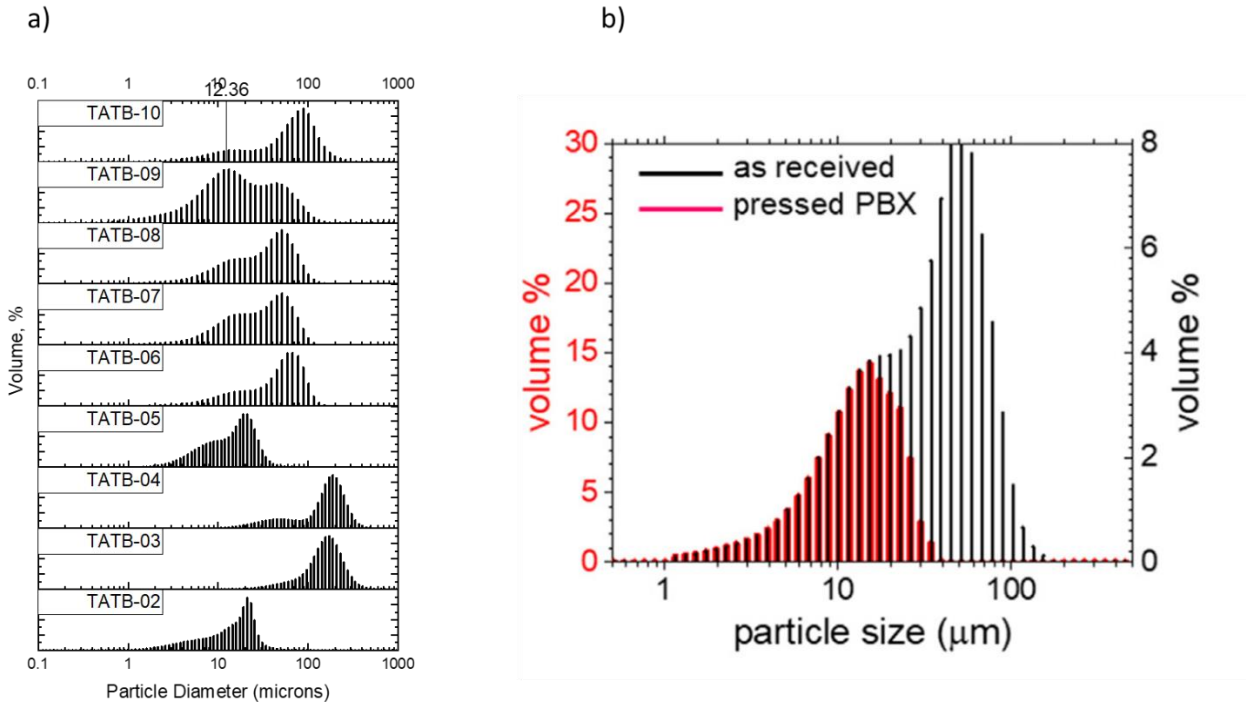

Figure 4.1 Comparison of powder size distributions of different lots using light-scattering particle sizing (a). The affect of applying a hydraulic press to the PBX mixtures (b). In general, bimodal particle size distributions have higher packing fractions, though press extrusion has a strong bias against particles > 20 μm equivalent diameter.

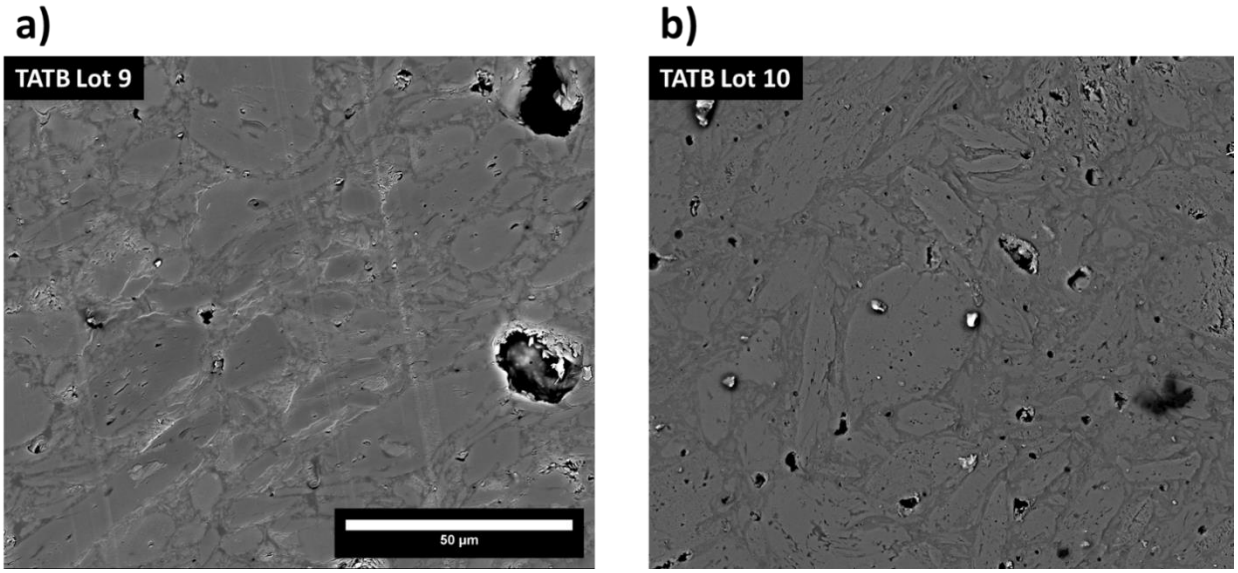

Figure 4.2 Electorn micrographs of a cross section of TATB PBX cross sections of TATB lot 9(a) and 10(b)

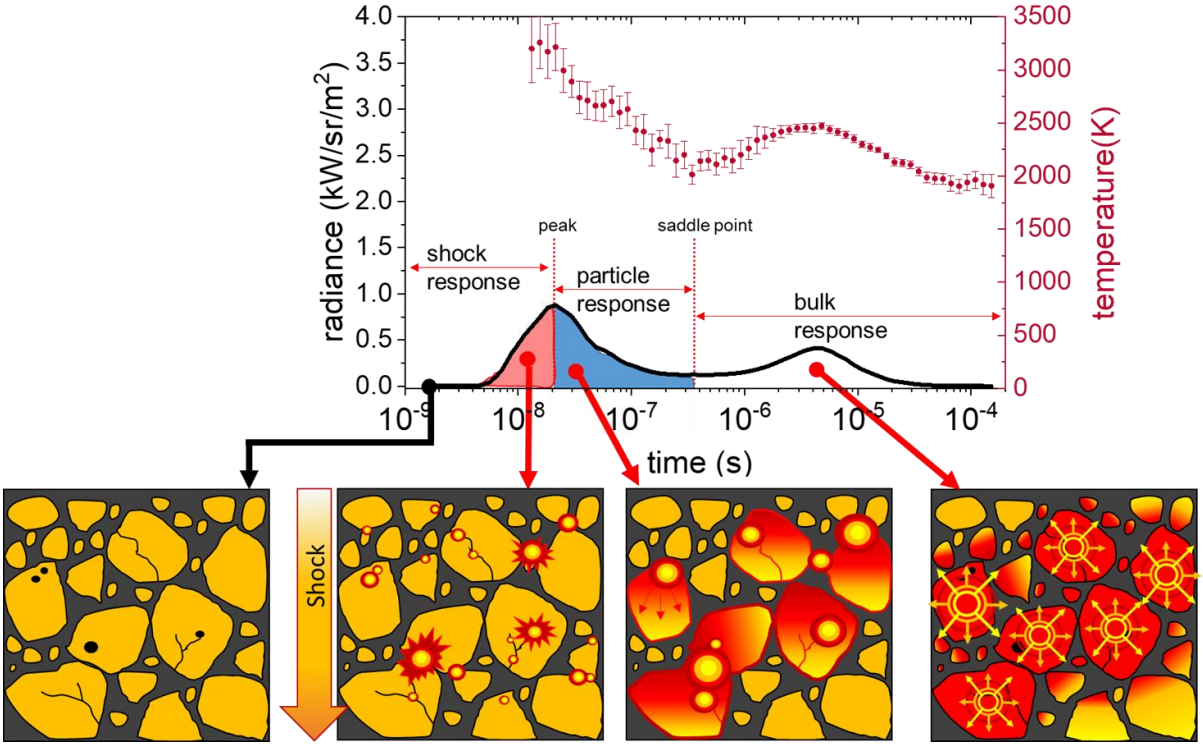

Figure 4.3 An example of a typical 'two peak' emission response of initiated TATB (top). At each time stage, the quantity of light released is indicative of how fast heat can spread at each successive phase of the initiation and growth process of hot spots, depicted by the images on the bottom.

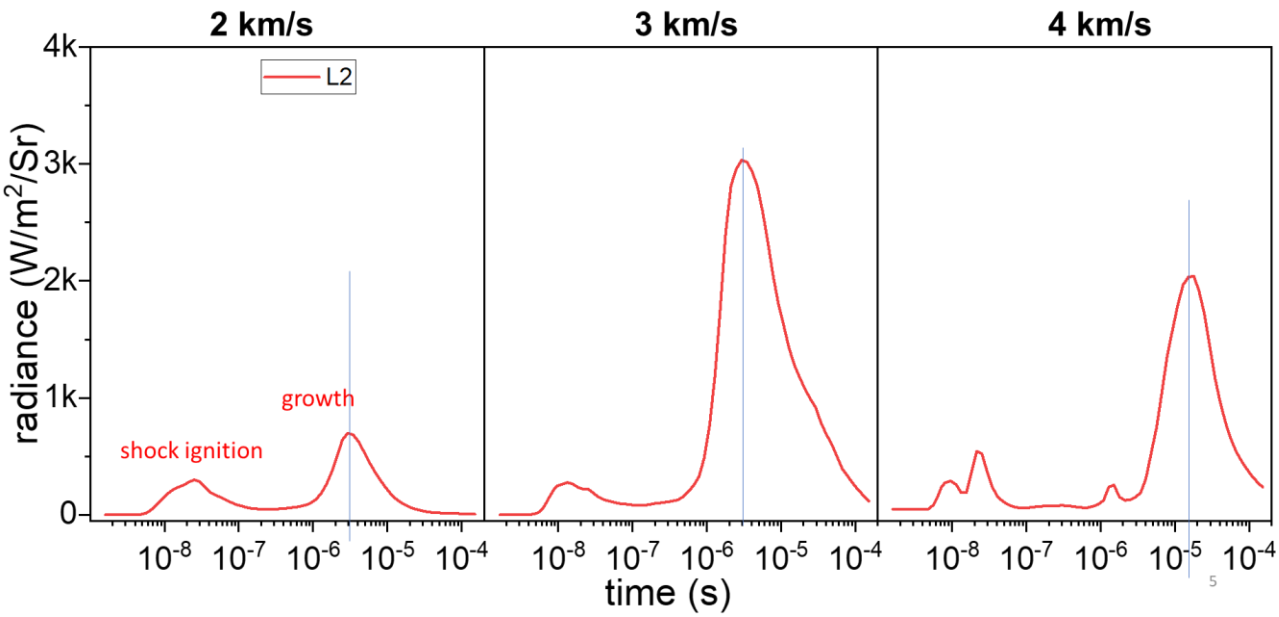

Figure 4.4 Examples of radiance histories at 3 selected velocities for TATB PBX made with lot 2 powder.

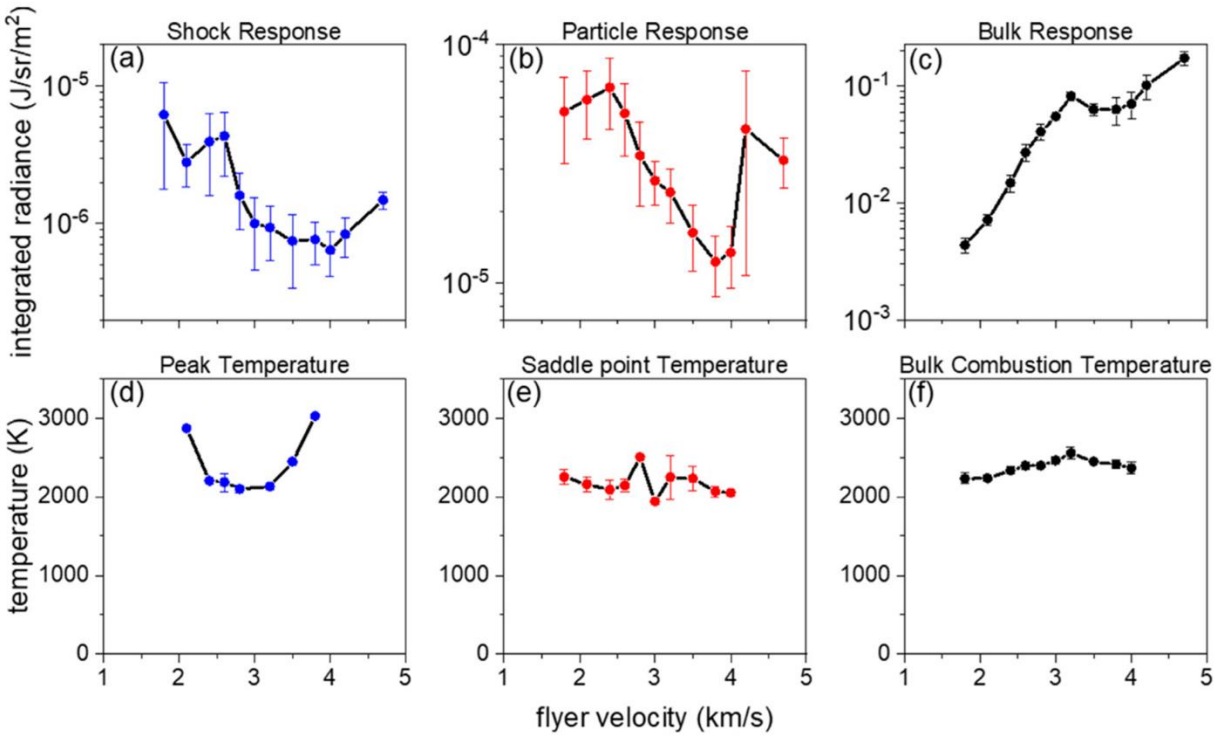

Figure 4.5 Box plots demonstrating the velocity dependence of a single TATB powder composition. Emission radiance integrals: (a) shock response, (b) particle scale response, (c) bulk response. Temperatures: (d) hot spot temperature measurement, (e) saddle point or end of particle response, (f) temperature at end of bulk combustion phase.

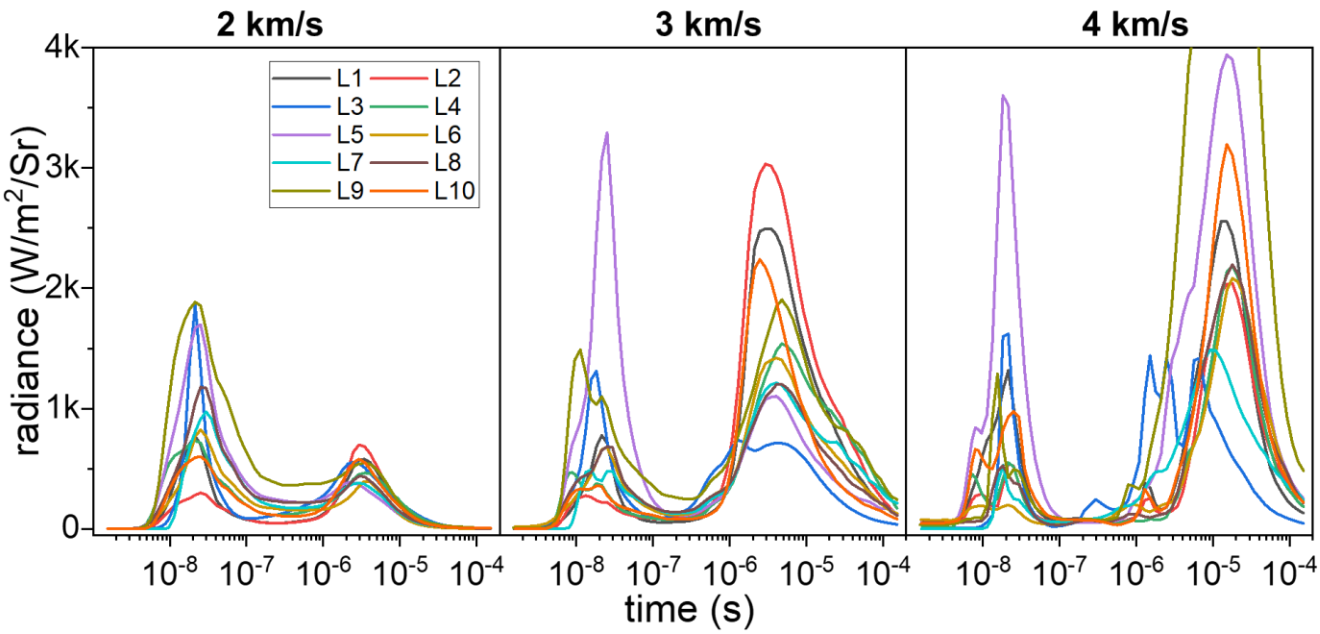

Figure 4.6 Comparison of 80 wt.% TATB mixed with 20 wt.% PDMS using different TATB powders (see Fig 4.1 for 'as received' particle size distributions of these powders.

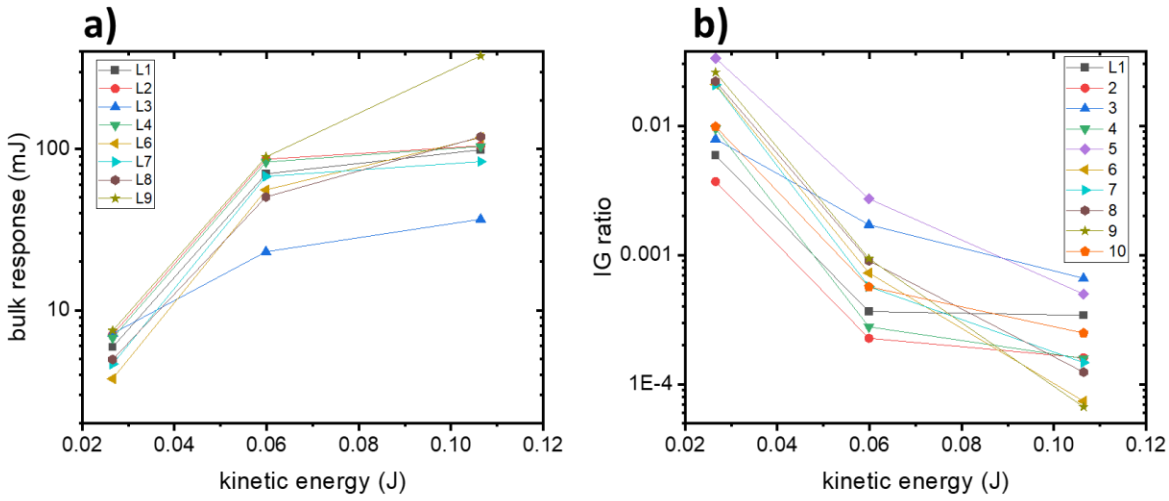

Figure 4.7 Comparison of bulk response integrals of all 10 TATB lots at various impact energies (a). A comparison of the ratio of shock ignition integral to bulk response integral (IG ratio)(b). This shows a monotonic increase in bulk response, as expected, but bulk response integral increases much faster than the shock ignition integral.

4.5 References

1. Dobratz, B. M. *Properties of Chemical Explosives and Explosive Simulants*; UCRL--51319, UCRL--51319(REV.1), 4285272; 1972; p UCRL--51319, UCRL--51319(REV.1), 4285272.

2. Boddu, V. M.; Viswanath, D. S.; Ghosh, T. K.; Damavarapu, R. 2,4,6-Triamino-1,3,5-Trinitrobenzene (TATB) and TATB-Based Formulations—A Review. *J. Hazard. Mater.* **2010**, *181* (1–3), 1–8.

3. Manner, V. W.; Yeager, J. D.; Patterson, B. M.; Walters, D. J.; Stull, J. A.; Cordes, N. L.; Luscher, D. J.; Henderson, K. C.; Schmalzer, A. M.; Tappan, B. C. In Situ Imaging during Compression of Plastic Bonded Explosives for Damage Modeling. *Materials* **2017**, *10* (6), 638.

4. Akhtar, M.; Dlott, D. D. Comparing the Shock Sensitivity of Insensitive Energetic Materials. *J. Appl. Phys.* **2022**, *131* (6), 065103.

5. Bassett, W. P.; Johnson, B. P.; Salvati, L.; Dlott, D. D. Hot-Spot Generation and Growth in Shocked Plastic-Bonded Explosives Studied by Optical Pyrometry. *J. Appl. Phys.* **2019**, *125* (21), 215904.

6. Bergman, T. L.; Lavine, A. S.; Incropera, F. P.; DeWitt, D. P. *Fundamentals of Heat and Mass Transfer*, 8th ed.; Wiley: Hoboken, NJ, 2011.

7. Bassett, W. P.; Dlott, D. D. Multichannel Emission Spectrometer for High Dynamic Range Optical Pyrometry of Shock-Driven Materials. *Rev. Sci. Instrum.* **2016**, *87* (10), 103107.

8. Branstetter, J. R. Some Practical Aspects of Surface Temperature Measurement by Optical and Ratio Pyrometers.

9. Bassett, W. P.; Johnson, B. P.; Salvati, L.; Nissen, E. J.; Bhowmick, M.; Dlott, D. D. Shock Initiation Microscopy with High Time and Space Resolution. *Propellants Explos. Pyrotech.* **2020**, *45* (2), 223–235.

10. Banishev, A. A.; Shaw, W. L.; Bassett, W. P.; Dlott, D. D. High-Speed Laser-Launched Flyer Impacts Studied with Ultrafast Photography and Velocimetry. *J. Dyn. Behav. Mater.* **2016**, *2* (2), 194–206.

11. Curtis, A. D.; Dlott, D. D. Dynamics of Shocks in Laser-Launched Flyer Plates Probed by Photon Doppler Velocimetry. *J. Phys. Conf. Ser.* **2014**, *500* (19), 192002.

12. Zhang, W.; Salvati, L.; Akhtar, M.; Dlott, D. D. Shock Initiation and Hot Spots in Plastic-Bonded 1,3,5-Triamino-2,4,6-Trinitrobenzene (TATB). *Appl. Phys. Lett.* **2020**, *116* (12), 124102.

13. Barua, A.; Zhou, M. Computational Analysis of Temperature Rises in Microstructures of HMX-Estane PBXs. *Comput. Mech.* **2013**, *52* (1), 151–159.

14. Tarver, C. M.; Chidester, S. K.; Nichols, A. L. Critical Conditions for Impact- and Shock-Induced Hot Spots in Solid Explosives. *J. Phys. Chem.* **1996**, *100* (14), 5794–5799.

15. Johnson, B. P.; Zhou, X.; Ihara, H.; Dlott, D. D. Observing Hot Spot Formation in Individual Explosive Crystals Under Shock Compression. *J. Phys. Chem. A* **2020**, *124* (23), 4646–4653.

16. Johnson, B. P.; Zhou, X.; Dlott, D. D. Shock Pressure Dependence of Hot Spots in a Model Plastic-Bonded Explosive. *J. Phys. Chem. A* **2022**, *126* (1), 145–154.

17. Roy, S.; Johnson, B. P.; Zhou, X.; Nguyen, Y. T.; Dlott, D. D.; Udaykumar, H. S. Hot Spot Ignition and Growth from Tandem Micro-Scale Simulations and Experiments on Plastic-Bonded Explosives. *J. Appl. Phys.* **2022**, *131* (20), 205901.

18. Desmond, K. W.; Weeks, E. R. Influence of Particle Size Distribution on Random Close Packing of Spheres. *Phys. Rev. E* **2014**, *90* (2), 022204.

19. Ye, X.; Li, Y.; Ai, Y.; Nie, Y. Novel Powder Packing Theory with Bimodal Particle Size Distribution-Application in Superalloy. *Adv. Powder Technol.* **2018**, *29* (9), 2280–2287.

20. Bassett, W. P.; Johnson, B. P.; Neelakantan, N. K.; Suslick, K. S.; Dlott, D. D. Shock Initiation of Explosives: High Temperature Hot Spots Explained. *Appl. Phys. Lett.* **2017**, *111* (6), 061902.

21. Patterson, B. M.; Kuettner, L.; Henderson, K.; Yeager, J. D.; Hill, L. The Wormholes Within: A Study of 1, 3, 5-Triamino-2, 4, 6-Trinitrobenzene Crystal Morphology by Micro and Nano-Scale X-Ray Computed Tomography and Its Effects Upon the Shock Sensitivity of Detonation. *Propellants Explos. Pyrotech.* **2022**, *47* (4).

CHAPTER 5: HOW GRAIN CLUSTERING INFLUENCES SHOCK INITIATION IN PLASTIC EXPLOSIVES

5.1 Introduction

A simple plastic-bonded explosive (PBX) consists of powdered energetic material (EM) and a polymer binder, and when a shock wave is introduced, it can undergo a violent mechanochemical reaction. The intensity of the shock response is complicated to predict because it depends on the kinetics of EM decomposition and the microstructure of the powder-binder mixture. Here we describe and interpret a series of experiments where we studied shocked PBX by varying the EM mass fraction from 0.1-0.85. Changing mass fraction while keeping grain morphology constant will isolate grain aggregation. Specifically answering the question of how hot spots evolve when long range interactions are limited by cluster sizes. The PBX consisted of HMX powder (cyclotetramethylene-tetranitramine), a powerful EM with a heat of explosion of about 12 kJ/cm^3, with poly-dimethylsiloxane (PDMS) binder. We shocked tiny cylindrical PBX charges (1 mm diameter x 90 μm) with 2-4 km/s thin flyer plate impacts that produced shocks of roughly 20 GPa pressure lasting about 4 ns. We measured the time-resolved spectral radiance with nanosecond time resolution in the visible region.

The spectral radiance, measured against a calibrated intensity standard to enable quantitative comparison of emission intensities, can be wavelength-integrated to get the radiance, and can be fit to a graybody model to get temperatures. We used short-duration shocks and fast optical detectors to time resolve two general types of phenomena: shock ignition and reaction growth.

It is critical for models of PBX shock initiation to move away from phenomenological systems such as Tarver and Lee's Initiation and Growth model, which relied entirely on

experimental data to predict the kinetics of initiation[1], into truly predictive models. The biggest impediment to the march away from parameterization is the complexity of the mesoscale inside of PBXs, since micron-scale defects such as cracks, interfaces, delamination, and voids can create many hot spots of varying sizes, temperatures, and thermal masses. Critical hot spot theory proposed by Tarver and Nichols sought to account for this by theorizing the size and temperature necessary for a hot spot to become 'critical', or self-propagate through the entire explosive[2], as well as models to account for multiple hot spots interacting[3].

Despite this, understanding how the microstructure, the arrangement and size distribution of grains, and defects and voids found in them, is essential to predicting the kinetics of hot spot growth after shock compression. Simulations done by Udaykumar have shown that mesoscale information, even down to the exact shape of voids is needed to inform continuum scale kinetics of shock to detonations[4,5,6]. There is very little experimental data that can display the effect of kinetics of hot spot growth to micron-scale specificity; mesoscale-informed simulations currently rely on hydrodynamic codes and continuum-scale experimental data. Consequently, there is disagreement about very fundamental kinetic details during shock to detonations. The decomposition mechanisms, for example, are often adapted from thermogravimetric studies, or found phenomenologically from continuum scale experiments such as Tarver's HMX decomposition model[2]. It has been shown that while some mechanisms predict certain explosives very well, none of the available mechanisms are truly general[7]. Reaction rates are partially limited by mesoscale conditions, considerations such as heat transfer, thermal boundaries, and grain clusters, which cannot be tracked with continuum-scale experimental data.

There have been gradual improvements in collecting mesoscale-informed data on hot spot initiation, though. The work by Bassett *et al.* to measure and quantify shock-induced hot spot

generation in a in several PBX species.[8,9] Johnson *et al.*[10,11] continued this by measuring where hot spot formation occurs on the scale of a single HMX-grain provide an important first step to improving initiation and growth models[12]. However, what factors limit their kinetics is still subject to predictions who can only hope to match data sets on collected on several-millimeter length scales. This is a problem because continuum scale data inherently smears over microstructure details due to spatial averaging.

Varying the EM concentration changes the entire structure of the PBX, and dramatically affects shock ignition and growth due to micron-scale changes. HMX is a dense molecular solid (ρ = 1.91 g/cm^3) with a high acoustic velocity (~3.5 km/s) and bulk modulus (~15 GPa)[13]. PDMS is a polymer with much lower density (ρ = 0.97 g/cm^3) acoustic velocity (1.1 km/s) and bulk modulus (1 GPa). The HMX used here consists of fine polycrystals with sizes ranging from 2-30 μm. At the microstructure level, the interaction between the shock in the PBX and the microstructure creates an ensemble of so-called "hot spots" having a distribution of sizes and temperatures. The larger, hotter hot spots ignite the HMX, which undergoes deflagration, is a rapid exothermic reaction in a substance with both fuel (e.g. carbon) and oxidizer (e.g. NO_2 groups). Deflagration growth is not rate limited by fuel/oxidizer mixing but rather by heat transfer. In the hot spot ensemble, the smaller, colder hot spots extinguish but the larger, hotter hot spots, termed "critical hot spots" that release heat faster than thermal dissipation, grow so that an initially localized deflagration will spread throughout the shocked volume.

Inside a PBX, the HMX is not uniformly dispersed throughout the binder since it aggregates. This aggregation can strongly affect coupling to the shock, hot spot formation and reaction growth. In this study, we sectioned the PBX charges and used high-resolution scanning

electron microscopy (SEM) of the surfaces of multiple cross-sections to determine the PBX structure, which we then relate to and use to explain shock ignition and growth.

5.2 Experimental

5.2.1 HMX Plastic Explosive Preparation

The particle size distribution is determined by taking the HMX crystals and suspending it in Ethylene glycol (Fisher). A Horiba mastersizer is used to determine the particle size distribution, shown in Figure 5.1a. This data was verified by measuring the loose powder on a scanning electron microscope (SEM) (JEOL 7000F). 7 nm of a gold palladium coating was applied to the powder after being affixed to double-sided copper tape and an accelerating voltage of 10 KeV was used. Figure 5.1b is an example micrograph of the HMX powder. There is no further extrusion of the PBX to preserve the particle size distribution measured from the powder. HMX-based PBX was prepared by mixing 150 mg quantities of HMX crystals with PDMS (Sylgard 182, Dow) to the appropriate mass fraction, using hexanes as a process solvent by diluting the PDMS to a concentration of 70-80 mg PDMS/1 mL of hexanes. The hexanes are left to vaporize while mixing HMX and PDMS, then manual kneading is performed to better homogenize the mixture. The final mixture is cast into 1-mm diameter, 90 micron thick Kapton cylinders, and cured at 60-70° C for 8-12 hours. The standard error of the measurements propagates to 2% relative error for the final mass loading number.

5.2.2 Determining Grain Arrangements and Structure

The microstructure in HMX-based PBXs is determined with a combination of thin film slides and cross-sectional images. PDMS is a very soft binder which is difficult to section. An epoxy binder was used as a stand-in for taking cross-sectional images (see Chapter 3).

The base solution of PDMS is prepared by mixing Sylgard 182 base compound to 10 wt% of the curing compound. HMX powder is added in a quantity equal to between 1 to 10 wt.% of the base compound of PDMS. Using a 1 mL pipette, a single drop (~100 μL) quantity of HMX is added to the surface of a microscope slide. A #1 coverslip is placed overtop and pressed evenly using a second piece of glass until fully extruded. The slide is placed in a 70˚ C oven for 8-16 hours to fully cure. The thickness of these samples has been measured by an optical profilometer (Keyence VK-X1000) and is verified to be in between 18-25 μm thick (see Appendix D). The slides are taken to a metallurgical microscope. Using a 10X (NA = 0.25) objective and a bright-field imaging with collinear lighting source, a cross polarized light image is taken at several locations throughout each slide. Spatial calibration is done using a USAF 1951 resolution test target.

The cross polarized light configuration results in a high signal to noise, making simple thresholding sufficient for image layering. The image is converted to a binary image where the particle phase is the foreground and the PDMS is the background using Fiji/ImageJ. The concentration is defined by the ratio of foreground pixels to background pixels, converted to a mass fraction using known densities of HMX and PDMS, respectively. To collect cross-sectional images, HMX powder is mixed with epoxy (Loctite Abelstik® 24) and cured at room temperature for 24 hours. The blocks are cross sectioned using a microtome (Leica Cryo) at room temperature. Pre-facing is done with a glass blade with the final facing performed by a 6mm diamond blade (Diatome Histo®). The finished surface is sputter coated with 12nm of Gold-Palladium to be electrically conductive for electron microscopy.

The SEM images are produced using a JEOL-7000F with a back-scattered electron detector. Images were collected at an accelerating voltage of 15 kV with the current setting at 10.

The higher beam current allowed for sufficient contrast between the HMX and PDMS binder, making image thresholding possible. Images were taken at 230x and 450x for all measured concentrations.

The images are first converted to a binary image through thresholding in Fiji[14]. The particles identified in the image were clustered using an agglomerative algorithm. This technique determines the size and location of HMX grain clusters by looking for groups of two or more particles whose borders are one-pixel apart due to there being a 1-pixel boundary defining the particle edges. The reported cluster size is the mean of the length and width of the clusters' minimum-area bounding rectangles. The ratio of HMX pixels to total pixel count, or the volume fraction, is converted to mass fraction using the known density of HMX and Sylgard® 182. A minimum of 3 images were processed for every targeted concentration. The code used to execute this can be found in Appendix C.

5.2.3 Quantifying Clustering Behavior

Density correlation of individual particles is performed to view the bulk clustering tendencies of each concentration. For each HMX (foreground) pixel, a search radius of r is drawn and the number of pixels in the region defined as:

$$\nu^{(2)}(r, r') = \sum_i \sum_{j \neq i} \delta(r_i - r)\delta(r_j - r') \quad (5.1)$$

Where $\nu^{(2)}$ is the frequency of pairs ij within r and r' apart from each other. This is then converted to a density correlation by summing over all space by the following relationship:

$$g^{(2)}(r, r') = \langle \nu^{(2)}(r, r') \rangle / \rho^2 \quad (5.2)$$

$$g(r) = \frac{1}{A\rho^2} \left\langle \sum_i \sum_{j \neq i} \delta(r_{ij} - r) \right\rangle \quad (5.3)$$

Since this analysis will be treating these images semi-discretely, it acts more as a density correlation than a pair correlation. This is calculated using an image matrix M_{ij} defined such that:

$$M_{ij} = \begin{cases} 0 \text{ if PDMS} \\ 1 \text{ if HMX} \end{cases} \quad (5.4)$$

By polling every pixel for HMX pixels within the range $r + dr$

$$g(r) = \frac{1}{(2\pi r dR)N\rho_{bulk}} \sum_i^N \sum_{j \neq i} \delta(r_i - r)\delta(M_i - 1) \quad (5.5)$$

Where A is the area of the $r + dr$ ring. This gives the local probability of HMX being in ring $r + dr$. This, in effect, counts the number of particles that are exactly distance r apart, normalized to the area and number density. A pictoral description of this analysis is shown in Figure 5.2. This is the volume density of HMX in distance r from a random point inside an HMX particle. Numbers above 1 imply higher than average density of HMX particle being found, while numbers below 1 imply lower than average density. In general, $\lim_{r \to \infty} g = 1$. From here, the radius at which $g(r)$ crosses below 1 is then defined as the effective cluster size where it becomes less probable to find as much HMX as the total density of the image. While this isn't an exact identity of a 'cluster', it does define the range at which HMX is more likely to be found at higher quantities than average. Because it acts as a descriptive statistic describing long range interactions of randomly generated hot spots, density correlation is used a metric of clustering.

At higher concentrations (practically above 60 wt.%), the noise of this process rises dramatically. Evidence from cross sectional data suggests this is due to the grains percollating past 40-50 wt.%. Qualitatively, the particles become very large and interconnected, so the equal weighting of all HMX pixels will inevitably show that $g \to 1$ quite rapidly and doesn't deviate above or below it relative to the noise floor. As a result, at the higher concentrations this metric begins to fail, and it is only practical for samples exhibiting distinct clustering (i.e. from 0-60 wt.% HMX in PDMS).

5.2.4 Density Correlation Calculation Procedure

Analysis is conducted using a python script which counts up the number of particles within distance r + dr of each pixel using the kdtree module. The image is first reduced from a 800 x 600 μm rectangular field to a circular field of 300 μm radius (half the smallest dimension). This is done for ease of edge correction (rectangular edge corrections are more computationally costly). The maximum search radius was 50 microns (or 100 um diameter), reducing the effect of edge correction approximations and being sufficient to show convergence. Accepted best practice for this type of analysis is to use a search field no greater than 50% of the total field, or a maximum of 75 μm. The step size was 2 pixels or ~ 0.5 microns in an image scale of 3.6 pixels/micron. Ideally dR should be as near zero as possible, however aliasing plagues low distances because of the square pixel grid. 2 was tested to be a minimum before noise was qualitatively unacceptable.

5.2.5 Shock Compression Measurement Procedure

Shock compression experiments are done with a tabletop laser-driven flyer plates, shown in Figure 5.3. A near-IR pulsed laser is focused onto a 25-micron thick aluminum foil, generating a 500 micron-diameter projectile, called the flyer plate[15]. The flyer plate is given approximately 375 microns of free space to accelerate to its terminal velocity, which can range from 1.5 km/s up to 4.5 km/s. The PBX target material is cast into 90 microns deep, 1-mm diameter polyimide cylinders. The velocity of the projectile is measured by a photon doppler velocimeter (PDV) which measures the doppler shift of a 1550 nm probe laser reflecting off the flyer surface[16]. The auto emission caused by shock initiation is measured by optical pyrometry for radiance and emission temperature. This pyrometer consists of a 32-channel array of photomultipliers connected to 1.25 GHz digitizers; this setup was designed by Basset *et al*.[17] Light in the range of

400-800 nm is measured for spectrum, spectral radiance, and temperatures. For every shock experiment, the data is digitized to create a spectrum every 2 ns over 200 microseconds total collection. The final data is binned into 30 bins per time decade to save on the computational and memory cost of processing this many fits. For all reported PBX concentrations, 30-50 shock experiments were performed to gather statistics and ensure repeatability. For further details, see Chapter 2. The time dependent traces of radiance at different time regimes for HMX PBX mixtures is shown in Figure 5.4.

5.2.6 Approximating Equal Pressure For Different HMX Concentrations

The shock wave pressure depends on the Hugoniot relations between the target and flyer material, as well as the flyer velocity. This data was interpolated from available data on PDMS and HMX-based PBXs and pure HMX to approximately match 20 GPa for all HMX compositions.[18,19] Changing the concentration of HMX inside of PDMS changes how shock waves interact with the bulk medium. This presents a challenge for controlling for only clustering behavior of HMX crystals. When HMX concentration in PDMS changes there is a simultaneous change in bulk density, bulk energy density, bulk acoustic impedance, as well as several other bulk mechanical properties. An ideal scenario to carry out a controlled experiment is to fix the shock pressure; because energy density is a linear function of concentration, it is easier to decouple this from structural changes. The challenge is that shock pressure is typically predicted by phenomenological equation of state referred to as the Hugoniot[20]. The ability to measure pressure is therefore only explicitly available to systems that already measure shock particle velocity and shock velocity over a wide range of pressures. Such data is available for very limited HMX PBX compositions, such as PDMS[19], pressed HMX, and higher concentrations of HMX[18], but not for intermediate concentrations such as 10-90 wt%.

Given the lack of data, this study sought to make the best possible estimate to match 20 GPa for all compositions given available data. In many materials, the shock velocity is related to the particle velocity by the following relationship:

$$U_s = a + bu_p \quad (5.6)$$

Where U_s is shock velocity, u_p is the particle velocity, A and b are material-specific parameters. The pressure is related to this equation by the following equation set:

$$P = \left(Au_p + Bu_p^2\right) \quad (5.7)$$

Since parameters A and B are only known for 100% HMX, 90 wt% HMX and 0 wt% HMX in PDMS, they must be interpolated for the remaining concentrations. A linear fit of these two parameters as a function of concentration were made, which resulted in the interpolated parameter set $\{A_c, B_c\}$ st $c \in [10,90]$, where c is the concentration of HMX in PDMS in mass fraction. From here, pressure estimates can be approximated by finding the intersect of the forward-facing pressure curve of the PBX with the backward facing curve of the aluminum foil at a given flyer velocity. A plot of different estimated Hugoniot curves for HMX loading conditions is shown in Fig 5.5.

Using these Hugoniots allows an estimate of the necessary flyer velocity for each concentration to reach a given pressure, plotted in Figure 5.6. For all concentrations, shock compression data was collected in the range of 2-4 km/s with at least 4 given pressures. The radiance integral and temperature results are interpolated from the best-fit curves provided by measured radiance temperatures across this velocity range. The velocity-radiance data generally fits best to power-law relationships, reflecting a large change in radiance output after a threshold pressure. This is consistent with observations of HMX single crystal and polycrystalline grains, which had ignition thresholds of around 30 GPa[11]. While 20 GPa is near an important elbow for

HMX, when using this method to approximate equal pressure the resultant trends are relatively insensitive to 10% changes in Hugoniot parameters.

5.3 Results

5.3.1 PBX Structures

The raw output of the density correlation function is shown in the first plot. The plot itself heavily biases low concentration samples because a cluster weighs more heavily against an otherwise small average density. For ease of reading, these results can be plotted under equal weight without information loss through the following transformation $g \rightarrow C$:

$$C(r) = \rho_0 g(r) - \rho_0 \qquad (5.8)$$

This is effectively a correction factor on bulk density ρ_0 to account for clustering normalized by density. The plot of $C(r)$ for different concentrations can be found in Figure. 5.6. This behaves as a function starting at zero, peaking at near mode particle radius (~ r=0.5+dR) then declining after.
Notably, the rate of decline slightly changes as a function of concentration. As concentration goes up, rate goes down, signifying more particles. We will be evaluating the zero crossing point, where HMX clusters are most probable to end. Figure 5.7 shows this point as a function of image concentration over a range from 5 wt.% to 57 wt.%. It shows a linear increase from 0 to ~35 wt.% followed by a flattening or very weak increase in concentration after 40 wt%, maximum cluster size ranging from 28 to 33 μm. As stated previously, the output becomes too noisy after 60 wt% due to interconnection of particles.

From this data, it can be hypothesized that as more HMX is added from 0 wt.%, it begins to form clusters that increase in size. At the limit of 30-40 wt.%, excess HMX appears to be no longer increasing in size, transitioning to a new percolation phase where more clusters of ~30 μm are forming and moving closer to one another. It can be speculated from here that around 60-65

wt% particle clusters begin to interconnect, and large, contiguous structures of HMX form rather than strictly clusters. Beyond 75 wt.%, theoretical calculations as well as imaging evidence from SEM conclude that a packing limit is reached for this particle size distribution of HMX crystals.

5.3.2 Radiance Integrals

To quantify the reaction progress, a method of integrating the energy release from auto-emission was used. This technique is like that employed for analyzing TATB in the previous chapter. Radiance is a measure of light power per solid angle and unit area. Since this is a quantity of energy release dependent on the temperature, an intensive property, coupled to volume, an extensive property, it can be approximated as a stand-in for free energy release. The time points used as integral boundaries are represented by Figure. 5.9. Given the rather high shot variability, radiance is integrated separately for each individual shock experiment and the results plotted are the median with error bounds represented by the median absolute deviation.

For the shock response, the physical interpretation is how much energy is created as a direct result of mechanical energy from the shock wave being converted to thermal mass to initiate the reaction. The integral bounds are from time zero to the local maxima in the 10-20 ns region, which straddles the expected shock transit time for these samples. These results are shown in Figure. 5.10. The particle response is the integral from the peak of the shock response to the 'saddle point' where the radiance derivative is zero. This represents the heat transfer occurring from the hot spots to the surrounding HMX density. This appears to be a monotonically increasing function of HMX concentration, shown in Figure. 5.11. Finally, the 'growth' integral represents the coalescence of hot spots and slower burn dynamics. The size of this integral is representative of the success of the HMX fully reacting within the time frame of the experiment.

This is integrated from the saddle point to the end of experiment, or 200 μs. Figure 5.12 plots this value as a function of concentration.

5.4 Discussion

5.4.1 Lower Concentration Limits (0-60 wt.%)

The cluster size estimates can be plotted against the concentration-dependent growth response of radiance data to yield Figure. 5.13. This plot provides one possible explanation for the nonlinear behavior in HMX concentration dependence: Before cluster size reaches ~23 μm, the growth behavior is limited by energetic material quantity, and after that it is rate limited by more complicated kinetics.

To understand these effects better, earlier stages of the emission data can be evaluated. The particle response integral in Figure. 5.11, indicative of the efficiency by which hot spots were able to conduct heat across a particle shows weak to no change until ~30 wt% where it begins to rise exponentially. From 0-30 wt.% this effect can be explained by the fact that shock response doesn't begin rising substantially until >30 wt.%, indicative of the limited quantity of sites to produce hot spots available. However, as concentration goes up, the temperature of these sites begins to drop substantially which can be seen in Figure 5.14. The 0 wt.% data reflects data from PDMS, indicating isolated, void induced hot spots. The simultaneous rise in HMX particle response and drop in temperature implies a limited quantity of 'critical' hot spots are being spread further and further as cluster size rises to create a drop in temperature from heat conduction. For this time frame, we consider heat transfer across PDMS to be unlikely due to the large difference in heat conductivity. The conclusion from this is that smaller clusters will have higher temperatures since PDMS acts as a poor heat sink, trapping heat in a particle. As cluster size increases, while more emission is seen, the temperature is lower, represented by Figure.

5.14. This means that emissivity is increasing with concentration, corresponding to volume of reacted material[9]

$$\phi = V^{*}\varepsilon \quad (5.9)$$

If assuming constant graybody emissivity of HMX, a rise in emissivity constants signifies that a higher relative volume of HMX is at a given emission temperature. The effect of this is that longer timescale deflagration chemistry must now contend with lower starting temperatures as concentration rises.

Ordinarily this wouldn't be a concern, as even 2000 K is sufficient to burn the HMX (and in practice it does). However, the design of experiment heavily limits the rate it can fully burn in. We hypothesize that for the thin samples supported by foil impactors, the 1-200 μs time regime is still heavily limited by reaction kinetics. The emission history is most heavily biased towards energy released in the 1-10 μs times due to the light being produced by the sample peaking at 2 μs and dropping rapidly, reaching near the noise floor in the 20-30 μs region. Further, when performing integration over a log time scale to remove the potential bias of the long-time duration tail, the results are imperturbable to the choice of integration end point. This provides evidence that the differences in growth response integrals are most heavily biased by the radiance peak from 1-10 μs after shock compression, a clear and rapid time limit that can be tipped by different starting kinetics.

5.4.2 Higher Concentration Limits (>75 wt%)

The narrative begins to shift as HMX grains enter a new percolation phase. As referenced earlier, the definition of a cluster begins to blur once structures begin to interconnect. Beyond 60 wt% heavily interconnected systems begin to be observed. At this point, packing dynamics need to be included into discussion to explain the microstructure. 60 wt.% corresponds to ~45 vol%

HMX in PDMS. For perfectly monodisperse spherical particles, the theoretical maximum packing limit is 64 vol%. HMX polycrystalline grains are not perfectly monodisperse, nor are they spherical. The particles are unimodally polydisperse with more complicated geometries. Previous studies on polydisperse systems provide an estimate of spherical particle packing limits.[21]

$$\phi_{RCP} = \phi^{*}_{RCP} + c_1 S\delta + c_2 S\delta^2 \qquad (5.10)$$

Where ϕ_{RCP} represents the maximum packing fraction of the polydisperse spheres, $\phi^{*}_{RCP} = 0.634$ is the theoretical packing fraction of monodisperse hard spheres,S is the skewness factor of the lognormal size distribution found in Figure. 5.1a. δ is the polydispersivity of particles, and $c_1 = 0.0658, c_2 = 0.0857$ represent parameters used to fit data of polydispersity of $0.10 < \delta < 0.40$.[21]

If HMX particles are assumed to be perfectly spherical, the experimental particle size distribution yields a value of $\phi_{RCP} = 0.73$ or about 85 wt%. In practice, the real value should be notably lower than this due to the highly irregular shapes of particles often better representing hard disks than spheres, yielding a lower than ideal particle size distribution. This outcome can be verified by cross-sectional measurements from SEM, and example is given in Figure. 5.15 showing near maximum packing of a frame at $\phi = 0.65$ or 80 wt.%. Void spaces seen in the images are packing inefficiencies indicative that packing is nearly ideal. For polydisperse matrices of hard disks, this behavior is readily predicted by theoretical work on the subject by Lu and Torquato.[22]

Large rises in shock, particle, and particularly growth responses at ~75 wt.% coincide neatly with packing limits. At this point, how the microstructure couples to shock response becomes quite complicated due to several factors convoluting. A dramatic rise in void sites,

delaminations, stress on crystals due to packing inefficiency and the grains being totally interconnected are all very likely to contribute to the dramatically higher sensitivity observed. Further insights on the matter are given in Chapter when discussing dense TATB-based PBXs.

5.5 Conclusions

The plateau between 30 and 60 wt.% HMX samples can be explained by cluster size effect. As cluster size increases, hot spots spread further into the sample, causing a large rise in radiance and a fast drop in temperature resulting in a roughly linear increase of emissivity (i.e. emission volume) with respect to concentration. This is to be expected of linearly increasing the quantity of HMX if the quantity of critical hot spots changes very little. It has been demonstrated in previous papers that many sources of hot spots, namely those produced from delaminations and voids, are low thermal mass and generally don't tilt the scales significantly[6,10], but we would expect the quantity of them to increase with concentration. Although energy production is certainly increasing as a function of concentration, clearly energy dissipation must be covariant to produce a net-zero effect on the energy released by the system. What's being observed here then is a system that is acutely sensitive to the decomposition kinetics. As a result, experiments of this nature can act as a benchmark for validating multi-scale simulations, where the exact HMX decomposition models tend to vary wildly simply to match available datasets.

5.6 Figures

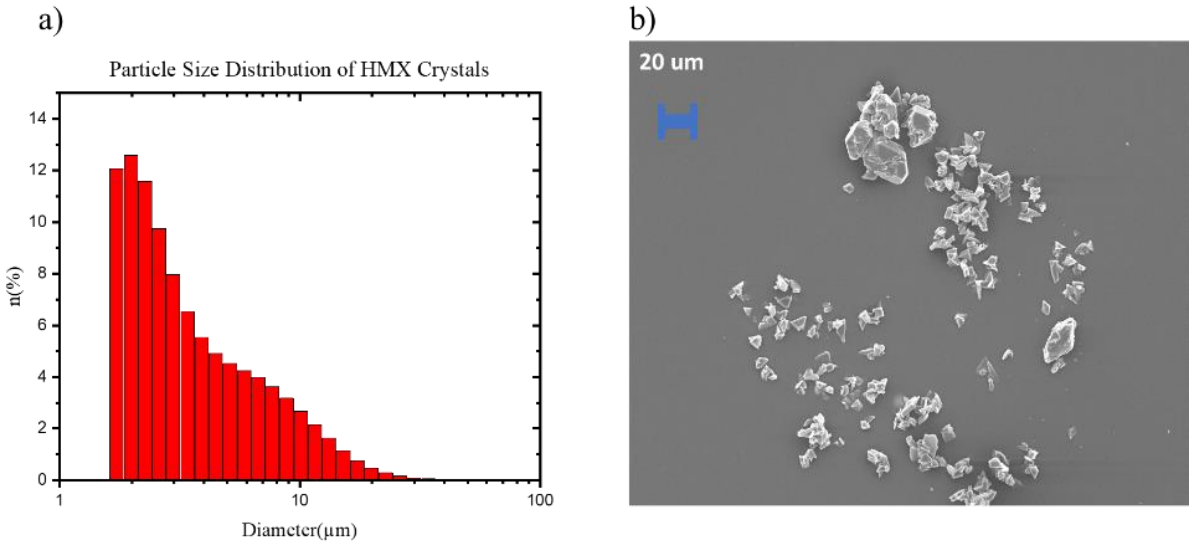

Figure 5.1 Number size distribution of HMX powder using light scattering (a), SEM micrograph of HMX powder used in PBX samples (b)

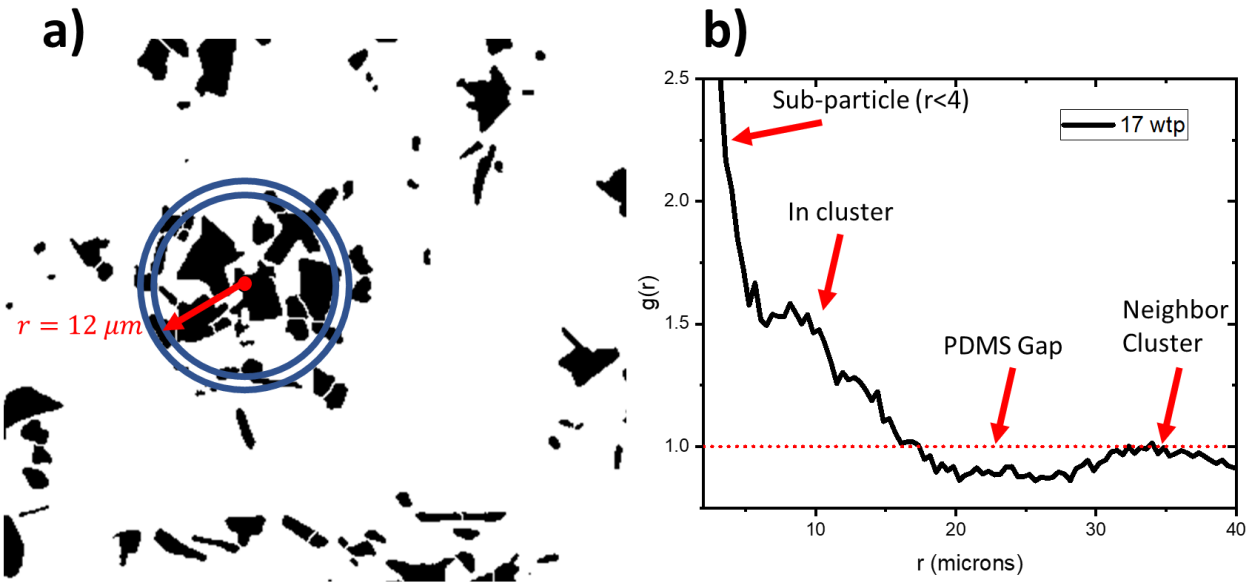

Figure 5.2 Visual representation of the density correlation calculations in PBX cross-sections. Larger numbers represent high probability of finding HMX mass from a random intra-crystalline point relative to the bulk average, numbers below 1 represent lower than average probability of finding HMX density. Thus for clustered sample it is a stand-in estimate for the quantity of HMX available for a hot spot to react with without *a priori* knowledge of where it is formed.

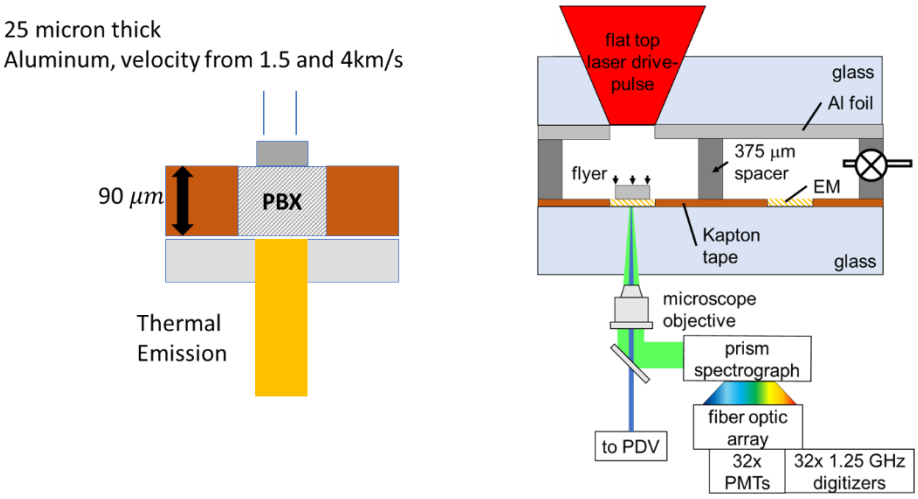

Figure 5.3 Schematic of the flyer plate impact geometry, and of an array of flyer plates and PBX charges where thermal emission is collected with a 10X microscope objective and ported to a 32-channel optical pyrometer. PDV = photon Doppler velocimeter

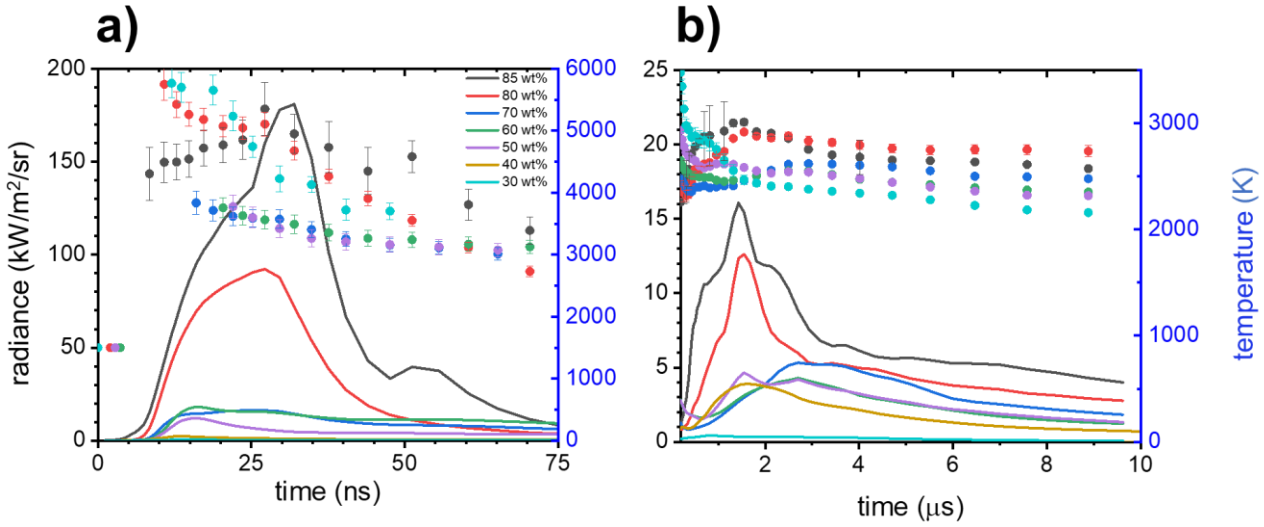

Figure 5.4 Averaged time-dependent radiance of the shock response (a) and the deflagration burning stage of HMX initiation (b) for several different HMX concentrations in PDMS.

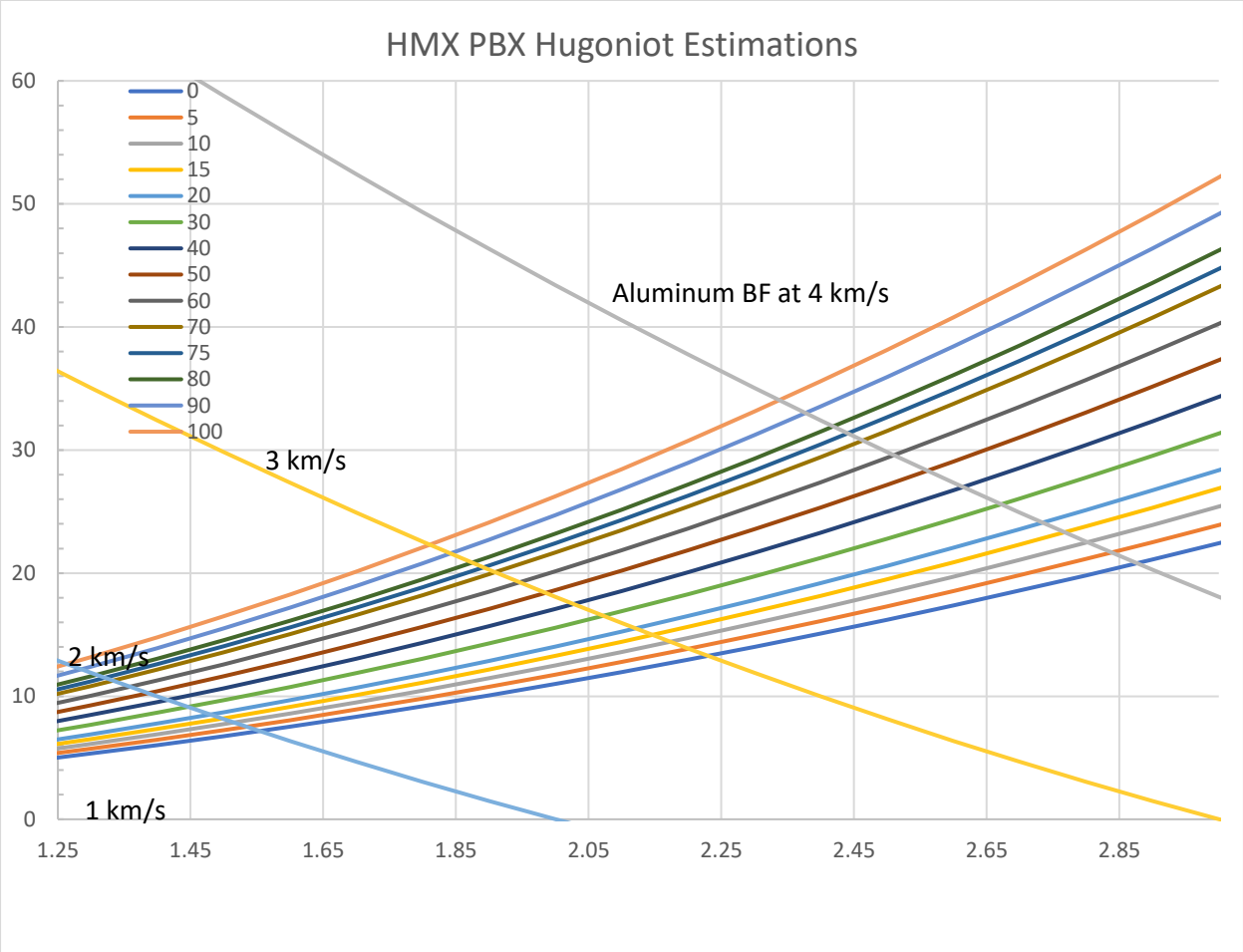

Figure 5.5 Graph of the P-u_p curves estimated for several HMX-PDMS ratios.

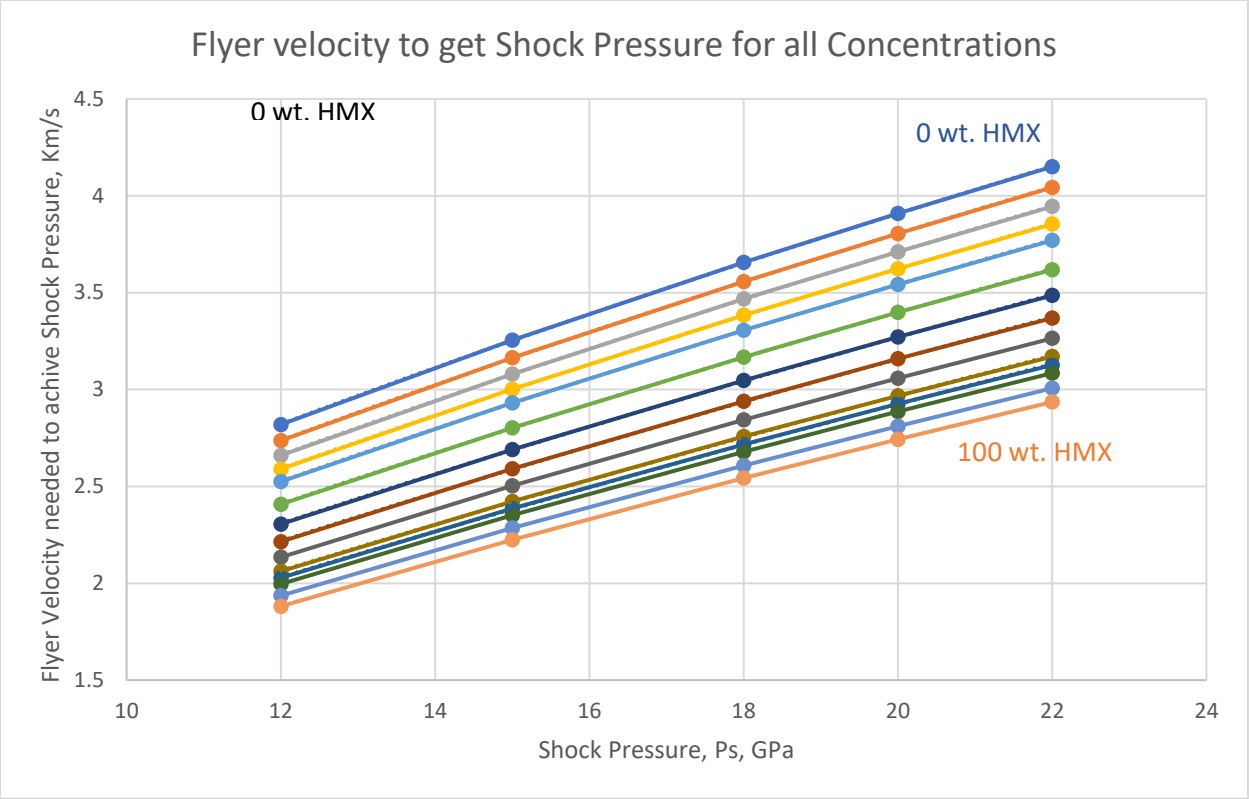

Figure 5.6 Curves of estimated shock pressure versus flyer velocity for various HMX-compositions.

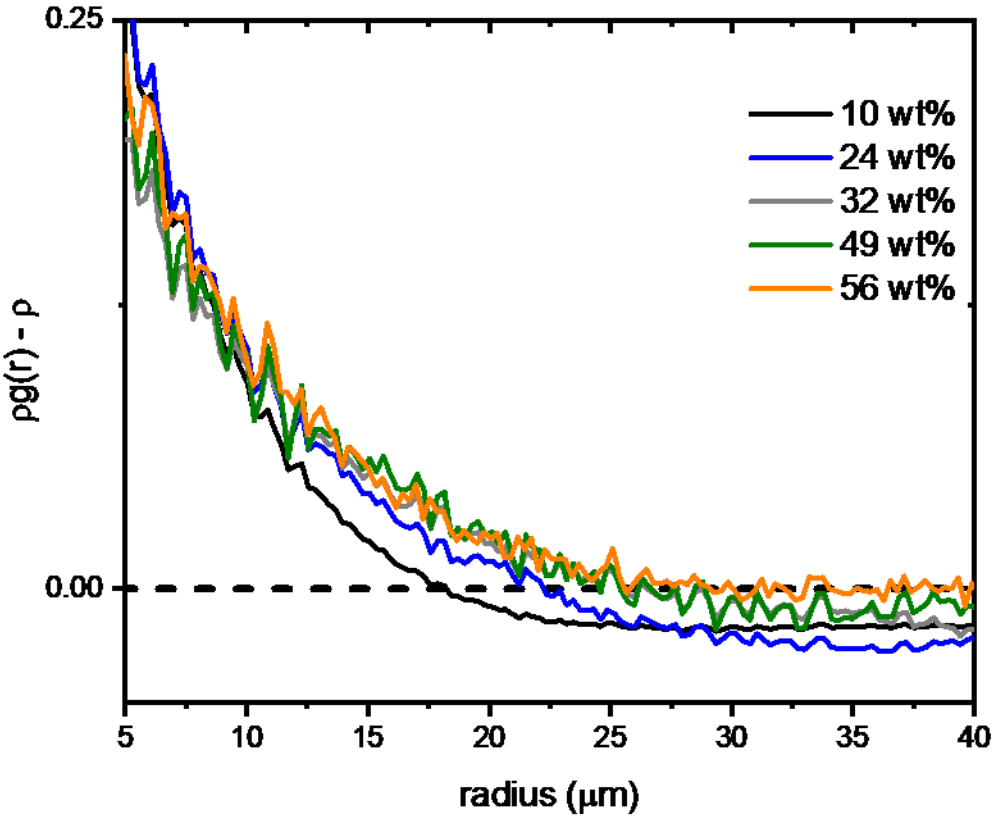

Figure 5.7 Plot of 'relative HMX density', measured by the difference between absolute density and bulk density (Eq 5.8). The point of crossing zero is a stand-in for cluster size, and a mild shoulder between r=10 to r~25 represents a higher density of HMX at higher concentrations.

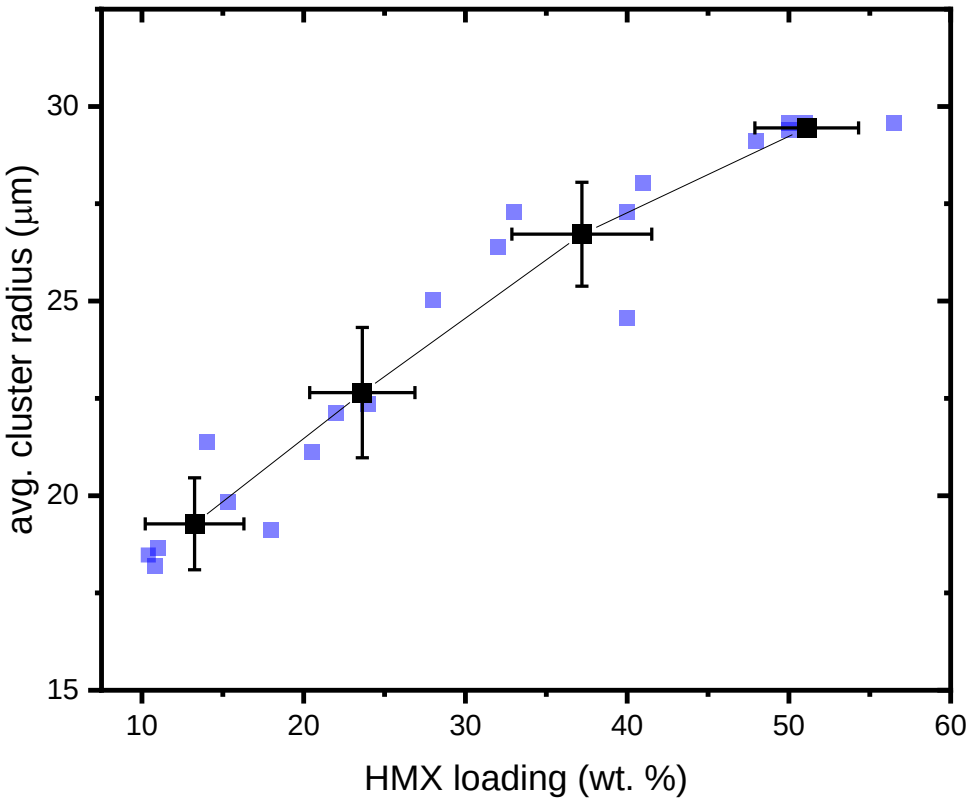

Figure 5.8 Cluster radius, derived from density correlation calculations, versus HMX concentration. Calculated from thin-film slides of HMX in PDMS. This shows a monotonic increase in cluster size but the slope slows dramatically as a function of concentration. This is likely from a new percolation phase being reached near 50 wt%, where clusters begin connecting by branches.

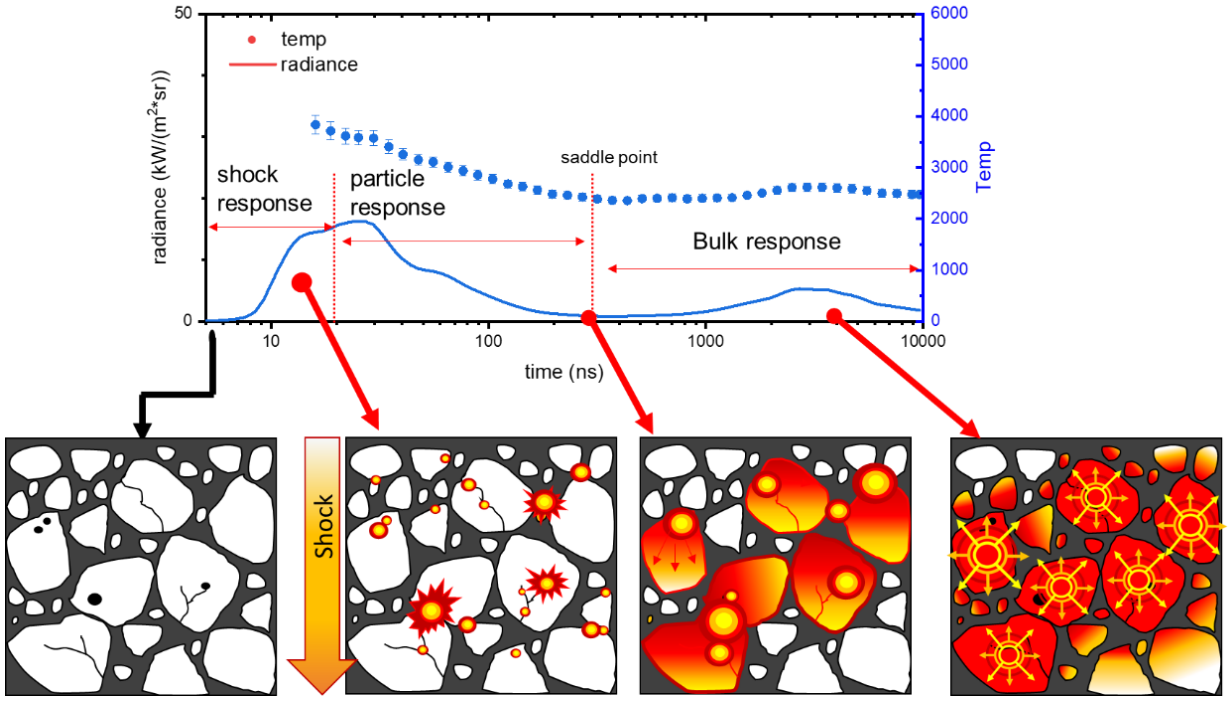

Figure 5.9 Schematic of the radiance integration process. Hot spots and mechanical coupling to thermal mass is represented by time-zero to nanosecond peak integration. Nanosecond peak to $\frac{dR}{dt} = 0$ 'saddle point' represents the particle-scale response, and longer time burning is represented by the 'saddle point' to end of measurement (200 μs) integral.

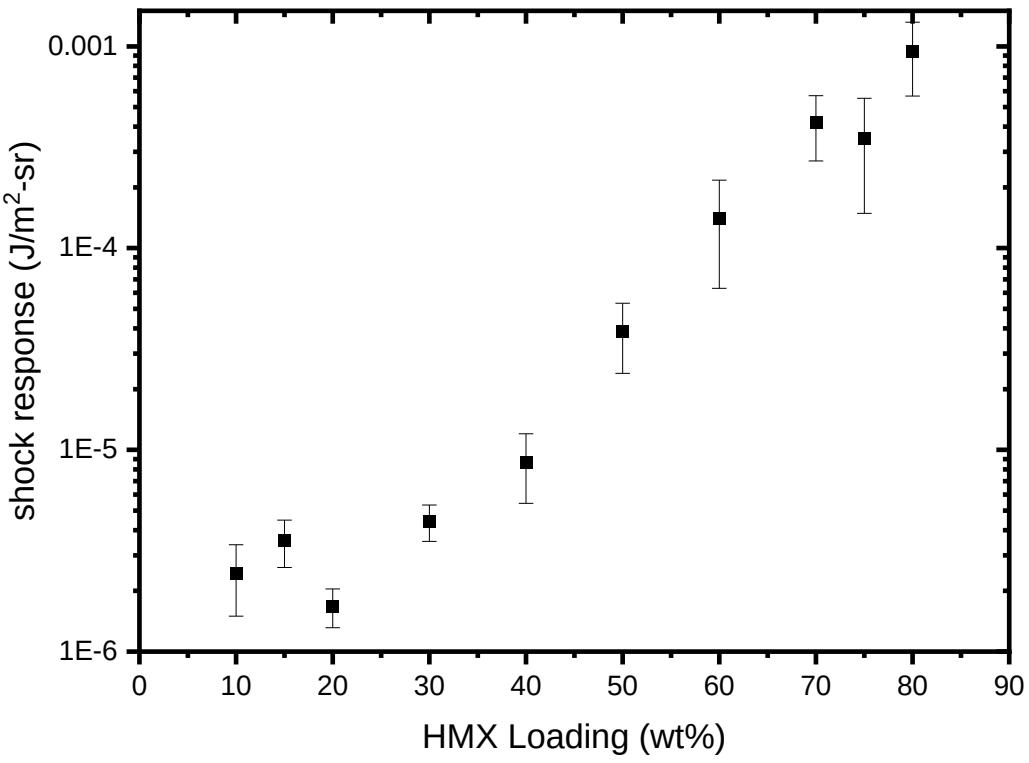

Figure 5.10 Median shock-response integral of HMX PBX mixtures from 20 GPa shock loading as a function of concentration.

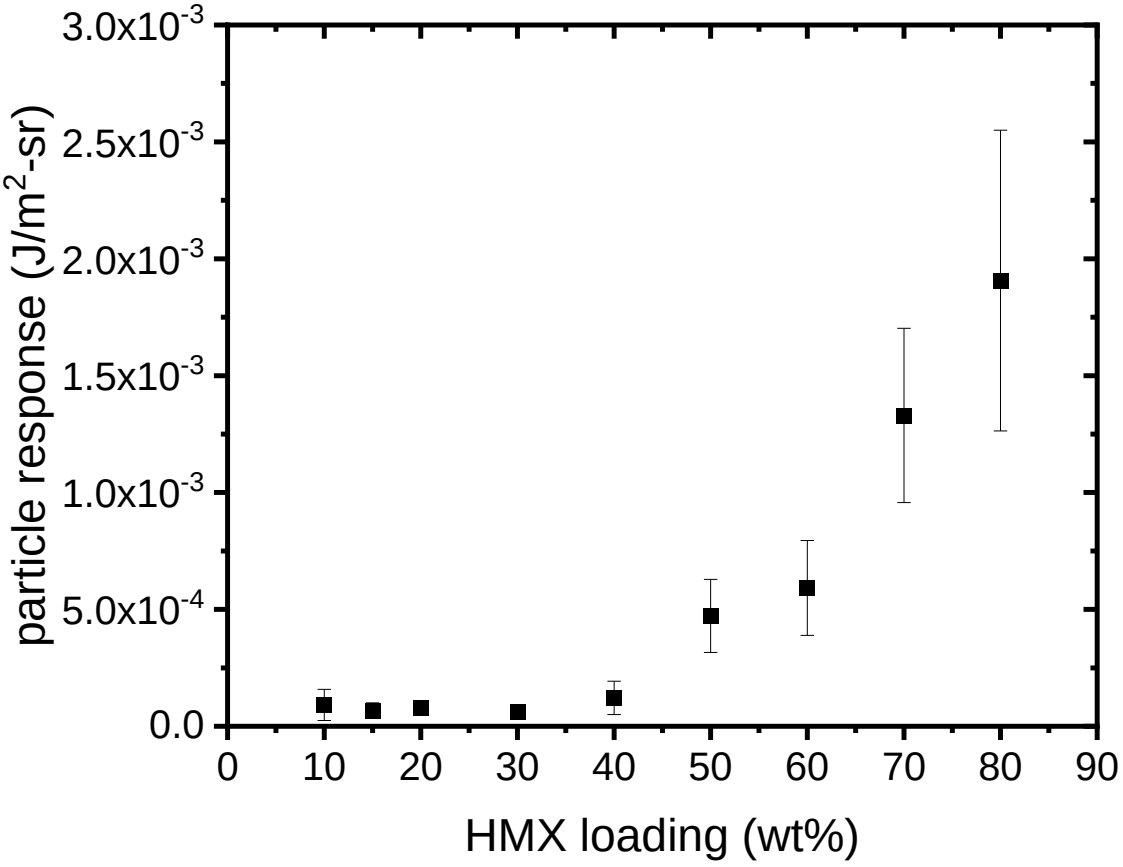

Figure 5.11 Median particle-response integral of HMX PBX mixtures from 20 GPa shock loading as a function of concentration.

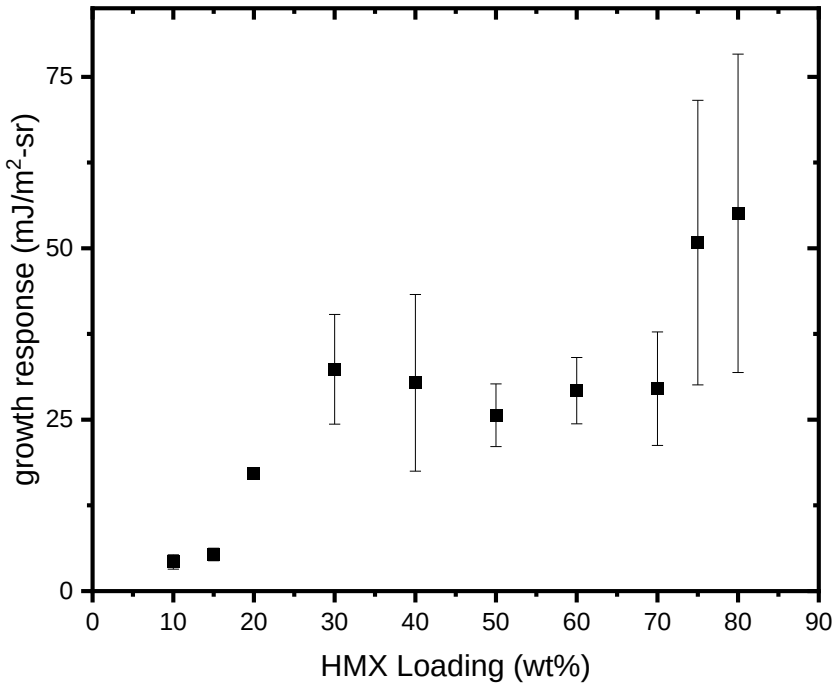

Figure 5.12 Plot of growth response integral as a function of HMX concentration in PBX at 20 GPa shock loading. This shows a jump in energy release from 15-30 until dipping or hitting a plateau at 40-70 wt.%. After this, the response integral jumps dramatically, likely due to a highly interconnected sample at the maximum packing fraction, creating increasingly large numbers of defects for hot spots to grow.

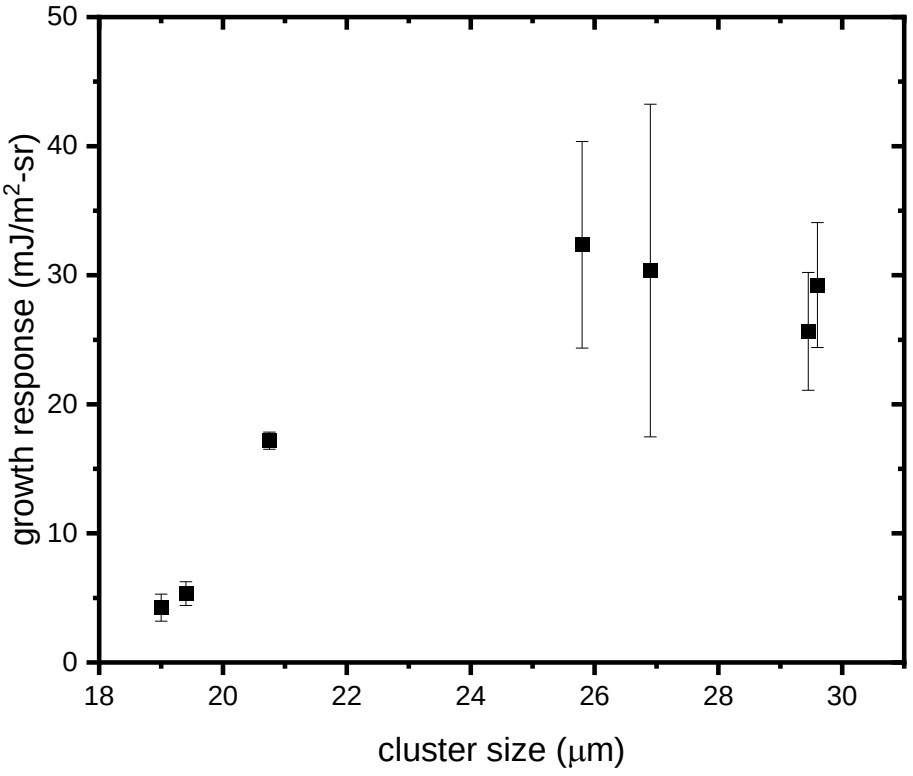

Figure 5.13 Growth response integral plotted as a function of derived cluster radius. This can only be measured out to ~30 μm, representing the limiting size for this analysis, or about 60 wt%. This provides a possible explanation that the growth integral is not cluster-size limited, but rather limited by heat dissipation *via* conduction.

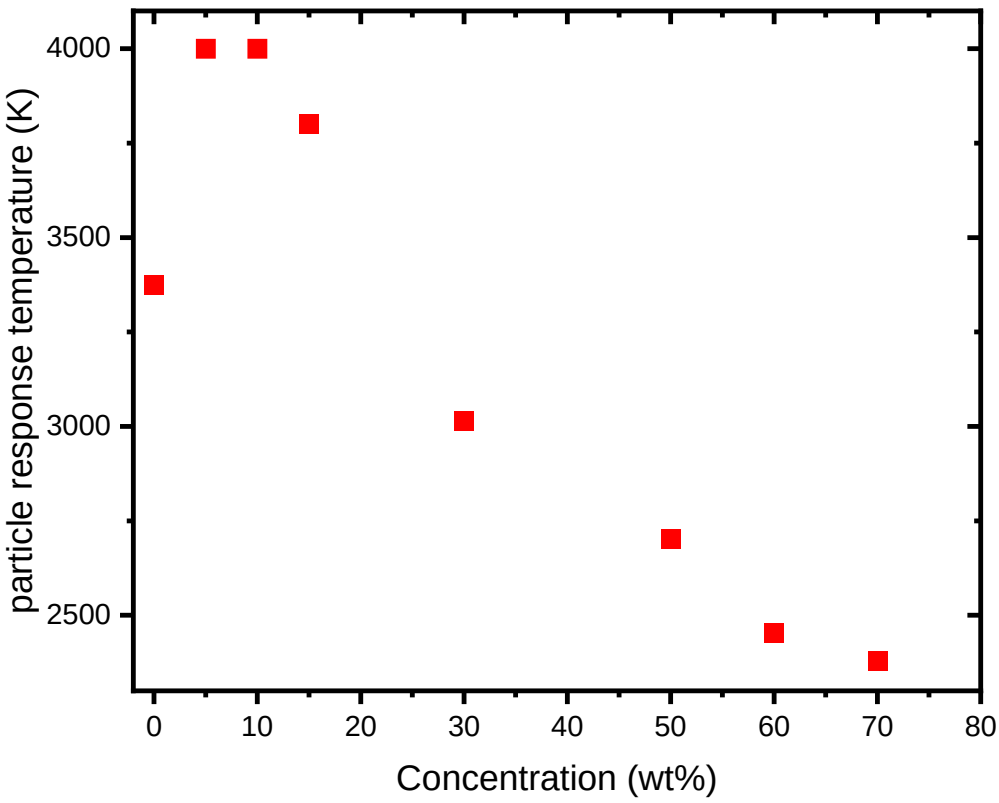

Figure 5.14 Plot of the average temperature measured at the saddle point, called ‘particle response temperature’ versus concentration. This quantity is initially quite high but drops rapidly as concentration increases, likely due to conduction.

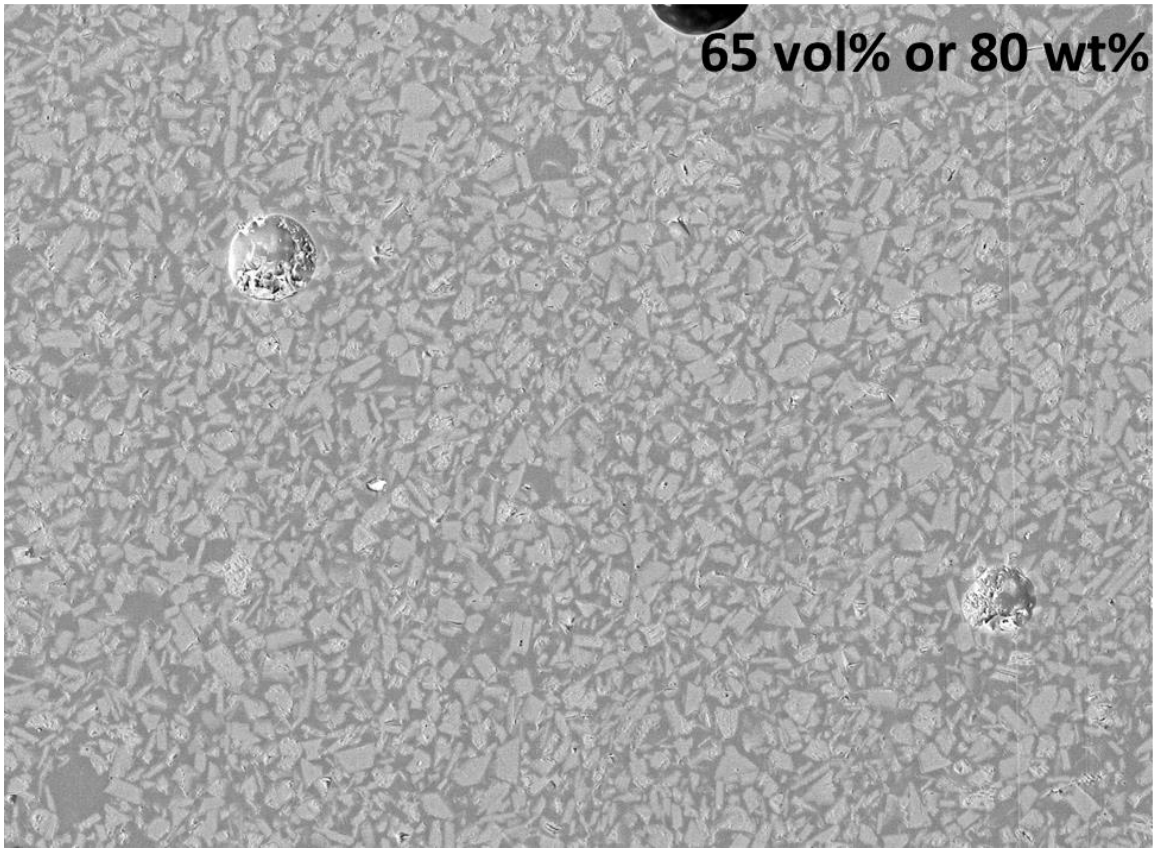

Figure 5.15 SEM micrograph of 80 wt% HMX in epoxy, showing the formation of packing inefficiencies. The nature of these inefficiencies, i.e large, isolated void formations, behaves consistently with treatment as hard disks.

5.7 References

1. Lee, E. L.; Tarver, C. M. Phenomenological Model of Shock Initiation in Heterogeneous Explosives. *Phys. Fluids* **1980**, *23* (12), 2362.

2. Tarver, C. M.; Chidester, S. K.; Nichols, A. L. Critical Conditions for Impact- and Shock-Induced Hot Spots in Solid Explosives. *J. Phys. Chem.* **1996**, *100* (14), 5794–5799.

3. Menikoff, R.; Shaw, M. S. Reactive Burn Models and Ignition & Growth Concept. *EPJ Web Conf.* **2010**, *10*, 00003.

4. Nguyen, Y.; Seshadri, P.; Sen, O.; Hardin, D. B.; Molek, C. D.; Udaykumar, H. S. Multi-Scale Modeling of Shock Initiation of a Pressed Energetic Material I: The Effect of Void Shapes on Energy Localization. *J. Appl. Phys.* **2022**, *131* (5), 055906.

5. Nguyen, Y. T.; Seshadri, P. K.; Sen, O.; Hardin, D. B.; Molek, C. D.; Udaykumar, H. S. Multi-Scale Modeling of Shock Initiation of a Pressed Energetic Material. II. Effect of Void–Void Interactions on Energy Localization. *J. Appl. Phys.* **2022**, *131* (21), 215903.

6. Das, P.; Udaykumar, H. S. Mechanisms of Shock-Induced Initiation at Micro-Scale Defects in Energetic Crystal-Binder Systems. *Shock Waves* **2022**, *32* (7), 593–616.

7. Rai, N. K.; Koundinyan, S. P.; Sen, O.; Schweigert, I. V.; Henson, B. F.; Udaykumar, H. S. Evaluation of Reaction Kinetics Models for Meso-Scale Simulations of Hotspot Initiation and Growth in HMX. *Combust. Flame* **2020**, *219*, 225–241.

8. Bassett, W. P.; Johnson, B. P.; Neelakantan, N. K.; Suslick, K. S.; Dlott, D. D. Shock Initiation of Explosives: High Temperature Hot Spots Explained. *Appl. Phys. Lett.* **2017**, *111* (6), 061902.

9. Bassett, W. P.; Johnson, B. P.; Salvati, L.; Dlott, D. D. Hot-Spot Generation and Growth in Shocked Plastic-Bonded Explosives Studied by Optical Pyrometry. *J. Appl. Phys.* **2019**, *125* (21), 215904.

10. Johnson, B. P.; Zhou, X.; Ihara, H.; Dlott, D. D. Observing Hot Spot Formation in Individual Explosive Crystals Under Shock Compression. *J. Phys. Chem. A* **2020**, *124* (23), 4646–4653.

11. Johnson, B. P.; Zhou, X.; Dlott, D. D. Shock Pressure Dependence of Hot Spots in a Model Plastic-Bonded Explosive. *J. Phys. Chem. A* **2022**, *126* (1), 145–154.

12. Roy, S.; Johnson, B. P.; Zhou, X.; Nguyen, Y. T.; Dlott, D. D.; Udaykumar, H. S. Hot Spot Ignition and Growth from Tandem Micro-Scale Simulations and Experiments on Plastic-Bonded Explosives. *J. Appl. Phys.* **2022**, *131* (20), 205901.

13. Dobratz, B. M. *Properties of Chemical Explosives and Explosive Simulants*; UCRL--51319, UCRL--51319(REV.1), 4285272; 1972; p UCRL--51319, UCRL--51319(REV.1), 4285272.

14. Schindelin, J.; Arganda-Carreras, I.; Frise, E.; Kaynig, V.; Longair, M.; Pietzsch, T.; Preibisch, S.; Rueden, C.; Saalfeld, S.; Schmid, B.; Tinevez, J.-Y.; White, D. J.; Hartenstein, V.; Eliceiri, K.; Tomancak, P.; Cardona, A. Fiji: An Open-Source Platform for Biological-Image Analysis. *Nat. Methods* **2012**, *9* (7), 676–682.

15. Brown, K. E.; Shaw, W. L.; Zheng, X.; Dlott, D. D. Simplified Laser-Driven Flyer Plates for Shock Compression Science. *Rev. Sci. Instrum.* **2012**, *83* (10), 103901.

16. Curtis, A. D.; Banishev, A. A.; Shaw, W. L.; Dlott, D. D. Laser-Driven Flyer Plates for Shock Compression Science: Launch and Target Impact Probed by Photon Doppler Velocimetry. *Rev. Sci. Instrum.* **2014**, *85* (4), 043908.

17. Bassett, W. P.; Dlott, D. D. Multichannel Emission Spectrometer for High Dynamic Range Optical Pyrometry of Shock-Driven Materials. *Rev. Sci. Instrum.* **2016**, *87* (10), 103107.

18. Marsh, S. P. *LASL Shock Hugoniot Data*; University of California Press, Berkeley, 1980.

19. Armstrong, M. R.; Grivickas, P. V.; Sawvel, A. M.; Lewicki, J. P.; Crowhurst, J. C.; Zaug, J. M.; Radousky, H. B.; Stavrou, E.; Alviso, C. T.; Hamilton, J.; Maxwell, R. S. Ultrafast Shock Compression of PDMS-based Polymers. *J. Polym. Sci. Part B Polym. Phys.* **2018**, *56* (11), 827–832.

20. Forbes, J. W. *Shock Wave Compression of Condensed Matter: A Primer*; Springer Berlin Heidelberg: Berlin, Heidelberg, 2012.

21. Desmond, K. W.; Weeks, E. R. Influence of Particle Size Distribution on Random Close Packing of Spheres. *Phys. Rev. E* **2014**, *90* (2), 022204.

22. Lu, B.; Torquato, S. Nearest-Surface Distribution Functions for Polydispersed Particle Systems. *Phys. Rev. A* **1992**, *45* (8), 5530–5544.

CHAPTER 6: SPATIAL IMAGING OF HMX CLUSTERS BEING INITIATED

The following chapter acts as a continuation of the study on the role of HMX grain clustering in the previous chapter. In that chapter, it was shown that the difference in ignition performance observed in HMX is likely due to heat transfer limiting the ability of localized pockets of heat, or 'hot spots', to spread and coalesce. However, these observations relied on characterizing the materials *a priori* and carefully measuring auto emission spectra. This chapter will briefly cover the use of nanosecond gated photography to *spatially* track reaction progress. A spatial mapping can allow for much more explicit calculations such as fitting kinetic models to see how the topology of grain arrangements change the performance of explosive mixtures. Unfortunately, the step of doing such calculations reaches beyond the scope of this dissertation. This chapter serves to share the methods by which this data can be collected, qualitative observations of selected grain arrangements and the possibilities for its use in the future. Examples will be shown from a low concentration HMX mixture and a high concentration HMX mixture in PDMS films.

6.1 Introduction

The implications of the 'hot spot' model of shock to detonation (SDT) on the storing and handling of polymer bonded explosives (PBX) is profound, but poorly understood. Much of these problems stem from a lack of spatially aware experimental data, such as *in situ* photography with micron resolution. Features on the micron scale, which can be changed simply from sourcing the powder differently, can dramatically affect the sensitivity of materials. A central goal of this dissertation has been to provide high-quality data on how hot spots spread and coalesce, which is needed for predictive models to unify molecular dynamics at nanometer

scale with fluid dynamics models at millimeter scales. After hot spots form, they must spread across grains and coalesce with other hot spots to catch up with the shock front, that part is clear.[1,2] However, predictive models need to fit details like quantity of hot spots, how fast they're spreading, and reaction kinetics dictating this process to existing data of large scale data on shock sensitivity. The result is inconsistency on these details, especially decomposition models, with no way of predicting sensitivity *a priori*.[3] This chapter explores high speed photography of crystal grains arranged in clusters of various sizes, shapes, and proximities, as a tool to ameliorate these problems.

Grain clusters offered one form of relief to this problem. The previous chapter showed how deflagration performance scales nonlinearly with concentration, likely because grain percolation resulted in thermal mass being leeched by neighboring HMX particles. The data was compelling but ultimately incomplete because there was no way to spatially track these hot spots, which is a vital benchmark for predictive models. The current state of the art in simulations, for example, is a multiscale, structurally aware system called the 'meso-informed ignition and growth model'. In this, a sub-grid of grain arrangements are created, then hot spots, usually generated from void collapse of various kinds, are initialized and spread. By sampling enough of these systems, the 'meso scale', or micron-sized structures, can be modeled.[4,5] A workflow can be imagined where grain clusters of various shapes and sizes can be made, shock compressed, and have their emission photographed to cross-referenced to predictions of this grain arrangement.

The specific details on how hot spots form in grain clusters is complicated and beyond the scale of this study: it requires a combination of fluid dynamics models and experimental data on heavily simplified systems.In fact, such a workflow was already established by Roy *et. al.*

working alongside the Dlott group to model large single crystals of HMX.[6] The goal of that work was to elucidate how hot spots form during shock waves of large (~200 μm) single crystals of HMX shock compressed at various over-driven conditions.[7,8] The goal of this chapter, on the other hand, is to advance that work one step further with the information learned so far about HMX clusters. Using small-grained, polycrystalline HMX powder such as in Fig 6.1(a), HMX clusters in polydimethyl siloxane (PDMS) are spin coated to a 1-grain deep, shown in Fig 6.2. This is representative of cross section of a PBX with where groups of HMX clusters can be examined and compared to the behavior inside a single crystal. When shock compressing these thin layers at 20 GPa, a high-speed camera capable of collecting 20-100 ns exposure times is aimed at the sample, and the progress of hot spots spreading can be tracked (Fig 6.3). This work will exhibit the experimental techniques and qualitative results yielded from tracking whole clusters.

6.2 Experimental

Shock compression experiments are conducted using laser driven flyer plates on the shock compression microscope described in previous chapters, and previous work.[9,10] Chapter 2 can be referred to for more detail. The PBX layers are impacted with 25 μm Aluminum (Al-1100) flyer plates at 3.6 ± 0.2 km/s. Based on the concentrations of HMX thin layers used in this chapter (10-40 wt%), this is about 17-21 GPa shock impact (Fig 6.3). This makes the impacts consistent with experiments done in the previous work on HMX clusters. Details on these estimates can be found in Chapter 5 and Appendix F. The flyer plate remains intact for these experiments and can be recovered. Figure 6.4 is an example of an optical profile of an impact crater of these layers. The disc in the middle is an aluminum flyer plate, which is ~500 μm in

diameter and ~18 μm tall. The thinner remaining aluminum is not surprising due to the nature of laser driven flyer plates.

6.2.1 HMX Powder Preparation

HMX was extracted from a stock of N-5 material by dilution in acetone followed by a filtration through no. 55 filter paper in a Buchner funnel. To achieve a consistent particle size distribution, HMX is then recrystallized again using the following procedure: 300 mg of HMX is measured then dissolved in acetone to saturation. Following this, a 3 mL pipette is used to crash precipitate the HMX using several successive 3 mL aliquots DI water. The crystals are filtered through no. 55 filter paper using a Buchner funnel then air dried for 30 minutes.

The particle size distribution is determined by taking the HMX crystals and suspending it in Ethylene glycol (Fisher). A Horiba mastersizer is used to determine the volumetric particle size distribution, and converted to a number size distribution for Fig 6.1(a). This data was verified by measuring the loose powder on a scanning electron microscope (SEM) (JEOL 7000F). 7 nm of a gold palladium coating was applied to the powder after being affixed to double-sided copper tape and an accelerating voltage of 10 KeV was used. An example of the HMX powder micrographs are shown in Fig 6.1(b). It is worth noting, as was done in the previous chapter, that the HMX grains form many platelet-like structures, making spherical estimations of particle sizes inaccurate for the purposes of packing dynamics.[11] These consist of polycrystalline HMX grains that are within 40 μm length scales, thus the thin film produced is matched to approximately the longest possible grain: between 40-50 μm.

6.2.2 HMX PBX Thin Film Layers

For this study, two concentrations of HMX in PDMS were chosen for spin-coating layers. A low concentration (~5 wt.%) and a higher concentration (~40 wt.%). To prepare the PDMS

layers, Sylgard 182 PDMS (Ellesworth Adhesives) was dissolved in Hexanes in a 1:2.5 Hexanes to PDMS ratio to achieve a viscosity amenable to 50 μm layers. HMX crystals are added to this mixture to achieve ~1 wt.% mass fraction of HMX (for low concentration) and 5 wt.% (for high concentration) with respect to the quantity of PDMS. A spin coater was used to cast the PDMS film. Onto a 2”x2” piece of Pyrex glass, 1 mL of the HMX-PDMS mixture is drop casted to even distribution. The glass is spun at 680 RPM for 60 seconds to reach an approximate layer thickness of 50 ± 4 microns. The PDMS is cured in an oven at 70°C for approximately 12 hours. The spin coating procedure results in a final HMX layer of a higher concentration than the stock solution. The final concentration is estimated from the fraction of cross-sectional area, but is generally larger than the stock solution, like thin layer preparation techniques seen in previous chapters. The thickness and uniformity of the PDMS layer is verified by optical profilometry. A Keyence VK-X1000 Scanning Laser Microscope is used to measure the step height and surface roughness of the final layer. Figure 6.2(b) is a typical light microscope image of the resultant thin film, in this case for a low concentration HMX mixture. It contains a wide sampling of different cluster sizes and proximities.

6.2.3 Multiframe Camera Photography

Images of the HMX clusters as they’re emitting light due to heat generation are collected using a high speed camera, and this data is super-imposed to static images of the HMX grain clusters that were collected before each shock experiment. The scheme for data collection is displayed in Fig 6.3. As the HMX thin film is emitting light after being shocked, the light is collected by an objective and directed for imaging. It is first focused down using a tube lens and sent through an aperture that acts as a spatial filter. The spatial filter is set to make the field of view less than 250 μm-radius centered on the impact site. The field of view is below the radius

of the flyer plate itself to avoid light pollution caused by the shear wave on the edge of the flyer, likely due to high curvature in this region.[12,13]

The images are collected by a high speed, multiframe camera consisting of 8 individual image sensors. The time delays and exposure times can be adjusted down to nanosecond resolution to meet the time resolution needs of the experiment. For this experiment, we isolate the region between 0-1000 ns, when we expect the hot spots to form and spread, and begin the process of deflagration. Constant frame rates are used throughout this chapter, where the frames are sequential, and the exposure time is kept constant.

Finally, a dichroic mirror is used to separate the 1550 nm probe light for the photon doppler velocimeter, which tracks flyer velocity and can determine exact time of impact. Before the emission reaches the camera, 10% of the light is collected *via* a beam splitter to send to the emission pyrometer. The emission pyrometry similar to what was described in previous work[14,15] and in Chapter 2, except that the lens array is changed to allow the device to collect light from the entire frame compared to a ~60x90 μm window used in previous studies.[7] Collecting emission data will allow for comparisons of the time dependent light emission and light temperature over the entire shock initiation event. This gives a known point of comparison to explain what is happening in the subsequent photographs. However, collecting temperature data with emission pyrometry creates an extreme bias towards high temperatures inside the field of view. In fact, a 2000K emission can be poisoned with as little as 1 vol.% of 4000K light in the field of view. This is an important detail to keep in mind during these comparisons; quantitative photography and emission pyrometry act more as compliments than direct comparisons. This point will be addressed later.

Another important limitation to emission photography is the sensitivity. Visible light emitted over nanoseconds is very difficult to capture with decent signal to noise, a problem which gets worse as the temperature of the emitting body drop. In general, radiant intensity of blackbody emission scales proportional to T^4, however in the visible bandwidth being studied (400-750 nm), this scaling is closer to T^6. Photomultiplier tubes, such as those used in the emission pyrometry, are far more sensitive than the image intensified CMOS sensors used in this camera. It was previously determined that emissions below 2000K are effectively undetectable with this design of experiment.[7]

6.3 Results

The process of spatially mapping auto emission during ignition is shown in Fig 6.4. Preceding each shock experiment, static images of the grain clusters are collected using an external light source. Using the image processing software Fiji[16], thresholding is performed to create an outline of where the HMX clusters are located. During the shock, light emission images consist of separated sights of light, the hot spots, which will spread, fade away, and new ones appear at different times. This is impossible to interpret without overlaying the location of the original explosive grain clusters.

For simplicity, this section will only cover two sets of experiments: a low concentration slide containing several isolated clusters of varying sizes, and a higher concentration slide consisting of large clusters often interconnected by branches. In chapter 5, this was referred to as the effect of HMX entering a new percolation phase between 40-60 wt.%: large isolated clusters first get bigger as more HMX is added, then as they reach proximity with each other, begin to interconnect. It would be desirable to work on a wide array of concentrations, there is first a need

for robust methods to quantify shape factors of clusters and compare to growth rates. This section will mostly remain qualitative since that work is still in progress.

6.3.1 Low Concentration HMX in PDMS

The thin films of HMX in PDMS being shock compressed are roughly 5 vol.% or 10 wt.%. They tend to exhibit highly localized clusters. Figure 6.6 is a representative example of how these clusters behave when shock compressed. The collection begins at flyer impact time and are sequentially captured at 100 ns exposures for 8 frames (equivalent of 10 million frames per second). Figure 6.6(a) reflects the efficacy of photography for showing where hot spots form and how they spread. Upon impact, some low intensity loci of emission can be noticed in the center of many of the clusters. In the next 100 nanoseconds these hot spots spread across the cluster and grow more intense. For the next 200 nanoseconds the hot spots decay and disappear. The emission is likely not intense enough to observe by the camera due to the lower temperatures of these regions. After this, emission from the edges of the field of view begin to light up. This is possibly due to the high heat produced by the shear wave along the edges of the flyer plate moving inward in this time span.

The emission pyrometry data collected during experiments can quantify the spectral radiance and color temperatures occurring during this experiment, the lineout of this experiment is graphed in Fig 6.6(b). It exhibits three peaks in contrast to the two peaks observed in previous work in this dissertation. An initial nanosecond peak, typical of hot spot formations from material defects is observed, as expected.[7,15] Following this is a ~200 nanoseconds full width half maximum peak rising at 50-70 nanoseconds after impact. A temperature increase to ~4000K is also observed at this time. Finally, a third peak occurs after 300 nanoseconds. While there are still quite high observed temperatures during this time period, the photography shows this time

period to be filled with somewhat uncorrelated noise. For these experiments, the third peak can be safely ignored due to a factor little mentioned before: the binder contribution. It is not clearly understood why, but some emission can be observed in PDMS when shock compressed, so much HMX mixtures below 10 wt.% end up producing *less* emission in the microsecond regime than neat PDMS layers. For the purposes of this experiment, this region can be safely ignored, and discussions will be focused on the first two peaks which are clearly reflective of hot spot behavior and ignition of the crystals.

Figure 6.7 provides a set of image frames to compare to the emission pyrometry they produce. Except for shot 4, shots 1,7 and 9 don't differ significantly in terms of particle size or shape factors. None of these particles behave particularly effectively, exhibiting very little hot spot emission in the nanosecond region and only shot 1 having notable reaction propagation. Most of the emissions from these samples are, in fact, noise from the edges due to the shear band formation, as previously mentioned.[12,13] The emission of shot 4 is the one displayed in Fig 6.6, which features the largest clusters of the group.

6.3.2 High Concentration HMX in PDMS

To compare the effect of clusters becoming interconnected or HMX percolating, a higher concentration sample was chosen. The concentration ranges from 40-55 wt.% and tend to lack any isolated clusters, with everything having at least a single point of contact. Because of this, the overlay is now shaded in blue where HMX is present to better contrast the binder phase from the HMX phase.

Figure 6.8 is a representative example of this sample, with a concentration of about 50 wt.%. The emission pyrometry trace of this experiment is shown in Figure 6.8(b). The time range chose now only goes to 160 ns with shorter exposures due to the limited utility of data beyond

300 ns, as mentioned in the previous section. At initial flyer impact, hot spots in disparate sights are formed. The precise locations of hot spot formation appears purely stochastic from limited studies using k-means clustering analysis. The hot spots produced tend to reach their apogee near 100-120 ns after impact and begin to decay thereafter. The size of these hot spots ranges from 20-50 μm in major axis length. Figure 6.9 provides a close-up of a different shot at the apogee of the hot spot length, approximately 80 ns after impact. All of the initial hot spots have been able to spread within the cluster during this time frame but their length appears capped to ~50 μm length. The camera will only pick up emission from sites that are well above the 2000K limit, especially for the very short 20 ns exposure time. Furthermore, Figure 6.8(b) shows the emission pyrometry of the shock experiment showing how the reaction propagation due to the hot spot and the longer-time deflagration from HMX decomposition begin to convolute, forming the familiar two-peak structure that has been analyzed in previous chapters.

6.4 Discussion

The origin of hot spots gives some indication of what structural factors may affect sensitivity. For single crystals studied by Johnson *et al* and Roy *et al*, there were two main sources of hot spots: crystal vertices due to shock reflections, and crystalline defects.[6,7] The defect-driven hot spots were found to be much more effective. The nanosecond peaks observed in the pyrometry data [Fig. 6.6(b)] were also able to be isolated in polycrystals[7], being the result of either crystallite junctions, slip planes or internal voids[6,17]. The hot spots formed in clusters of HMX are consistent with the nature and time dependence of these types of hot spots. The hot spots tend to originate in the center of the clusters and the time dependence of the second emission peak is consistent with behavior of large polycrystals.

Clusters of HMX are not individual polycrystals, they are far more complicated. They are collectives of small single crystals and polycrystals stacking together to form complicated structures. There remain very important questions to answer: do voids formed by packed crystals differ from voids inside of crystals? Are these complicated shapes concentrating shock energy *via* reflections across shock impedance boundaries?[18] Answering these questions requires a much more extensive review of different HMX structures, like changing out polycrystals for single crystals, changing cluster sizes, or even particle size distribution. The questions circling how hot spots form will remain a rich field of study going forward, and this is an effective method of studying it.

This study can offer a few observations that may enrich this discussion. When cross-referencing analysis on the scale of single grains, performed by cross-sectional SEM of analogue materials [Fig 6.10(a)] and the amount of light produced between 0-15 ns after impact in Chapter 5 [Fig 6.10(b)], an interesting trend can be observed. These particle scale images can be quantified in terms of the percentage of HMX grain boundaries within 2 pixels of another boundary. Based on this information, a clear power-law relationship can be drawn where the quantity of impedance boundaries are clearly covariant with the amount of hot spots produced by HMX PBXs. This provides one possible explanation for how hot spots form in these clusters.

The alternative explanation, crystallite boundaries due to the polycrystalline nature of these HMX powders, can be contrasted to the observations in Fig 6.7. Many isolated groups just of a few HMX crystals, sometimes even fewer, are found in most of these samples. However, very little hot spot emission can be seen and it results in relatively ineffective hot spot propagation. Shot 4, also shown in Fig 6.6, in contrast has large, dense, and highly structured clusters and does produce clear hot spots that effectively propagate through the crystal.

6.5 Conclusions

Methodology was produced that is reliably able to photograph and trace micron-scale hot spots propagating through representative cross-sections of PBXs. By creating spin-coated, thin films of HMX-based PBX materials that are approximately 1 grain layer thick, emission observed in nanosecond photography can clearly be mapped to specific clusters and tracked as they travel through the clusters. Two samples were compared, a low HMX sample that displayed isolated clusters, and a high concentration where HMX enters a new percolation phase: highly interconnected. The contrast between these two reflect that hot spots in fine powder samples possibly originate from the high quantity of grain-binder boundaries, in comparison to crystalline defects as is noticed in large (~200 μm length) HMX. The data shown is consistent with observations in Chapter 5 about how hot spot propagation may be capped to certain length scales below 50 μm, the limited sample size makes it difficult to draw hard conclusions from this convenient observation.

However, the relatively small sample size currently available for analysis makes conclusions impossible to draw at the time of writing. To advance further, robust methods to quantify size and shape factors over large quantities of photographs are needed. More obviously, a sample size consisting of several hundred photographed samples would be desired to make any method of statistical analysis compelling. The study performed in this chapter seeks to open the discussion of photography as a quantitative tool for measuring reaction kinetics in PBXs with very complicated structures.

In terms of instrumentation, the next step to take would be to spatially map the temperature of the light being emitted by these clusters. Techniques like this often adopt the name ‘hyperspectral imaging’, where the images are informed by the spectrum of light produced.

Using multiple frames allows an experiment to cleverly apply spectral filters to allow certain colors to reach certain frames, then the ratio of light intensity between two frames gives an estimate of temperature. This can be performed with either bandpass filters or notch filters. In the case of bandpass filters, temperatures observed in these experiments, often ranging from 3000-5000K, would be estimated to be most amenable to one frame measuring 400-650 nm, and another measuring light beyond 650 nm.

6.6 Figures

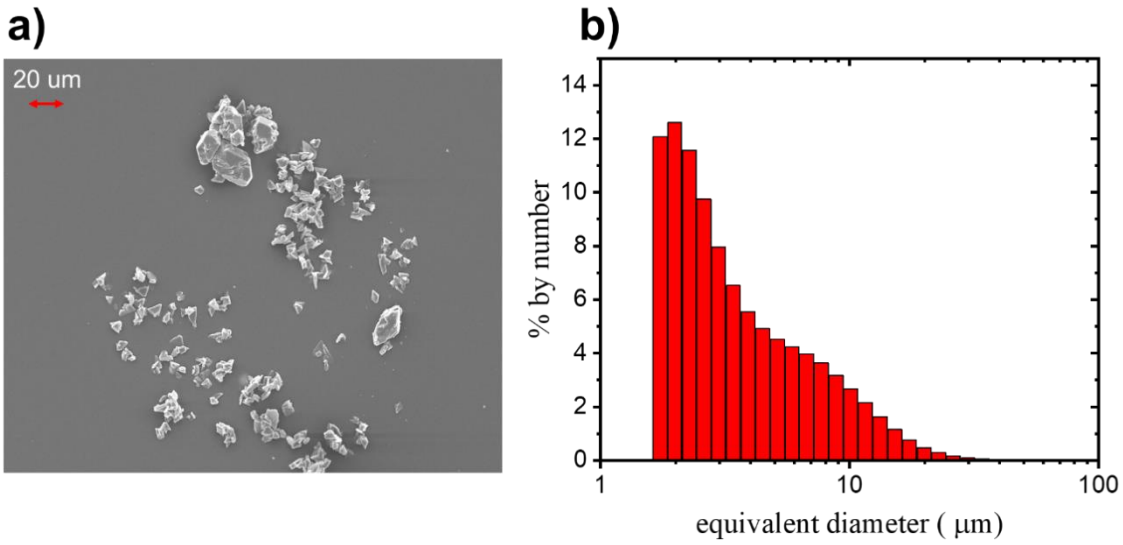

Figure 6.1 SEM micrograph of HMX powder used in experiments (a) and their number size distribution (b).

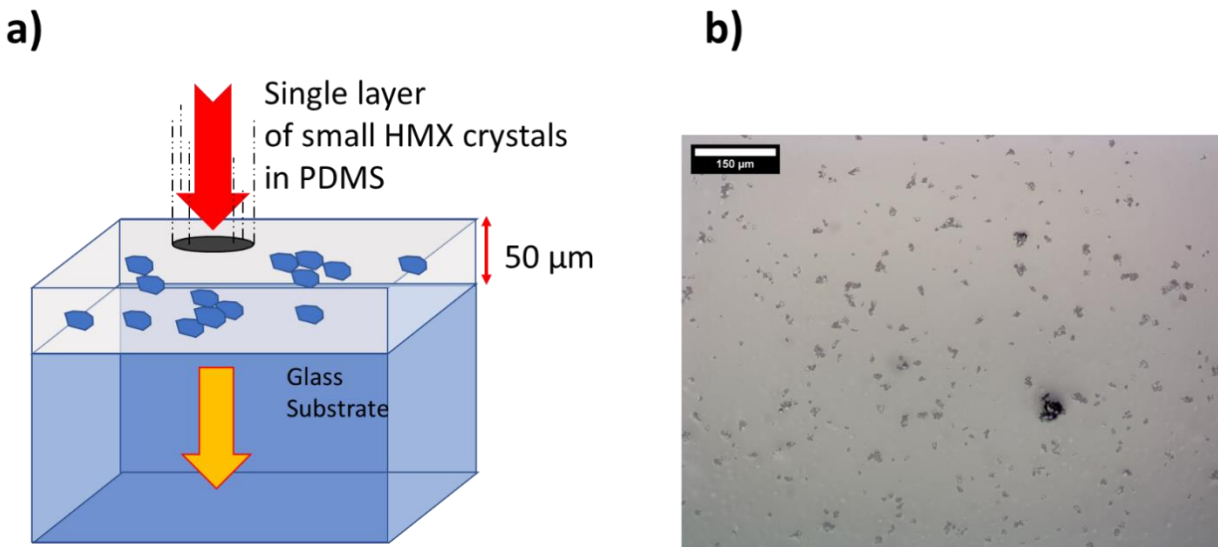

Figure 6.2 Visual depiction of the HMX-based PBX thin films (a) and a light microscope image of the HMX clusters embedded in PDMS films (b). Based on these, the film thickness used should accommodate the largest possible HMX size to avoid protrusions, making ~50 µm the film thickness of choice for cross-sectional analogues.

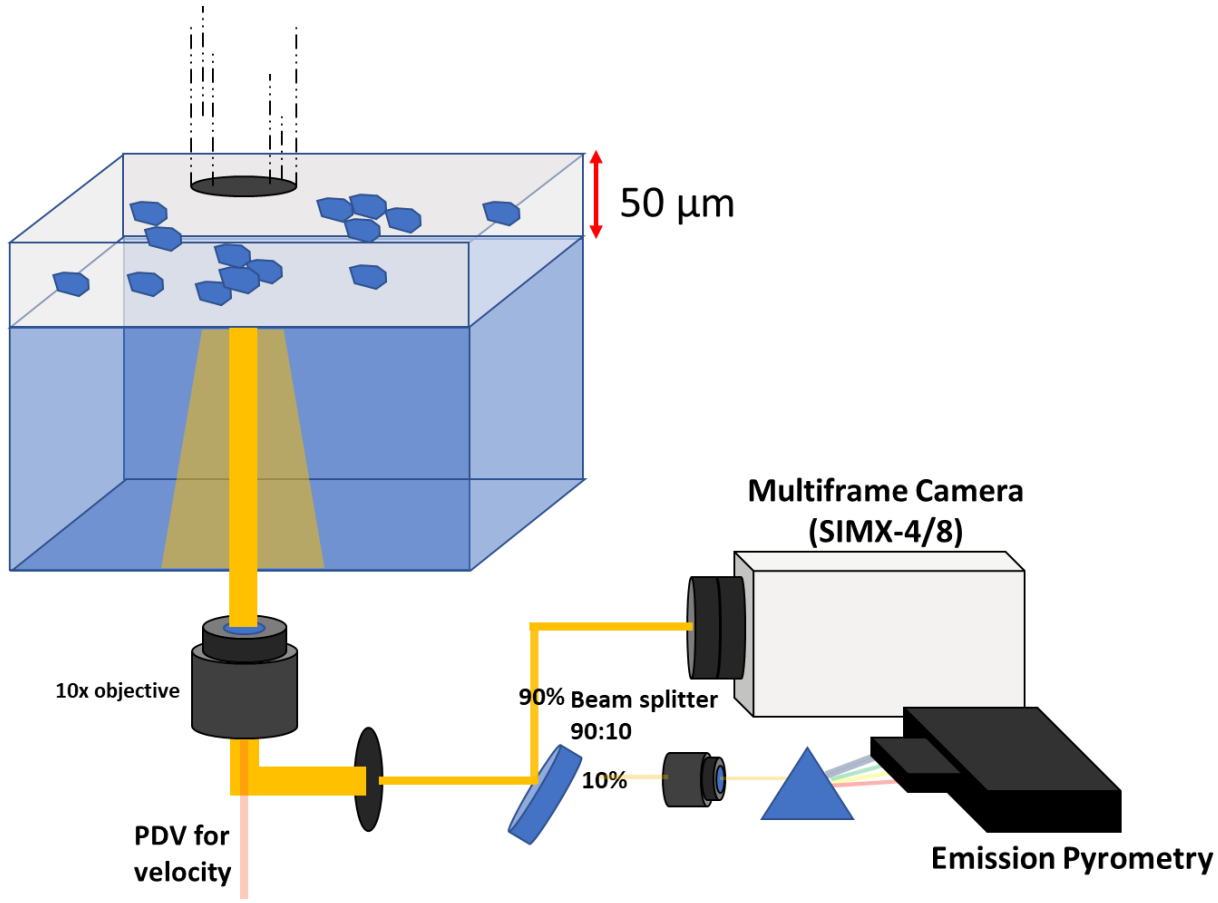

Figure 6.3 Visual depiction of the technique used to collect light for simultaneous photography and emission pyrometry of thin films of HMX. The light is collected by an objective lens and directed through a 90%R 10%T beam splitter, the bulk of the light is used for photography and a 10% sample is taken to collect spectral radiance and color temperature of the overall light.

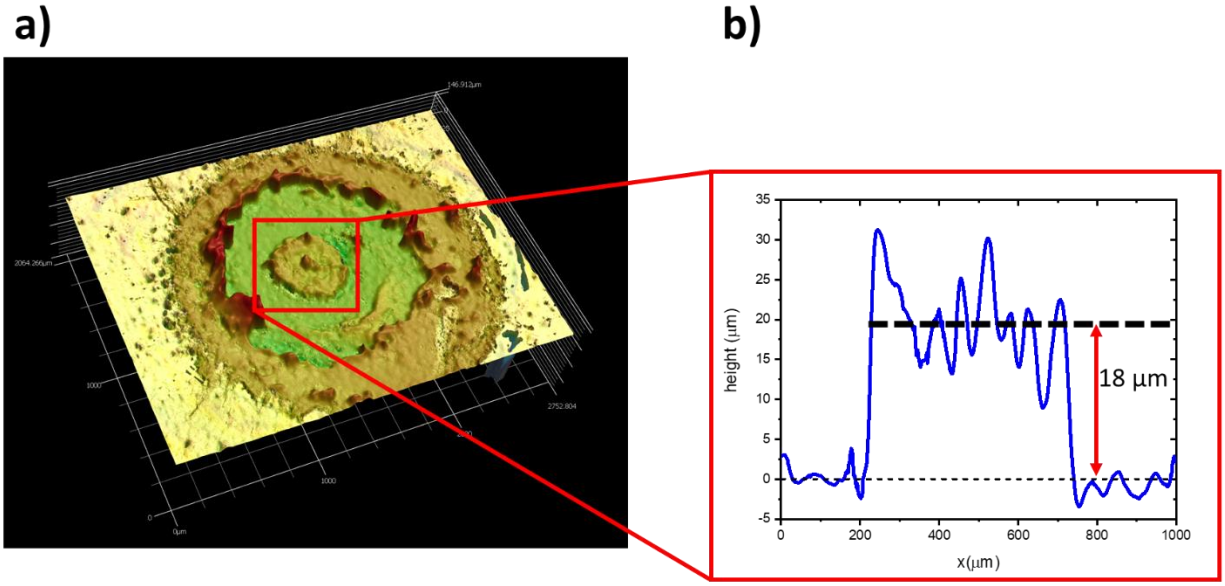

Figure 6.4 Depth profile of an HMX thin film post mortem (a) showing the extent of damage to an HMX thin film, spanning about 1 mm diameter. The 500 μm-diameter flyer plate can be seen in the center of the crater, with its depth profile (b) showing that the leftover projectile is 18-20 μm thick after the laser-launching process.

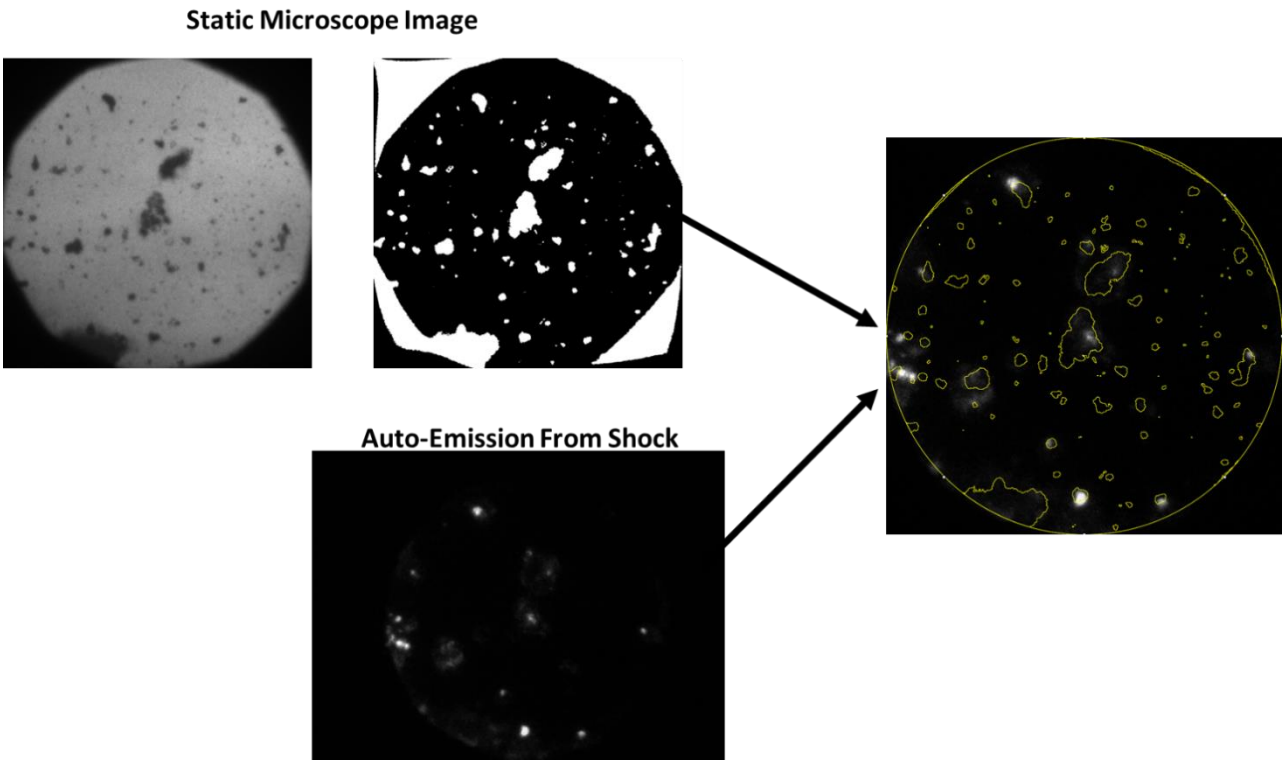

Figure 6.5 Representation of the image processing performed to map auto emission in photographs to the background photos showing the pristine HMX clusters. After thresholding static background images, a trace of the clusters is overlayed on shock-compressed layers to map where hot spots form inside each cluster.

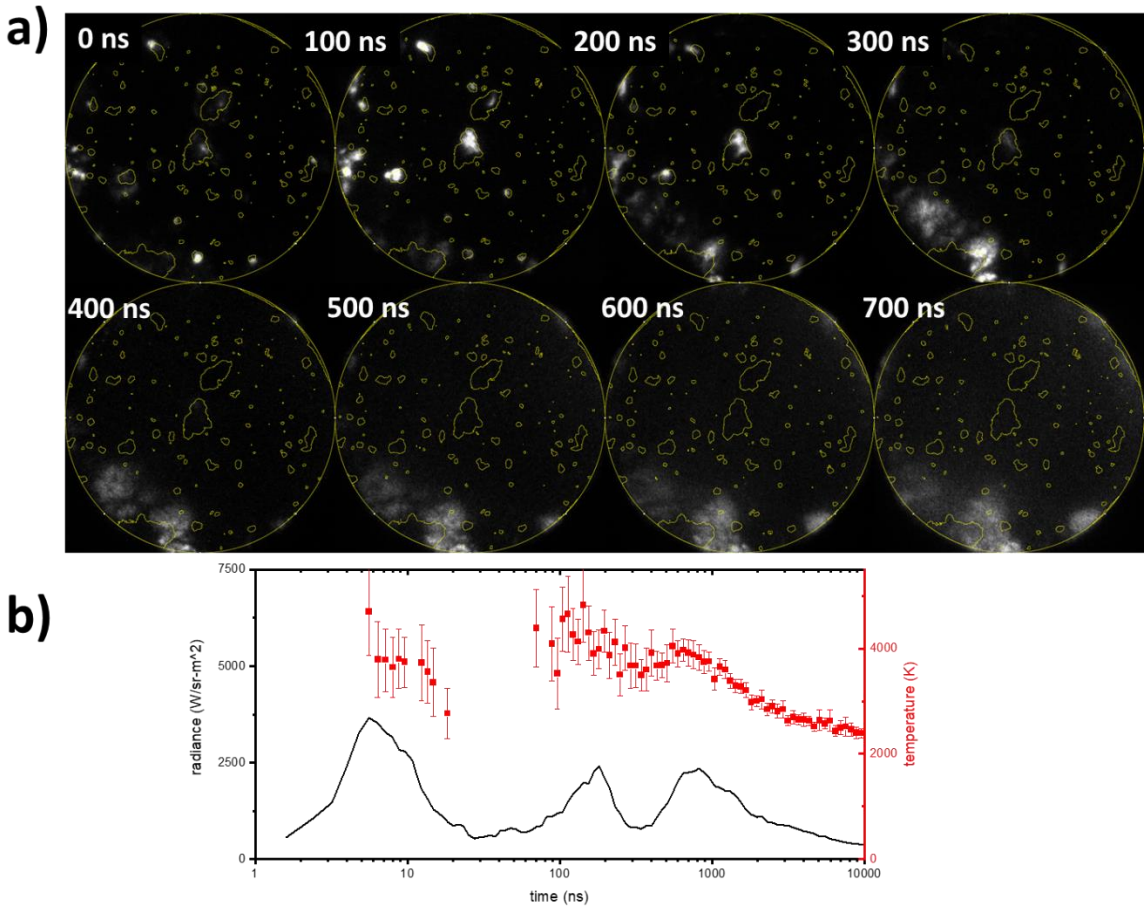

Figure 6.6 A photographic timeline of the shock ignition of a ~15 wt.% HMX film hit by a 3.5 km/s flyer plate (a). The data collected from emission pyrometry for this experiment is simultaneously observed (b). The time stamp in the top right corner represents the time exposure began. Each frame collects data over 100 ns, thus this spans an 800 ns timeline.

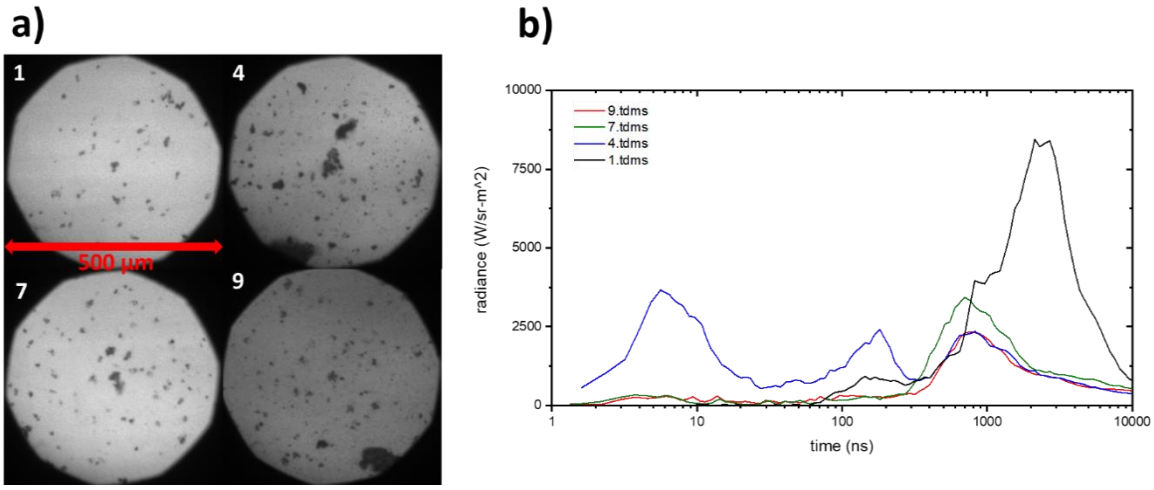

Figure 6.7 Comparison of several samplings of sparsely concentrated HMX clusters in PDMS thin films. When impacted by a 3.5 km/s flyer plate, yield emission traces that are compared (b).

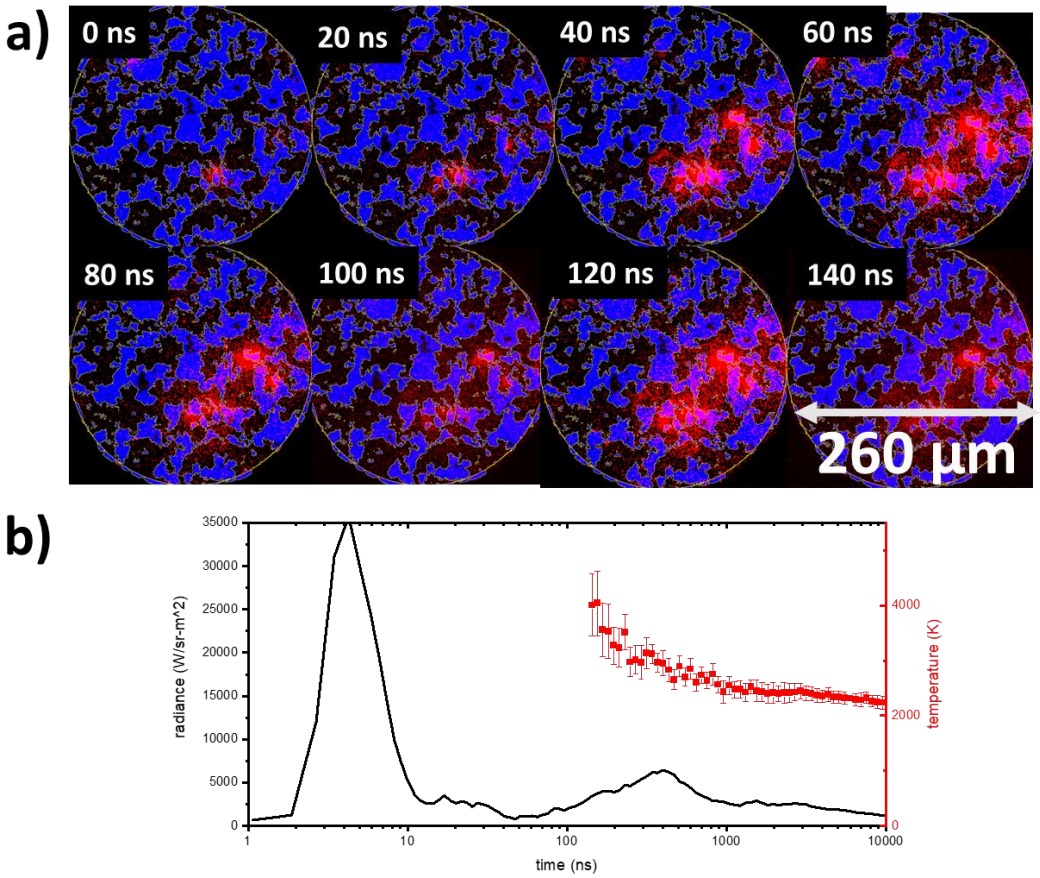

Figure 6.8 A photographic timeline of the shock ignition of a ~50 wt.% HMX film hit by a 3.5 km/s flyer plate (a). Because the HMX is so dense, the cluster traces are filled in with blue to contrast the HMX (blue) from the PDMS (black). The data collected from emission pyrometry for this experiment is simultaneously observed (b). The time stamp in the top right corner represents the time exposure began. Each frame collects data over 20 ns, thus this spans a 160 ns timeline.

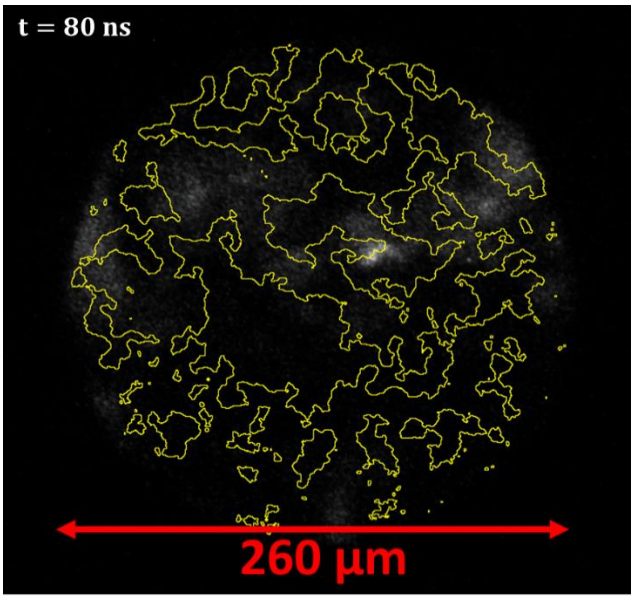

Figure 6.9 Close up of a frame displaying ~50 wt.% HMX in PDMS, impacted by a flyer plate at 3.5 km/s. The frame selected shows 80-100 ns after flyer plate impact. The maximum observed length of the hot spots is generated in this frame. After this time stamp it begins to decay.

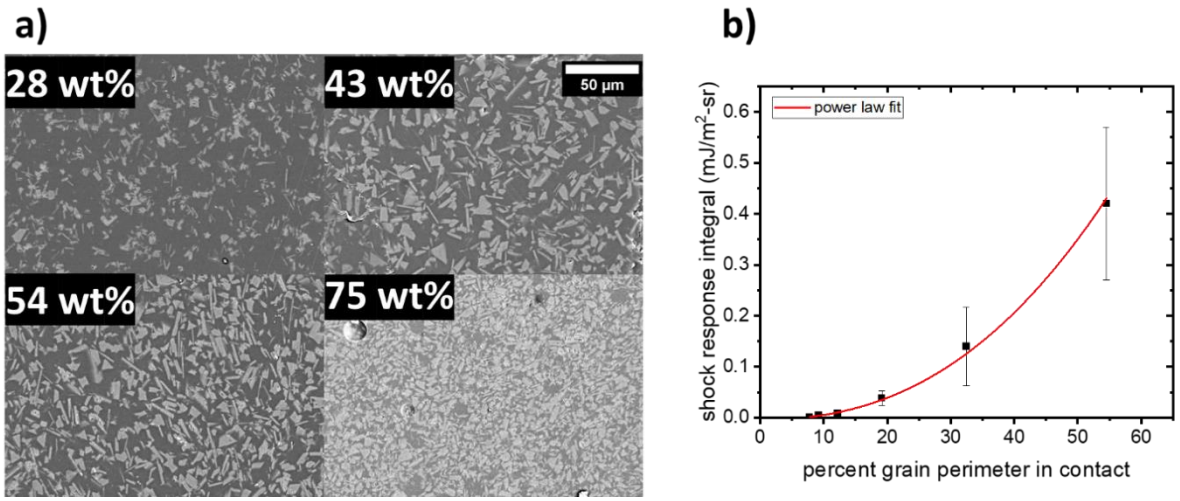

Figure 6.10 SEM micrographs of HMX-based PBX cross sections at various concentrations (a). When the quantity of light generated in the first 15 ns after shock compression is compared to the amount of grain boundaries in contact with one another, the following power-law relation is generated(b).

6.7 References

1. Tarver, C. M.; Chidester, S. K.; Nichols, A. L. Critical Conditions for Impact- and Shock-Induced Hot Spots in Solid Explosives. *J. Phys. Chem.* **1996**, *100* (14), 5794–5799.

2. Menikoff, R.; Shaw, M. S. Reactive Burn Models and Ignition & Growth Concept. *EPJ Web Conf.* **2010**, *10*, 00003.

3. Rai, N. K.; Koundinyan, S. P.; Sen, O.; Schweigert, I. V.; Henson, B. F.; Udaykumar, H. S. Evaluation of Reaction Kinetics Models for Meso-Scale Simulations of Hotspot Initiation and Growth in HMX. *Combust. Flame* **2020**, *219*, 225–241.

4. Nguyen, Y.; Seshadri, P.; Sen, O.; Hardin, D. B.; Molek, C. D.; Udaykumar, H. S. Multi-Scale Modeling of Shock Initiation of a Pressed Energetic Material I: The Effect of Void Shapes on Energy Localization. *J. Appl. Phys.* **2022**, *131* (5), 055906.

5. Nguyen, Y. T.; Seshadri, P. K.; Sen, O.; Hardin, D. B.; Molek, C. D.; Udaykumar, H. S. Multi-Scale Modeling of Shock Initiation of a Pressed Energetic Material. II. Effect of Void–Void Interactions on Energy Localization. *J. Appl. Phys.* **2022**, *131* (21), 215903.

6. Roy, S.; Johnson, B. P.; Zhou, X.; Nguyen, Y. T.; Dlott, D. D.; Udaykumar, H. S. Hot Spot Ignition and Growth from Tandem Micro-Scale Simulations and Experiments on Plastic-Bonded Explosives. *J. Appl. Phys.* **2022**, *131* (20), 205901.

7. Johnson, B. P.; Zhou, X.; Ihara, H.; Dlott, D. D. Observing Hot Spot Formation in Individual Explosive Crystals Under Shock Compression. *J. Phys. Chem. A* **2020**, *124* (23), 4646–4653.

8. Johnson, B. P.; Zhou, X.; Dlott, D. D. Shock Pressure Dependence of Hot Spots in a Model Plastic-Bonded Explosive. *J. Phys. Chem. A* **2022**, *126* (1), 145–154.

9. Brown, K. E.; Shaw, W. L.; Zheng, X.; Dlott, D. D. Simplified Laser-Driven Flyer Plates for Shock Compression Science. *Rev. Sci. Instrum.* **2012**, *83* (10), 103901.

10. Curtis, A. D.; Dlott, D. D. Dynamics of Shocks in Laser-Launched Flyer Plates Probed by Photon Doppler Velocimetry. *J. Phys. Conf. Ser.* **2014**, *500* (19), 192002.

11. Desmond, K. W.; Weeks, E. R. Influence of Particle Size Distribution on Random Close Packing of Spheres. *Phys. Rev. E* **2014**, *90* (2), 022204.

12. Bhowmick, M.; Basset, W. P.; Matveev, S.; Salvati, L.; Dlott, D. D. Optical Windows as Materials for High-Speed Shock Wave Detectors. *AIP Adv.* **2018**, *8* (12), 125123.

13. Stekovic, S.; Springer, H. K.; Bhowmick, M.; Dlott, D. D.; Stewart, D. S. Laser-Driven Flyer Plate Impact: Computational Studies Guided by Experiments. *J. Appl. Phys.* **2021**, *129* (19), 195901.
14. Bassett, W. P.; Dlott, D. D. Multichannel Emission Spectrometer for High Dynamic Range Optical Pyrometry of Shock-Driven Materials. *Rev. Sci. Instrum.* **2016**, *87* (10), 103107.

15. Bassett, W. P.; Johnson, B. P.; Neelakantan, N. K.; Suslick, K. S.; Dlott, D. D. Shock Initiation of Explosives: High Temperature Hot Spots Explained. *Appl. Phys. Lett.* **2017**, *111* (6), 061902.

16. Schindelin, J.; Arganda-Carreras, I.; Frise, E.; Kaynig, V.; Longair, M.; Pietzsch, T.; Preibisch, S.; Rueden, C.; Saalfeld, S.; Schmid, B.; Tinevez, J.-Y.; White, D. J.; Hartenstein, V.; Eliceiri, K.; Tomancak, P.; Cardona, A. Fiji: An Open-Source Platform for Biological-Image Analysis. *Nat. Methods* **2012**, *9* (7), 676–682.

17. Cawkwell, M. J.; Sewell, T. D.; Zheng, L.; Thompson, D. L. Shock-Induced Shear Bands in an Energetic Molecular Crystal: Application of Shock-Front Absorbing Boundary Conditions to Molecular Dynamics Simulations. *Phys. Rev. B* **2008**, *78* (1), 014107.

18. Menikoff, R. Hot Spot Formation from Shock Reflections. *Shock Waves* **2011**, *21* (2), 141–148.

CHAPTER 7: TABLETOP SHOCK TO DETONATION USING VELOCIMETRY

7.1 Overview[3]

This chapter will shift to shock-to-detonation events. In comparison to shock to deflagration, shock to detonation studies rely on producing the detonation directly from the shock wave rather than indirectly from hot spots growing and coalescing. Studies of shock to detonation on these short time and spatial resolutions fill a gap in experimental data. Reaction mechanisms are discernable from ultrafast laser ablation experiments, and continuum scale dynamics are learned from much larger scale gas-gun experiments. Previous chapters have shown that predictive models, which are mostly phenomenological, often fail to be general. This, in part, is because methods of connecting reaction kinetics to fluid dynamics and microstructure lack intermediate scale experiment data to develop *ab initio* models for explosive shock to detonation. This chapter will cover how to create shock to detonations from thin flyer plates, how to measure them, and what experiments can be done. These discussions move away from using HMX and mostly discuss Pentaerythritol tetranitrate (PETN), a much more sensitive explosive. The focus of this chapter is using these techniques to verify if the PETN-based PBX is producing a self-sustaining shockwave, a precursor to a full detonation, and how to leverage that for further experiments.

[3] Portions of this chapter were adapted from the experimental sections of two original research articles including: Salvati, L.; Johnson, B. P.; Bassett, W. P.; Dlott, D. D. Probing Shock-Initiation of Plastic-Bonded Explosives with a Tabletop Microscope; Portland, OR, USA, 2020; p 030027 and Zhang, W.; Salvati, L.; Akhtar, M.; Dlott, D. D. Shock Initiation and Hot Spots in Plastic-Bonded 1,3,5-Triamino-2,4,6-Trinitrobenzene (TATB). *Appl. Phys. Lett.* **2020**, *116* (12), 124102, with the permission of AIP Publishing.

The Dlott group showed that detonations can be produced on a tabletop in tiny samples of liquid nitromethane (NM), an example of a homogeneous explosive[1]. When a shocked explosive charge has a small diameter, planar shocks can be quenched by edge waves, which limits the run distance available for the shock-to-detonation transition (SDT). In NM we input powerful short-duration (4 ns) shocks that produced detonations over a run distance of less than 0.2 mm[1]. In the present work, we discuss efforts to produce detonations on a tabletop in a pentaerythritol tetranitrate (PETN) based plastic-bonded explosive (PBX). Unlike homogeneous explosives, in plastic-bonded explosives (PBX), the shock-to-detonation transition (SDT) can be strongly affected by microstructure, which can concentrate the shock energy in small volumes in various ways to produce hot spots[2]. In the present work, we sought to idealize the problem by minimizing the importance of hot spots using PBX charges having small particle sizes and minimal void volume. This study uses the tabletop shock compression microscope developed in the Dlott group, which produces planar shocks with laser-launched flyer plates, and has optical probes that measure velocities, pressures and temperatures with nanosecond time and micrometer spatial resolution[3]. The projectiles are 0.5 mm diameter aluminum flyer plates that produce 4 ns shocks, and our optical probes were focused on the center 0.1 mm of the shocked volume. We can estimate that the run distance before edge waves arrive is about 0.25 mm[1]. A detonation is a shock wave sustained by heat and pressure-generating chemical reactions. These reactions, to an observer moving at the detonation velocity, have a reaction zone that appears unchanging in time, where the reaction zone refers to the region between the von Neumann spike (VNS) at the leading edge of the detonation and the plane where the shock drops to sonic velocity, called the Chapman-Jouguet plane (C-J plane). Ordinarily, this is in reference to charges greater than the critical

diameter for edge wave quenching. However, despite the small scale of these experiments, we can produce microscopic detonations that share many commonalities with kilogram-scale detonations. In NM, for example we showed that our microscopic shocks had the same velocity, VNS pressure, C-J pressure and reaction zone length and duration as seen in many prior measurements and theoretical studies[1]. Even though these shocks do not propagate long distances (>300 μm), they are useful for studies of microscopic mechanisms of SDT, since the material immediately behind the shock front in our microscopic detonations is in the same state as in a kilogram-scale detonator. We studied a PBX produced in our laboratory, composed of 80% PETN and 20% Sylgard 182 binder[4]. This PBX has the same composition as previously-studied formulations denoted XTX-8003 (also similar to LX-13)[5,6,7]. To avoid confusion with these similar but not necessarily identical materials, we will denote the PBX used here as X-PETN. This extrudable paste can be used to produce arrays of hundreds of tiny cylindrical charges for high repetition rate studies of SDT. We assume our X-PETN has similar properties to XTX-8003, which has a known unreacted Hugoniot and equation of state[5,7].

7.2 Experimental Methods

7.2.1 X-PETN Preparation

The PBX charges were made as previously described in other publications[4,8], and characterized with scanning electron microscopy, X-ray computed tomography (CT) (Fig. 1e), and optical profilometry (see appendix D or Table 7.1). The PETN used here is prepared by crash-precipitation. PETN is saturated in acetone solution (15 g PETN/100 mL Acetone)[6], then DI water is rapidly added to the solution to yield a fine powder. Figure 7.01a shows an SEM micrograph of some PETN powder, it usually forms needle-like crystals averaging 10 μm length across the major axis. The number-based particle size distribution from image analysis of several powder

micrographs is shown in Fig. 7.01b. The powders actually used in experiment are expected to be finer due to press extrusion, which tends to reduce the quantity of large particles beyond 50 microns.

A Sylgard stock solution is prepared by mixing ~80 mg/mL of Sylgard 182 in hexanes. Doing this allows the mixture to be easily stirred with PETN powder. PETN powder is added to equate to 80 wt.% PETN and 20 wt.% Sylgard 182 base compound. The mixture is stirred for ~3 hours in a fume hood to allow the hexanes to vaporize. The mixture is manually kneaded to homogenize. To press out the voids, the mixture is extruded through a hydraulic press *via* a pellet press. It is pressed to 2000 pounds, then kneaded once more to ensure binder is evenly distributed. Hydraulic press extrusion is important to mention because it was previously shown that this step dramatically reduces hot spot temperatures in X-PETN[8]. When applying cross-sectional SEM techniques demonstrated in Chapter 3, it was proven that this is partially because the particle size distribution is reduced, resulting in closer packing with fewer packing inefficiencies (see Ch 4). Figure 7.02c depicts a cross sectional image of 80 wt% PETN and 20 wt% epoxy (Loctite Abelstik 24), an effective X-PETN analogue material for imaging purposes (see Chapter 3 for more detail). Both by CT scan and cross sections the X-PETN is close to homogenous with only some sub-micron scale voids across the sample. The density was 99 ± 3% of the theoretical maximum density (1.53 g/mL)[8]. Finally, since we assume the material to be similar to XTX-8003, we utilize its known the Hugoniot relation[5,7]:

$$Us = 1.49 + 3.30u_p \qquad (7.1)$$

a detonation velocity of 7.30 km/s and a detonation pressure of 17.0 GPa.

7.2.2 Shock Compression Experiments

This extrudable material was packed into 1 mm diameter sample wells ranging from 30 μm to 250 μm deep using a Teflon spatula. Due to limitations of our well preparation methods, we could not make sample charges thinner than 30 μm. The target arrangement is depicted in Figs. 7.02. Unless otherwise stated, the flyer plates used are 25μm aluminum (Al-1100) foil, measuring ~500 μm in diameter. Based on data of XTX in literature, 1-mm diameter X-PETN cylinders are above the estimated failure diameter. However, past the 250 μm depth the exit shock waves may not necessarily be treated as totally 1-dimensional inside of the PDV probing region. When we probe the shock profile with PDV, we use windows with the thin (100 nm) Au mirror (Fig. 7.02c), and when we measure optical emission, we use windows with no mirror. The optical pyrometer is an emission spectrometer which measures spectral radiance from 450-825 nm at 0.8 ns intervals[9] (also see Ch. 2.6.2). We previously showed the X-PETN emission spectra are primarily thermal in nature.[4]

7.2.3 Using PDV to Probe Shock Waves

Placing a 100-nm Au-coating on the bottom surface of the sample, the interface between X-PETN and the glass window becomes highly reflective to the 1550 nm PDV beam. In this case, the shock wave will be used to interpret the mechanical work performed on the glass by tracking the particle velocity of the glass surface at 1) different flyer velocities with a constant X-PETN thickness and 2) different X-PETN thicknesses and constant flyer velocities. From the shock Hugoniot, shock velocity of glass can be derived. Based on this information, both pressure and flux can be calculated[10]:

$$J(t) = \frac{1}{2}\rho_0(U_s u_p)u_p = \frac{1}{2}\rho_0\left(Au_p^2 + Abu_p^3\right) \quad (7.2)$$

The time integral yields fluence

$$\phi(t) = \int_0^t J(x)dx \quad (7.3)$$

Figure 7.03 is a scheme of the workflow used to interpret PDV data according to these equations. An interferogram is interpreted into a particle velocity of glass, usually using fringe counting (or Fourier Transform in lower SNR scenarios). The velocity history is converted to fluence using equations 7.01 and 7.02 and the peak value as $u_p(t) = 0$ is crossed is used as the fluence. This integration is done individually then averaged to retain statistics.

7.2.4 Emission Pyrometry for Detonation Experiments

Emission pyrometry is used to track the reaction progress of the X-PETN charge. Unlike previous chapters involving deflagration, which occurs over several microseconds, reaction progress within a detonation is mostly complete inside the reaction zone. This means most of the emission occurs over tens of nanoseconds at most.[11,12] The rapid burst of energy created by a detonation wave was previously shown in liquid nitromethane, an optically transparent material.[1]

However, X-PETN is quite opaque even at 30 μm-thick, which makes interpretations more challenging. These problems include how to measure time-zero for graphing, how occlusion affects early time emission data, and how emission temperature is most appropriately determined. The question of timing is simple linear math, there are a few ways to determine this. Time of flight estimates taken from PDV usually are performed on empty Kapton wells with precisely measured depths. If the flyer plate is allowed to fly to terminal velocity before impacting the sample, the time of impact can be calculated using the time of flight in an empty well, $t_{f,0}$ by:

$$t_{impact} = t_{f,0} - \frac{L_{sample}}{v_f} \quad (7.4)$$

The emission pyrometer is synchronized to the moment of flyer launch, which means during data analysis time zero can be approximated as t_{impact} with respect to the moment the

flyer launches. In practice, these estimates usually prove true to a precision of $\pm 3\ ns$. The sources of error will be enumerated in the next sub section, but most of it is caused by the imprecision of the X-PETN extrusion process.

The question of opacity, however, is less straightforward. During the detonation process, the reaction is proceeding simultaneously in time and space. The PETN reacts fully over less than 10 ns while the shock wave is travelling at 4-7 km/s. For the case of 30 μm deep X-PETN, this can be considered instantaneous. For thicker samples, care must be taken when interpreting radiance data in the nanosecond range; fully reacted material will be emitting through a layer of unreacted material. Previous experiments verified that the 5*RMS rising edge of the emission peak corresponds closely to time of flyer impact (see Appendix F), the 10%-90% rise time will change as a function of input pressure and thickness. In the case of a 33 GPa shock, or ~4 km/s flyer impact, this will change from 3 ns through 30 μm to 12.5 ns through 255 μm of X-PETN, representing the affect of occlusion during early emission. This will also lower the radiance flux dramatically as a function of thickness, meaning that approximating radiance as free energy will no longer hold if comparisons are made between two thicknesses of materials.

7.2.5 High Speed Photography

To provide qualitative information on how the emissions of X-PETN is changing over time, a high-speed gated camera is used. These experiments were performed using a single-frame intensified CMOS camera (Andor iStar) with an exposure time of 5 ns. By directing the output emission into this camera, a 2-D spatial map of the luminous reaction front of X-PETN can be viewed with 5 ns resolution. Instead of previous chapters which use a multi frame camera for one single experiment, these ‘movies’ were produced by repetitively acquiring single images on fresh

charges being shock compressed. Experimental data verifying the time resolution of this camera are found in Appendix F.

7.2.6 Error Analysis

Unless otherwise stated, shock waves are signal averaged over at least 20 shots. This provides testament to the consistency of the shock responses and trends shown in these studies. Shock waves produced by these explosives are generally much less sensitive to small inconsistencies in microstruture, due to them already being so homogeneous compared to the HMX PBX samples.

The surface roughness and well thickness was estimated by optical profilometry on a sub-sampling of filled XTX wells. A laser microscope (Keyence VK-X1000, 10X objective) was used to measure the relative height of the extruded sample, the Kapton wells themselves, and precision of depth estimates. The results are shown in Table 7.1.

Table 7.1. Profilometry results on a sub-sampling of X-PETN filled Kapton wells. It shows how shallow samples tend to be overfilled and deep samples tend to be underfilled.

Listed depth (um)	**Depth of Empty Well**	**X-PETN-Filled depth**
30	29.02 +/- 0.44	40.6+/- 10.22
65	66.230+/- 1.93	69.63 +/- 4.97
90	93.07 +/- 0.44	91.72 +/- 5.9
165	165.1 +/- 0.73	164.54 +/- 9.8

The surface roughness and thickness accuracy of sample preparation is inversely proportional to the thickness of the sample: the thinner the sample the harder it is to make totally level. As a result the 30 μm samples will exhibit the most thickness error.

For these experiments, X-PETN is totally opaque to the PDV probe, and therefore velocity tests are performed on empy, transparent spots with similar flight times to the experiment. Flyer velocities generally are consistent to within 3% of the target velocity. This means for a reported 4 km/s flyer speed it is expected to actually be 4 ± 0.13 km/s. This level of precision is more than sufficient to reach the conclusions made in this chapter.

Unlike the studies performed on liquid NM, because the sample is opaque, shock velocities need to be inferred rather than directly measured. The results of these measurements will be reported but not heavily leaned upon due to the level of uncertainty involved.

7.3 Results

7.3.1 Velocity Dependence at 30 Micron Depth

Figure 7.4 shows the temperature profiles of the 30 μm thick charge with different flyer velocities averaged over samples sizes of at least 20 duplicates. The earliest time we show is 10 ns because that is about the time the shock has transited the entire PBX charge. Early time signals exhibit relatively high noise but are still assumed thermal. The initial temperature, about 4500K and the final temperature, about 2800K, do not change much with impact velocity. However, the highly stochastic nature of the initial emission temperatures results in significant spreading of the experimental temperatures in the first emission traces. The cooling rate, the rate at which the spectral temperature drops from 4500K to 2800K, however. At 3.1 km/s and below this cooling takes about 200 ns, and at 3.3 km/s and above it is much faster, about 25 ns. In previous work, we concluded the 4500K traces are from hot spots and, based on the graybody emissivity, the initial hot spot density was roughly 10-20% at the highest impact velocities[8], the rapid cooling results from volume expansion of the PBX, and the 2800K temperature results from combustion of X-PETN outside the shocked cylinder. This timeline is represented in Fig. 7.5.

High speed camera data of X-PETN charges, shown in Fig. 7.6 appears to corroborate this finding. Hot spots are visible in the first 5 ns, followed by a uniform luminous front the same diameter as the flyer plate. Then a black formation coming from the center outward is visible immediately after, likely a result of product gasses creating a void in the middle of the sample. This simultaneously makes a void in the sample and cools the area enough to no longer emit light at the same intensity. This expansion continues over the next several tens of nanoseconds.

Figure 7.7a shows how different amplitude 4 ns shocks propagate through our thinnest charges, 30 μm of X-PETN. When the impact velocity hits 3.5 km/s or approximately 25 GPa, the spike amplitude increases and the tail extends to longer time, while the output shock fluence exceeds the input energy of the flyer plate. The shock fluence over different velocities is shown in Figure 7.07b. Increasing the impact velocity from 3.5 to 4.5 km/s does not increase the spike amplitude or pressure. This is consistent with the shock energy exiting the glass being mostly from the chemical energy being released in PETN. Residual mechanical energy from the flyer plate is likely dissipated from a relief wave and the shock wave spreading in the transverse direction.

7.3.2 X-PETN Depth Dependence at Constant Shock Pressure

Figure 7.08 shows how the shock produced by one of the higher-velocity impacts (4 km/s) propagates through the X-PETN out to at least 255 μm. The spike propagates without loss to the end of the run. The tail, however, grows with distance, although measurable growth stops at 255 μm. Figure 7.09 shows the time-of-flight approximations for shock velocity show this reaction front travelling through different depths of materials. It is around 3.4 ± 0.25 km/s across 30 microns and gradually increasing as a function of charge thickness up to 6.8 ± 0.8 km/s at 255 μm. This is well above the bulk sound speed of unreacted XTX-8003, but still short of the literature detonation velocity of 7.3 km/s[6], especially in the shorter distances. Section 7.2.3 mentions some source of

error for these time-of-flight estimates, which will tend to be more dramatic at shorter distances. However, there could be many reasons for the discrepancy between literature and experimental data. One is the fact that X-PETN created in the lab is not identical to XTX-8003 created in a factory. If the mechanical properties of the PDMS are different to factory conditions, i.e., the curing conditions vary, this could materially impact shock velocity as well. Finally, lower shock velocities were also noticed in time-of-flight measurements for NM detonations. The difference was attributed to a failure in extrapolation of the logarithmic 'Pop Plot' to predict nanosecond detonation kinetics[1]. Thus there may be some rate limiting behavior in this time regime[1]. This is not a phenomenon that will be explored in this dissertation.

7.3.3 Measuring the Chapman-Jouget Plane in Experimental Data

In Chapter 1 the concept of a Chapman-Jouget (C-J) plane is discussed in greater detail. The concept refers to the spatial plane inside a detonating material in which mass flow is sub-sonic with respect to the detonation wave. That is, any reaction that occurs behind this plane are too slow to contribute to the detonation wave. Measuring the pressure of this point is often indicative of reaction kinetics. For example, the distance between the initial spike and the C-J plane, known as the reaction zone, is dominated by the kinetics of autocatalytic breakdown int the explosive.[11] In this case it acts as a litmus test for whether the material deflagrating is potentially developing a detonation state, as was shown in thin nitromethane samples[1,12].

The exact values of the C-J plane are usually only given as a pressure, the explosive in this state is a combination of solid and gas-state intermediate materials, this makes calculations of glass particle velocity more complicated than unreacted XTX. The Jones Wilkins-Lee (JWL) equation of state (for near-ideal explosives) of these materials must be employed based on the known properties of XTX.[6,12]

There are literature values for XTX-8003 Hugoniot, the product equation of state and detonation velocity of 7.3 km/s[6,7]. Based on these values the particle velocity of the CJ plane interacting with the glass witness is predicted be at 1.55 km/s. It should be noted that the data used for this prediction was collected on kilogram scale experiments. The exact calculations for this can be found in Appendix E.

In a traditional run to detonation experiment, the pressure decay to exhibit a discontinuity at the particle velocity associated with the C-J plane. Two factors that make this difficult to observe are the short duration of shock support and the effect of averaging shock pressure graphs. Brief discontinuities can be seen on some individual interferograms. Shown in Fig. 7.10 is an interferogram of a 560 μm deep X-PETN charge at 4.0 km/s. A clear plateau is visible, the long distance allowing the detonation to potentially stabilize, however this signal is inconsistent from shot to shot. There is some evidence that this could, in fact, be a traditionally defined C-J plane. At shorter length scales however, the short duration places this on the very edge of our velocity and time resolution.

There is precedent to address the problem of shock support, however. It has been observed in other thin-foil initiators that a second-order discontinuity will be observed at the end of the reaction zone. If the pressure wave is evaluated over several run distances, the post-reaction zone gradient will begin to fall as a function of distance. Fig. 11 shows this occurring. The effect is made more prominent by the lack of shock support. Because of this, Fig. 7.11a, performed on an 18 μm flyer plate (at higher speed to compensate for lack of energy) shows a larger negative slope than for the typical 25 μm aluminum at 4 km/s in Fig. 7.11b. Figures 7.10 and 7.11 serve as evidence that there could possibly be a C-J plane inside the X-PETN in the particle velocity range of 1.5-1.7 km/s. This matches the prediction of the C-J plane from available data on XTX samples.

7.3.4 Predicting the Von Neumann Spike

Inside the Zel'dovich von Neumann-Doring framework of detonation waves, the leading wave of the material is compressed to a pressure-volume state much higher than the C-J plane to induce a fast reaction to propagate the wave. This is referred to as the von Neumann spike. This state can be predicted using a P-u_p diagram of the unreacted material. The initial state of the unreacted XTX can be connected to an estimate of the state of the von Neumann spike by the Rayleigh line of D = detonation velocity.[12,13] Based on available data on XTX-8003, calculations predict this value at 25 GPa.

This prediction coincides with observations that the X-PETN shock response transforms to a detonation wave after reaching shock pressures of 25 GPa. This is interesting because it appears that for these thin foils with 4 ns shock durations, holding the VN pressure for 4 ns is sufficient to develop a detonation wave over short distance (within 30 μm run distance) very quickly (within 5 ns). It is likely beneficial that the reaction zone of PETN is <10ns, which is relatively short compared to other high explosives such as HMX, CL-20 or TATB.[11]

7.3.5 Conclusions on X-PETN Shock to Detonation

We can summarize our most important results as follows. Flyer impacts above 2 km/s creates high initial temperatures around 4500K, and these temperatures appear to be independent of flyer velocity. The high temperatures rapidly cool to 2800K, and the already rapid cooling rate increases dramatically above 3.3 km/s. The 4 ns input shock in X-PETN produces a shock with a spike and a tail. The spike amplitude does not increase with impacts above 3.5 km/s, and the spike propagates without losing amplitude out to at least 0.56 mm. There is evidence to say that this could, in fact, be attributed to a detonation forming in the thin explosive, but we cannot conclude it has fully reached steady state detonation in this short time after initiation. Within the framework

of the nonequilibrium Zel'dovich von Neumann Doering (ZND) model, [14,15] the initiating pressure spike pressure is congruent to predictions of the Von-Neumann (VN) spike for X-PETN at flyer velocities of 3.5 km/s and above, also corroborated by lack of observed pressure increase when raising the impact velocity up to at least 4.5 km/s. Further, the increase in cooling rates seen in samples impacted above the 3.5 km/s threshold support the idea of a large volumetric expansion along the gas product isentrope. However, time of flight approximations for shock velocity are still well short of literature values for a steady-state detonation in this material. providing evidence that we are clearly seeing chemistry evolving to sustain the initial shock front in these explosives. Though we cannot conclude that these samples exhibit proper kinetics to reach a steady-state detonation in such short times or distances. At shorter times we do see ignition that produces 4500K hot spots, but even at the highest flyer velocities used here, 4.5 km/s, the hot spot density was small, 10-20%.[4] Such a hot spot density will eventually cause the entire sample to react.[16] However, at these high-pressure, nanosecond pulse duration experiments, it remains unclear if shock initiation mechanisms are homogeneous or heterogeneous in nature. To answer these questions, we propose modifying the porosity of the model explosive to view changes in reaction kinetics. Using longer shock durations, such as the 10-15 ns range, will likely also alter shock initiation kinetics and limit axial expansion of the reaction to enrich our discussion of the shock-to-detonation process observed in these experiments.

7.3.6 Modifying the Porosity of X-PETN

Porosity is known to be a large contributor to the formation of hot spots upon shock compression. When a pocket of gas is compressed adiabatically it will produce very high temperatures (4500K and above).[8] These could possibly contribute to the sensitivity and reaction kinetics of a shock to detonation.[16] It was proven in previous studies that press extrusion reduces

the presence of micron-scale pores or voids, dramatically lowering the initial temperatures during shock experiments.[8] A CT scan of unpressed X-PETN can be found in Fig. 7.11a, exhibiting pores on the order of several microns and producing > 4500K temperature transients over 10s of nanoseconds, compared to the < 10 ns seen in nanoporous X-PETN. However it is an open question whether this could possibly increase the energy output of the shock.

In theory, since the hot spot model is traditionally considered a much slower process than the shock to detonation process seen in this chapter, it would have a minimal effect on the output shock wave. To test this, a 90 μm deep sample of X-PETN was made without press extrusion and compared to a 90 μm sample with press extrusion to remove macroscopic pores. For both samples at least 20 individual shots were taken. The pressure was chosen at 4 km/s or ~33 GPa with a 25 μm Al-foil, similar to previous experiments. The pressure was chosen to be well above the threshold to avoid possible difference in the ignition sensitvity and focus only on energy output. The result is shown in Fig. 7.11b. The shock fluence of porous X-PETN is consistently and significantly lower than pressed, nanoporous X-PETN.While the former produces significantly more excess heat, it appears to come at the cost of soaking up mechanical energy produced by the propagating shock wave. While it can maintain a similar spike pressure, it is less capable of holding that pressure for very long, indicative of even lower reaction progress inside of the reaction zone. From the standpoint of energy fluence, sub-micron pores in materials perform result in far better performance than micron-scale pores. The extra heat produced by hot spot generation is, as predicted, ineffective at shifting reaction-zone kinetics. Hot spot models of shock to detonation, which mostly rely on heat conduction phenomena, is far too slow (100s of nanoseconds in PETN or HMX-like thermal conductivities) to match the speeds of molecular decomposition occurring inside of PETN to propagate the shock wave.

7.3.7 X-PETN Shock Duration Dependence

A serious limitation of the shock compression microscope is the vanishingly small shock duration relative the the micron length scale of the XTX charges. The ability for a detonation wave for form depends both on the chemical energy released from the intial pressure spike and the ability to maintain a high PV state long enough for the reaction to become self sustained. The interplay between shock pressure and shock duration is not new. Walker and Wasley theorized a 'critical energy' fluence parameter for shock to detonation relating the shock pressure P to the shock duration τ (defined as full-width half max pressure) by the following formula[17]:

$$E_{critical} = \frac{P^2\tau}{\rho_0 U_s} = Pu_p\tau = constant \qquad (7.5)$$

Unsurprisingly, this model is also phenomenological, and while verified for durations down to <1 ns, seems to only be verified for lengths far longer than the < 500 μm run distances used in this chapter.[12,17,18] With a lack of *ab initio* methods to predict this critical energy, it serves little use to predicting the performance of new formulations or optimising explosives. Notably there appears to be no literature entries on $E_{critical}$ for XTX. It has been proven now that for $\tau = 5\ ns$, $E_{critical} = 25\ GPa\ \times 2.01\frac{\mu m}{ns} \times 5\ ns \sim 250\ GPa - \mu m$. By altering shock duration in the shock-to-detonation experimetns, two questions can be evaluated: If the shockwave being observed is a detonation then fluence output should be roughly independent of shock duration. Further, does this criterion hold up on the micron distance scale? This study only addresses the first question in the interest of verifying that a detonation is being observed.

Using the standard Al-1100 foils, 18, 25 and 37 μm thick flyer plates were made and impacted on X-PETN samples which were 90 μm deep. These flyers represent 3-ns, 5-ns, and 7-ns duration shocks, respectively. The limitations of the launch laser hamstring what shock pressures can be used for 37 μm flyer plates; 3.55 km/s is the maximum velocity available for that

thickness, which is still above the critical pressure for X-PETN so should be comparable to a 4 km/s impact. The exiting shock particle velocity history was measured and plotted in Fig. 12. The affect of shock duration appears minimal, with the slight increase in energy output for 37 μm likely being the consequence of the relief wave arriving later from the extra material thickness. This is further evidence that the chemically supported shockwave produced by X-PETN is a detonation.

In order to test the critical energy criterion and limitations of this theory, a wider range of velocity and flyer thicknesses are needed. The limitations on the shock compression microscope are threefold: the launch laser fluence and the transmission limits of the glass backing the flyer plate, and the limitations of thin foils. Chapter 2 has shown the limited range of available flyer thicknesses and their respective velocities. For testing critical energies, velocities well above 3 km/s are needed but cannot be reached for anything thicker than 37 μm, so thinner flyer plates would be necessary. Below 18 μm, however, aluminum flyer plates begin to disintegrate at the upper end of 3 km/s; because of this, basic assumptions of the metal being cold and 1-dimensional will no longer hold. The solution is a higher-fluence laser and analysis of different flyer window materials. The methods of solving this problem will be addressed in the next Chapter.

7.4 Application of X-PETN as a Booster Material

Deflagration of TATB has been studied in a previous chapter. Its burn dynamics can be dramatically changed through the microstructure of the crystals themselves[19,20]. It varies significantly compared to HMX or PETN: it's extensive graphitic crystal structure creates excellent thermal conductivities, making it easy to distribute heat. It's far from an ideal candidate to try to bring up to detonation pressures inside of a short distance. This, however, is an interesting opportunity to leverage the detonation wave created by X-PETN to engineer a shock-to-detonation experiment with TATB-based PBX.

7.4.1 Overview

The high explosive 1,3,5 triamino 2,4,6 trinitrobenzene (TATB)[21] is unusual among explosives for being insensitive to shock initiation while retaining high energy output. Due to its low sensitivity, studies on TATB explosives generally require large explosive charges or large guns for initiation. Here, we have been able to produce and study hot spots and thermal explosions, defined as rapid volume expansion driven by shock-induced heating, with high throughput on a tabletop, in TATB in a plastic-bonded explosive (PBX) form denoted X-TATB (TATB with 20% Sylgard 182 binder). The X-TATB can be fabricated in arrays of hundreds of 1 mm diameter explosive minicharges. We used laser-launched miniflyer plates (0.5 mm in diameter), which themselves were ineffective in initiating TATB, to initiate minicharges of a more sensitive explosive,[22] X-PETN, which produced shocks of sufficient strength and duration to initiate TATB. TATB is interesting and unusual for other reasons[23]: it crystallizes in an extensive planar hydrogen-bonding arrangement having a layered structure like graphite[21]; its reaction products include a relatively high concentration of mixed carbon–nitrogen–oxygen clusters, other spots, and nanodiamonds;[23] and it has a yellow color,[24,25,26] indicating blue-absorbing electronic transitions that complicate the problem of measuring reaction temperatures by Raman spectroscopy[24] or optical pyrometry.[26] Using our flyer plate X-PETN/X-TATB scheme, we could produce hot spots and strong explosions in TATB and study them in detail by high-speed optical and optomechanical diagnostics that include photon Doppler velocimetry (PDV), optical pyrometry, and 5ns videophotography.

7.4.2 Preparation of Two-Layer Explosives

Ultrafine PETN17 and ultrafine dry-aminated TATB[26] were fabricated into PBX with 20 wt.% Sylgard 182 binder. The procedure for both matches the procedures for X-PETN outlined in

Section 7.2.1. No recrystallization is performed on TATB due to its limited solubilities, and as such it is prepared as received (courtesy of Lawrence Livermore National Labs). We call these formulations X-PETN and X-TATB. The relatively high binder concentration makes the PBX extrudable, and so it can be fabricated into minicharge arrays [Fig. 7.11f]. Figure 7.11(e) shows the absorption spectrum of X-TATB, which was obtained using the Kubelka–Munk transformation on diffuse reflectance measurements. The X-TATB was pressed in a hydraulic press to a density >98%, as verified using x-ray computed tomography [Fig. 7.11(g)].[4,26] To fabricate two-layer arrays, we used 75 x 75 x 6.35 mm^3 Pyrex glass substrates. Onto a substrate, we placed a 40 μm-thick Kapton adhesive tape with an array of about 280 1 mm diameter holes. These holes were packed with X-TATB using a Teflon spatula. A 100 μm-thick stainless steel spacer with a complementary array of 1.5 mm holes was epoxied (Loctite Abelstik 28) to the Kapton layer, and the holes were packed with X-PETN, taking care to minimize gaps between the two layers. Figures 7.11(a) and 7.11(b) show a schematic for characterizing shocks produced by flyer plates or explosive minicharges in Pyrex glass windows. In those experiments, the windows were coated with a thin (100 nm) Au mirror, and the velocity profile of the explosive/window interface was monitored by PDV.[27] Knowing the material velocity imparted to the window, we can determine the shock energy fluence[10] (also see 7.2.3 and Fig. 7.03). This shock fluence is the time integral of the shock kinetic energy per unit area entering the window computed using the Pyrex Hugoniot[5] as described previously.[10,28]

7.4.3 Results

Figure 7.12(b) shows the shock output by 100 μm long X-PETN charges, and Fig. 7.12(d) shows the corresponding temperature profiles. These shocks have about the same peak velocities as the flyer plate shocks in Fig. 7.12(a), but have a duration (full-width half maximum) of about

25 ns. The shocks from flyer plate initiated X-PETN have a longer duration and greater energies than the 4 ns shocks from flyer plates alone. We experimented with using different length X-PETN charges keeping the flyer plate at its maximum velocity, 4 km/s. As shown in Fig. 7.12(c), the output shock energies from X-PETN did increase, lengthening the charge to 250 μm, but still longer charges showed no improvement since the shock loses planarity after 250 μm.[1] Since there was little improvement in lengthening the X-PETN charges past 100 lm, we used 100 lm X-PETN in all other measurements.

Figure 7.12(e) shows shocks from X-TATB initiated by X-PETN. We wanted to use thin X-TATB samples to minimize shock propagation delays. We ended up using 40 lm thick X-TATB, which was about the thinnest that made a good solid PBX charge. This thickness was also enough to block thermal emission from the X-PETN, and so the thermal emission we observed from the two-layer samples was entirely from X-TATB (*vide infra*). Figure 7.12(e) shows that when the X-PETN shock enters the X-TATB, the material velocity in the glass window slows from about 2.5 km/s to about 1.8 km/s. The X-PETN and X-TATB shock results are summarized in Fig. 7.12(f),whereweplot the shock fluence output into a Pyrex glass window from flyer plates, X-PETN, or X-PETN initiated X-TATB. A few error bars representing 95% confidence limits are shown. The flyer plate fluence nominally increases like the square of the velocity, but there is some deviation due to the mechanical response of the Pyrex window. The X-PETN or X-PETN initiated X-TATB fluences have a sigmoidal shape, indicating that they explode at a threshold of about 3.4 km/s. The fluence delivered by X-PETN is greater than just the flyer plate, and keep in mind that a lot of flyer plate fluence is due to the lower-amplitude longertime tail. The fluence delivered by X-PETN initiated X-TATB is a bit higher than the flyer plate alone, but less than the X-PETN. So, in the current arrangement, the X-TATB is slightly attenuating the shocks from X-PETN. Figure

7.13 shows X-TATB time-dependent radiance and temperature profiles extracted from the spectral radiance via graybody approximation.22,23 X-TATB was initiated by either the 4 ns shock from a flyer plate or the 25 ns shock from the X-PETN initiator. In order to deal with the problem posed by the time-dependent TATB absorption of the blue part of the thermal emission, temperatures in Figs. 7.13(b) and 7.13(d) were calculated using only emission in the red spectral region 650–850 nm, where, as shown in Fig. 7.11(e), TATB does not absorb.[26] The temperature points are the average of at least 25 shots, and the error bars indicate 95% confidence intervals.

When X-TATB is initiated by the flyer plate alone [Fig. 7.13(a)], the thermal emission was a burst lasting about 15 ns. The rise time of the thermal emission is caused by ~10 ns needed for the input shock to propagate through and breakout of the 40 μm-thick X-TATB peak, about 20 ns, some of the temperatures are well above 3000 K [Fig. 7.13(b)]. Based on previous pyrometric temperature measurements,13,24,25 3000 K is too high to be due to steady combustion, and so, during the first few tens of nanoseconds, we observed hot spots ranging from 2500 K to 3500 K. After the hot spot period, the temperature is always about 2500 K regardless of flyer plate impact velocity. This 2500 K is reasonable for TATB combustion. [19,20,26] So flyer plate initiation of X-TATB briefly produces hot spots followed by a much longer period of steady combustion.

When X-TATB is initiated by X-PETN [Figs. 7.13(c) and 7.13(d)], the radiance lasts longer and the hot spots are hotter (3500–4000 K) than with flyer plate initiation. The hot spot temperatures are about the same whether the X-PETN is delivering a lower-energy (<3.4 km/s) or higher-energy (>3.4 km/s) shock, which suggests that hot spot formation is more sensitive to the input shock duration than to shock strength, at least above some ignition threshold. The subsequent behavior is quite different with shocks produced by flyer plates below and above the X-PETN explosion threshold of about 3.4 km/s. With the lower-energy shock into X-TATB [e.g., 2.1 km/s

in Fig. 7.13(c)], there is no sharp peak in the radiance. Instead the radiance remains steady for hundreds of nanoseconds, but at a level quite a bit higher than with flyer plate initiation [Fig. 7.13(a)]. The steady value of the radiance in Fig. 7.13(c) indicates X-TATB combustion, rather than explosion, but the level of combustion appears higher than that with flyer plate initiation.

With the higher-energy shock input from X-PETN [e.g., 4.2 km/s in Figs. 7.13(c) and 7.13(d)], the radiance becomes a burst, lasting more than twice as long as with flyer initiation. Furthermore, there is an incredibly fast cooling process [Fig. 7.13(d)]that starts at about 30ns, where the temperature drops from 3500 K to 2000 K in 20 ns ($\frac{dT}{dt} = 7.5$ at 1010 K/s). Such a cooling rate cannot reasonably result from thermal conduction or radiation, and so it must indicate cooling in a rapid adiabatic volume expansion produced by an explosion.[4,29]

To alleviate concerns that the X-TATB thermal emission is contaminated by X-PETN emission passing through the X-TATB, we note that the temperature profile from the X-TATB [Fig. 7.13(d)] has significant differences from the X-PETN temperature profile [Fig. 7.12(d)]. If some of the emission originated from the X-PETN charge, the emission in Fig. 3(d) would onset sooner than observed. In addition, the time dependence of the rapid cooling indicating X-TATB explosion is different, as are the hot-spot temperatures and the longer-time combustion temperatures.

7.4.4 Discussion

It would be useful to have the ability to produce actual tabletop detonations in TATB using shocks generated by our flyer plates. Producing reproducible detonations on command, on a tabletop, would allow us to study the establishment of the reaction zone in real time,[1] probe how a detonation responds to external perturbations, and use the detonations for other experiments, for example, cornerturning experiments. 26 In order to create a tabletop detonation from a short-

duration input shock, the input shock needs to produce widespread ignition and an explosion within a geometry that allows the detonation to form before the shock loses planarity. Our group has been able to accomplish tabletop detonations in nitromethane (NM), a liquid explosive, using 4 ns input shocks whose pressures were a bit above the von Neumann spike pressure (the pressure at the leading edge of the detonation). Although initiation of NM began in hot spots, an explosion caused the hot spots to coalesce and uniformly ignite the hot volume within a few nanoseconds. The detonation was fully established after a run distance of 170 μm, while the detonation shock remained planar for over 250 μm.[1]

So far, however, it is unclear if we can produce detonations in X-PETN and has not been possible in X-TATB. We can estimate the velocities that would be produced by actual detonations in our Pyrex windows. The simplest way is to use the tabulated steady detonation velocity and the window and the unreacted explosive Hugoniot, but the steady detonation pressure against the window is actually generated by the mixture of product gases. In that case, we can approximate the equation of state of the product gases using a JWL (Jones–Wilkins–Lee) equation of state. (See Appendix E). The needed information is available[6] for XTX-8003, a commercial explosive with the same composition of X-PETN[7,30] but not for X-TATB, and so we used data for PBX-950219 that is 95% TATB. Our best estimate of the window velocity during steady detonation is 1.55 km/s for X-PETN and 2.5 km/s for PBX-9502 (it is likely lower for X-TATB that is 80% TATB), and these values are shown in Figs. 7.14(c) and 7.14(e).

With the X-PETN, Fig. 7.14(c) shows that we are not extracting all the energy from the explosive. With the X-TATB, Fig. 7.14(e) shows that we are not producing a strong enough explosion and we probably are not extracting all the energy. The incomplete energy extraction in X-TATB is, we believe, a consequence of the short duration of the input shock since TATB is

known to rapidly form clusters that retard the subsequent energetic reactions.[31] Since X-TATB reacts more strongly with 25 ns input shocks from PETN than with 4ns input shocks from flyer plates, longer-duration input shocks are most likely needed to fully initiate X-TATB. The incomplete energy extraction in X-PETN is, we believe, a consequence of the microstructure. As seen in Fig. 4(c), the shocked X-PETN microstructure creates both hot spots and colder spots, and with our short-duration input shocks, there is not enough time for the hot spots to ignite all the colder spots. We need to better understand hot spot growth[16] in these materials in order to overcome the incomplete ignition produced by our shortduration shocks.

7.5 Summary and Conclusions

In this chapter, it was established that a PETN-based PBX, XTX-8003, is an effective platform for shock to detonation experiments. When the material is subjected to pressures at or above the von-Neumann spike pressure, it creates a chemically sustained shock wave that travels at least up to 560 μm, whose energy fluence spikes far above the kinetic energy provided by the flyer plate alone. The spike pressure and C-J pressure observed in experiments match those predicted from literature[6,7], and the reaction zone is consistent with predictions from previous work.[11] Emission pyrometry and high speed photography of the autoemission revealed the rapid formation of product gas resulting in rapid, adiabatic expansion creating a drop in temperature. All of these factors combined provide compelling evidence that this chemically generated shock wave is in fact a detonation wave forming within 10 ns and 30 microns. Because of this rapid speed of reaction, the time and space resolution currently available on the shock compression microscope is insufficient to track the sub-detonation state likely achieved even earlier in the shock-to-detonation process. A thinner cylindrical charge of X-PETN would be required to increase time resolution of the experiment. The current methods utilize Kapton tape laser etched into cylinders,

a more sophisticated method of cylinder formation would be required to reduce the thickness even further. Possibilities include laser cutting thin metal foils, or photoresist lithography. The main reason to do this is to determine the run distance required for a detonation to form. When this was done in liquid nitromethane it was determined that the Pop plot model of pressure and distance to detonation dependence missed important rate limiting behavior in nitromethanes decomposition chemistry.[1]

Determining if the Walker-Wasley model of critical energy fluence holds at these micron-scale run distances would also enrich discussions on how reaction kinetics contribute to shock sensitivity. Most importantly, being able to compare these between different secondary explosives such as HMX or CL-20. These explosives are far less sensitive than PETN-based explosives, which makes studying shock to detonations on this time and distance scale challenging; 25 μm flyer plates either need to go above 5 km/s or thicker flyer plates, or higher duration shocks, need to reach at nearly 4 km/s. Neither of these are possible with the current laser-launched flyer plates. A discussion on making laser launched flyer plates will occur in the proceeding chapter.

The other option is to leverage the X-PETN as a booster material to initiate shock to detonations in far less sensitive materials such as X-TATB. This chapter showed, however, that while it dramatically increases the shock energy output by the X-TATB compared to a flyer plate alone, it comes far short of actually generating a detonation wave in the material. Rapid gas formation is observed but the fast reaction doesn't appear to be fast enough to sustain the detonation wave over 100 μm. This method could be explored in other materials, such as HMX or CL-20, which are less shock sensitive than PETN but far more sensitive than TATB. Furthermore, the 'booster method' is non-ideal compared to flyer initiated experiments since the use of an explosive booster removes the ability to throttle the input shock wave since the shockwave

produced by X-PETN is instantaneous with respect to the experimental time frame. Other options would be tuning the concentration of PETN in PDMS in order to reduce the shock energy.

This chapter has outlined how the shock compression microscope can be used to track shock-to-detonation phenomena in general, and prove that detonation waves can be formed and tracked in X-PETN. Furthermore the X-PETN detonation wave shows promise as a method to initiating harder-to-initiate materials in order to observe rate-limiting behavior and improve phenomenological models being used to predict shock-to-detonation in plastic explosives.

7.6 Figures

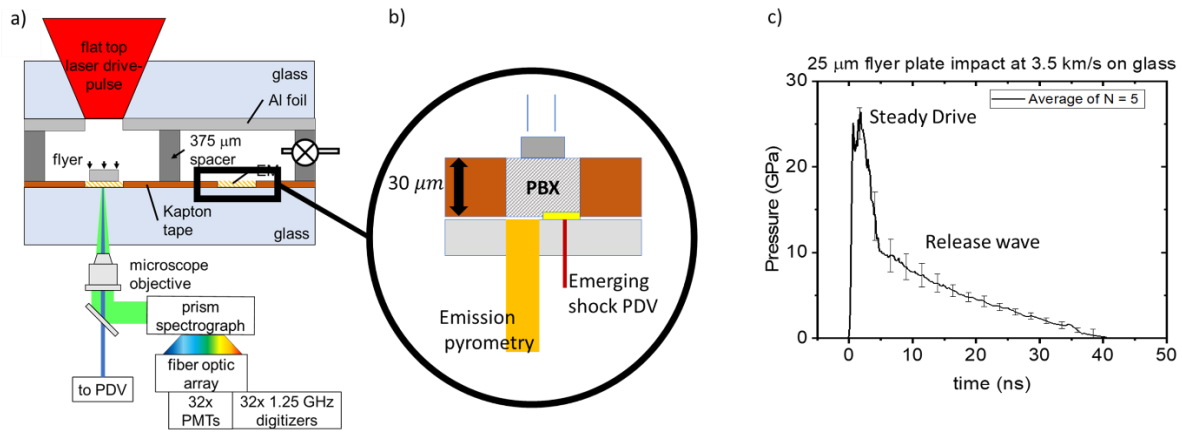

Figure 7.1 Diagram of the design of experiment (a) the shock compression microscope used, as described previously, with a Kapton tape layer creating cylindrical wells of X-PETN. (b) a thin layer of gold is placed at the glass-explosive interface to directly observe the particle velocity of an exiting deflagration or detonation shock, the kapton tape creates 30 μm deep cylinders of explosive. (c) An example of particle velocity of an aluminum glass interface coated in gold when shocked at 3.5 km/s, showing the drive to be about 4 ns.

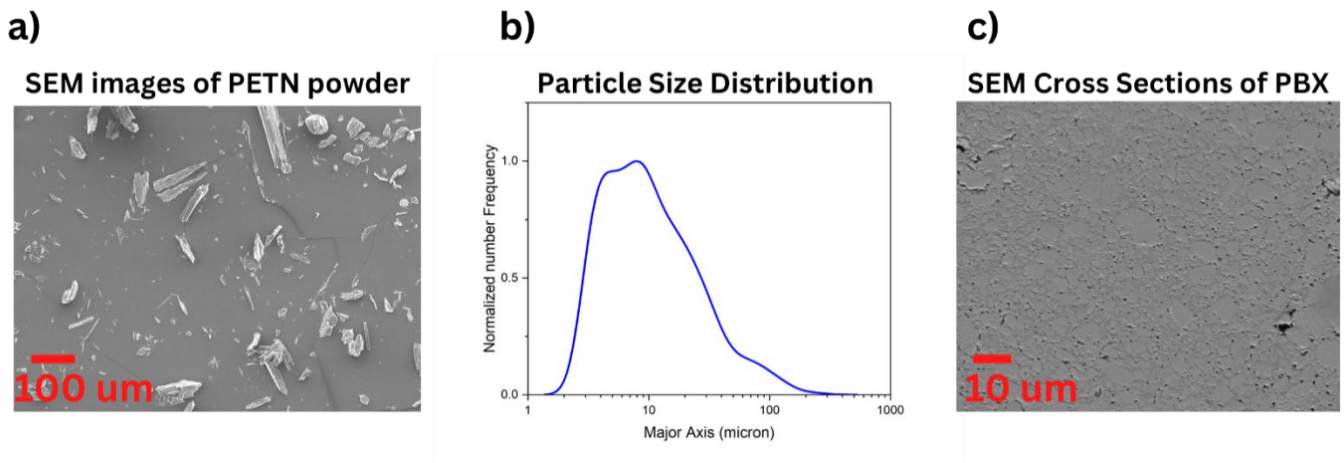

Figure 7.2 The Pentaerythritol tetranitrate (PETN) sample used in polymer bound explosives. (a) SEM micrograph of some of these powders, which form needle like structures, a combination of fine and large structures. (b) Number-based particle size distribution of PETN crystals used in this experiment. Note that due to observations of press extrusion in Chapter 4 that end particle size distributions will be biased towards <20 μm particles. (c) Cross sectional view of X-PETN using microtome and SEM imaging.

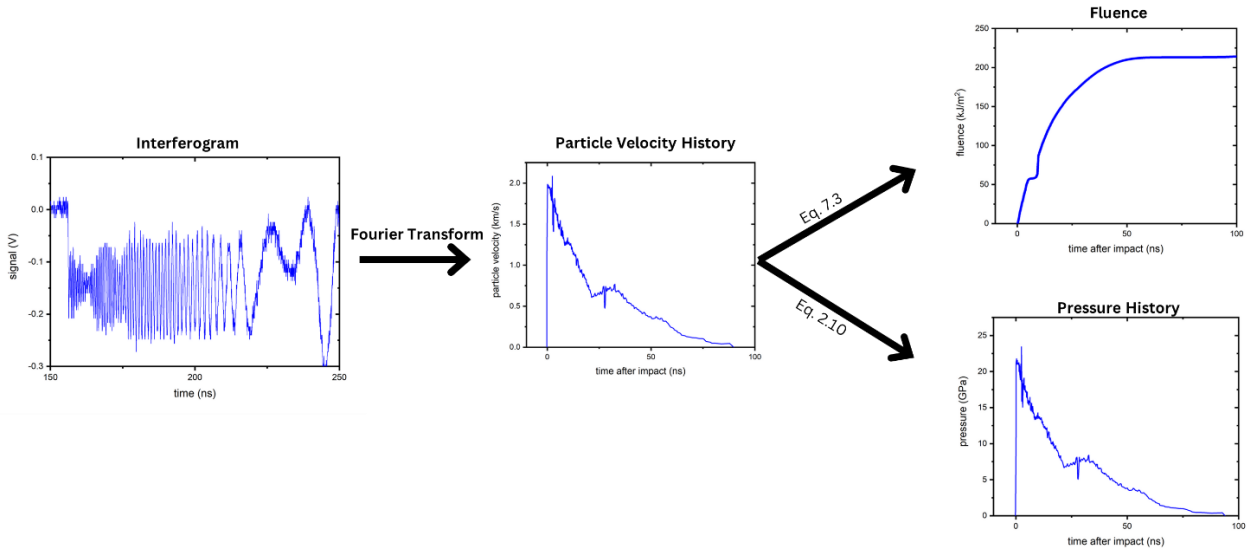

Figure 7.3 Diagram of the workflow used to generate particle velocity, pressure and fluence. An interferogram is Fourier transformed to a particle velocity, which is then converted to fluence (where the peak is recorded) and pressure, depending on which is appropriate in the context of discussion.

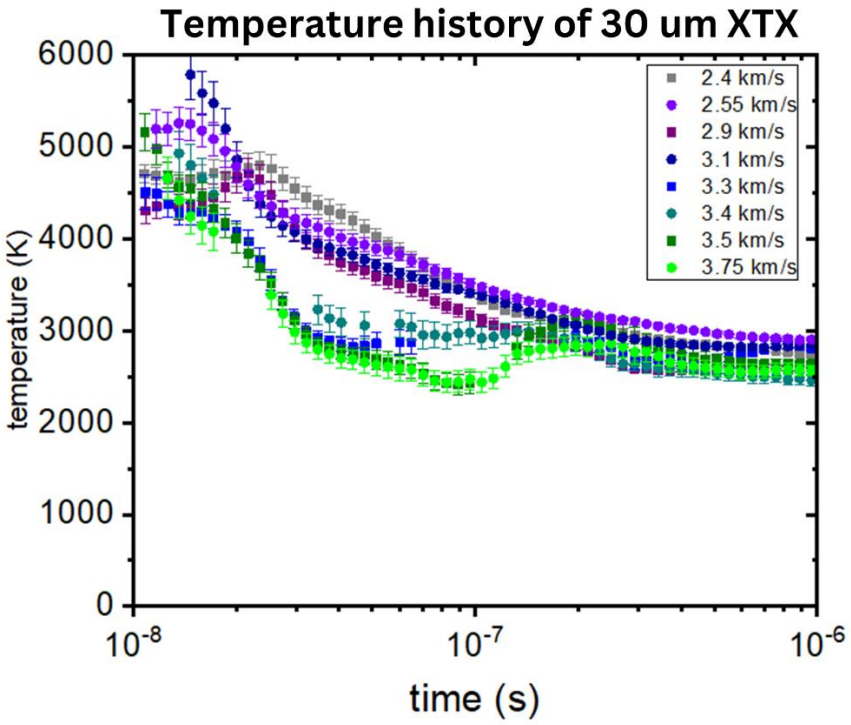

Figure 7.4 X-PETN time-dependent temperature history across several flyer velocities. Behavior is uniform up until about 3.4 km/s, corresponding to 26 GPa impact pressure, where a rapid cooling event can be observed.

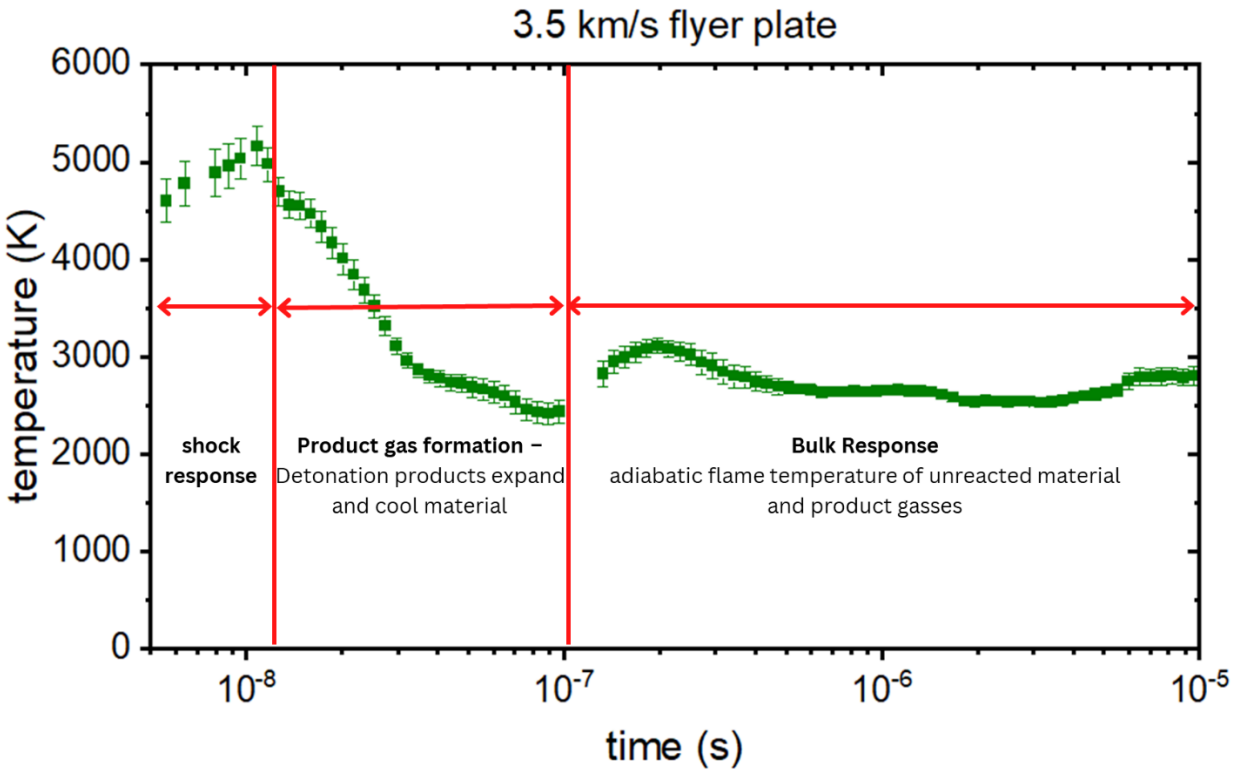

Figure 7.5 A breakdown of the interpretation for temperature histories of shock impacts above 3.4 km/s or 26 GPa. It is believed that an onset of an emerging detonation wave results in immediate adiabatic expansion to cool the emission temperature quickly.

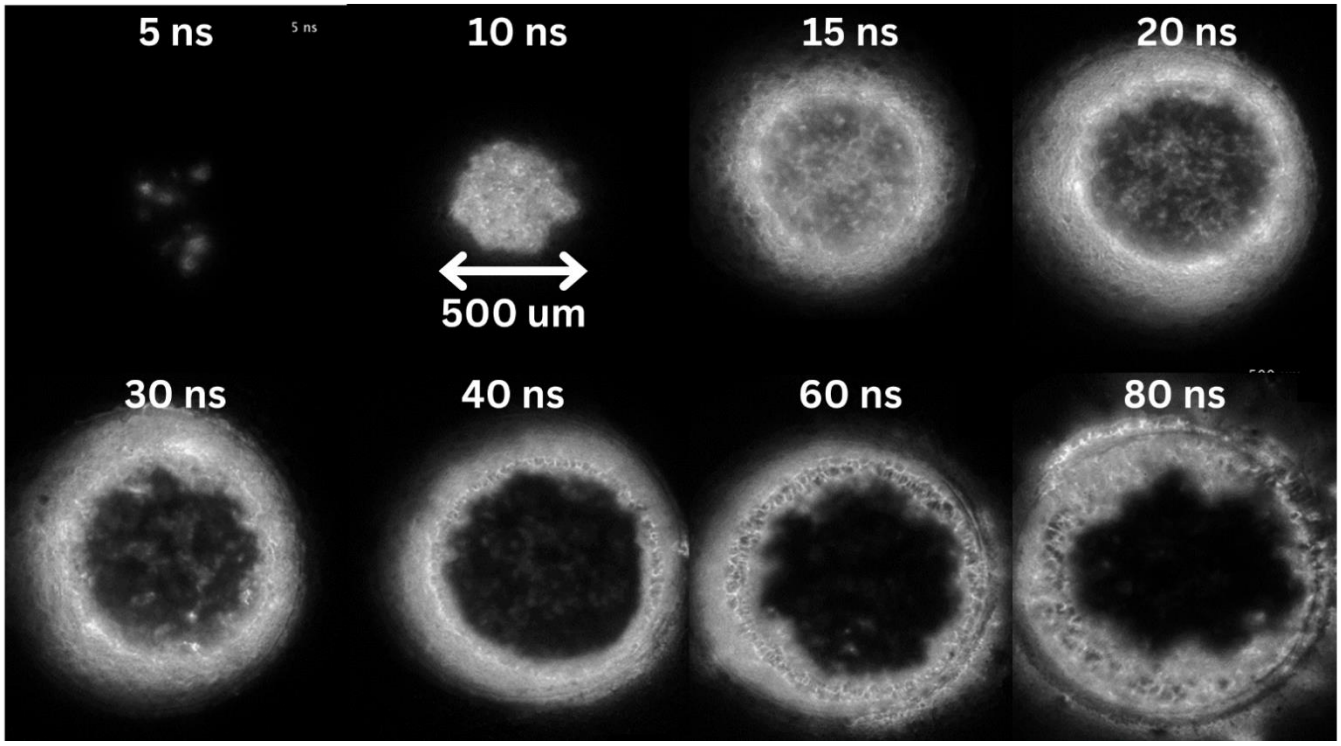

Figure 7.6 High speed photographic captures of the shock initiation timeline in the first 100 ns of X-PETN igniting. These are separate experiments stitched together to make one video. Initial hot spots can be seen immediately on impact, a uniform luminous front can be seen in the shape of the flyer plate, corresponding to the time where the shock exits the material. From there the light fans outward, then a black cloud rapidly takes over.

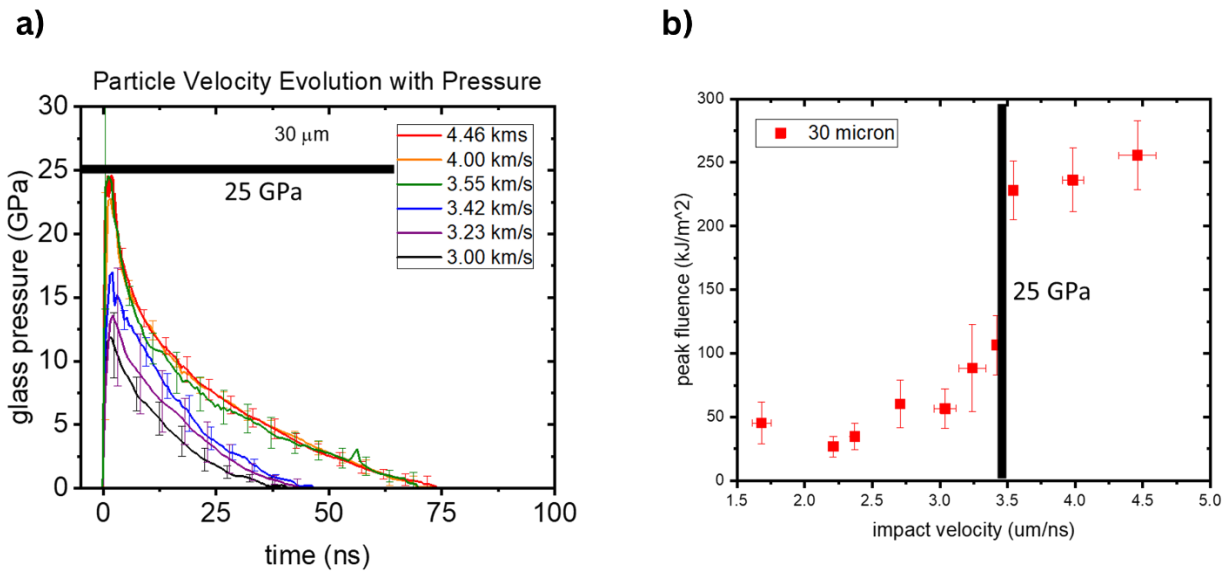

Figure 7.7 X-PETN shock wave pressure history at different impact velocities (a) and the peak fluence across different shock pressures (b).

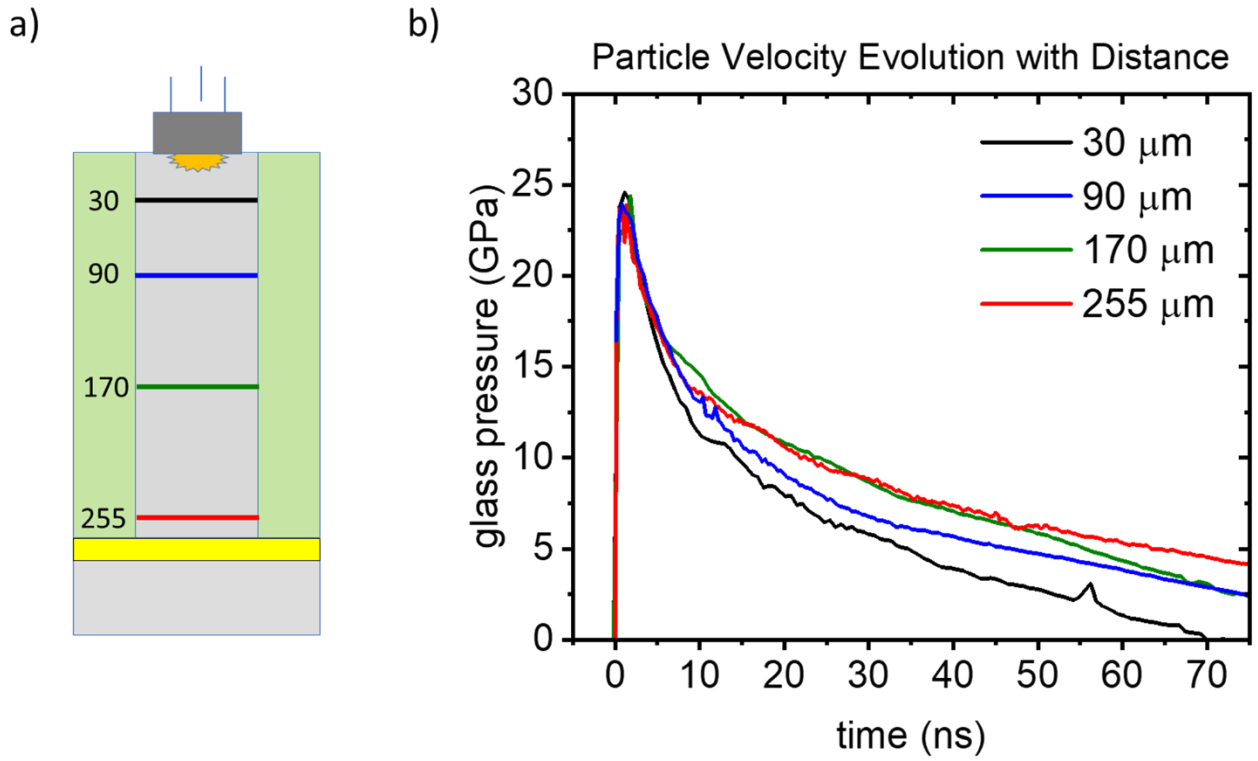

Figure 7.8 X-PETN shock wave pressure history over various lengths of X-PETN material. Different depths of X-PETN cylinders are created and observed at the sample-glass interface, representing pressure gauges at different points down stream from the initial shock (a). As distance increases, the slope of the shock pressure decay decreases (b), representing increasing distance from the rarefaction wave produced by shock reflections on the side and back of the cylinder and flyer plate respectively.

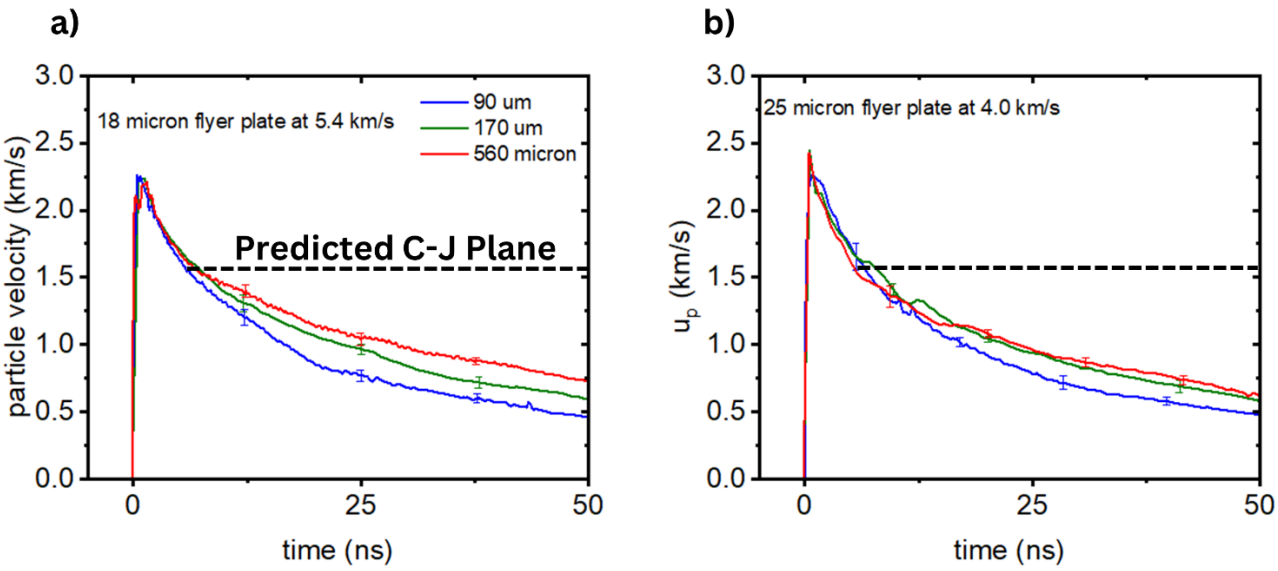

Figure 7.9 Length dependent particle velocity histories for two different thicknesses of flyer plates. (a) 18 μm flyer plates representing a faster approaching rarefaction caused by the thinner material. (b) 25 μm flyer plates, typical of most experiments in this chapter. In both cases the prediction of the CJ plate, where it is expected for length dependence to be emphasized, is pointed out at 1.55 km/s.

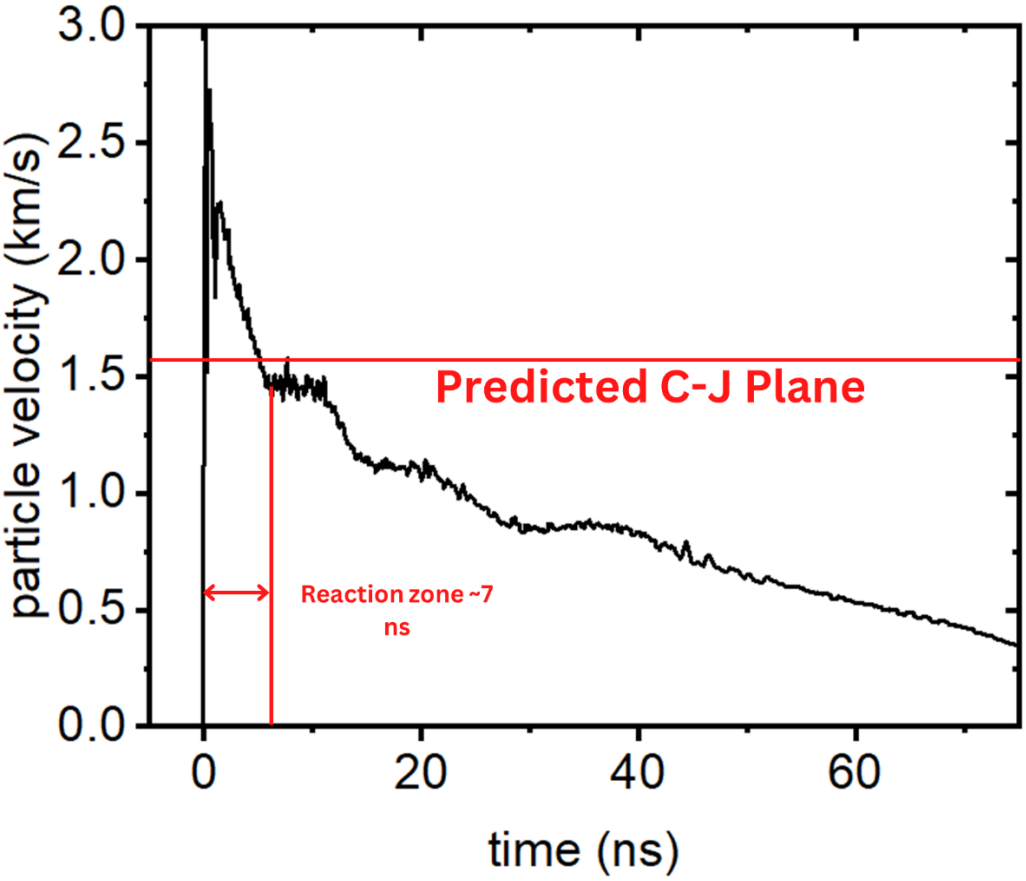

Figure 7.10 Example of X-PETN particle velocity history of a thick sample, showing a planar feature at ~1.5 km/s. This possibly shows resemblance to a ZND detonation wave.

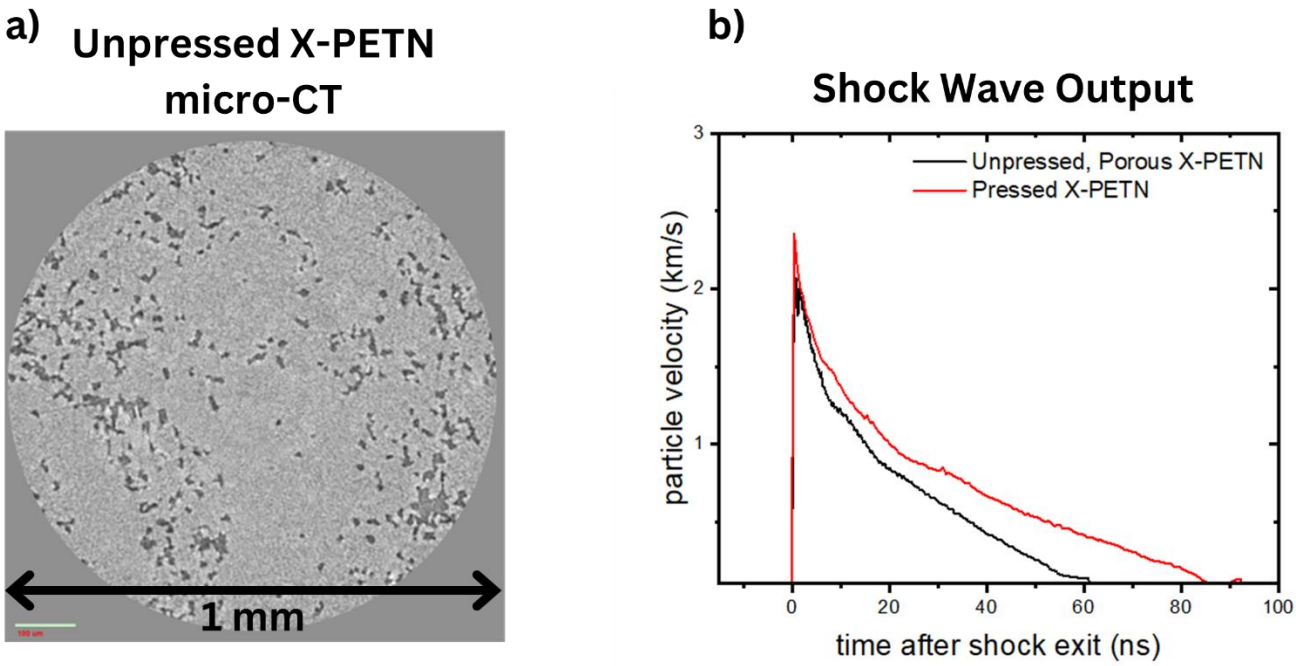

Figure 7.11 Effects of micron-sized pores on shock wave generation in 90 micron-thick X-PETN: (a)An X-Ray CT of an X-PETN well that hasn't been hydraulically pressed, expressing large void spaces. (b) When comparing shock wave generation to pressed X-PETN that has mostly sub-micron sized voids, the shock wave is significantly dampened.

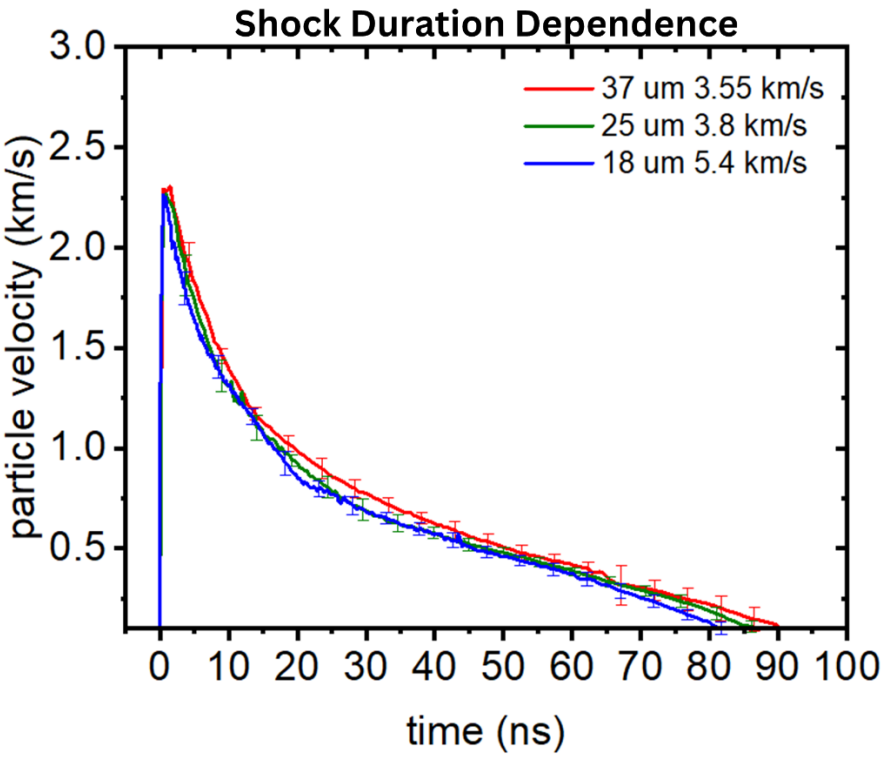

Figure 7.12 Shock duration dependence on shock wave generation of 90 μm-thick wells of deflagrating X-PETN. Three different particle velocity histories of three >3.4 km/s flyer plates of different thicknesses on a 90 μm-thick X-PETN sample.

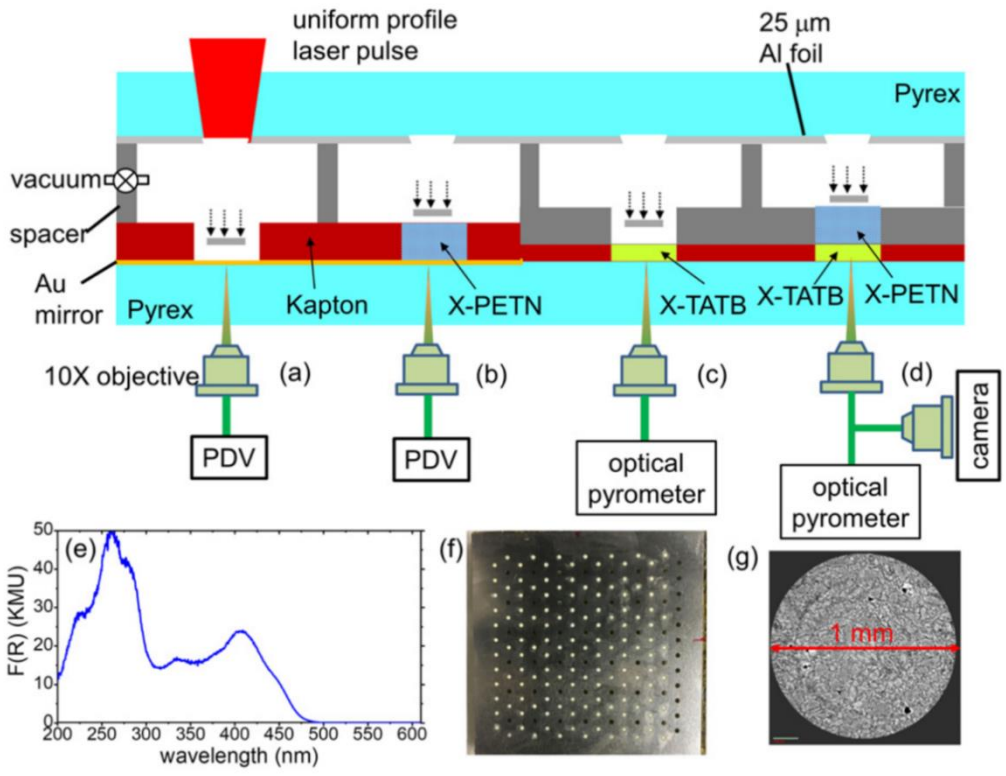

Figure 7.13 Diagram of TATB-booster experiment. (a-d) Cylindrical well design in order of increasing complexity. (b) 100 μm X-PETN, (c) 40 μm X-TATB (80 wt.% TATB, 20 wt.% TATB). (d) 100 μm X-PETN preceeding a 40 μm TATB layer. (e) TATB absorption spectrum, showing heavy blue absorption. (f) Picture of the two-layer sample array. (g) X-Ray CT of X-TATB samples used. PDV=Photon Doppler Velocimeter.

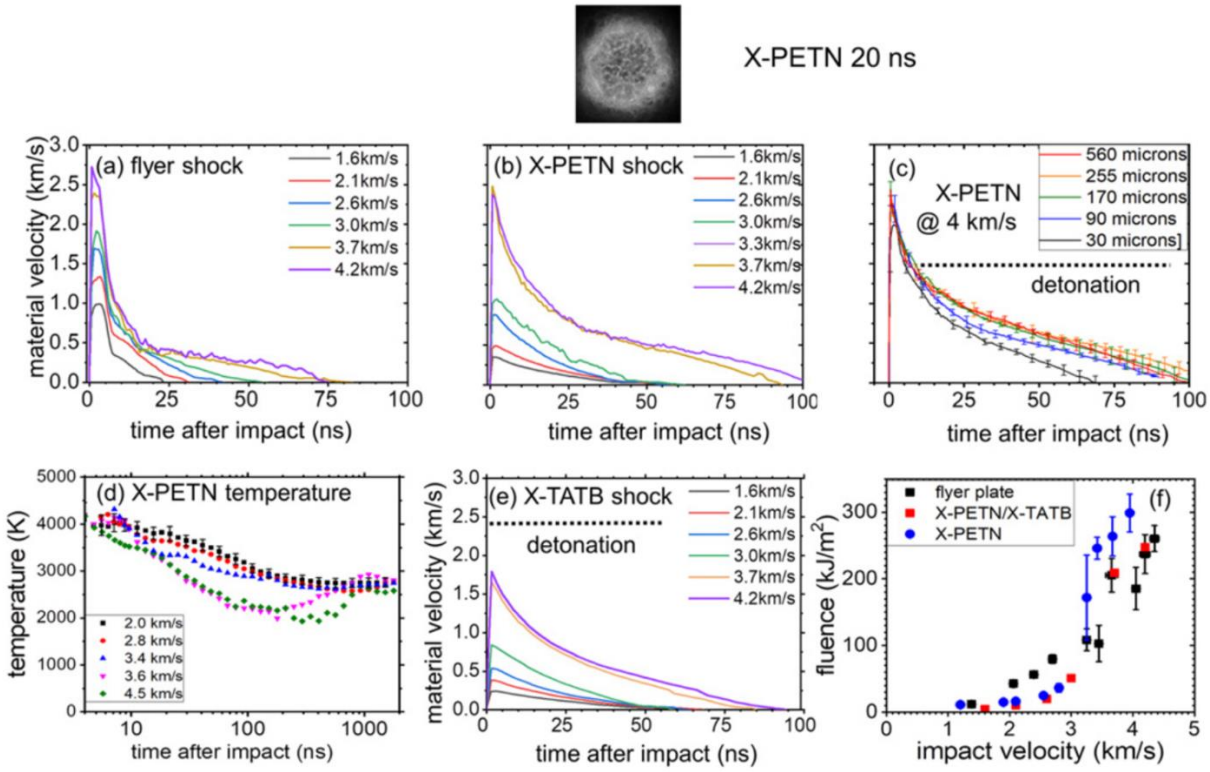

Figure 7.14 Particle velocity history comparison of shock waves in (a) empty samples, (b) X-PETN over different pressures, (c) 4 km/s (33 GPa) X-PETN depth dependence, (d) X-PETN temperature history. (e) When the X-PETN is used to initially shock the 40 μm TATB layer, the particle velocity of the shock wave still falls below TATB's expect detonation velocities. (f) Peak shock fluence of X-PETN versus the boosted TATB sample.

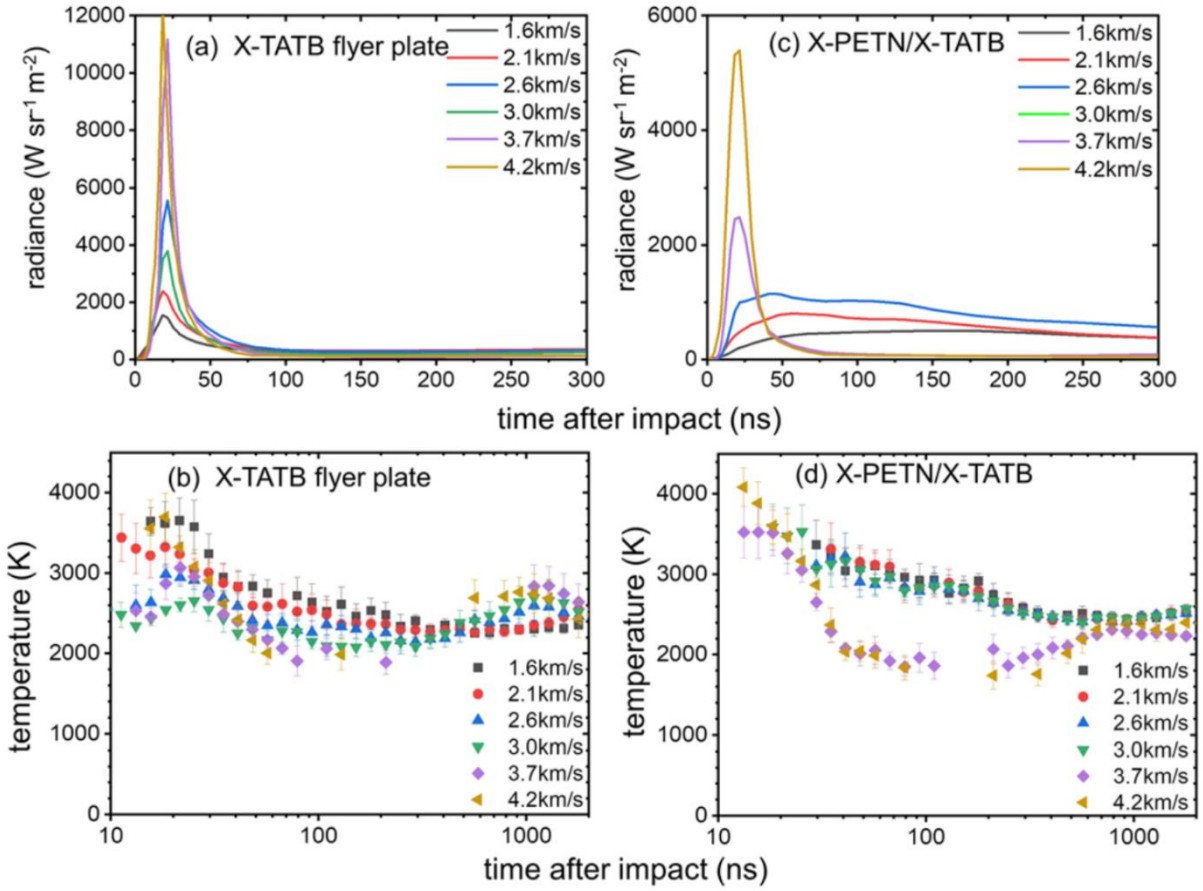

Figure 7.15 Emission radiance and temperature history comparison of shock waves in (a-b) neat X-TATB, (c-d) X-PETN-initiated X-TATB.

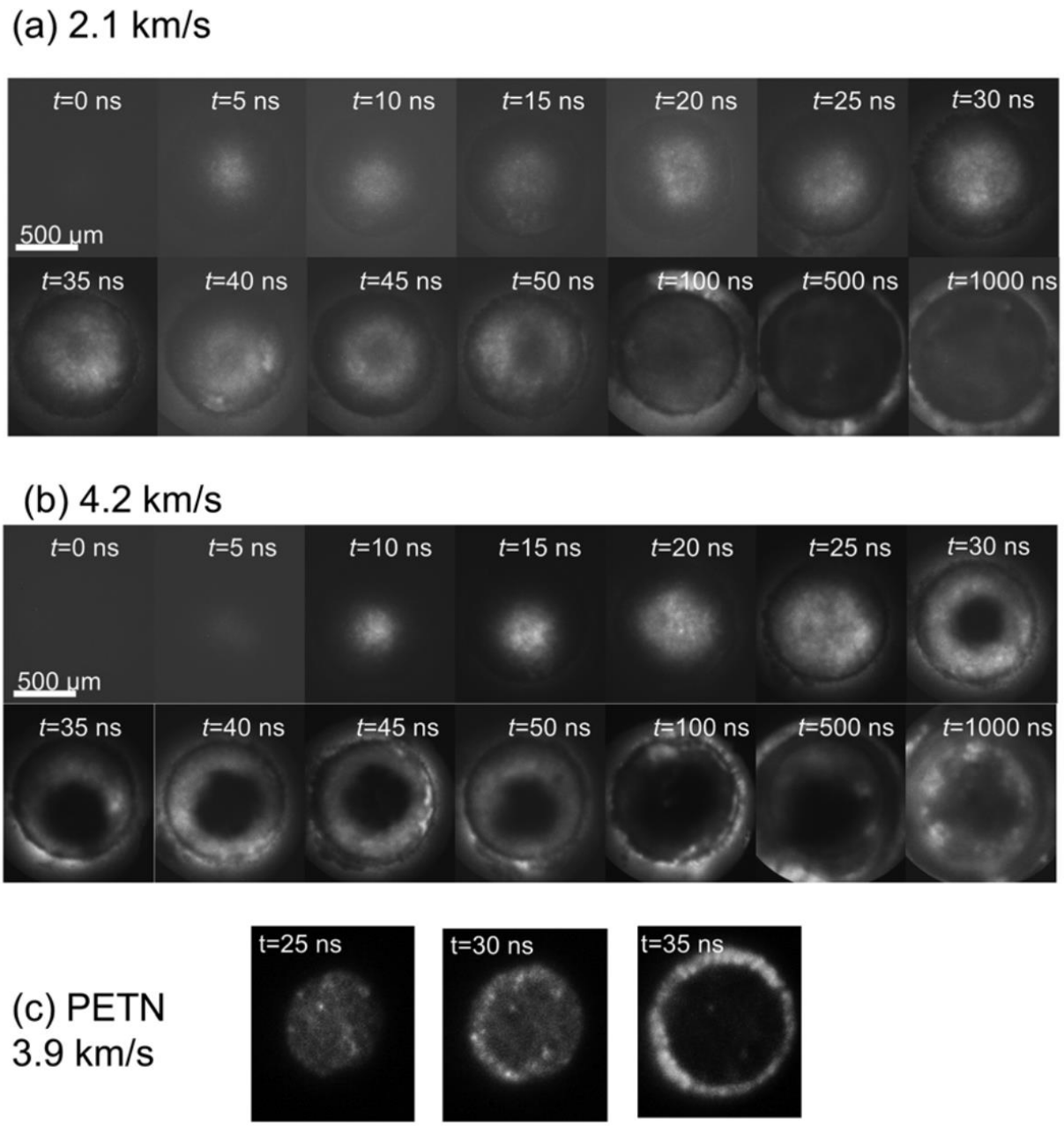

Figure 7.16 High speed photographs of X-PETN-initiated X-TATB layers at (a) 2.1 km/s flyer plate impact and (b) 4.1 km/s flyer plate impact. (c) For comparison, a video of 3.9 km/s X-PETN (neat) sample

7.7 References

1. Bhowmick, M.; Nissen, E. J.; Dlott, D. D. Detonation on a Tabletop: Nitromethane with High Time and Space Resolution. *J. Appl. Phys.* **2018**, *124* (7), 075901.

2. Field, J. E. Hot Spot Ignition Mechanisms for Explosives. *Acc. Chem. Res.* **1992**, *25* (11), 489–496.

3. Dlott, D. D. Laser Pulses into Bullets: Tabletop Shock Experiments. *Phys. Chem. Chem. Phys.* **2022**, *24* (18), 10653–10666.

4. Bassett, W. P.; Johnson, B. P.; Salvati, L.; Dlott, D. D. Hot-Spot Generation and Growth in Shocked Plastic-Bonded Explosives Studied by Optical Pyrometry. *J. Appl. Phys.* **2019**, *125* (21), 215904.

5. Marsh, S. P. *LASL Shock Hugoniot Data*; University of California Press, Berkeley, 1980.

6. Dobratz, B. M. *Properties of Chemical Explosives and Explosive Simulants*; UCRL--51319, UCRL--51319(REV.1), 4285272; 1972; p UCRL--51319, UCRL--51319(REV.1), 4285272.

7. Stirpe, D.; Johnson, J. O.; Wackerle, J. Shock Initiation of XTX-8003 and Pressed PETN. *J. Appl. Phys.* **1970**, *41* (9), 3884–3893.

8. Bassett, W. P.; Johnson, B. P.; Neelakantan, N. K.; Suslick, K. S.; Dlott, D. D. Shock Initiation of Explosives: High Temperature Hot Spots Explained. *Appl. Phys. Lett.* **2017**, *111* (6), 061902.

9. Bassett, W. P.; Dlott, D. D. Multichannel Emission Spectrometer for High Dynamic Range Optical Pyrometry of Shock-Driven Materials. *Rev. Sci. Instrum.* **2016**, *87* (10), 103107.

10. Zhou, X.; Miao, Y.-R.; Banlusan, K.; Shaw, W. L.; Strachan, A. H.; Suslick, K. S.; Dlott, D. D. Shock Wave Dissipation by Metal Organic Framework; St. Louis, MO, USA, 2018; p 150043.

11. Bdzil, J. B.; Stewart, D. S. The Dynamics of Detonation in Explosive Systems. *Annu. Rev. Fluid Mech.* **2007**, *39* (1), 263–292.

12. Forbes, J. W. *Shock Wave Compression of Condensed Matter: A Primer*; Springer Berlin Heidelberg: Berlin, Heidelberg, 2012.

13. Fickett, W.; Davis, W. C. *Detonation*; University of California Press: Berkeley, CA, 1979.

14. Tarver, C. M. Multiple Roles of Highly Vibrationally Excited Molecules in the Reaction Zones of Detonation Waves. *J. Phys. Chem. A* **1997**, *101* (27), 4845–4851.

15. Tarver, C. M.; Forbes, J. W.; Urtiew, P. A. Nonequilibrium Zeldovich-von Neumann-Doring Theory and Reactive Flow Modeling of Detonation. *Russ. J. Phys. Chem. B* **2007**, *1* (1), 39–45.

16. Tarver, C. M.; Chidester, S. K.; Nichols, A. L. Critical Conditions for Impact- and Shock-Induced Hot Spots in Solid Explosives. *J. Phys. Chem.* **1996**, *100* (14), 5794–5799.

17. Walker, F. E.; Wasley, R. J. A General Model for the Shock Initiation of Explosives. *Propellants Explos. Pyrotech.* **1976**, *1* (4), 73–80.

18. Bowden, M.; Maisey, M. P.; Knowles, S. Shock Initiation of Hexanitrostilbene at Ultra-High Shock Pressures and Critical Energy Determination; Chicago, Illinois, 2012; pp 615–618.

19. Akhtar, M.; Salvati, L.; Valluri, S. K.; Dlott, D. D. Shock Ignition and Deflagration Growth in Plastic-Bonded TATB (1, 3, 5-Trinitro-2, 4, 6-Triaminobenzene) Microstructures. *Appl. Phys. Lett.* **2022**, *121* (6), 064101.

20. Akhtar, M.; Dlott, D. D. Comparing the Shock Sensitivity of Insensitive Energetic Materials. *J. Appl. Phys.* **2022**, *131* (6), 065103.

21. Boddu, V. M.; Viswanath, D. S.; Ghosh, T. K.; Damavarapu, R. 2,4,6-Triamino-1,3,5-Trinitrobenzene (TATB) and TATB-Based Formulations—A Review. *J. Hazard. Mater.* **2010**, *181* (1–3), 1–8.

22. Park, S. D.; Armstrong, M. R.; Kohl, I. T.; Zaug, J. M.; Knepper, R.; Tappan, A. S.; Bastea, S.; Kay, J. J. Ultrafast Shock-Induced Reactions in Pentaerythritol Tetranitrate Thin Films. *J. Phys. Chem. A* **2018**, *122* (41), 8101–8106.

23. Willey, T. M.; Hoffman, D. M.; van Buuren, T.; Lauderbach, L.; Gee, R. H.; Maiti, A.; Overturf, G. E.; Fried, L. E.; Ilavsky, J. The Microstructure of TATB-Based Explosive Formulations During Temperature Cycling Using Ultra-Small-Angle X-Ray Scattering. *Propellants Explos. Pyrotech.* **2009**, *34* (5), 406–414.

24. McGrane, S. D.; Aslam, T. D.; Pierce, T. H.; Hare, S. J.; Byers, M. E. Temperature of Shocked Plastic Bonded Explosive PBX 9502 Measured with Spontaneous Stokes/Anti-Stokes Raman. *J. Appl. Phys.* **2018**, *123* (4), 045902.

25. Saint-Amans, C.; Hébert, P.; Doucet, M.; de Resseguier, T. Erratum: " *In-Situ* Raman Spectroscopy and High-Speed Photography of a Shocked Triaminotrinitrobenzene Based Explosive". *J. Appl. Phys.* **2015**, *117* (10), 109902.

26. Bassett, W. P.; Johnson, B. P.; Dlott, D. D. Dynamic Absorption in Optical Pyrometry of Hot Spots in Plastic-Bonded Triaminotrinitrobenzene. *Appl. Phys. Lett.* **2019**, *114* (19), 194101.

27. Bhowmick, M.; Basset, W. P.; Matveev, S.; Salvati, L.; Dlott, D. D. Optical Windows as Materials for High-Speed Shock Wave Detectors. *AIP Adv.* **2018**, *8* (12), 125123.

28. Zhou, X.; Miao, Y.; Suslick, K. S.; Dlott, D. D. Mechanochemistry of Metal–Organic Frameworks under Pressure and Shock. *Acc. Chem. Res.* **2020**, *53* (12), 2806–2815.

29. Salvati, L.; Johnson, B. P.; Bassett, W. P.; Dlott, D. D. Probing Shock-Initiation of Plastic-Bonded Explosives with a Tabletop Microscope; Portland, OR, USA, 2020; p 030027.

30. Golopol, H.; Hetherington, N.; North, K. Aging Effects on the Detonation Velocity of XTX-8003. *J. Hazard. Mater.* **1980**, *4* (1), 45–55. https://doi.org/10.1016/0304-3894(80)80022-7.

31. Manaa, M. R.; Reed, E. J.; Fried, L. E.; Goldman, N. Nitrogen-Rich Heterocycles as Reactivity Retardants in Shocked Insensitive Explosives. *J. Am. Chem. Soc.* **2009**, *131* (15), 5483–5487.

Appendix A: Velocimetry Data Processing

A.1 Overview

The following section describes the software interface built to analyze bulk data lots of PDV velocities. The base code is based on work by William Shaw[1] in the Dlott Group and expanded to calculate pressures, velocities and fluences from PDV Data[2,3,4]. While the fundamental details for analysis were adapted from work in Dan Dolan's group at Sandia[5].

The base of the code is built in Matlab (2019A) using the GUIDE framework. It is an object oriented code with codes handled by sub-classes. The total skeleton of the program will not be fleshed out for brevity, simply the relevant classes and the user-end structure.

A.2 Base Code – Class instantiation, definition and attributes

```
classdef MainPDVData < handle
    %The main class that contains all types of PDV files (Either STFT or
    %fit peak data)
    properties(Access = private)
        mainFig;
        ScopeTime;
        ScopeVolt;
        TimingParams = Osc_Timing_Properties('PDVTimingParams.txt');
        Toffset
        WindowCorrections
        DataStorage; %Cell array with all derived results
        handles; %data handle from main GUI data
        ProgBar;
        ProgText;
        Prog;
        timing_vector = 3;
        HugoniotDictionary; %Containers.map structure for hugoniot parameters;
        %Each entry listed as Us = A + b*up^2 + c*up a value associated
        %with a key is [A,b,c,rho]
    end
    properties(Access = protected)
    end
    methods
        function obj = MainPDVData(mainFig)
            %initialize
            obj.mainFig = mainFig;
            obj.handles = guidata(obj.mainFig);
            obj.ProgBar = obj.handles.ProgressBar;
            obj.ProgText = obj.handles.InfoText;
            obj.WindowCorrections = obj.WindowCorrectionDB('WindowCorrectionDB.txt');
            obj.HugoniotDictionary = obj.getHugoniotDictionary('HugoniotDB.txt');
            obj.Prog=0; obj.ProgressBar(); T = length(obj.handles.fileNames);
```

A.3 Read PDV Text File

```
function [ScopeTime,ScopeVolt,Toffset] = Readtxt(obj,idx)
    name = obj.handles.fileNames{idx};
    name = strsplit(name,'Ch'); name = name{1};
    switch obj.handles.ChCount
        case 2
            Ch_List = 1:2:3;
            timing_vector = 2;
        case 4
            Ch_List = 1:4;
            timing_vector = 3;
    end
    j = 1;
    for i = Ch_List
        channel_name=strcat(name,sprintf('Ch%d.txt',i));
        fid = fopen(fullfile(obj.handles.filePath,channel_name));
        textscan(fid,'%s',31);
        file = fscanf(fid,'%f',[2,1])';
        while ~feof(fid)
            curr = fscanf(fid,'%f',[2,5000])';
            if ~isempty(curr)
                file = [file; curr];
            end
        end
        fclose(fid);
        if i==1
            ScopeTime = file(:,1) + abs(file(1,1));
        end
        ScopeVolt(:,j) = file(:,2);
        clear file
        j = j+1;
    end
    [maximum, maximum_index] = max(ScopeVolt(:,timing_vector));
    time_vector = ScopeTime(1:maximum_index);
    index90 = length(time_vector(time_vector<=maximum*0.9));
    time90 = ScopeTime(index90).*1e9;
    scope_offset = obj.TimingParams.TrigOffset;
    time_offset = -time90 + scope_offset;
    ScopeTime = ScopeTime.*1e9 + time_offset;
    Toffset = time_offset;

end
function ProgressBar(obj)
    DisplayStatus(obj.ProgBar,obj.ProgText,obj.Prog)
end
function FillParams(obj)
    set(obj.handles.Time0Text,'String',obj.TimingParams.TrigOffset);
    set(obj.handles.Time0Text2,'String',obj.TimingParams.TrigOffset);
    set(obj.handles.Time0Text,'Enable','Off');
    set(obj.handles.Time0Text2,'Enable','Off');
    set(obj.handles.TargetMaterialMenu,'String',keys(obj.HugoniotDictionary));
end

function [maxSize,maxidx] = MaxDataSize(obj,idx_list)
    %find max size of selected datastorage objects
    maxSize = 0;maxidx = 0;
    for i = 1:length(idx_list)
        k = idx_list(i);
        if length(obj.DataStorage{k}.Velocity)>maxSize
            maxSize = length(obj.DataStorage{k}.Velocity);
            maxidx = k;
        end
```

```
            end
        end

        function [AvgT0] = AvgT0(obj,idx_list)
            T0Mat = [];
            for i = 1:length(idx_list)
                k = idx_list(i);
                T0Mat(i) = obj.DataStorage{k}.T0;
            end
            AvgT0 = mean(T0Mat);
        end
```

A.4 Short-time Fourier transform

```
classdef STFTData < handle
   properties
       Peak = NaN;
       Duration = NaN;
       Fluence = NaN;
       Velocity;
       VelTime;
       T0;


   end
   properties(Access = private)
        ScopeTime;
       ScopeVolt;
       STFTParams;
       ProgHandles;
       Prog;
       TParams;
       ChCount;
       timing_vector = 3;
   end
   methods
       function obj = STFTData(T,V,STFTParams,TParams,ProgHandles)
           obj.ScopeTime = T;
           obj.ScopeVolt = V;
           obj.TParams = TParams;
           obj.STFTParams = STFTParams;
           obj.ProgHandles = ProgHandles;
           [obj.VelTime,obj.Velocity] = obj.Transform();
       end
       function [VelTime,Velocity] = Transform(obj)
            SampleSpacing = obj.ScopeTime(2) - obj.ScopeTime(1);
            SampleFreq = (SampleSpacing*1E-9)^(-1);
            TimeWindow = obj.STFTParams{2};
            r = round(SampleFreq.*(TimeWindow*1E-9));
            SampleRate = 0.08;
            test = round(SampleRate/SampleSpacing);
            obj.ChCount = size(obj.ScopeVolt);
            obj.ChCount = obj.ChCount(2); %number of column vectors;
            switch obj.ChCount
                case 2
                    obj.timing_vector = 2;
                case 4
                    obj.timing_vector = 4;
            end
            if test ==0
                test = 1;
            end
            obj.Prog = 0;
            cAmp = obj.Detrend();
```

```
            for i = 1:obj.ChCount
                if i==obj.timing_vector
                    continue
                end
                [STFT,f,t] = spectrogram(cAmp(:,i),hamming(r),r-test,10*r,SampleFreq);
                %%
                obj.Prog = (2*i)/12;
                obj.ProgressBar()
                %%
                if i == 1
                    STFT_tot = abs(STFT);
                else
                    STFT_tot = STFT_tot + abs(STFT);
                end
            end
            %%
            obj.Prog = 9/12; obj.ProgressBar();
            %%
            STFT_tot = STFT_tot./(obj.ChCount-1);
            velocity_axis = f.*0.775./1e9;
            VelTime = (t.*1e9)'+obj.STFTParams{3};
            %%
            obj.Prog = 10/12; obj.ProgressBar();
            %%
            Vcut = obj.STFTParams{1};
            if Vcut > 0
                filter = length(velocity_axis(velocity_axis<Vcut));
                STFT_tot(1:filter,:)=0;
                clear filter
            end
            [mx locs]=max(STFT_tot,[],1);
            velocity_lineout=velocity_axis(locs);
            obj.Prog = 11/12; obj.ProgressBar();
            % Fit the FFT at each time step to better resolve the velocity. I use a
% polynomial since this is much, much less computationally expensive then a
            % gaussian fit.
            velocity_lineout_fit = velocity_lineout;
            for i=1:length(velocity_lineout)
                if velocity_lineout(i) > 0.1 && (locs(i)+2)<length(velocity_axis)
p = polyfit(velocity_axis((locs(i)-2):(locs(i)+2)),STFT_tot((locs(i)-
2):(locs(i)+2),i),2);
                    peakPosition = -p(2)./(p(1)*2);
                    velocity_lineout_fit(i) = peakPosition;
                else
                    velocity_lineout_fit(i) = 0;
                end
            end
            Velocity = velocity_lineout_fit;
            obj.Prog = 1; obj.ProgressBar();

        end
        function ProgressBar(obj)
            DisplayStatus(obj.ProgHandles{1},obj.ProgHandles{2},obj.Prog);
            drawnow;
        end
    end
        methods(Access = private)
            function [cAmp] = Detrend(obj)
                switch obj.ChCount
                    case 4
                        A = [0.35,0.37,1,0.34]; %Correction factor
                    case 2
```

```
                        A = [1,1];
                end
                 for i = 1:obj.ChCount
                    if i ==obj.timing_vector
                        cAmp(:,i) = obj.ScopeVolt(:,i);
                        continue
                    end
                    t0 = obj.findT0(obj.ScopeTime,obj.ScopeVolt);
                    obj.T0 = obj.ScopeTime(t0);
                    fitvals =
polyfit(obj.ScopeTime(t0:end),obj.ScopeVolt(t0:end,i),1);
                    meanvals = polyval(fitvals,obj.ScopeTime);
                    cAmp(:,i) = (obj.ScopeVolt(:,i)-meanvals)./A(i);
                end
            end
        end
        methods(Static)
            function [t0] = findT0(ScopeTime,ScopeVolt)
                 s = 0;
                 i = 1;
                 for j=1:(0.05*length(ScopeTime))
                     s=s+ScopeVolt(j,i)^2;
                 end
                 rMS(i)=sqrt(s/(0.05*length(ScopeTime)));
                 i = 1;
                 try
                 while (abs(ScopeVolt(i,1)) < 5*rMS(1))
                     i = i+1;
                 end
                 catch
                     i = 1000;
                 end
                 t0 = i;
             end
        end
end
```

A.5 Peak-Finding Algorithm

A.5.1 Calling PeakFit Datatype Instance

```
         function PeakAlg(obj,idx)
             ProgHandles = {obj.handles.ProgressBar,obj.handles.InfoText};
             Thresh = str2double(get(obj.handles.ThreshEdit,'String'));
             obj.DataStorage{idx} =
PeakFitData(obj.ScopeTime{idx},obj.ScopeVolt{idx},obj.TimingParams,ProgHandles,Thresh)
;
             obj.ApplyWindowCorrection(idx);
             obj.PlotData(idx);
         end
```

A.5.2 PeakFit Datatype Class and Methods

```
classdef PeakFitData < handle
   properties
        Velocity;
        VelTime;
        T0;
        PeakVolt;
        Peak;
        Duration;
        Fluence
```

```
    end
    properties(Access = private)
        ScopeTime;
        ScopeVolt;
        Thresh;
        TParams;
        ProgHandles;
        Prog;
    end
    methods
        function obj = PeakFitData(T,V,TParams,ProgHandles,Thresh)
            obj.ScopeTime = T;
            obj.ScopeVolt = V;
            obj.TParams = TParams;
            obj.ProgHandles = ProgHandles;
            obj.Thresh = Thresh;
            [obj.VelTime,obj.Velocity,obj.PeakVolt] = obj.PeakDet4();
        end
        function AddPeak(obj,Xnew,Ch)
            [~,Xidx] = min(abs(Xnew-obj.ScopeTime));
             Tnew = obj.ScopeTime(Xidx);
             Ynew = obj.ScopeVolt(Xidx,Ch);
             obj.PeakVolt{Ch}=sortrows([obj.PeakVolt{Ch};Tnew,Ynew]);
             obj.CalcVelocity();
        end
        function DeletePeak(obj,Xdel,Ch)
             [~,Xidx] = min(abs(Xdel-obj.PeakVolt{Ch}(:,1)));
             obj.PeakVolt{Ch}(Xidx,:)=[];
             obj.CalcVelocity();
        end

    end
    methods(Access = private)
        function [VelTime,Velocity,PeakVolt] = PeakDet4(obj)
            k = 1;
            x0 = obj.findT0(obj.ScopeTime,obj.ScopeVolt);
            x0 = x0-2;
            obj.T0 = obj.ScopeTime(x0);
            PD_Indicator = size(obj.ScopeVolt); %Determining if 1 or 3 PDs is at play
            if PD_Indicator(2) ==2
                ChList = [1]; %Only use channel 1 from Scope
            else
                ChList = obj.TParams.ChList;
            end
            for j = 1:length(ChList)
                  i = ChList(j);
                  sAmp(:,k) = smooth(obj.ScopeVolt(:,i),5);
                  rMS(k) = obj.fRMS(obj.ScopeTime,obj.ScopeVolt(:,i));
       [high{k},low{k}] = obj.peakdet(sAmp(x0-
0.001*length(obj.ScopeTime):end,k),(rMS(k)*obj.Thresh),obj.ScopeTime(x0-
0.001*length(obj.ScopeTime):end));
                  peakPositions{k} =
sortrows([obj.ScopeTime(x0),obj.ScopeVolt(x0,i);high{k}(:,1),high{k}(:,2);low{k}(:,1),
low{k}(:,2)]);
                  [sAmp_test] =
obj.fSmoothData2(obj.ScopeTime,obj.ScopeVolt(:,i),peakPositions{k},0.1);
                  if length(sAmp_test) == length(obj.ScopeTime)
                     sAmp(:,k) = sAmp_test;
                  end
                  [high{k},low{k}] =
obj.peakdet(sAmp(x0:end,k),(rMS(k)*obj.Thresh),obj.ScopeTime(x0:end));
```

```
                peakPositions{k} =
sortrows([obj.ScopeTime(x0),obj.ScopeVolt(x0,i);high{k}(:,1),high{k}(:,2);low{k}(:,1),
low{k}(:,2)]);
                %Call the fitting program that uses a third 2nd order polynomial to
fit the
                %data about each peak found above. This gives the most precise
position for
                %each max or min.
                [high{k},low{k}] =
obj.fFitPeaks(obj.ScopeTime,obj.ScopeVolt(:,i),high{k},low{k});
                peakPositions{k} =
sortrows([obj.ScopeTime(x0),obj.ScopeVolt(x0,i);high{k}(:,1),high{k}(:,2);low{k}(:,1),
low{k}(:,2)]);

xyPeaks{k}=sortrows([obj.ScopeTime(x0),sAmp(x0,k);high{k}(:,1),high{k}(:,2);low{k}(:,1
),low{k}(:,2)]);
                idx_0 = length(xyPeaks{k}(xyPeaks{k}(:,1)<=obj.ScopeTime(x0),1));
                velocity{k}=0.3875./diff(xyPeaks{k}(idx_0+1:end,1));

xPeaks{k}=xyPeaks{k}(idx_0+1:end,1);xPeaks{k}(length(velocity{k}))=[];
                k = k+1;
            end
                velocity0 = 0;
                if length(ChList) == 3

XYMAT=sortrows([xPeaks{1},velocity{1};xPeaks{2},velocity{2};xPeaks{3},velocity{3};obj.
ScopeTime(x0),velocity0]);
                else
                    XYMAT = sortrows([xPeaks{1},velocity{1};obj.ScopeTime(x0),0]);
                end
                velocityTime=XYMAT(:,1);
                velocity_final=XYMAT(:,2);
                x = smooth(velocity_final(3:end),3);
                velocity_final(3:end) = x;
                lineout_time = XYMAT(:,1);
                %VelTime0 = velocityTime-velocityTime(1,1);
                VelTime = lineout_time;
                Velocity = velocity_final;
                PeakVolt = xyPeaks;
                %{
             for k = 1:3
                peakPositions1{k}(:,1) = peakPositions{k}(:,1)-velocityTime(1,1);
                xPeaks{k} = xPeaks{k};
             end
                %}



        end
        function [T,V,pV] = PeakDet5(obj)
            %divide into blocks of 500
            Volt = obj.ScopeVolt(:,1); Volt = Volt(4000:end); Nv = length(Volt);
            Ns = 100;
            for seg = 1:Nv/Ns
                sp = (seg-1)*Ns+1;
                if seg*Ns > Nv
                    ep = Nv;
                else
                    ep = seg*Ns;
                end

                Y = Volt(sp:ep);
            Y = detrend((Y)); N = length(Y);
```

```
            L = ceil(N/2)-1;
            %L = 250;
            m = zeros(L,N);
            for k = 1:L
                %w = 2*k;
                for i = (k+2):(N-k+1)
                    if and((Y(i-1) > Y(i-k-1)),Y(i-1) > Y(i+k-1))
                         m(k,i) = 0;
                    else
                        r = rand();
                        m(k,i) = r+1;
                    end
                end
            end
            gamma = sum(m,2);
            [~,lambda]= min(detrend(gamma));
            %lambda = 136;
            M = m(1:lambda,:);
            j = 1;
            for i = 1:N
                %{
                X = (1/lambda)*sum(m(:,i));
                Y = (m(:,i)-X).^2; Y = Y.^(0.5);
                Y = sum(Y);
                sigma(i) = (1/(lambda-1))*Y;
                %}
                %sigma = std(M(:,i));
                sigma(i) = (lambda-1)^(-1)*sum(((M(:,i)-
(1/lambda)*sum(M(:,i))).^2).^(0.5));
                if sigma(i) ==0
                    p(j) = i;
                    j = j+1;
                end
            end
            p(1:2) = [];
            P{seg} = p;
            X = sp:ep;
            figure(3); hold on;plot(X,Y);plot(X(p),Y(p),'bo')
            end
            P;
            hold off;



        end
        function CalcVelocity(obj)
            x0 = obj.findT0(obj.ScopeTime,obj.ScopeVolt);
            x0 = x0-2;
            for k = 1:length(obj.PeakVolt)
                 idx_0 =
length(obj.PeakVolt{k}(obj.PeakVolt{k}(:,1)<=obj.ScopeTime(x0),1));
                velocity{k}=0.3875./diff(obj.PeakVolt{k}(idx_0+1:end,1));

xPeaks{k}=obj.PeakVolt{k}(idx_0+1:end,1);xPeaks{k}(length(velocity{k}))=[];
            end
             try

XYMAT=sortrows([xPeaks{1},velocity{1};xPeaks{2},velocity{2};xPeaks{3},velocity{3};obj.
ScopeTime(x0),0]);
             catch
                XYMAT=sortrows([xPeaks{1},velocity{1};obj.ScopeTime(x0),0]);
             end
```

```
            %velocityTime=XYMAT(:,1);
            velocity_final=XYMAT(:,2);
            x = smooth(velocity_final(3:end),3);
            velocity_final(3:end) = x;
            lineout_time = XYMAT(:,1);
            %new_time = obj.ScopeTime-velocityTime(1,1);
            obj.VelTime = lineout_time;
            obj.Velocity = velocity_final;
        end
    end
    methods(Static)
        function [rMS] = fRMS(time,rVolts1)
            s=0;
            for i=1:(0.02*length(time))
                s=s+rVolts1(i,1)^2;
            end
            rMS=sqrt(s/(0.02*length(time)));
        end
        function [sVolts] = fSmoothData2(rTime,rVolts1,peakPositions,num)
            peakPositionsIndex = [];
            for i=1:length(peakPositions(:,1))
                peakIndex = find(rTime >= peakPositions(i,1),1,'first');
                peakPositionsIndex = [peakPositionsIndex;peakIndex];
            end

            indexDifference = [peakPositionsIndex(1);diff(peakPositionsIndex)];


            sVolts =
smooth(rVolts1(1:peakPositionsIndex(1)),(indexDifference(1)*num));

            smoothDistance = round((indexDifference(2)*num));
            z = 2;

            while smoothDistance<1
                smoothDistance = round((indexDifference(z+1)*num));
                z = z+1;
            end

            for i = 2:(length(peakPositions(:,1))-10)
                if round((indexDifference(i)*num)) > (1+1/4)*smoothDistance
                    smoothDistance = round((1+1/4)*smoothDistance);
                elseif round((indexDifference(i)*num)) < (1-1/4)*smoothDistance
                    smoothDistance = round((1-1/4)*smoothDistance);
                else
                    smoothDistance = round((indexDifference(i)*num));
                end
                if i==length(peakPositions(:,1))
                    disp('here')
                end
                test = smooth(rVolts1((peakPositionsIndex(i-1)-
smoothDistance):(peakPositionsIndex(i)+smoothDistance)),smoothDistance);
                sVolts = [sVolts;test(smoothDistance+1:end-smoothDistance-1)];
            end
            test = smooth(rVolts1((peakPositionsIndex(end)+1)-100:end),(50));
            sVolts = [sVolts;test(101:end)];
        end


            %%
        function [newHigh,newLow] = fFitPeaks(xData,yData,high,low)
            %Title: findPeaks
            %Author: Gino Giannetti & William Shaw
```

```
%Date: 2014-6-10
%Updated 2014-12-31

%Purpose: find maximums and minimums of input data more accurately than
%         peakdet method using curve fitting. For use in shock compression
data.
%         Note-uses peakdet in the process (Removed dependency 2014-12-31)

%Input: high and low are previous max and min arrays found by peakdet.
%       xData and yData are the raw x and y data
%       indFirstMove is the index in the x and y data where the object in
%       question first moves

%Output: new maximum and minimum arrays of the data

% Setting up while loop

oldPeaks = sortrows([high(:,1),high(:,2);low(:,1),low(:,2)]);
newHigh = [];
newLow = [];
a=0;
b=0;
k=1;

warning('off','MATLAB:polyfit:RepeatedPointsOrRescale');
while (k <= (length(oldPeaks(:,1))))

% Finding section to curve fit
    switch k
        case 1
            a = ((oldPeaks(k,1)-oldPeaks(k+1,1)))/2 + oldPeaks(k,1);
            b = ((oldPeaks(k+1,1)-oldPeaks(k,1)))/2 + oldPeaks(k,1);
        case length(oldPeaks(:,1))
            a = ((oldPeaks(k,1)-oldPeaks(k-1,1)))/2 + oldPeaks(k-1,1);
            b = ((oldPeaks(k,1)-oldPeaks(k-1,1)))/2 + oldPeaks(k,1);
        otherwise
            a = ((oldPeaks(k,1)-oldPeaks(k-1,1)))/2 + oldPeaks(k-1,1);
            b = ((oldPeaks(k+1,1)-oldPeaks(k,1)))/2 + oldPeaks(k,1);

    end

    c=length(xData(xData<=a));
    d=length(xData(xData<=b));

    if c<0
        c=1;
    end

    if(isempty(c) || isempty(d))
        display('peak could not be found');
    end

    if c > length(xData) || d > length(xData)
        k=k+1;
    else
        xTemp = xData((c):(d));
        yTemp = yData((c):(d));

        % curve fitting polynomial
        p = polyfit(xTemp,yTemp,2);
        peakPosition = -p(2)./(p(1)*2);
        if peakPosition > xData(end)
```

```
                peakIndex = 1;
            else
                peakIndex = find(xData >= peakPosition,1,'first');
            end

            % Don't allow peak positions to change by more than 1 ns
            positionChange = peakPosition-oldPeaks(k,1);
            if abs(positionChange) < 1
                Temp = [peakPosition,yData(peakIndex)];
            else
                Temp = [oldPeaks(k,1), oldPeaks(k,2)];
            end

            %Assign high or low value.
            if (p(1)<=0)
                newHigh = [newHigh;Temp];
            else
            newLow = [newLow;Temp];
            end

            k=k+1;
        end
    end
    warning('on','MATLAB:polyfit:RepeatedPointsOrRescale');
end

    %% Peak determining routine
function [maxtab, mintab]=peakdet(v, delta, x)
    %PEAKDET Detect peaks in a vector
    %        [MAXTAB, MINTAB] = PEAKDET(V, DELTA) finds the local
    %        maxima and minima ("peaks") in the vector V.
    %        MAXTAB and MINTAB consists of two columns. Column 1
    %        contains indices in V, and column 2 the found values.
    %
    %        With [MAXTAB, MINTAB] = PEAKDET(V, DELTA, X) the indices
    %        in MAXTAB and MINTAB are replaced with the corresponding
    %        X-values.
    %
    %        A point is considered a maximum peak if it has the maximal
    %        value, and was preceded (to the left) by a value lower by
    %        DELTA.

    % Eli Billauer, 3.4.05 (Explicitly not copyrighted).
    % This function is released to the public domain; Any use is allowed.

    maxtab = [];
    mintab = [];

    v = v(:); % Just in case this wasn't a proper vector

    if nargin < 3
      x = (1:length(v))';
    else
      x = x(:);
      if length(v)~= length(x)
        error('Input vectors v and x must have same length');
      end
    end

    if (length(delta(:)))>1
      error('Input argument DELTA must be a scalar');
    end
```

```
            if delta <= 0
              error('Input argument DELTA must be positive');
            end

            mn = Inf; mx = -Inf;
            mnpos = NaN; mxpos = NaN;

            lookformax = 1;

            for i=1:length(v)
              this = v(i);
              if this > mx, mx = this; mxpos = x(i); end
              if this < mn, mn = this; mnpos = x(i); end

              if lookformax
                if this < mx-delta
                  maxtab = [maxtab ; mxpos mx];
                  mn = this; mnpos = x(i);
                  lookformax = 0;
                end
              else
                if this > mn+delta
                  mintab = [mintab ; mnpos mn];
                  mx = this; mxpos = x(i);
                  lookformax = 1;
                end
              end
            end
        end
        function [t0] = findT0(ScopeTime,ScopeVolt)
            s = 0;
            i = 1;
            for j=1:(0.05*length(ScopeTime))
                s=s+ScopeVolt(j,i)^2;
            end
            rMS(i)=sqrt(s/(0.05*length(ScopeTime)));
            i = 1;
            try
            while (abs(ScopeVolt(i,1)) < 5*rMS(1))
                i = i+1;
            end
            catch
                i = 1000;
            end
            t0 = i;
        end
    end
end
```

A.6 Applying Window Corrections

```
        function ApplyWindowCorrection(obj,idx)
            Material = get(obj.handles.WindowCorrectionList,'String');
            Material = Material{get(obj.handles.WindowCorrectionList,'Value')};
            WCF = obj.WindowCorrections.(Material);
            obj.DataStorage{idx}.Velocity = obj.DataStorage{idx}.Velocity./WCF;
        end
```

A.7 Average Multiple Curves

```
        function AverageSelected(obj)
```

```
            FileList = get(obj.handles.FileList,'Value');
            [maxSize,maxidx] = obj.MaxDataSize(FileList);
            TimeMatrix(:,1) = obj.DataStorage{maxidx}.VelTime;
            DataMatrix = [];
            for i = 1:length(FileList)
             idx = FileList(i);
DataMatrix(:,i) =
resample(obj.DataStorage{idx}.Velocity,maxSize,length(obj.DataStorage{idx}.VelTime));
            end
            AvgMat = mean(DataMatrix,2);
            obj.DataStorage{end+1} = struct();
            obj.ScopeTime{end+1} = obj.ScopeTime{end};
            obj.ScopeVolt{end+1} = obj.ScopeVolt{end};
            %%
            obj.DataStorage{end}.Velocity = AvgMat;
            obj.DataStorage{end}.VelTime = TimeMatrix;
            obj.DataStorage{end}.T0 = obj.AvgT0(FileList);
            idx = length(obj.DataStorage);
            obj.handles.fileNames = [obj.handles.fileNames, {'AvgCalc'}];
            set(obj.handles.FileList,'String',obj.handles.fileNames');
            obj.PlotAvg(idx);
end
```

A.8 Fluence Calculation

```
        function FluenceDurationCalc(obj)
            idx = get(obj.handles.FileList,'Value');
            %x0 = obj.DataStorage{idx}.T0;
            %In order to calculate for PDV where flyer is visible, it is
            %easier and more general to have user input x0
            axes(obj.handles.WaveformAxis);
            title('select start');
            [x0,~] = ginput(1);
            title('select end');
            [xf,~] = ginput(1);
            obj.DataStorage{idx}.Duration = xf-x0;
            MIndex = get(obj.handles.TargetMaterialMenu,'Value');
            MList = get(obj.handles.TargetMaterialMenu,'String');
            Material = MList{MIndex}; Properties = obj.HugoniotDictionary(Material);
            rho = Properties(4);A = Properties(1); b = Properties(2); c =
Properties(3);
            up = obj.DataStorage{idx}.Velocity;
            time = obj.DataStorage{idx}.VelTime;
            up(time<x0) = 0;
            up = up(time<xf);
            time = time(time<xf);


            %Us = A+b*up^2 + c*up
            %Run exceptions for glass:
            if strcmp(Material,'Pyrex')
                for i = 1:length(up)
                    if up(i) < 0.568
                         cg = 1.861;%% note: these are specific to GLASS, from the
glass hugoniot --> that is why the constants change for different velocities
                         Ag = 3.879;
                         bg = 0;
                        Flux(i) = 0.5.*rho.*(Ag+bg.*up(i).^2+cg.*up(i)).*up(i).^2;
                    else
                        Flux(i) = 0.5.*rho.*(A+b.*up(i).^2+c.*up(i)).*up(i).^2;
                    end
                end
            else
                Flux = 0.5.*rho.*(A+b.*up.^2+c.*up).*up.^2;
```

```
            end
            obj.DataStorage{idx}.Fluence = trapz(time,Flux);
            obj.DataStorage{idx}.Peak = max(up);
            set(obj.handles.FluenceEdit,'String',obj.DataStorage{idx}.Fluence);
            set(obj.handles.DurationEdit,'String',obj.DataStorage{idx}.Duration);
            set(obj.handles.PeakEdit,'String',obj.DataStorage{idx}.Peak);
        end
```

A.9 Save to Text Files

```
        function Vel2Text(obj)
            hdr1 = {}; hdr2 = {}; hdr3 = {};
            max_vector_size = [];
                for i=1:length(obj.DataStorage)
                    max_vector_size(i) = length(obj.DataStorage{i}.VelTime);
                end
                max_vector_size = max(max_vector_size);
            full_save = {};
            Response = questdlg('Rising Edge as 0 ns?',...
                'Time Axis Inquiry','Yes','No','No');

            for i = 1:length(obj.DataStorage)
                switch Response
                    case 'Yes'
                        Offset = obj.DataStorage{i}.T0;
                    case 'No'
                        Offset = 0;
                end
                curr_size = length(obj.DataStorage{i}.VelTime);
                save_data = [];
                save_data(1:max_vector_size,1:2) = NaN;
                hdr1 = [hdr1,'Time','Velocity'];
                hdr2 = [hdr2,'ns','km/s'];
                hdr3 = [hdr3, obj.handles.fileNames{i},obj.handles.fileNames{i}];
                save_data(1:curr_size,:) = [obj.DataStorage{i}.VelTime-
Offset,obj.DataStorage{i}.Velocity];
                full_save{i} = save_data;
            end
            if ~isempty(full_save)
                work_dir = pwd;
                cd(obj.handles.filePath); filter = {'*.txt'};
                [save,save_path] = uiputfile(filter,'Save PDV file');
                if save_path ==0
                    cd(work_dir);
                    error('SaveFunc:CancelInput','Save Cancelled');
                end
                fmt = repmat('%s\t ', 1, length(hdr1));
                fmt(end:end+1) = '\n';
                %open save file and write headers
                fid = fopen(fullfile(save_path,save), 'w');
                fprintf(fid, fmt, hdr1{:});
                fprintf(fid,fmt, hdr2{:});
                fprintf(fid,fmt, hdr3{:});
                fclose(fid);
                %now insert data vector
                dlmwrite(fullfile(save_path,save),full_save,'-
append','delimiter','\t');
                cd(work_dir);
            end
        end
```

A.10 Reading Data Directly From Oscilloscope

What follows is the code used during lab operations to extract data from the lab oscilloscope collecting a digitized readout of the 3-Channel multiplexed PDV system (see Chapter 2). It uses in-built VISA API code in Matlab's (2019A) libraries to extract the digitized data directly from the scope. The selected excerpts show how the program calls the code and accesses the readout of the program. For more details on the codes directly analyzing the results see A.2.3 and A.2.4, as well as Chapter 2 for more details. The GUI layout is shown in Fig A.5.

A.10.1 Selected Scripts

```
% --- Executes just before Oscilloscope_Controller is made visible.
function Oscilloscope_Controller_OpeningFcn(hObject, eventdata, handles, varargin)
% This function has no output args, see OutputFcn.
% hObject    handle to figure
% eventdata  reserved - to be defined in a future version of MATLAB
% handles    structure with handles and user data (see GUIDATA)
% varargin   command line arguments to Oscilloscope_Controller (see VARARGIN)

% Choose default command line output for Oscilloscope_Controller
handles.output = hObject;
handles.read_counter = 0;
handles.TekScope = Oscilloscope_Device(handles.LogText);
handles.WaveformLibrary = {};

% Update handles structure
guidata(hObject, handles);


% --- Executes on button press in ReadDataButton.
function ReadDataButton_Callback(hObject, eventdata, handles)
% hObject    handle to ReadDataButton (see GCBO)
% eventdata  reserved - to be defined in a future version of MATLAB
% handles    structure with handles and user data (see GUIDATA)
set(handles.LogText,'String','Aqcuiring Scope Data, please wait...');
drawnow;
try Amplitude = handles.TekScope.FetchOscilloscopeData();
    set(handles.LogText,'String','Fetched Scope Data, processing...')
    drawnow;
    StoreAndProcess(hObject,eventdata,handles,Amplitude);
catch
    set(handles.LogText,'String','Sorry, couldnt read any data :(');
    pause(2);
    handles.TekScope.FakeOscilloscopeData();
    set(handles.LogText,'String','');
end


function StoreAndProcess(hObject,eventdata,handles,Amplitude)
    handles.read_counter = mod(handles.read_counter,3)+1;
    k = handles.read_counter;
    handles.WaveformLibrary{k} = WaveformData(Amplitude,handles.v_cutoff,k,...
        handles.lineout_axes, handles.volt_readout);
```

```
handles.WaveformLibrary{k}.plotData();
handles.read_counter = handles.read_counter +1;
set(handles.LogText,'String','Done');
drawnow;
pause(2); set(handles.LogText,'String','');
guidata(hObject,handles);
```

A.11 Figures

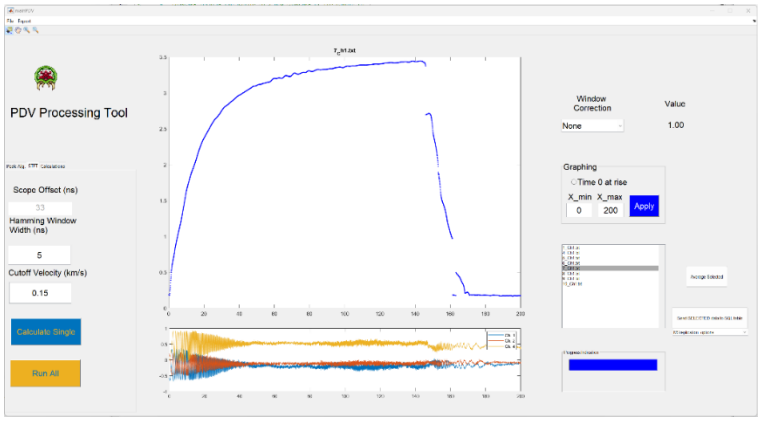

Figure A.1. Top-level user interface for PDV analysis code described in this section

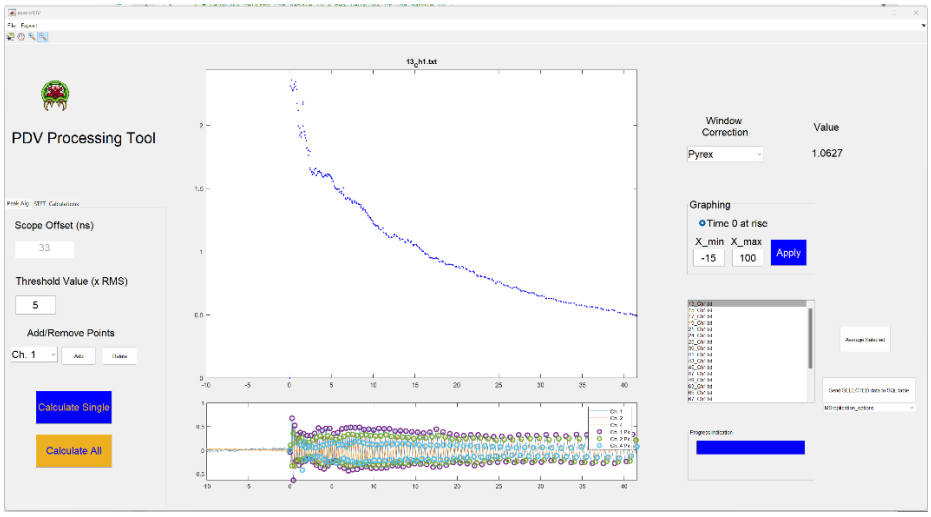

Figure A.2. Example results from fring-counting based PDV analysis

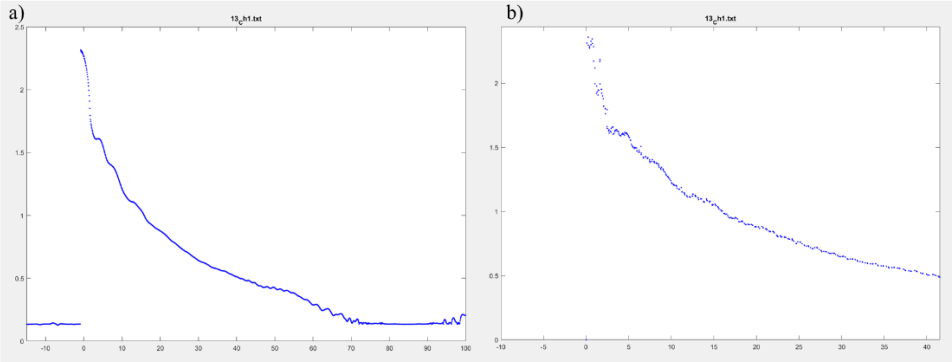

Figure A.3. Glass window shock analyzed by STFT(a) and fringe counting methods (b).

A.12 References

1. Shaw, W. L. REACTIVE SOLIDS UNDER SHOCK COMPRESSION. 230.

2. Zhou, X.; Miao, Y.; Suslick, K. S.; Dlott, D. D. Mechanochemistry of Metal–Organic Frameworks under Pressure and Shock. *Acc. Chem. Res.* 2020, *53* (12), 2806–2815.

3. Salvati, L.; Johnson, B. P.; Bassett, W. P.; Dlott, D. D. Probing Shock-Initiation of Plastic-Bonded Explosives with a Tabletop Microscope; Portland, OR, USA, 2020; p 030027.

4. Zhang, W.; Salvati, L.; Akhtar, M.; Dlott, D. D. Shock Initiation and Hot Spots in Plastic-Bonded 1,3,5-Triamino-2,4,6-Trinitrobenzene (TATB). *Appl. Phys. Lett.* 2020, *116* (12), 124102.

5. Jones, S.; Dolan, D. *THRIVE : A Data Reduction Program for Three-Phase PDV/PDI and VISAR Measurements.*; SAND2008-3871, 942210; 2008; pp SAND2008-3871, 942210.

Appendix B: Radiance Analysis Codes

B.1 Overview

B.2 Radiance Integration Methods

This script is added with permission from the primary author, Siva Kumar Valluri. This code was used to interpret radiance integrals in data reported in Chapter 4 and Chapter 5 after taking output files from the pyrometer data produced by the codes used in Appendix B. The script uses Python 3.9, and the Scipy, Numpy, and Pandas libraries.

B.2.1 Radiance Analyzer Python Code

```
"""
Created on Fri Mar 18 15:57:53 2022

@author: Siva Kumar Valluri
"""

import os
import glob
import io
import numpy as np
import math
#from scipy.interpolate import interp1d
#from scipy.interpolate import CubicSpline
from scipy.interpolate import PchipInterpolator as pcip
from scipy.signal import find_peaks
import matplotlib.pyplot as plt
from scipy import integrate
import pandas as pd
import statistics as stat

#functions used:-------------------------------------------------------------------
------------------------------------------------------------------------------

def fit_derivative_and_integral(x,y):
    #f = interp1d(x, y, kind='cubic')
```

```
    #f = CubicSpline(x,y)
    f=pcip(x, y, axis=0, extrapolate=None)
    x_new= np.logspace(math.log10(x[0]), math.log10(x[-1]), num=500,
endpoint=True,base=10.0)
    logx_new=[math.log10(x_new[i]) for i in range(len(x_new))]
    y_new=f(x_new)
    dydlogx=np.gradient(y_new,logx_new)
    dydx=np.gradient(y_new,x_new)
    cd=integrate.cumtrapz(y_new, x_new)
    cdf=np.array([0])
    cdf=np.append(cdf,cd)
    cd2=integrate.cumtrapz(y_new,logx_new)
    cdf2=np.array([0])
    cdf2=np.append(cdf2,cd2)
    return [x_new,y_new,dydlogx,dydx,cdf,cdf2]


def peak_and_saddlefinder(x,y,dydlogx,x2,y2,z2): #x-fitted time, y-fitted
Radiance, dRdlogt, unfitted t_2, unfitted T, unfitted T_error
    pks, _ = find_peaks(y,height=0)
    #extreme points
    xx=[x[pks[i]] for i in range(len(pks))]
    yy=[y[pks[i]] for i in range(len(pks))]
    cutofftime1=100#use 100 if time scale in ns instead of seconds
    cutofftime2=1000 #use 1000 if time scale in ns instead of seconds

    #Peak-1 identification and temperature at peak 1
    pkp1=[x for x in xx if x<cutofftime1]
    indexp=[xx.index(x) for x in pkp1]
    pkv1=[yy[x] for x in indexp]
    bb=[pkv1[x]/max(pkv1) for x in range(len(pkv1))]
    Peakvalue=yy[bb.index(next(x for x in bb if x > 0.3))] #0.5 value is to
ensure that first 'signifcant' peak over 0.5Imax is chosen
    Peakposition=xx[yy.index(Peakvalue)]
    diff=np.absolute(x2-Peakposition)
    index_T=diff.argmin()
    a=y2[index_T-2:index_T+2]
    a_error=z2[index_T-2:index_T+2]
    PeakTemp=np.nanmean(a)
    error1=np.nanmean(a_error)

    #Saddle point identification and temperature at saddle point
    new=dydlogx-min(dydlogx)+10
    log_new=[math.log10(new[x]) for x in range(len(new))]
    av=np.mean(log_new[0:40])
```

```
    d_a1=np.absolute(x-cutofftime1)
    i1=d_a1.argmin() #index for where x (time) is closest to 100ns
    d_a2=np.absolute(x-cutofftime2)
    i2=d_a2.argmin() #index for where x (time) is closest to 1000ns
    difference_array = np.absolute(log_new-av)
    indexs = difference_array[i1:i2].argmin()+i1
    Saddlepoint=x[indexs]
    Saddlevalue=y[indexs]
    diff_2=np.absolute(x2-Saddlepoint)
    index_T2=diff_2.argmin()
    a1=y2[index_T2-2:index_T2+2]
    a1_error=z2[index_T2-2:index_T2+2]
    SaddleTemp=np.nanmean(a1)
    error2=np.nanmean(a1_error)
    BulkTemp=y2[index_T2:-1]
    MaxBulkTemp=max(BulkTemp)
    MedianBulkTemp=stat.median(BulkTemp)
    FinalBulkTemp=np.nanmean(BulkTemp[-5:-1])

    return
[xx,yy,Peakvalue,Peakposition,PeakTemp,error1,Saddlepoint,Saddlevalue,SaddleTemp,
error2,indexs,index_T,index_T2,MaxBulkTemp,MedianBulkTemp,FinalBulkTemp]


def peak_finder(x,dydlogx,cutofftime1,cutofftime2):
    pks, _ = find_peaks(dydlogx,height=0)
    #extreme points
    xx=[x[pks[i]] for i in range(len(pks))]
    yy=[dydlogx[pks[i]] for i in range(len(pks))]

    #Peak-1 identification
    pkp1=[x for x in xx if x<cutofftime1]
    indexp=[xx.index(x) for x in pkp1]
    if len(indexp)==0:
        Peakvalue=math.nan
        Peakposition=math.nan
    else:
        Peakvalue=max([yy[x] for x in indexp])
        Peakposition=xx[yy.index(Peakvalue)]
    #Peak-2 identification
    pkp2=[x for x in xx if x>cutofftime2]
    indexp2=[xx.index(x) for x in pkp2]
    Peakvalue2=max([yy[x] for x in indexp2])
    Peakposition2=xx[yy.index(Peakvalue2)]
    return [Peakposition,Peakvalue,Peakposition2,Peakvalue2]
```

```
def plotmepls(xr,yr,x2,y2,x_ex,y_ex,px,py,sx,sy,x):
            fig, ax1 = plt.subplots()
            ax1.set_xlabel('time,s')
            ax1.title.set_text('Radiance and dR/dlogt plots along with extrema in
run '+str((x/2)+1))
            plt.xscale('log')
            ax1.set_ylabel('Radiance, W/Sr.m^2', color = 'black')
            ax1.plot(xr, yr, color = 'black')
            plt.scatter(x_ex,y_ex,s=15,marker = 'o',color = 'black')
            plt.scatter(px,py,s=40, marker = 'o',color = 'r')
            plt.scatter(sx,sy,s=40, marker = 'o',color = 'r')
            ax2 = ax1.twinx()
            ax2.set_ylabel('dR/dlogt, arb', color = 'blue')
            ax2.plot(x2, y2, color = 'blue')
            ax2.tick_params(axis ='y', labelcolor = 'blue')
            return plt.show()

def plotme2pls(x_r,y_r,x_t,y_t,x_ex,y_ex,x_s,y_s,px,py,pt1_x, pt1_y,pt2_x,
pt2_y,x):
            fig, ax1 = plt.subplots()
            ax1.set_xlabel('time,s')
            ax1.title.set_text('Radiance and Temperature plots along with extrema
in run '+str((x/2)+1))
            plt.xscale('log')
            ax1.set_ylabel('Radiance, W/Sr.m^2', color = 'black')
            ax1.plot(x_r, y_r, color = 'black')
            ax1.tick_params(axis ='y', labelcolor = 'black')
            plt.scatter(x_s,y_s,marker = '^',color = 'blue')
            plt.scatter(x_ex,y_ex,marker = 'o',color = 'black')
            plt.scatter(px,py,marker = '^',color = 'blue')
            ax2 = ax1.twinx()
            ax2.set_ylabel('Temperature, K', color = 'red')
            plt.scatter(x_t, y_t, s=25,color = 'red')
            ax2.plot(x_t, y_t, color = 'red')
            plt.scatter(pt1_x, pt1_y, s=100,marker = '*',color = 'blue')
            plt.scatter(pt2_x, pt2_y, s=100,marker = '*',color = 'blue')
            ax2.tick_params(axis ='y', labelcolor = 'red')
            return plt.show()
#Body---------------------------------------------------------------------------
-------------------------------------------------------------------------

# Change location as needed and use double back slashes
os.chdir('C:\\Users\\salva\\Box\\Project 4- Dilution of PBX\\Raw Data\\Processed
PMT\\HMX\\20 wtp')
```

```
path = os.getcwd()
txt_files = glob.glob(os.path.join(path, "*radiance.txt"))
txt_files_2 = glob.glob(os.path.join(path, "*grayTemp.txt"))



folder_name=path.rpartition('\\')[2] #folder name is assumed sample/condition
detail


Excelwriter = pd.ExcelWriter(str(folder_name)+'.xlsx', engine='xlsxwriter')
Dlist=[]
namecounter=[]
for t in range(len(txt_files)):

    #reading txt file: Radiance data
    temps=[]
    with io.open(txt_files[t], mode="r") as f:
        next(f) #label
        next(f) #units
        next(f) #file name
        #copying data
        for line in f:
            temps.append(line.split())

    temp=np.array(temps, dtype=np.float32) #actual temporary file
    temps=[]

    #reading txt file: corresponding temperature data
    temps_2=[]
    with io.open(txt_files_2[t], mode="r") as f:
        next(f) #label
        next(f) #units
        next(f) #file name
        #copying data
        for line in f:
            temps_2.append(line.split())

    temp_2=np.array(temps_2, dtype=np.float32) #actual temporary file
    temps_2=[]

    file_analyzed = txt_files[t].split('\\')[-1]
    file_analyzed = file_analyzed.split('.txt')[0]
```

```
    #pocessing each sample: has several runs in txt file
    Dmain = pd.DataFrame(columns = ['Peak-I-x','Peak-I-y','Peak
T/K','Error','transition-x','transition-y','Transition T','Error2','Area-Shock
rise','Area-decay','Area-Growth','NArea-Shock rise','NArea-decay','NArea-
Growth','Peak-I-MaxRate-x','Peak-I-Maxrate-y','Peak-II-Maxrate-x','Peak-II-
Maxrate-y','MaxBulkT/K','MedianBulkT/K','FinalBulkT/K'])
    for i in range(0,np.shape(temp)[1],2):

        #Radiance
        t_1=[temp[j,i] for j in range(len(temp[:,i])) if temp[j,i]>0] #accepting
positive values for time
        R=[temp[j,i+1] for j in range(0,len(t_1),1)] #accepting non-NAN values
for radiance

        #Temperature
        corr=int(i*(3/2))
        t_2=[temp_2[j,corr] for j in range(len(temp_2[:,corr])) if
temp_2[j,corr]>0] #accepting positive values for time
        T=[temp_2[j,corr+1] for j in range(len(t_2))] #accepting all Temperature
values
        T_error=[temp_2[j,corr+2] for j in range(len(t_2))] #accepting all
Temperature error values



        #Fitting radiance data and arriving at instantaneous differential and
cumulative integral values
        f_and_d=fit_derivative_and_integral(t_1,R) #tuple with new fit x and y
and dydx
        t_fit=f_and_d[0]   #Time in nano seconds
        R_fit=f_and_d[1]   #Radiance W/Sr.m^2
        dRdlogt=f_and_d[2] #Derivative of Radiance on log of time
        dRdt=f_and_d[3]    #Derivative of Radiance as a function of time
        Rcdf=f_and_d[4]    #Cumulative Integral on linear timescale
        Rcdflogt=f_and_d[5]   #Cumulative Integral on logscale


        #Extrema location in Radiance, differnatial radiance and corresponding
Temperature at extrema identifed
        p_and_s=peak_and_saddlefinder(t_fit,R_fit,dRdlogt,t_2,T,T_error)
        t_extreme=p_and_s[0]
        R_extreme=p_and_s[1]
        Peakvalue=p_and_s[2]
        Peakposition=p_and_s[3]
        PeakTemp=p_and_s[4]
        error=p_and_s[5]
```

```
        Saddlepoint=p_and_s[6]
        Saddlevalue=p_and_s[7]
        SaddleTemp=p_and_s[8]
        error2=p_and_s[9]
        index=p_and_s[10] #index of saddle point in t_fit data
        index_T=int(p_and_s[11])#index of Peak1 in t_2 data
        index_T2=int(p_and_s[12]) #index of Saddle point in t_2 data
        MaxBulkTemp=p_and_s[13]
        MedianBulkTemp=p_and_s[14]
        FinalBulkTemp=p_and_s[15]

        #Max dRdlogt location and values for nano and micro second peaks
        p2p=peak_finder(t_fit,dRdlogt,Peakposition,Saddlepoint)
        Peak1maxdiffposition=p2p[0]
        Peak1maxdiffvalue=p2p[1]
        Peak2maxdiffposition=p2p[2]
        Peak2maxdiffvalue=p2p[3]

        #Area under curve in three sections identified
        A_shockrise=Rcdf[np.where(t_fit == Peakposition)]
        A_decay=Rcdf[index]-A_shockrise
        A_bulk=Rcdf[-1]-A_decay

        #Normalized Area: Integral of Radiance on logtime
        A_s=Rcdflogt[np.where(t_fit == Peakposition)]
        A_d=Rcdflogt[index]-A_s
        A_b=Rcdflogt[-1]-A_d

        #Writing data
        AllXY =
np.column_stack((Peakposition,Peakvalue,PeakTemp,error,Saddlepoint,Saddlevalue,Sa
ddleTemp,error2,
A_shockrise,A_decay,A_bulk,A_s,A_d,A_b,Peak1maxdiffposition,Peak1maxdiffvalue,Pea
k2maxdiffposition,Peak2maxdiffvalue,MaxBulkTemp,MedianBulkTemp,FinalBulkTemp))
        X = pd.DataFrame(AllXY,columns = ['Peak-I-x','Peak-I-y','Peak
T/K','Error','transition-x','transition-y','Transition T','Error2','Area-Shock
rise','Area-decay','Area-Growth','NArea-Shock rise','NArea-decay','NArea-
Growth','Peak-I-MaxRate-x','Peak-I-Maxrate-y','Peak-II-Maxrate-x','Peak-II-
Maxrate-y','MaxBulkT/K','MedianBulkT/K','FinalBulkT/K'])
        Dmain = Dmain.append(X)


        #print("done")

        #Plots
```

```
        #plotmepls(t_fit,R_fit,t_fit,dRdlogt,t_extreme,R_extreme,Peakposition,Pea
kvalue,Saddlepoint,Saddlevalue, i)
        #plotme2pls(t_fit,R_fit,t_2,T,t_extreme,R_extreme,Saddlepoint,Saddlevalue
,Peakposition,Peakvalue,t_2[index_T],PeakTemp,t_2[index_T2],SaddleTemp, i)

    #fname  = "%s.csv" %(folder_name)
    #Dmain.to_csv(fname)
    Dlist.append(Dmain)
    namecounter.append(file_analyzed)
    print("txt file "+str(t+1)+" complete")

for i, file in enumerate (Dlist):
    file.to_excel(Excelwriter, sheet_name=str(namecounter[i]),index=False)

Excelwriter.save()
Excelwriter.close()
```

APPENDIX C: IMAGE ANALYSIS PROGRAMS

C.1 Overview

The following provides the functional portions of code used to analyze PBXs for microstructure features such as particles, boundaries, interconnections, and importantly clusters. These are used at various stages in Chapters 3,4 and 5.

C.2 Clustering Size/Frequency Count

This code takes images with high enough resolution to view individual particles and analyzes their size and clustering tendencies. Code posted here with permission from Siva Valluri, the original author.

```
"""
Cluster Finder with Stats: Custom contact
definition##########################################################################
#####################################################################
Requires:
-contours generated by opencv
-segmented image
-address to save images
-name for the segmented image
-choice2-Do you want to save images generated?
-choice3-Do you want to SEE images generated?

Returns:
-Cluster statistics as a dataframe: min area bounding rectangle,
number of particles in cluster, Indices of particles in cluster

#####################################################################
#####################################################################
"""
#usr/bin/python3

def
Cluster_Finder_with_Statistics(contours,img_gray,address,imagename,cho
ice2,choice3):
    import numpy as np
```

```
    from scipy.spatial import cKDTree
    import pandas as pd
    from scipy.spatial import ConvexHull
    import cv2

    Cluster_Statistics_df=pd.DataFrame()
    Cluster_Statistics_df = pd.DataFrame(columns = ['Image
Title','Rect fit-width/pixel','Rect fit-height/pixel','Number of
particles in cluster','Indices of particles in cluster'])

    #Converting contour tuple into list of particle perimeters
    List_of_particle_perimeters = []
    for contour in contours:
        particle_perimeter=contour[:,0,:]
        List_of_particle_perimeters.append(particle_perimeter)


    ##########################################################################
##################Finding contacting particle
pairs##########################################################################
######################
    Contact_points_df = pd.DataFrame()
    Contact_points_df = pd.DataFrame(columns = ['Contact-x/pixel',
'Contact-y/pixel', 'Particleindex-1', 'Particleindex-2'])

    #Plotting to verify code
    #plt.figure()
    #for i in List_of_particle_perimeters:
        #plt.plot(i[:, 0], i[:, 1], "-", markersize=5) #Negative sign
to correct for the way python reads the image

    List_of_contacting_particle_indices = []
    for current_particle_index in
range(0,len(List_of_particle_perimeters),1):
        other_particle_perimeter_indeces=
list(np.arange(0,len(List_of_particle_perimeters),1))
        other_particle_perimeter_indeces.remove(current_particle_index
)

        for other_particle_index in
other_particle_perimeter_indeces:
            kd_tree1 =
cKDTree(List_of_particle_perimeters[current_particle_index])
            kd_tree2 =
cKDTree(List_of_particle_perimeters[other_particle_index])
```

```
            number_of_contact_points=kd_tree1.count_neighbors(kd_tree2
, r=2) #Second input term is radius of survey
            contact_indexes = kd_tree1.query_ball_tree(kd_tree2, r=2)
            for i in range(len(contact_indexes)):
                for j in contact_indexes[i]:
                    x =
int((List_of_particle_perimeters[current_particle_index][i,
0]+List_of_particle_perimeters[other_particle_index][j, 0])/2)
                    y =
int((List_of_particle_perimeters[current_particle_index][i,
1]+List_of_particle_perimeters[other_particle_index][j, 1])/2)
                    c = int(current_particle_index)
                    o = int(other_particle_index)

                    Dataset1 = np.column_stack((x,y,c,o))
                    X1 = pd.DataFrame(Dataset1,columns = ['Contact-
x/pixel', 'Contact-y/pixel', 'Particleindex-1', 'Particleindex-2'])
                    Contact_points_df = pd.concat([Contact_points_df,
X1], ignore_index=True)
                    #Plotting just the defined 'contact points'
                    #plt.scatter(x,y,s=20) #code verification
                    #Connecting the points
                    #plt.plot([List_of_particle_perimeters[current_par
ticle_index][i, 0],
List_of_particle_perimeters[other_particle_index][j,
0]],[List_of_particle_perimeters[current_particle_index][i, 1],
List_of_particle_perimeters[other_particle_index][j, 1]], "-r")
            if number_of_contact_points>0:
                pair_indices=np.array([current_particle_index,other_pa
rticle_index])
                List_of_contacting_particle_indices.append(pair_indice
s)

    result_df = Contact_points_df.drop_duplicates(['Contact-x/pixel',
'Contact-y/pixel'],ignore_index=True)

    #########Finding clusters by going through pairs and ensuring
'friend-of-friends' are grouped together as one
cluster#########################################################################
#########################
    Particle_indices_in_Cluster = []
    while len(List_of_contacting_particle_indices)>0:
        first, *rest = List_of_contacting_particle_indices
        first = set(first)
```

```
        lf = -1
        while len(first)>lf:
            lf = len(first)

            rest2 = []
            for r in rest:
                if len(first.intersection(set(r)))>0:
                    first |= set(r)
                else:
                    rest2.append(r)
            rest = rest2
        Particle_indices_in_Cluster.append(first)
        List_of_contacting_particle_indices = rest

    #Converting Cluster indices tuple into list of lists again
    for cluster in range(0,len(Particle_indices_in_Cluster),1):
        Particle_indices_in_Cluster[cluster]=list(Particle_indices_in_
Cluster[cluster])


    ##########################################################################
#########
    boundingboxes_of_clusters = []
    Hulls_of_clusters = []
    for cluster in Particle_indices_in_Cluster:
        Circumference_Points_of_Cluster = []
        Circumference_Points_of_Cluster = np.array([0,0])
        for particle_index in range(0,len(cluster),1):
            Circumference_Points_of_Cluster =
np.vstack((Circumference_Points_of_Cluster,np.array(List_of_particle_p
erimeters[int(cluster[particle_index])])))

        Circumference_Points_of_Cluster=np.delete(Circumference_Points
_of_Cluster,0,0)
        Hull=ConvexHull(Circumference_Points_of_Cluster)
        hull_points = Circumference_Points_of_Cluster[Hull.vertices]
        Hulls_of_clusters.append(hull_points)

        rect = cv2.minAreaRect(hull_points)

        #data no.2 and 3
        rect_width=rect[1][0]
        rect_height=rect[1][1]

        box = cv2.boxPoints(rect)
```

```
        box = np.int0(box)
        boundingboxes_of_clusters.append(box)

        #data no.4
        number_of_particle_in_cluster =len(cluster)

        Dataset1 =
np.column_stack((imagename,rect_width,rect_height,number_of_particle_i
n_cluster,str(cluster)))
        X1 = pd.DataFrame(Dataset1,columns = ['Image Title','Rect fit-
width/pixel','Rect fit-height/pixel','Number of particles in
cluster','Indices of particles in cluster'])
        Cluster_Statistics_df = pd.concat([Cluster_Statistics_df, X1],
ignore_index=True)

    Hulls_of_clusters=tuple(Hulls_of_clusters)
    boundingboxes_of_clusters=tuple(boundingboxes_of_clusters)
    #Plotting particles (contours) identified and their bounding
boxes#################################################################
###
    if choice3.lower() in  ["y","yes","yippee ki
yay","alright","alrighty"]:
        image_copy = img_gray.copy()
        image_copy = cv2.cvtColor(image_copy, cv2.COLOR_GRAY2BGR)
        cv2.drawContours(image=image_copy, contours=Hulls_of_clusters,
contourIdx=-1, color=[0,0,250], thickness=0.5, lineType=cv2.LINE_AA)
        cv2.drawContours(image=image_copy, contours=contours,
contourIdx=-1, color=[0,0,250], thickness=1, lineType=cv2.LINE_AA)
        cv2.drawContours(image=image_copy,
contours=boundingboxes_of_clusters, contourIdx=-1, color=[0,250,0],
thickness=2, lineType=cv2.LINE_AA)
        cv2.imwrite(str(address)+'\\'+'Clusters identified in image
.tif', image_copy)
        if choice2.lower() in  ["y","yes","yippee ki
yay","alright","alrighty"]:
            cv2.imshow('Clusters identified', image_copy)
            cv2.waitKey(0)

    return Cluster_Statistics_df, result_df
```

C.3 Density Correlation: K,L and G functions

C.3.1 Autocorrelation (G) function calculation

The following Python code is used to analyze HMX thin films for their density correlations. From here clustering tendencies can be compared. Author Lawrence Salvati, using Astropy and Scipy modules in python.

```
#usr/bin/python3

import numpy as np
import pandas as pd
from astropy.stats import RipleysKEstimator
import matplotlib.pyplot as plt
import scipy.stats as st
import cv2
from scipy.spatial import KDTree
import random

save_name = file_name_string
#import image
dR = 3 #pixel units
rho_I = 0
rho_II = 1
unit_conv = 4.8 #pixels per micron
im = cv2.imread(image_file_string,0)
im = im/255
cv2.imshow('image',im)
"Boundaries of Image, a circle with radius R for edge correction"
xCenter = int(len(im[:,0])/2)
yCenter = int(len(im[0,:])/2)
D = min((xCenter,yCenter))*2
R = D/2
yMin = int((D-len(im[0,:]))/2)
xMin = int((D-len(im[:,0]))/2)
xMax = int(len(im[:,0]) - xMin)
yMax = int(len(im[0,:]) - yMin)
frame_area = np.pi*R**2
rMin = 0.25 #minimum search radius in microns
rMax = int(.50*R) #maximum search radius in pixels, make this no more
than 0.25*smallest dimension of search area
r = np.arange(rMin*unit_conv,rMax,step = 1) #currently pixel units
```

```
M = len(r)
A = np.transpose(np.where(im==0)) #list of all indices s.t. pixel
value = 0 (HMX)
im_kd = KDTree(A) #kd tree of HMX locations
Ar = im_kd.query_ball_point((int(xCenter),int(yCenter)),r=R) #All A in
range of bounding circle
X  = Ar
random.shuffle(X)
X = A[X]
N = 5000
#N = len(X)
Rho = np.zeros((N,M))
G = np.zeros((N,M))

for i in range(N):
    for j in range(M):
        #calculate weight factor (edge correction)
        dij = np.sqrt((X[i,0]-xCenter)**2+(X[i,1]-
yCenter)**2)#distance from center
        idxR = im_kd.query_ball_point(X[i,:],r=r[j])
        idxRdR = im_kd.query_ball_point(X[i,:],r=(r[j]+dR))
        dA = np.pi*((r[j]+dR)**2-r[j]**2)
        #dA = 2*np.pi*r[j]*dR
        if dij + r[j] < R:
            w = 1
        else:
            w = r[j]**2*np.arccos((dij**2+r[j]**2-
R**2)/(2*dij*r[j]))+R**2*np.arccos((dij**2+R**2-r[j]**2)/(2*dij*R)) -
0.5*np.sqrt((-dij+r[j]+R)*(dij+r[j]-R)*(dij-r[j]+R)*(dij+r[j]+R))
            w = w/(np.pi*r[j]**2)
        G[i,j] = (len(idxRdR) - len(idxR))/(dA*w)
        Rho[i,j] = len(idxR)/(np.pi*r[j]**2)
        '''
        for m in range(int(X[i,0]-r[j]),int(X[i,0]+r[j])):
            for n in range(int(X[i,1]-r[j]),int(X[i,1]+r[j])):
                    if np.sqrt((m-X[i,0])**2+(n-X[i,1])**2) < r[j]:
                        I[j,i] = I[j,i]+(im[m,n])
        I[j,i] = I[j,i]/(np.pi*r[j]**2)
        '''
    print(i)
Vrel = len(Ar)/frame_area
Rho_mean = np.mean(Rho,0)
G_mean = np.mean(G,0)
print(Vrel)
Vrel = np.ones(len(r))*Vrel
```

```
plt.plot(r/unit_conv,G_mean/Vrel,r/unit_conv,np.ones(len(r)))

print(G.max())
DataSet = np.column_stack((r/unit_conv,(G_mean),Rho_mean,Vrel))
Results = pd.DataFrame(DataSet,columns = ['Search Radius
(micron)','Pair Correlation function (vol frac)','Local Density (vol
frac)','Bulk Density (vol frac)'])
Results.to_csv(save_name)
plt.show()
```

C.3.2 Ripley's K and L clustering tests

```
# usr/bin/python 3
'''This script will take SEM cross section data and analyze global
clustering statistics. Primarily this will rely on K(r) function
under the assumption that HMX particles are roughly unimodal and thus
point processes. While an imperfect comparison this will give a
method by which to compare the propensity to form clusters and
channels as concentration changes'''

'''The work flow is as follows: a binarized image (marked up as a 8-
bit file) will be imported and the particle centroids can then be
determined. Using this data
a number density inside of a search radius is given per particle. Then
a random number generator will simulate pseudorandom distributions to
provide a
relation to complete spatial randomness (CSR). Because these are not
point processes and in fact particles of finite size (Mode size 4
microns)'''

'''K function is rigorously defined as
K(r) = N**(-1)*E[number of extra events within distance r of a
randomly chosen event]
Thus being a measure of statistical non-randomness. Because this is
assumed to be events of a fixed size,
this is modeled as a Matern Hard Core Process. Thus the model by which
expectation value of extra events is defined is as follows:
K(r) = ((2 pi rho)/(exp(-rho pi del**2)))*sum_0t(r*k(r)dr)

where rho is the intensity of a poisson process and
del is the critical distance s.t
del geq r_min else del =0
```

```
k(r) is probability of retaining a pair of events separated by a
distance r:

i.e:
if d < del:
    k(r) = 0
else:
    k(r) = exp(-rho V(d,del))

Where V is the intersect area between two circles of radius del
separated by distance d


'''
###CREDITS FOR SIMULATION###
# Simulate Matern hard-core point processes (Type I/II) on a
rectangle.
# Author: H. Paul Keeler, 2019.
# Website: hpaulkeeler.com
# Repository: github.com/hpaulkeeler/posts
# For more details, see the post:
# hpaulkeeler.com/simulating-matern-hard-core-point-processes/

# 230x SEM images correspond to 2.4 pixels per micron so a minimum
distance of 5 pixels will be imposed'''
# 48pixels/10 um, so 4.8 pixels per micron
# All units will be in pixels until converted
#518/100um for Thermo 350x image
#or 5.18 px/micron
#248/100
#import modules
import numpy as np
import pandas as pd
from astropy.stats import RipleysKEstimator
import matplotlib.pyplot as plt
import scipy.stats as st


unit_conv = 4.8 #pixels per micron
#read from csv make xy info a dataframe
img_name = '40wtp_450x_001.csv'
save_name = '40_wtp_Results_001.csv'
XY = pd.read_csv(img_name)
z = XY[['X','Y']].to_numpy()
rMin = 3 #minimum search radius in microns
```

```
"Boundaries of Image"
xMin = 0
xMax = max(z[:,0])+rMin*4
yMin = 0
yMax = max(z[:,1])+rMin*4
rMax = 0.25*yMax #maximum search radius in microns
r = np.linspace(rMin*unit_conv,rMax,250) #currently pixel units
frame_area = (xMax-xMin)*(yMax-yMin)
Kest = RipleysKEstimator(area = frame_area,x_max = xMax,y_max =
yMax,x_min = xMin,y_min = yMin)
N = len(z[:,0])
N_hat = N/frame_area
#generate random coordinates
'''
iterations = 100
L = np.zeros((len(r),iterations))
for i in range(iterations):
    x_rand = np.random.rand(len(z[:,0]))*x_max
    y_rand = np.random.rand(len(z[:,0]))*y_max
    z_rand = np.column_stack((x_rand,y_rand))
    L[:,i] = Kest.Lfunction(data = z_rand,radii = r, mode = 'ripley')
'''

numbSim=10**1; #number of simulations

#Parameters for the parent and daughter point processes
lambdaPoisson=N_hat;#density of underlying Poisson point process
radiusCore=int(rMin*unit_conv);#radius of hard core

#Extended simulation windows parameters
rExt=radiusCore; #extension parameter -- use core radius
xMinExt=xMin-rExt;
xMaxExt=xMax+rExt;
yMinExt=yMin-rExt;
yMaxExt=yMax+rExt;
#rectangle dimensions
xDeltaExt=xMaxExt-xMinExt;
yDeltaExt=yMaxExt-yMinExt;
areaTotalExt=xDeltaExt*yDeltaExt; #area of extended rectangle

###START Simulations START####
#initialize arrays for collecting statistics
L_I = np.zeros((len(r),numbSim))
L_II = np.zeros((len(r),numbSim))
L_P = np.zeros((len(r),numbSim))
```

```
#H_P = np.zeros((len(r),numbSim))
numbPointsAll=np.zeros(numbSim); #number of Poisson points
numbPointsAll_I=np.zeros(numbSim); #number of Matern I points
numbPointsAll_II=np.zeros(numbSim); #number of Matern II points
#loop through for each simulation
for ss in range(numbSim):

    #Simulate Poisson point process for the parents
    numbPointsExt=
np.random.poisson(areaTotalExt*lambdaPoisson);#Poisson number
    #x and y coordinates of Poisson points for the parent
    xxPoissonExt=xMinExt+xDeltaExt*np.random.rand(numbPointsExt);
    yyPoissonExt=yMinExt+yDeltaExt*np.random.rand(numbPointsExt);

    #thin points if outside the simulation window
    booleWindow=((xxPoissonExt>=xMin)&(xxPoissonExt<=xMax)&(yyPoissonE
xt>=yMin)&(yyPoissonExt<=yMax));
    indexWindow=np.arange(numbPointsExt)[booleWindow];
    #retain points inside simulation window
    xxPoisson=xxPoissonExt[booleWindow];
    yyPoisson=yyPoissonExt[booleWindow];

    numbPoints=len(xxPoisson); #number of Poisson points in window
    #create random marks for ages
    markAge=np.random.rand(numbPointsExt);

    ###START Removing/thinning points START###
    booleRemoveI=np.zeros(numbPoints, dtype=bool);#Index for removing
points -- Matern I
    booleKeepII=np.zeros(numbPoints,dtype=bool);#Index for keeping
points -- Matern II
    for ii in range(numbPoints):
        distTemp=np.hypot(xxPoisson[ii]-xxPoissonExt,yyPoisson[ii]-
yyPoissonExt);  #distances to other points
        booleInDisk=(distTemp<radiusCore)&(distTemp>0); #check if
inside disk

        #Matern I
        booleRemoveI[ii]=any(booleInDisk);

        #Matern II
        #keep the younger points
        if len(markAge[booleInDisk])==0:
            booleKeepII[ii]=True;
```

```
            #Note: if markAge(booleInDisk) is empty,
keepBooleII[ii]=True.
        else:
            booleKeepII[ii]=all(markAge[indexWindow[ii]]<markAge[boole
InDisk]);


    ###END Removing/thinning points END###

    #Remove/keep points to generate Matern hard-core processes
    #Matérn I
    booleKeepI=~(booleRemoveI);
    xxMaternI=xxPoisson[booleKeepI];
    yyMaternI=yyPoisson[booleKeepI];

    #Matérn II
    xxMaternII=xxPoisson[booleKeepII];
    yyMaternII=yyPoisson[booleKeepII];

    #Update statistics
    numbPointsAll[ss]=numbPoints;
    numbPointsAll_I[ss]=len(xxMaternI);
    numbPointsAll_II[ss]=len(xxMaternII);
    L_I[:,ss] = np.sqrt(Kest(data =
np.column_stack((xxMaternI,yyMaternI)),radii = r, mode =
'ripley')/np.pi)-r
    L_II[:,ss] = np.sqrt(Kest(data =
np.column_stack((xxMaternII,yyMaternII)),radii = r, mode =
'ripley')/np.pi)-r
    L_P[:,ss] = np.sqrt(Kest(data =
np.column_stack((xxPoisson,yyPoisson)),radii = r,mode =
'ripley')/np.pi)-r
    #H_I[:,ss] = Kest.Hfunction(data =
np.column_stack((xxMaternI,yyMaternI)),radii = r, mode =
'ripley')/np.pi)-r
    #H_II[:,ss] = Kest.Hfunction(data =
np.column_stack((xxMaternII,yyMaternII)),radii = r, mode =
'ripley')/np.pi)-r
    #H_P[:,ss] = Kest.Hfunction(data =
np.column_stack((xxPoisson,yyPoisson)),radii = r,mode = 'ripley')

###END Simulations END####

##Plotting
plt.figure(0)
```

```
markerSize=6; #marker size for the Poisson points
#plt.plot(xxPoisson/unit_conv,yyPoisson/unit_conv,
'ro',markerfacecolor="None",markersize=markerSize);
#plt.plot(xxMaternII/unit_conv,yyMaternII/unit_conv,
'rx',markersize=markerSize/2);
plt.scatter(z[:,0]/unit_conv,z[:,1]/unit_conv)
#plt.plot(xxMaternII/unit_conv,yyMaternII/unit_conv,
'b+',markersize=markerSize);
plt.legend(('Particle Centroid'));


CI_I = st.norm.interval(alpha=0.975,
                loc=np.mean(L_I,1),
                scale=st.sem(L_I,1))
CI_II = st.norm.interval(alpha=0.975,
                loc=np.mean(L_II,1),
                scale=st.sem(L_II,1))
CI_P = st.norm.interval(alpha = 0.975,
                loc = np.mean(L_P,1),
                scale = st.sem(L_P,1))

'''
plt.plot(r/unit_conv, Kest.poisson(r), color='green', ls=':',
label=r'$K_{pois}$ - Complete Spatial Randomness')
plt.plot(r/unit_conv, Kest(data=z, radii=r, mode='ripley'),
color='yellow',
         label='$K_{ripley}$')
plt.xlabel('Search Radius (microns)')
plt.ylabel('K-function (normalized # events inside search radius)')
plt.legend()
'''
L_data = Kest.Lfunction(data = z,radii = r, mode = 'ripley')-r
#L_data = np.sqrt(Kest(data = z,radii = r, mode =
'translation')/(np.pi))-r
plt.figure(1)
#plt.plot(r/unit_conv,CI_I[1]-r+2,'--',color = 'k',label = 'CSR, Type
I 97.5% CI')
#plt.plot(r/unit_conv,CI_I[0]-r+2,'--',color = 'k')
plt.plot(r/unit_conv,CI_P[1],'--',color = 'k',label = 'CSR, Poisson
Process 97.5% CI')
plt.plot(r/unit_conv,CI_P[0],'--',color = 'k')
#plt.plot(r/unit_conv,CI_II[1],'--',color = 'g',label = 'CSR, Type II
97.5% CI')
#plt.plot(r/unit_conv,CI_II[0],'--',color = 'g')
plt.plot(r/unit_conv,L_data,'g', label = 'data')
```

```
plt.xlabel('Search Radius (microns)')
plt.ylabel('L-function')
plt.legend()



###SAVE DATA AS CSV###
#Start by generating pandas dataframe
DataSet =
np.column_stack((r/unit_conv,L_data,CI_P[0],CI_P[1],CI_I[0],CI_II[1]))
Results = pd.DataFrame(DataSet,columns = ['Search Radius','L
function','CSR 97.5 Lower Bound','CSR 97.5 Lower Bound','Matern I
Process Upper','Matern I Lower'])
Results.to_csv(save_name)
print(len(xxPoisson))
print(len(z[:,0]))
plt.show()
'''
```

APPENDIX D: SAMPLE CHARACTERIZATION DATA

D.1 Thermogravimetry on TATB Samples

To control against any substantial change in decomposition kinetics attributed to changes in crystallite size or grain morphology, thermogravimetry analysis (TGA) experiments were conducted on the various TATB powders, where sufficient powder samples were available. The experiments were conducted using a TA Instruments Q50 Thermogravimetric analyzer. The crucible is filled with 1 mg of TATB powder. Heating rate was kept at 20 Kpm under a nitrogen (inert) atmosphere. Figure D.1 displays the derivative thermogravimetry (DTG) of all powders to observe if there are significant differences in thermal decomposition behavior between samples. The difference in peak shapes were not deemed to be significant, particularly when extrapolating to the regime of shock-induced or even hot spot induced heating rates.

D.2 X-Ray Diffraction Data on Recyrstallized HMX Powder

This work relied on a fixed method of recrystallizing HMX. Most literature points to *beta*-HMX being the dominant crystalline phase in standard laboratory conditions. However, to be thorough, the powder XRD measurements were collected for record. Powder XRD was collected using a Bruker D8 Advanced XRD system. Figure D.3 is the powder XRD spectrum of the HMX powder used in all the HMX studies (Chapters 3-6). There is no substantial evidence of polymorphism. Crystallite size and strain was unable to be measured due to literature reference data being inadequate.

D.3 Optical Profilometry Data on Thin-Layer HMX film in PDMS

Optical profilometry was performed on thin layers to verify the approximate height from spin coating. Using a Keyence VK-X1000 with pitch resolution of approximately 200 nm. Height is analyzed by step height from a reference plane; using a razor blade, a section of the

PDMS film is shaved off to leave the bare glass surface visible to the field of view. Using either image stitching or a single image field, step height can be determined. Figure D.4 is an example of the step height measurement of a PDMS-HMX spin coated film. There is both micron-scale roughness and slight bulging towards the center of the glass, that must be considered. The availability of PDV for these measurements allows exact time of flight to be determined in spite of inconsistency of the surface. What is important is that this approximate thickness and smoothness can be repeatably created by spin coating. (See Chapter 6 for procedure)

D.4 Optical Profilometry on Kapton wells filled with Plastic Explosive Samples

Using the procedure in D.4, the depth of empty Kapton wells, used frequently in these experiments, as well as the exact height and roughness of cast PBX cylinders can be determined. Figures D.5 and D.6 show representative examples of the surfaces created from 30 micron and 90 micron Kapton wells, respectively. It is very consistently less consistent trying to fill 30 micron wells with the current extrusion procedure. As a result, 90 μm-deep wells were preferred. Despite the difference in optical thickness, it optimized precision for a given thickness. The results determined from 10 measurements of each well depth are shown in Table D.1.

Table D.1 of Accuracy and precision of Kapton Well measurements based on optical profilometry data.

Listed depth (um)	Actual depth	Filled depth
40*	29.02 +/- 0.44	40.6+/- 10.22
65	66.230+/- 1.93	69.63 +/- 4.97
90	93.07 +/- 0.44	91.72 +/- 5.9
165	165.1 +/- 0.73	164.54 +/- 9.8

D.5 Figures

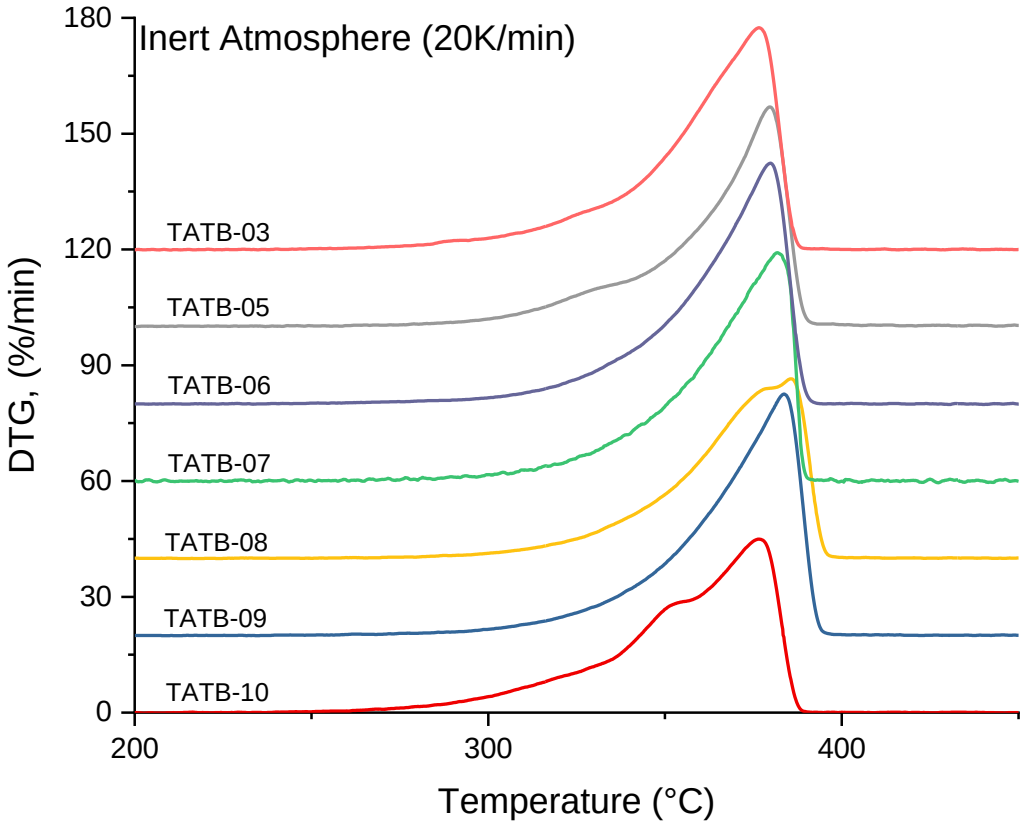

Figure D.1 TGA of all TATB powders available for studies in Chapter 4.

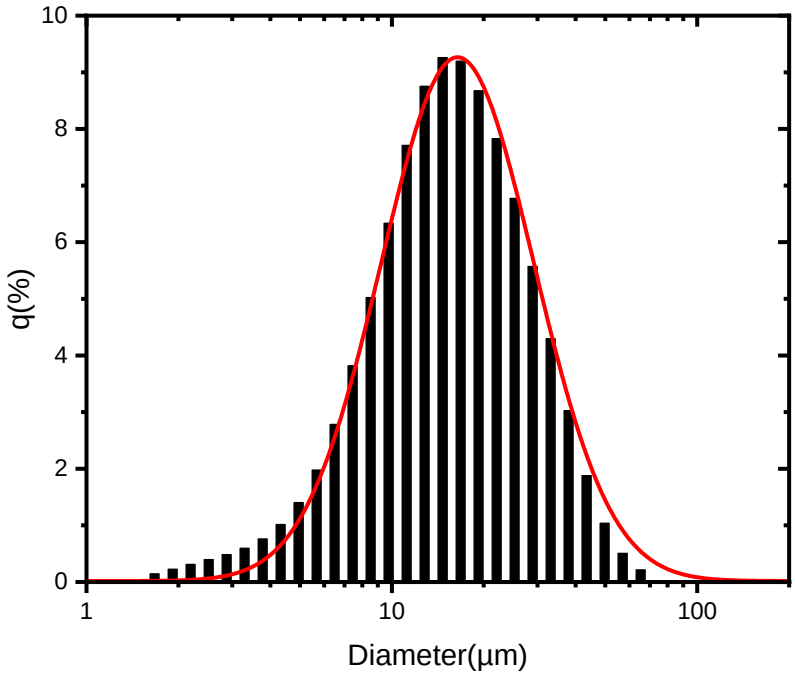

Figure D.2 Raw output of volume-based particle size distribution (from Horiba particle sizer) of HMX powder with lognormal fit.

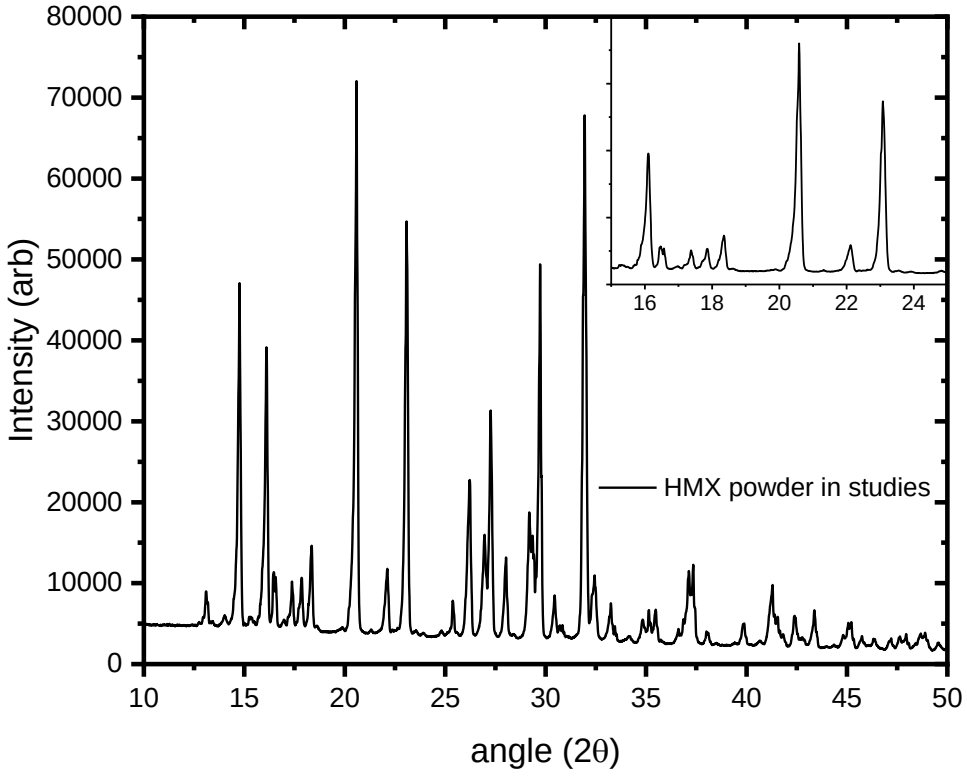

Figure D.3 Powder XRD of HMX powder

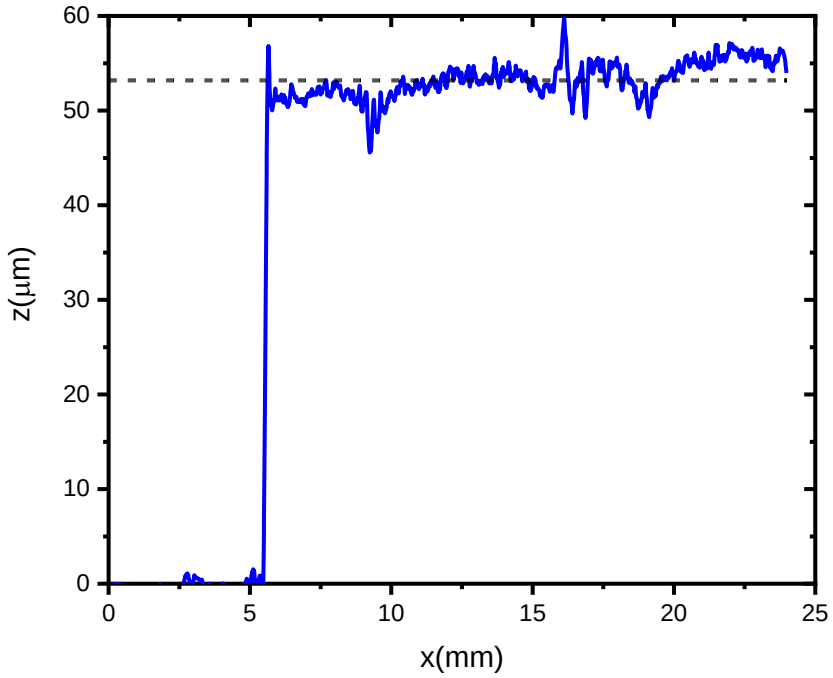

Figure D.4 Optical profilometry of spin-coated PDMS HMX mixture on glass.

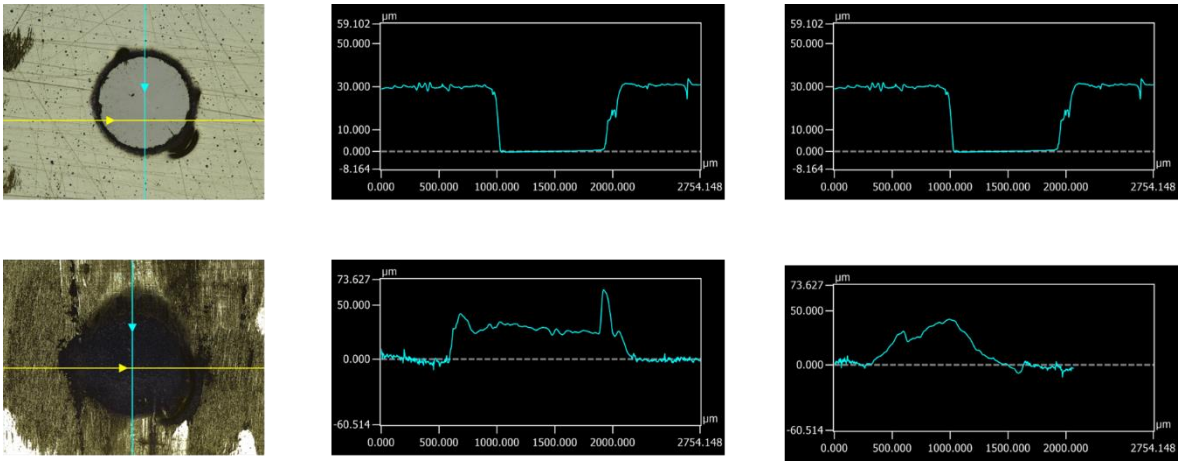

Figure D.5 Optical depth profile of 30-µm polyimide well empty (top) and filled with PDMS-based PBX (bottom)

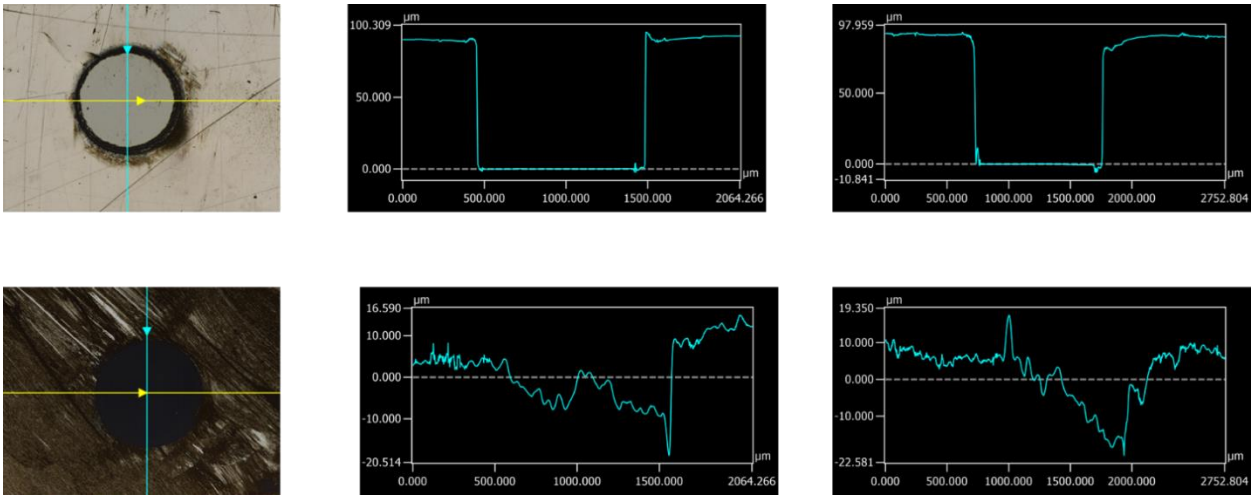

Figure D.6 Optical depth profile of 90-µm polyimide well empty (top) and filled with PDMS-based PBX (bottom)

APPENDIX E: METHODS OF ESTIMATING SHOCK PRESSURE

This section will explain the finer details of how various pressure estimates were established in this dissertation. The goal of this section is simply to provide a traceable source of calculations and parameters to support or contextualize claims made about pressures.

E.1 Shock Impedance and the Hugoniot Parameters

Estimates for shock pressure used in this dissertation often rely on estimates based on the practice of shock impedance matching between two different materials. It is infinitely preferable to simply know the particle velocity at the shock interface along with the two material Hugoniots. However, in many cases throughout this work, some of those conditions may not be true. Shock impedance is defined as the material density multiplied by the shock wave speed:

$$Z_{shock} = \rho_0 U_s \qquad \text{(E.1)}$$

Where Z_{shock} refers to the shock impedance, U_s is the shock wave velocity, and ρ_0 is the material density under initial conditions (usually STP). If the material Hugoniot equations of the material are available, shock velocity can be calculated from the observable variable, u_p, or particle velocity:

$$U_s = A + bu_p \qquad \text{(E.2)}$$

This relationship is usually linear with empirical parameters A, b available in literature databases.[1,2] There are sometimes exceptions to this, the only example seen in this dissertation is Pyrex glass which exhibits a somewhat complicated shock hugoniot. It can either be represented as a step function:

$$\{A, b\} = \begin{cases} \{1.73, 1.55\} : u_p < 1.7\ km/s \\ \{5.03, -0.176\} : u_p > 1.7\ km/s \end{cases} \qquad \text{(E.3)}$$

Alternatively a quadratic fit proves adequate for simpler treatment by computer algorithms:

$U_s \approx A + b_2 u_p^2 + b_1 u_p$ (E.4)

Using equation E.3, a list of common Hugoniot Parameters can be found in Table E.1

Table E.1 List of Hugoniot Parameters for common materials.

Material	ρ_0	A	b_2	b_1
Aluminum 1100	2.70	5.35	0	1.34
PETN-Pressed TMD	1.600	1.32	0	2.58
XTX-8003 (80 wt.% PETN 20 wt.% PDMS)	1.53	1.49	0	3.30

E.2 Shock Impedance Matching

When a shock reaches an interface between two different materials, those materials are likely to have different densities and sound speeds. This point will be an impedance boundary for shock waves as well, since shock speed is related to material sound speed (primarily by Hugoniot parameter A)[3]. The result is a transmitted shock wave and reflected shock wave such that pressure and particle velocity are continuous across the boundary. This is a necessary condition to conserve mass and energy flow. This is the main principle behind impedance matching.

This dissertation deals primarily with two cases: shock waves produced by flyer plates impacting materials and shock waves transmitted into a transparent amorphous or crystalline window material. In the former situation, Aluminum foil used in flyer plates (Al 1100) will always have a higher impedance than the target materials used in this dissertations with almost no exceptions. In the latter situation, shocked materials will very likely be lower impedance than the window material, either glass or crystalline.

E.2.1 Estimation of Shock Pressure from Aluminum Flyer Plates

To estimate the pressure a flyer plate imparts onto a victim sample, the particle velocity at the aluminum-target material interface is needed. From there, pressure in the victim material can be determined by the simple equation:

$$P = \rho_0 U_s u_p \qquad \text{(E.5)}$$

When aluminum impacts a material of lower impedance, a shock wave is generated by the movement of the material-aluminum interface. A shock wave is transmitted into the victim material, higher magnitude wave is reflected into the aluminum foil. Impedance matching is performed to make $\{P, u_p\}$ continuous across the material boundary. Thus, impedance matching is done by plotting material Hugoniots in $P - u_p$ space. For impacts, two forward-facing parabola are drawn, representing aluminum and the victim material. Since a wave is travelling backwards (in lab space) after reflection into the aluminum, another backward facing prabola must be drawn intersecting the two forward facing curves. Where this backward-facing curve intersects in u_p space dictates the calculated pressure. To draw it, the conditions for mass and energy conservation must be enumerated:

1. Pressure must be matched for aluminum reflecting into aluminum
2. Pressure must be matched for aluminum

In order for criterion 1 to be met in flyer plate experiments, the intersect for the backward facing aluminum P-u_p curve is simply the flyer velocity, u_f. Then, based on criterion 2, the intersect between the backward facing Aluminum hugoniot and the forward facing victim material hugoniot curve establishes the pressure of impact. Summarized as such:

$$\rho_{Al}[A_{Al}(u_p - u_f) + b_{Al}(u_p - u_f)^2] = \rho_{mat}[A_{mat}u_p + b_{mat}{u_p}^2] \qquad \text{(E.6)}$$

This is the mathematical dependence of flyer velocity on pressure in a given material.

It is important to note that the assertion of the reflection particle velocity as $u_f/2$ is actually an assumption since this value will slightly deviate from this in real experiments. The most robust pressure estimates rely on explicit measurements of u_p at material interfaces in order to calculate this pressure. However, in opaque materials (which consists of the majority of the samples used in this dissertation) optical velocimetry is impossible at this interface. Assuming an intersection at $u_f/2$ is a simplifying assumption that carries with it some error. This was the best available estimate, and from empirical evidene elsewhere does not significantly perturb the assertions made in this work.

E.2.2 Unknown Equations of State

Another source of uncertainty in pressure estimates is the fact that Hugoniot relations are extremely specific to the materials being predicted. Exact parameters for many materials being studied in this dissertation do not currently exist. Hugoniot parameters are determined from a wide range of experiments directly measuring particle velocity and shock velocity[1], the shock microscope is capable of doing this only for transparent materials.[4] Almost all plastic explosives are optically opaque unless the material thickness is significantly lower than 30 μm. As a result, in many cases throughout this dissertation only *comparisons* of materials with similar material properties can be used to estimate shock pressures. This is explicitly done in Chapter 5 in the case of HMX at very low concentrations. In this case, only limited data was available for HMX mixtures in soft binders: neat PDMS, 90 wt.% HMX in estane, and 100 wt.% HMX solvent pressed. Based on the Hugoniot relationship of equation E.2, parameters A, b can be plotted as a function of concentration. This yields a roughly linear relationship between parameters A, b and concentration. While these assumptions are significant, equalizing all of the results to 20 GPa using rough

assumptions still significantly improves the quality of the shock response data and does the best job possible based on what is currently available.

E.3 Estimating Equation of State for Reaction Products

The case in which shock impedance of the incoming boundary *higher* than the starting material is what happens when a shocked material reaches an optical window. This is the case when aluminum impacts ionic salts, or when high explosive reaches the glass window. In both cases, unlike the previous section, particle velocity is directly observable in experiments, making pressure calculations trivial. The particle velocity from velocimetry is corrected for change in refractive index, then the real u_p and standard density of the target is put into equation E.5.

However, if the desire is to know the pressure of the material sending the shock through, things can be much more complicated if the material is actively reacting. Since this is the case for deflagrating or detonating explosives, a new equation of state is needed to approximate the backward facing Hugoniot curve to equalize the shock sent backward, since it can no longer be assumed that the material is unreacted, but instead a mixture of intermediates and product gasses. These calculations are necessary to estimate what observed particle velocity would match the Chapman Jouget state (CJ pressure) of an explosive to cross-reference with experimental particle velocities. The equation of state used is an approximation called the Jones-Wilkins Lee Equation of State (JWL).

E.3.1 Overview of Jones-Wilkins Lee Equation of State

The Jones-Wilkins-Lee (JWL) equation of state refers to a commonly used equation of state for gas mixtures typical of explosive reaction products.[5] It takes the general form:

$$P = A\left(1 - \frac{\omega}{R_1 V'}\right)e^{-R_1 V'} + B\left(1 - \frac{\omega}{R_2 V'}\right)e^{-R_2 V} + \frac{\omega\left(E - E_0^{gas}\right)\rho_0}{V'} \qquad \text{(E.7)}$$

Where V' is relative volume and E is internal energy. The rest of the variables are fitted parameters, often experimentally determined and placed in literature. In the case of PETN and TATB samples calculated here, they were derived from Dobratz *et al*.[6]

Hugoniot relations resemble Isentropes to a second order approximation[3] which allows equation E.7 to be simplified to an isentropic pressure by the second law of thermodynamics:

$$P = Ae^{-R_1V'} + Be^{-R_2V'} + CV'^{-(1+\omega)} \qquad \text{(E.8)}$$

From here, particle velocity can be determined by further derivation done in other literature to yield[3]:

$$u_p = u_{CJ} + \int_{v_{CJ}}^{v} \sqrt{F(v)}\, dv \qquad \text{(E.9)}$$

The terms u_{CJ}, v_{CJ} are the particle velocity and volume of the Chapman-Jouget state. These values can easy be found from literature for many explosives, including XTX-8003 and PBX-9502, the subjects of this seciton. The integrand is the following term:

$$F(v) = \frac{AR_1}{v_0} e^{-\frac{R_1 v}{v_0}} + \frac{BR_2}{v_0} e^{-\frac{R_2 v}{v_0}} + \frac{(1+\omega)C}{v_0}\left(\frac{v}{v_0}\right)^{-(2+\omega)} \qquad \text{(E.10)}$$

This needs to be numerically integrated using a Matlab program with parameters given by literature.[5,6] The functional parts of code used are in the following section

E.4 Simulation Code

The following code was written in Matlab by the author to solve E.8-E.10 for the particle velocity in which the unreacted pyrex hugoniot intersects with the reacted JWL equation of state for explosives with known parameters. In this case, XTX-8003, aka X-PETN.

E.4.1 Hugoniot Crossing Estimates

```
%part velocity < 1.7
%Material properties
A2 = 5.034;
b2 = -0.176;
%up associated with known Us
```

```
up1 = (Us1-A1)/b1;
%% Symbolically solving for up2 given Hugoniots
syms up
eqn = Pressure(rho1,2*up1-up,A1,b1)==Pressure(rho2,up,A2,b2);
%Equate pressure of BF material 1 hugoniot to FF material 2
hugoniot, which will be the same on both sides
up_2 = solve(eqn,up); %solve for up given known pressure at
boundary
Us_2 = A2+b2*up_2; %get Us or outgoing shock velocity
cross = vpa(up_2);
Up = linspace(0,4,100); P2 = Pressure(rho2,Up,A2,b2);
P1_bf = Pressure(rho1,2*up1-Up,A1,b1);
P1 = Pressure(rho1,Up,A1,b1); %plotting the graphs
figure(1);
plot(Up,P1,Up,P2,Up,P1_bf);
legend('XTX','Pyrex','XTX (bf)'); ylim([0 40]);
ylabel('Pressure');xlabel('particle velocity');
```

E.4.2 JWL Equation of State Calculations

The following code is used to numerically solve for the CJ particle velocity at the witness glass slide, followed by the subroutines used within it.

```
function [P,u] = BF_Isentrope(Vol)
%the lower portion of the BF Hugoniot follows the JWL Isentrope.
This
%applies to (u,V) states below CJ
%Want to determine CJ parameters:
D = 7.35;
rho = 1.53;
P_CJ = 17; %GPa
up_CJ = P_CJ/(rho*D); %CJ particle velocity;
syms V;
eqn = JWL_I(V) == P_CJ; %Set up equation to relate JWL isentrope
to CJ pressure
%{
V_CJ = solve(eqn,V); %solve for CJ volume
V_CJ = vpa(V_CJ);
V_CJ = double(V_CJ(1));
%}
V_CJ = 0.798;
fun = @(V) sqrt(F(V));
integrand = integral(fun,V_CJ,Vol);
u = up_CJ + integrand;
P = JWL_I(Vol);
```

```
function P = Pressure(rho,up,A,b)
    P = rho.*(A.*up + b.*up.^2);


function [P,u] = BF_Hugoniot(Vol)
%the upper portion of the BF Hugoniot. This
%applies to (u,V) states above CJ
D = 7.35;
rho = 1.53;
P_CJ = 17; %GPa
up_CJ = P_CJ/(rho*D); %CJ particle velocity;
V_CJ = 0.798;

P = JWL_generic(Vol);
u = -sqrt((P-P_CJ)*(V_CJ-Vol))+up_CJ;


function P = JWL_generic(V)
%Note this is the Isentrope EOS, not the general JWL eos for XTX
    A = 27.14;
    B = 0.1793;
    C = 0.01202;
    R1 = 7; R2 = 1.6; w = 0.35;
    P_CJ = 17; %GPA
    A = A*100; B = B*100; C = C*100; %Convert to GPa
    Q = 439000;
    %Isentropic JWL EOS
    P = (A.*(1-(w./(R1.*V)).*exp(-R1.*V)) + B.*(1-
(w./(R2.*V)).*exp(-R2.*V)) + (w./V).*((P_CJ.*(1-V)+Q)./2))./(1-
((w./V).*((0.798-V))./2));

function P = JWL(V)
    A = 27.14;
    B = 0.1793;
    C = 0.01202;
    R1 = 7; R2 = 1.6; w = 0.35;


    P = A.*exp(-R1.*V)+B.*exp(-R2.*V)+C.*V.^(-(w+1));

function P = Rayleigh(V)
    A = 27.14;
    B = 0.1793;
    C = 0.01202;
    R1 = 7; R2 = 1.6; w = 0.35;
```

```
    P = -1*(-A*R1*exp(-R1*V)-B*R2*exp(-R2*V)-C*(1+w)*V^(-
(2+w)))*(1-V);


%Symbolically derive volume at CJ state
syms V;
eqn = JWL(V)-Rayleigh(V) ==0;
solve(eqn,V);
```

E.5 X-PETN Case

Without employing JWL or a polytropic gas EOS, predicting the glass particle velocity at CJ conditions for XTX calculations would yield 1.8 km/s. In reality it is product gasses hitting the glass and thus requires the JWL equation of state.[3,8] The JWL parameters from literature are used[6] and ended up predicting 1.55 km/s as the expected particle velocity on glass. It is worth mentioning that these figures are used to approximate the behavior of very large explosive charges, which may be subject to significant differences in hydrodynamic properties compared to micron scale explosives.

E.6 References

1. Marsh, S. P. *LASL Shock Hugoniot Data*; University of California Press, Berkeley, 1980.

2. Armstrong, M. R.; Grivickas, P. V.; Sawvel, A. M.; Lewicki, J. P.; Crowhurst, J. C.; Zaug, J. M.; Radousky, H. B.; Stavrou, E.; Alviso, C. T.; Hamilton, J.; Maxwell, R. S. Ultrafast Shock Compression of PDMS-based Polymers. *J. Polym. Sci. Part B Polym. Phys.* **2018**, *56* (11), 827–832. https://doi.org/10.1002/polb.24589.

3. Forbes, J. W. *Shock Wave Compression of Condensed Matter: A Primer*; Springer Berlin Heidelberg: Berlin, Heidelberg, 2012.

4. Bhowmick, M.; Nissen, E. J.; Dlott, D. D. Detonation on a Tabletop: Nitromethane with High Time and Space Resolution. *J. Appl. Phys.* **2018**, *124* (7), 075901.

5. Urtiew, P. A.; Hayes, B. Parametric Study of the Dynamic JWL-EOS for Detonation Products. *Combust. Explos. Shock Waves* **1991**, *27* (4), 505–514.

6. Dobratz, B. M. *Properties of Chemical Explosives and Explosive Simulants*; UCRL--51319, UCRL--51319(REV.1), 4285272; 1972; p UCRL--51319, UCRL--51319(REV.1), 4285272.

7. Stirpe, D.; Johnson, J. O.; Wackerle, J. Shock Initiation of XTX-8003 and Pressed PETN. *J. Appl. Phys.* **1970**, *41* (9), 3884–3893.

8. Fickett, W.; Davis, W. C. *Detonation*; University of California Press: Berkeley, CA, 1979.

APPENDIX F: PROCEDURES AND INSTRUMENT SENSITIVITY

The following section covers various data used to determine the sensitivity of the measurement instruments, including but not limited to the time and spatial resolution, synchronization procedures and routine maintenance calibrations.

F.1 PDV

F.1.1 PDV Components

PDV is home-built, consisting of off-the-shelf fiber optic components. Software analysis is home built (See Appendix A). Table F.1 lists the components used, a diagram of PDV assembly can be found in Fig. 2.8. The source laser is an Optilab TWL-C-R tunable C-band laser. The oscilloscope used is an 8 GHz, 25 Gs/s DPO 70804 Digital Phosphor Oscilloscope.

F.1.2 PDV Alignment

Coarse alignment is done with a physical alignment target for the laser. After exiting the collimator, the PDV beam is bounced off 2 gold mirrors inside kinematic mounts before being reflected off a short-pass dichroic mirror (Thorlabs DMSP926B) to become collinear with the visible light beam. To ensure the beams are collinear, the objective is removed and a phosphorescent alignment target is placed along 1 mm diameter rails (Thorlabs VRC2SM1 on cage rails) to make a beam path at least 6 inches long. By moving the target along the top and bottom of the rail line, the beam can be aligned using the 2 gold mirrors.

Finer alignment is done with a piece of 30°C liquid crystal paper mounted on the sample plane of the microscope. The beam spot can be visibly seen through the CMOS camera or eyepiece, and finely aligned with the closest gold mirror to the center of the field of view. From here the flyer plate must be aligned to match the center of the field of view and maximize signal.

Table F.1 List of PDV components used for experiments in this dissertation.

MFG	*SKU*	*Description*
OEQuest	**BP1550-NTF1-FCA**	**Bandpass Filter 1530-1563**
OEQuest	**gEDFA-17**	**17 dBm Output, High Gain Rackmount EDFA**
OEQuest	**EDFA-MP-MSA**	**20 dBm EDFA Module, MSA Type**
OEQuest	**EDFA-I-16-B**	**16 dBm Inline Erbium-Doped Fiber Amplifier, Benchtop, +25 dB Gain**
OEQuest	**EDFA-C-24-M**	**C-Band EDFA Module, +24 dBm**
Digi-Key	**SCMR-100K20G-30-15-10**	**20 GHz Optical receiver**
OEQuest	**LC-3x3-1550-FCA**	**3x3 1550nm Coupler with FC/APC Connectors**
OEQuest	**DD600-P40**	**C-Band PM Type Motor Driven VOA with Fc/APC Connectors**
OEQuest	**CIRC-15-3-FCA**	**1550nm 3-Port Circulator with FC/APC Connectors**
OEQuest	**PMISO-15-D-FCA**	**1550nm PM Dual Stage Isolator with FC/APC connectors**
Newport	**F-POL-APC**	**Fiber Polarization Controller Male**
Newport	**F-CPL-S12151-FCAPC**	**Fiber Coupler, Single Wavelength, 1 x 2, 10/90, 1550 nm, FC/APC**
Newport		**Fiber Coupler, Wavelength Flattened, 1 x 2, 50/50, 1550nm, FC/APC**
Thorlabs	**P3-SMF28Y-FC-1**	**Single Mode Patch Cable, 1260-1625 nm, FC/APC, 900 um Jacket, 1m Long**
Thorlabs	**SMF-28-J9**	**SMF-28 Ultra with Ø900 µm Jacket, Ø125 µm Cladding (1 ft.)**
OEQuest	**TWL-C-R**	**C Band Tunable Wavelength Laser, 30mW, PM output, Rackmount**

F.1.3 Aligning Flyer Plate to PDV

Using a well aligned PDV beam, the flyer plate can be precisely aligned to closely match center field of view to ensure the planar shock region is being analyzed. A slow velocity (<2 km/s) is typically chosen to align the flyer plate, which also leaves a clean, round crater that makes visual inspection easy. A flyer is launched, and the signal strength of the PDV is optimized in the x and y-axes separately by moving the translation stages of the entire microscope itself. The flyer crater should visually appear nearly center of field of view. If it appears far off, then F.1.2 should be repeated.

F.1.4 PDV Timing

The time-zero by which all instruments synchronize is the moment the flyer plate begins moving. The oscilloscope is triggered by a photodiode pointed at scattered light from behind a corner mirror in the launch laser line. The 90% maximum rising edge of the photodiode pulse is used as a time zero reference, which has a known offset from the flyer launch. The offset is determined by ablating a glass window with 8 nm of chromium (*via* e-beam deposition). This creates a sharp rising edge on the PDV signal, the distance between the 90% maximum rising edge of the photodiode and the rising edge of the PDV signal is the offset used in data processing. The value is usually around ~-33 ns, but recalibrated yearly. The standard deviation of the flyer launch time is about 1 ns, representing the maximum time resolution possible for knowing impact time.

F.2 Emission Pyrometer

F.2.1 Spectral Calibration

Calibration is done using a home-built monochrometer with <~5 nm FWHM. The peak wavelength is verified by a calibrated spectrometer (Ocean Optics USB-4000). The light is

directed into the microscope *via* a fiber optic, and the monochrometer is adjusted until the signal voltage is isolated to a single PMT. The wavelength of this configuration is recorded by the spectrometer and recorded as the center wavelength of the PMT channel. The width of each channel is fixed and determined from previous work to be about 10 nm[1,2].

F.2.2 Radiance Calibration

Spectral radiance is calibrated based on an integration sphere/lamp combination that was previously calibrated (Labsphere 2IN-USS-MICROSCOPE-SF integration sphere and Ocean Optics HL-2000). The halogen light source is a black body source at 2.960 kK and the combination was calibrated by Labsphere, Inc. (Report Number 100457-1-1). The integration sphere is mounted in the microscope such that the output port is on the plane of the victim samples. The light is directed to the photomultiplier tubes and the digitizer is set to calibration mode in the software, which uses a 1 MOhm termination. This is done to increase the signal to noise ratio for the long duration, low intensity signal provided by the calibration source. The input signal strength of the PMTs during this calibration is used to create a multiplicative calibration factor to the measurement results. Calibration to measure everything in radiance units allows different experiments to be directly comparable to one another in a common unit of measurement (See Appendix B for Matlab implementation).

F.2.3 Analyzing Field of View (FOV)

Unless otherwise stated, since the main objective and the imaging optic of the emission to the photomultiplier tubes are identical (10X), the field of view is implied to be the width of the vertical slit of the spectrometer by the mode-field diameter of the fiber-optics at the imaging plane. Throughout this dissertation these are kept at 65 μm × 100 μm. To test this, a point source

of known size - a 50 μm MFD fiber (Thorlabs FG050LGA) coupled to an irradiance source (Stellarnet SL1-Cal) is placed at the focus of the objective. From there the source can be moved across the vertical and horizontal axis until the pyrometer no longer sees the signal. The distance between dark points is the size of the analysis window. This procedure is useful particularly if a condenser lens is used before the pyrometer objective to increase the field of view. This is used in Chapter 6 to analyze the radiance of light produced by a whole frame of the camera.

F.2.4 Determining Time Zero

For all equipment, time zero is strictly defined as the time that the launch laser arrives at the flyer plate. Otherwise stated, time zero for instruments is defined as when the flyer plate begins moving. The procedure to verify this utilizes the same procedure as F.1.4: An 8 nm layer of silver is hit with a launch laser pulse. The light produced is very intense, multiple ND filters are needed to properly attenuate the light produced. The rising edge of the light trace, defined as 5X root-mean-squared noise floor, should appear at 1-ns. The delay generator setting for the PMT digitizer triggering should be moved backward or forward until this is the case.

F.2.5 Alignment Procedures

Alignment of the pyrometer emission light is performed using a true point source of light: dye fluorescence. A ~30 μm thick spin coated layer of PMMA with 1 mM Rhodamine-6G is placed in the traditional sample holder. A 532 nm laser is focused on the rhodamine dye, creating a point source of fluoresced green-red light. The output light is sent through a 532-nm notch filter to remove the laser light, what is left is ~1mm diameter collimated beam of light that can be used for traditional alignment procedures.

F.2.6 Accounting for Thicker Sample Materials

To verify how the emissions of explosive charges relate to their depth and output shock wave, particularly at the rising edge, an experiment was devised simultaneously measuring PDV and PMT output at the same time. A 90 μm deep X-PETN charge (20% Sylgard 182, 80% ultrafine PETN, see Chapter 7) was placed in a sample well half occluded by a 100 nm gold layer. The PDV was slightly misaligned to overlap the occluded half and give a shock wave output and the PMT probe, or in this case a simple photodiode, was misaligned to view the clear section.

F.3 High Speed Photography

Note that intensity calibration is not covered in this dissertation, as it is not leveraged in the work. For more information on this, consult Belinda Pacheco Johnson's dissertation.[3]

F.3.1 Verifying Timing

To verify exposure times and timing accuracy, a bright light pulse of a short, known duration is required. Ideally, a pulse of duration less than the exposure window being tested. Two procedures will be shown: One based on a 90-fs white light pulse and one based on the 16 ns YAG pulse frequency doubled to 532 nm.

F.3.2 Using an Ultrafast Pulse

In this experiment, the timing of the camera acquisition is moved while the laser pulse is kept constant. Using a 90 fs ultrafast laser (Spectraphysics Solstace amplifier), a visible light pulse can either be generated from an OPA (Light Conversion Topaz-Prime) set at ~580 nm or white light generation. White light generation is simply focusing the 800 nm ultrafast pulse into a dielectric material such as C-cut sapphire. The output is filtered for 750+ nm light and

recollimated using an objective lens (Nikon CFI Plan Flour 4x). Either light source is directed into the external port of the shock compression microscope and imaged onto a mirror placed on the sample plane. This usually consists of a piece of glass with ~8 nm silver coating from e-beam deposition. The result is an intense point source of visible light in the ~100-200 femtosecond time range.

The timing of camera capture is moved backwards or forwards in time to track the delay settings at which the pulse appears or disappears, providing an effective exposure time. The nature of this experiment also reverses the time axis: the camera acquisition moving backwards is the same as the pulse moving forwards. As a result, the example results show the trailing edges matching up rather than the leading edges.

F.3.3 Using Launch Laser for Exposure Time

The launch laser is 16 nm which isn't ideal for testing resolution windows but will work when the exposure frames straddle the lead or falling edges (the leading edge is preferred because it is sharper. The launch laser is heavily attenuated, the variable attenuator is set to an output of <50 mJ energy, then a reflective ND filter set is placed in the way of the laser (ND of 2 and ND of 1.2). A beta barium borate (BBO) crystal is set on the plane of the launch laser focus (where the flyer is launched from). A near-IR filter is stacked below the crystal to filter any fundamental frequency light. This creates an intense, frequency-doubled (532 nm) pulse easily visible to detectors. The camera exposure window is moved backward or forward in time delay until the green light is dimmer, then moved further until it disappears. If the exposure window being tested is < 16 ns, the exposure is tested by the movement in delay time from which the camera image goes from dark to maximum brightness. This is representative of the length of time the rising edge takes to travel across the exposure window. If the exposure window is > 16

ns, measuring exposure time is simply the time it takes for the image to go from dark to bright to dark again.

F.3.4 Using Launch Laser to Verify Time-Zero

To verify the accuracy of the time delay, follow the procedure in Section F.4.3 to find the time delay needed for the light to go from full brightness to beginning to dim. Note that because the leading edge of the pulse needs to match the leading edge of the flyer plate, the camera needs to fully straddle the pulse, then move down in delay time until the light begins to get dimmer. This method fixes the timing of the camera to the same protocol as the PMT and PDV.

F.3.5 Verifying Spatial Resolution

Spatial resolution is determined by using an established image calibration target. In this case, the 1951 U.S. Air Force resolution chart (Thorlabs R1DS1P and R1DS1N) is used to determine the conversion from pixels to distance in any imaging (except SEM) in this dissertation. This provides information on the limiting resolution of a particular imaging setup, written in mm or line-pair per millimeter. The resolution is simply the value provided by the smallest line pair set that can be separated visually by camera:

$$Resolution = 2\left(N_{group} + \frac{N_{element}-1}{6}\right) \qquad \text{(F.1)}$$

Examples of these images can be found in Figure F.01. Rather than the resolution of the detector itself, the limiting factors more often are the optical assembly and the backlighting. For most applications in this dissertation, line pairs can be seen down to Group 7 - Element 6, implying a 230 lp/mm resolution or ~4 μm resolution limit. Most of the individual crystals and features studied in this dissertation have average lengths above 2 μm so this limit is acceptable.

F.3.6 Results: Single-Frame intensified CMOS (Andor iStar)

The single-frame intensified CMOS camera results don't qualify as a high-speed video per say. It is a stitching of several separate events at different time frames, which are accepted as identical events. This method is only used in Chapter 7, or the shock to detonation of PETN-based PBXs. These are highly homogeneous and only show heterogeneity in the very earliest time frames (<5 ns). The benefit of this method is the excellent contrast and image quality while providing <5 ns time resolution. Using the procedure in section F.4.2 for a femtosecond white light pulse and a 30 ns doubled YAG pulse, the time resolution results for various exposure times are graphed in Fig. F.2

F.4 Figures

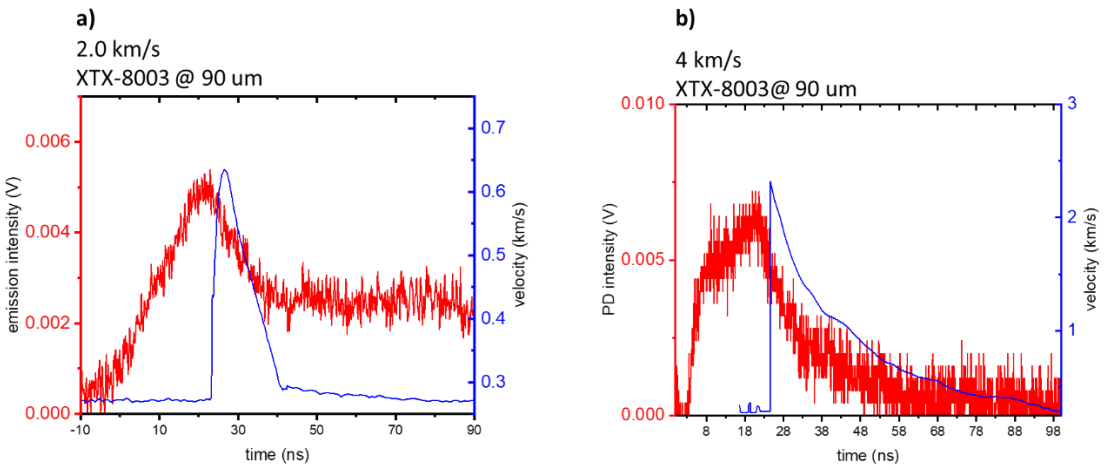

Figure F.1 Simultaneous measurement of emission photodiode and PDV data to show relative timing of the shockwave exiting the sample cylinder and the light emission of an X-PETN sample when shock initiated. Time zero is time of arrival for the flyer plate traveling at 2.0 km/s (a) and 4 km/s (b).

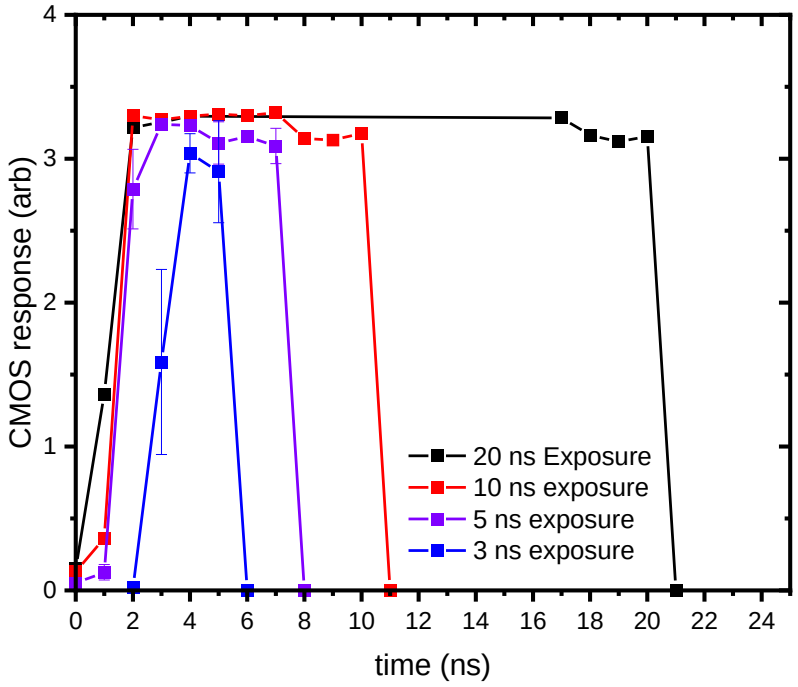

Figure F.2 Timing calibration of different exposure windows for iCMOS camera used in Chapter 7. Time zero is the time the CMOS is triggered, and the response is the amount of light from an ultrafast (~120 fs) light source when the light source is delayed by the x-axis time.

F.5 References

1. Bassett, W. P. SHOCK INITIATION OF EXPLOSIVES UNDER THE MICROSCOPE. 178.
2. Bassett, W. P.; Dlott, D. D. Multichannel Emission Spectrometer for High Dynamic Range Optical Pyrometry of Shock-Driven Materials. *Rev. Sci. Instrum.* **2016**, *87* (10), 103107.
3. Pacheco, B. TRACKING HOT SPOT DYNAMICS IN SOLID STATE EXPLOSIVES WITH SHOCK COMPRESSION MICROSCOPY. 259.